
Development of a Multiaxial Viscoelastoplastic Continuum Damage Model for Asphalt Mixtures

PUBLICATION NO. FHWA-HRT-08-073

SEPTEMBER 2009



U.S. Department of Transportation
Federal Highway Administration

Research, Development, and Technology
Turner-Fairbank Highway Research Center
6300 Georgetown Pike
McLean, VA 22101-2296

FOREWORD

The constitutive modeling of asphalt concrete behavior is a topic that has gained national importance in the past few years. Such modeling efforts have the explicit goal of providing for better design and analysis of asphalt pavement structures to resist failure and/or better predict when failure will occur. These efforts should thus provide the tools necessary to better utilize available resources and/or to gain maximum results from limited resources. One such modeling effort that encompasses the two main forms of pavement distress, cracking and permanent deformation, is the multiaxial viscoelastoplastic continuum damage (MVEPCD) model and finite element package, finite element program (FEP++). The MVEPCD model combines elements of viscoelasticity, continuum damage mechanics, and viscoplasticity to model the material behavior, and FEP++ is used to model the interaction of material and structure.

The MVEPCD model has been characterized and verified using asphalt concrete mixtures tested at the Federal Highway Administration's Accelerated Load Facility in McLean, VA. A novel approach to modeling this process is suggested and verified in this work. In light of practical concerns related to constant rate tests using the Asphalt Mixture Performance Tester and due to the complexities of performing true time-dependent analysis of cyclic fatigue tests, a refined and simplified viscoelastoplastic continuum damage model is presented. A robust FEP++ has been developed to account for the effects of loading and boundary conditions. Analysis can be performed in either two-dimensional or three-dimensional configurations. The resulting predictions are deemed reasonable and, thus, a reliable simulation of pavement response.

Cheryl Allen Richter
Acting Director, Office of Infrastructure
Research and Development

Notice

This document is disseminated under the sponsorship of the U.S. Department of Transportation in the interest of information exchange. The U.S. Government assumes no liability for the use of the information contained in this document.

The U.S. Government does not endorse products or manufacturers. Trademarks or manufacturers' names appear in this report only because they are considered essential to the objective of the document.

Quality Assurance Statement

The Federal Highway Administration (FHWA) provides high-quality information to serve Government, industry, and the public in a manner that promotes public understanding. Standards and policies are used to ensure and maximize the quality, objectivity, utility, and integrity of its information. FHWA periodically reviews quality issues and adjusts its programs and processes to ensure continuous quality improvement.

TECHNICAL REPORT DOCUMENTATION PAGE

1. Report No. FHWA-HRT-08-073	2. Government Accession No.	3. Recipient's Catalog No.	
4. Title and Subtitle Development of a Multiaxial Viscoelastoplastic Continuum Damage Model for Asphalt Mixtures		5. Report Date September 2009	
		6. Performing Organization Code	
7. Author(s) Y. Richard Kim, Ph.D. P.E., M.N. Guddati, Ph.D., B.S. Underwood, T.Y. Yun, V. Subramanian, S. Savadatti		8. Performing Organization Report No.	
9. Performing Organization Name and Address North Carolina State University Department of Civil, Construction, and Environmental Engineering Campus Box 7908 Raleigh, NC 27695		10. Work Unit No. (TRAIS)	
		11. Contract or Grant No. DTFH61-05-H-00019	
12. Sponsoring Agency Name and Address Office of Research and Technology Services Federal Highway Administration 6300 Georgetown Pike McLean, VA 22101-2296		13. Type of Report and Period Covered	
		14. Sponsoring Agency Code FHWA	
15. Supplementary Notes Project performed under FHWA DTFH61-05-H-00019; FHWA AOTR: Katherine Petros			
16. Abstract This report highlights findings from the FHWA DTFH61-05-H-00019 project, which focused on the development of the multiaxial viscoelastoplastic continuum damage model for asphalt concrete in both compression and tension. Asphalt concrete pavement, one of the largest infrastructure components in the United States, is a complex system that involves multiple layers of different materials, various combinations of irregular traffic loading, and various environmental conditions. The performance of this structure is closely related to the performance of asphalt concrete. To predict the performance of asphalt concrete with reasonable accuracy, a better understanding of its deformation behavior under realistic conditions is urgently needed. Over the past decade, the authors have been successful in developing uniaxial material models that can accurately capture various critical phenomena such as microcrack-induced damage that is critical in fatigue modeling, strain-rate temperature interdependence, and viscoplastic flow, which is critical for high temperature modeling. The resulting model is termed the viscoelastoplastic continuum damage model. However, to consider the complicated nature of in-service stress states, a multidimensional model is needed. To predict the performance of the real pavement structures, it is also important to incorporate the material model in a pavement model that considers the vehicle and climatic loads as well as the boundary conditions; the in-house finite element package has been developed for this purpose.			
17. Key Words Constitutive modeling, Asphalt concrete, Viscoelastic, Viscoplastic, Multiaxial, VECD, Damage mechanics		18. Distribution Statement No restrictions. This document is available through the National Technical Information Service, Springfield, VA 22161.	
19. Security Classif. (of this report) Unclassified	20. Security Classif. (of this page) Unclassified	21. No. of Pages 264	22. Price

SI* (MODERN METRIC) CONVERSION FACTORS

APPROXIMATE CONVERSIONS TO SI UNITS

Symbol	When You Know	Multiply By	To Find	Symbol
LENGTH				
in	inches	25.4	millimeters	mm
ft	feet	0.305	meters	m
yd	yards	0.914	meters	m
mi	miles	1.61	kilometers	km
AREA				
in ²	square inches	645.2	square millimeters	mm ²
ft ²	square feet	0.093	square meters	m ²
yd ²	square yard	0.836	square meters	m ²
ac	acres	0.405	hectares	ha
mi ²	square miles	2.59	square kilometers	km ²
VOLUME				
fl oz	fluid ounces	29.57	milliliters	mL
gal	gallons	3.785	liters	L
ft ³	cubic feet	0.028	cubic meters	m ³
yd ³	cubic yards	0.765	cubic meters	m ³
NOTE: volumes greater than 1000 L shall be shown in m ³				
MASS				
oz	ounces	28.35	grams	g
lb	pounds	0.454	kilograms	kg
T	short tons (2000 lb)	0.907	megagrams (or "metric ton")	Mg (or "t")
TEMPERATURE (exact degrees)				
°F	Fahrenheit	5 (F-32)/9 or (F-32)/1.8	Celsius	°C
ILLUMINATION				
fc	foot-candles	10.76	lux	lx
fl	foot-Lamberts	3.426	candela/m ²	cd/m ²
FORCE and PRESSURE or STRESS				
lbf	poundforce	4.45	newtons	N
lbf/in ²	poundforce per square inch	6.89	kilopascals	kPa

APPROXIMATE CONVERSIONS FROM SI UNITS

Symbol	When You Know	Multiply By	To Find	Symbol
LENGTH				
mm	millimeters	0.039	inches	in
m	meters	3.28	feet	ft
m	meters	1.09	yards	yd
km	kilometers	0.621	miles	mi
AREA				
mm ²	square millimeters	0.0016	square inches	in ²
m ²	square meters	10.764	square feet	ft ²
m ²	square meters	1.195	square yards	yd ²
ha	hectares	2.47	acres	ac
km ²	square kilometers	0.386	square miles	mi ²
VOLUME				
mL	milliliters	0.034	fluid ounces	fl oz
L	liters	0.264	gallons	gal
m ³	cubic meters	35.314	cubic feet	ft ³
m ³	cubic meters	1.307	cubic yards	yd ³
MASS				
g	grams	0.035	ounces	oz
kg	kilograms	2.202	pounds	lb
Mg (or "t")	megagrams (or "metric ton")	1.103	short tons (2000 lb)	T
TEMPERATURE (exact degrees)				
°C	Celsius	1.8C+32	Fahrenheit	°F
ILLUMINATION				
lx	lux	0.0929	foot-candles	fc
cd/m ²	candela/m ²	0.2919	foot-Lamberts	fl
FORCE and PRESSURE or STRESS				
N	newtons	0.225	poundforce	lbf
kPa	kilopascals	0.145	poundforce per square inch	lbf/in ²

*SI is the symbol for the International System of Units. Appropriate rounding should be made to comply with Section 4 of ASTM E380.
(Revised March 2003)

TABLE OF CONTENTS

EXECUTIVE SUMMARY	1
CHAPTER 1. INTRODUCTION	3
1.1. PROBLEM STATEMENT	3
1.2. OBJECTIVES	4
1.3. RESEARCH SCOPE	4
CHAPTER 2. CONSTITUTIVE MODELING WITH A MULTIAXIAL VISCOELASTOPLASTIC CONTINUUM DAMAGE MODEL	5
2.1. HISTORICAL PERSPECTIVE	5
2.2. MODELING APPROACH	5
2.2.1. Linear Viscoelasticity	6
2.2.2. Correspondence Principle	9
2.2.3. Continuum Damage	12
2.2.4. Viscoelastic Continuum Damage Theory	12
2.3. MULTIAXIAL VISCOELASTIC CONTINUUM DAMAGE MODEL	17
2.3.1. Review of Mechanistic Principles	17
2.3.2. Application of Schapery's Work Potential Theory	21
2.4. THEORY OF VISCOPLASTICITY	24
2.4.1. Flow Rule	25
2.4.2. Yield Criterion	26
2.5. VISCOPLASTIC MODELS	28
2.5.1. Simple Strain-Hardening Model	28
2.5.2. HISS-Perzyna Model	30
2.5.3. Unified Model	32
2.6. VISCOELASTOPLASTIC CONTINUUM DAMAGE MODEL	35
CHAPTER 3. SPECIMEN FABRICATION AND TESTING PROTOCOLS	37
3.1. MATERIALS	37
3.2. SPECIMEN FABRICATION	39
3.3. TEST SETUP	39
3.4. TEST PROTOCOLS	40
3.4.1. Complex Modulus Test	41
3.4.2. Constant Crosshead Rate Tests	41
3.4.3. Repetitive Creep and Recovery Tests	43
3.5. DATA ANALYSIS	48
CHAPTER 4. MVEPCD CHARACTERIZATION AND VERIFICATION IN TENSION	49
4.1. INTRODUCTION	49
4.2. MVECD CHARACTERIZATION IN TENSION	50
4.2.1. Linear Viscoelastic Characterization	50
4.2.2. Modeling Stress State Dependence of the $ E^* $	59
4.2.3. MVECD Damage Function Characterization	60
4.3. VISCOPLASTIC MODELING OF ASPHALT CONCRETE IN TENSION	78
4.4. MVEPCD MODEL VERIFICATION	79

4.5. t-TS WITH GROWING DAMAGE IN TENSION	81
4.6. ENGINEERING BEHAVIOR IN CONFINED TENSION	87
4.7. FATIGUE ANALYSIS WITH VECD MODEL	89
4.7.1. VECD Integrated Formulation Summary.....	89
4.7.2. Formulation of Lee, Daniel, and Kim	90
4.8. SIMPLIFIED ANALYSIS OF CYCLIC FATIGUE DATA.....	92
4.8.1. Correction Factor in Formulation of Lee, Daniel, and Kim.....	92
4.8.2. Rigorous Analysis of Pseudo Strain History Effects.....	94
4.8.3. Discussion of Simplified Model Approach.....	101
4.9. REFINED DERIVATION OF SIMPLIFIED FATIGUE MODEL.....	102
4.9.1. Identification of Tensile Loading Time.....	103
4.9.2. Defining Alpha	104
4.9.3. Failure in Cyclic Mode of Loading	104
4.9.4. Refined Simplified Model Derivation.....	105
4.9.5. Model Application.....	107
4.9.6. Simplifications to Refined Model	110
4.10. SUMMARY	113
CHAPTER 5. MVEPCD CHARACTERIZATION AND VERIFICATION IN	
COMPRESSION.....	115
5.1. ENGINEERING BEHAVIOR OF ASPHALT CONCRETE IN COMPRESSION ...	115
5.1.1. Constant Rate Compression	115
5.1.2. Repetitive Creep and Recovery Test	119
5.1.3. t-TS with Growing Damage in Compression	125
5.2. MVECD CHARACTERIZATION IN COMPRESSION	136
5.2.1. Linear Viscoelastic Characterization.....	136
5.2.2. Comparison of Zero-Mean and Zero-Maximum Deviatoric Stress Results.....	140
5.2.3. MVECD Damage Function Characterization.....	143
5.2.4. Comparison of MVECD Behavior in Compression and Tension	146
5.3. VISCOPLASTIC MODELING OF ASPHALT CONCRETE IN	
COMPRESSION.....	149
5.3.1. A Phenomenological Model Considering Pulse Time Effects	149
5.3.2. HISS-Perzyna Model.....	158
5.3.3. Development of a Viscoplastic Model Using Rate-Dependent Yield Stress	166
5.4. CHARACTERIZATION AND VERIFICATION OF THE VISCOPLASTIC	
MODEL	172
5.4.1. Calibration	172
5.4.2. Verification.....	175
CHAPTER 6. ENHANCEMENT OF VEPCD-FEP++ FOR PAVEMENT	
MODELING.....	181
6.1. DAMAGE IN VISCOELASTIC MATERIALS	181
6.1.1. The Original Model	181
6.1.2. Upgraded Constitutive Model	184
6.1.3. Damage Model	186
6.1.4. Finite Element Implementation	187
6.1.5. Verification.....	188
6.1.6. Implementation of Temperature Dependency	190

6.2. REDESIGN OF FEP++	192
6.2.1. Domain Module.....	192
6.2.2. Analysis Module.....	195
6.3. PREPROCESSOR.....	196
6.3.1. Input Stage.....	200
6.3.2. Analysis Stage.....	201
6.3.3. Postprocessing Stage.....	203
6.4. POSTPROCESSOR.....	203
CHAPTER 7. A SAMPLE 3D PAVEMENT SIMULATION USING FEP++.....	205
7.1. THE INPUT DATA	205
7.2. EFFECT OF TEMPERATURE	205
7.3. EFFECT OF MATERIAL	210
7.4. EFFECT OF WHEEL SPEED	213
CHAPTER 8. CONCLUSIONS AND FUTURE WORK	219
8.1. CONCLUSIONS	219
8.2. FUTURE WORK.....	220
APPENDIX. USER MANUAL FOR FEP++.....	223
A.1. INSTALLATION OVERVIEW	223
A.2. LIST OF INPUT DIALOGS	223
A.2.1. General Information Dialog.....	223
A.2.2. Material Properties Dialog	224
A.2.3. Elastic Material Properties Dialog.....	226
A.2.4. Viscoelastic Material Properties Dialog.....	227
A.2.5. Prony Coefficients Dialog	228
A.2.6. Layer Properties Dialog.....	230
A.2.7. Mesh Parameters Dialog.....	231
A.2.8. Load Properties Dialog.....	233
A.2.9. Analysis Parameters Dialog	235
A.2.10. Summary Dialog.....	237
A.2.11. Generating an Input File.....	238
A.2.12. Running Analysis	238
REFERENCES.....	241

LIST OF FIGURES

Figure 1. Graph. Schematic representation of dynamic modulus shifting process with unshifted data	10
Figure 2. Graph. Schematic representation of dynamic modulus shifting process with shifted data	10
Figure 3. Graph. Schematic representation of dynamic modulus shifting process with time-temperature shift factor.....	11
Figure 4. Graph. Constant crosshead test results in stress-strain space	11
Figure 5. Graph. Constant crosshead test results in stress-pseudo strain space.....	12
Figure 6. Graph. Comparison of refined and approximate damage calculation techniques	16
Figure 7. Graph. Comparison of refined and approximate damage characteristic relationship ...	16
Figure 8. Illustration. Mechanical analog for the viscoplastic model.....	26
Figure 9. Illustration. Isotropic hardening diagram	28
Figure 10. Illustration. Kinematic hardening diagram.....	28
Figure 11. Illustration. Strain decomposition from creep and recovery testing.....	30
Figure 12. Illustration. Typical yield surface of HISS model.....	31
Figure 13. Graph. Mixture gradation chart.....	38
Figure 14. Graph. Comparison of test lane and laboratory gradations	39
Figure 15. Graph. Stress history of VL testing (unconfined and 140 kPa confinement VL)	45
Figure 16. Graph. Stress history of VL testing (500 kPa confinement VL).....	45
Figure 17. Graph. Stress history of VLT testing (140 kPa confinement).....	47
Figure 18. Graph. Stress history of VLT testing (500 kPa confinement).....	48
Figure 19. Graph. Effect of 500 kPa confining pressure on the dynamic modulus in semi-log space.....	55
Figure 20. Graph. Effect of 500 kPa confining pressure on the dynamic modulus in log-log space.....	56
Figure 21. Graph. Effect of 500 kPa confining pressure on observed elasticity in the Control mixture	56
Figure 22. Graph. Effect of 500 kPa confining pressure on the log shift factor function.....	57
Figure 23. Graph. Effect of confining pressure on the relaxation spectrum.....	57
Figure 24. Graph. Use of the uniaxial relaxation spectrum for multiaxial test results	58
Figure 25. Graph. Effect of performing confined temperature/frequency sweep testing on the unconfined dynamic modulus	58
Figure 26. Graph. Multiaxial equilibrium characterization results.....	59
Figure 27. Graph. Multiaxial dynamic modulus model strength.....	60
Figure 28. Graph. C_{11} versus S for tension for Control-2006 mixture (5 °C reference).....	61
Figure 29. Graph. Effect of time-dependent Poisson's ratio on C_{12} calculation.....	62
Figure 30. Graph. C_{12} characteristic curve for Control-2006 mixture.....	63
Figure 31. Graph. C_{12} characteristic curve for Control-2006 mixture in semi-logarithmic space.....	64
Figure 32. Graph. Effect of different time-independent Poisson's ratio values on radial strain predictions.....	65
Figure 33. Graph. C_{12} versus S for tensile loading for Control-2006 mixture (5 °C reference) ...	66
Figure 34. Graph. S as a function of reduced time calculated by three different methodologies in arithmetic space for 5-1-T.....	70

Figure 35. Graph. S as a function of reduced time calculated by three different methodologies in arithmetic space for 5-3-T.....	70
Figure 36. Graph. S as a function of reduced time calculated by three different methodologies in arithmetic space for 5-4-T.....	71
Figure 37. Graph. S as a function of reduced time calculated by three different methodologies in arithmetic space for 5-5-T.....	71
Figure 38. Graph. S as a function of reduced time calculated by three different methodologies in logarithmic space for 5-1-T.....	72
Figure 39. Graph. S as a function of reduced time calculated by three different methodologies in logarithmic space for 5-3-T.....	72
Figure 40. Graph. S as a function of reduced time calculated by three different methodologies in logarithmic space for 5-4-T.....	73
Figure 41. Graph. S as a function of reduced time calculated by three different methodologies in logarithmic space for 5-5-T.....	73
Figure 42. Graph. Predicted and measured stress as a function of reduced time for different S calculation methodologies for 5-1-T.....	74
Figure 43. Graph. Predicted and measured stress as a function of reduced time for different S calculation methodologies for 5-3-T.....	74
Figure 44. Graph. Predicted and measured stress as a function of reduced time for different S calculation methodologies for 5-4-T.....	75
Figure 45. Graph. Predicted and measured stress as a function of reduced time for different S calculation methodologies for 5-5-T.....	75
Figure 46. Graph. C_{22} as a function of S calculated by different methodologies for 5-1-T.....	76
Figure 47. Graph. C_{22} as a function of S calculated by different methodologies for 5-3-T.....	76
Figure 48. Graph. C_{22} as a function of S calculated by different methodologies for 5-4-T.....	77
Figure 49. Graph. C_{22} as a function of S calculated by different methodologies for 5-5-T.....	77
Figure 50. Graph. Representative C_{22} versus S for tension using optimization methodology (5 °C reference).....	78
Figure 51. Graph. Effect of confining pressure on coefficient Y	79
Figure 52. Graph. Results of MVEPCD model simple verification for constant crosshead rate tests under 500 kPa confinement at 25 °C.....	80
Figure 53. Graph. Results of MVEPCD model verification for constant crosshead rate tests under 250 kPa confinement at 40 °C.....	80
Figure 54. Graph. Results of MVEPCD model verification for constant crosshead rate tests under 250 kPa confinement at 5 °C.....	81
Figure 55. Illustration. Schematic representation of first step for verifying the t-TS principle under growing damage, finding stress for different tests at a consistent strain level.....	82
Figure 56. Illustration. Schematic representation of the second step for verifying the t-TS principle under growing damage, finding reduced time for the stress found in the first step for each test.....	82
Figure 57. Illustration. Schematic representation of the third step for verifying the t-TS principle under growing damage, plotting the stress from the first step against the reduced time from the second step.....	83
Figure 58. Graph. Strain levels examined for verifying the t-TS principle under growing damage and confining pressure for the Control-2006 mixture.....	84

Figure 59. Graph. t-TS with growing damage under confinement verification at a 0.0001 ϵ level.....	84
Figure 60. Graph. t-TS with growing damage under confinement verification at a 0.0005 ϵ level.....	85
Figure 61. Graph. t-TS with growing damage under confinement verification at a 0.001 ϵ level.....	85
Figure 62. Graph. t-TS with growing damage under confinement verification at a 0.0022 ϵ level.....	86
Figure 63. Graph. t-TS with growing damage under confinement verification at a 0.004 ϵ level.....	86
Figure 64. Graph. t-TS with growing damage under confinement verification at a 0.007 ϵ level.....	87
Figure 65. Graph. Effect of 500 kPa confining pressure on strength mastercurves	88
Figure 66. Graph. Effect of 500 kPa confining pressure on ductility in constant crosshead rate tests	88
Figure 67. Illustration. A schematic representation of the concept of average dC/dt	93
Figure 68. Illustration. A schematic representation of the effect of the M factor on dC/dt used in calculation.....	93
Figure 69. Illustration. Mathematical equivalence of the formulation used by Lee, Daniel, and Kim.....	94
Figure 70. Illustration. Schematic representation of assumptions made for controlled stress cyclic loading to develop Q and M factors	96
Figure 71. Illustration. Schematic representation of assumptions made for controlled crosshead cyclic loading to develop Q and M factors.....	97
Figure 72. Graph. Damage characteristic comparison, cyclic to monotonic using equation 127 Control mixture.....	100
Figure 73. Graph. Damage characteristic comparison, cyclic to monotonic using equation 127 CRTB mixture.....	100
Figure 74. Graph. Damage characteristic comparison, cyclic to monotonic using equation 127 SBS mixture.....	101
Figure 75. Graph. Damage characteristic comparison, cyclic to monotonic using equation 127 Terpolymer mixture	101
Figure 76. Graph. Damage characteristic comparison, cyclic to monotonic using refined model Control mixture.....	108
Figure 77. Graph. Damage characteristic comparison, cyclic to monotonic using refined model CRTB mixture.....	108
Figure 78. Graph. Damage characteristic comparison, cyclic to monotonic using refined model SBS mixture.....	109
Figure 79. Graph. Damage characteristic comparison, cyclic to monotonic using refined model Terpolymer mixture	109
Figure 80. Graph. Damage characteristic comparison, cyclic to monotonic using refined simplified model Control mixture.....	110
Figure 81. Graph. Damage characteristic comparison, cyclic to monotonic using refined simplified model CRTB mixture	111
Figure 82. Graph. Damage characteristic comparison, cyclic to monotonic using refined simplified model SBS mixture.....	111

Figure 83. Graph. Damage characteristic comparison, cyclic to monotonic using refined simplified model Terpolymer mixture	112
Figure 84. Graph. Damage characteristic comparison, cyclic to monotonic using refined simplified model 9.5-mm Fine mixture	112
Figure 85. Graph. Stress-strain curves for unconfined constant strain-rate tests.....	116
Figure 86. Graph. Stress-strain curves for 500 kPa confinement constant strain-rate tests.....	116
Figure 87. Graph. Comparison of 500 kPa confinement and unconfined constant rate tests for 5 °C.....	117
Figure 88. Graph. Comparison of 500 kPa confinement and unconfined constant rate tests for 25 °C.....	117
Figure 89. Graph. Comparison of 500 kPa confinement and unconfined constant rate tests for 40 °C.....	118
Figure 90. Graph. Comparison of 500 kPa confinement and unconfined constant rate tests for 55 °C.....	118
Figure 91. Graph. Viscoplastic strain versus cumulative loading time (unconfined VL)	119
Figure 92. Graph. Viscoplastic strain versus cumulative loading time (140 kPa confinement VL).....	120
Figure 93. Graph. Viscoplastic strain versus cumulative loading time (500 kPa confinement VL).....	120
Figure 94. Graph. Viscoplastic strain versus cumulative loading time (unconfined VT testing).....	122
Figure 95. Graph. Viscoplastic strain versus cumulative loading time (500 kPa confinement for VT and RVT testing).....	122
Figure 96. Graph. Incremental viscoplastic strain rate versus viscoplastic strain (500 kPa confinement, 1,600 kPa deviatoric).....	123
Figure 97. Graph. Viscoplastic strain versus cumulative loading time (500 kPa confinement CLT).....	124
Figure 98. Graph. Viscoplastic strain versus cumulative loading time (140 kPa confinement VT).....	124
Figure 99. Graph. Stress-time curves for the Control mixture before the application of time-temperature shift factors at a 0.0001 strain level under uniaxial conditions	126
Figure 100. Graph. Stress-time curves for the Control mixture before the application of time-temperature shift factors at a 0.0005 strain level under uniaxial conditions	127
Figure 101. Graph. Stress-time curves for the Control mixture before the application of time-temperature shift factors at a 0.001 strain level under uniaxial conditions	127
Figure 102. Graph. Stress-time curves for the Control mixture before the application of time-temperature shift factors at a 0.003 strain level under uniaxial conditions	128
Figure 103. Graph. Stress-time curves for the Control mixture before the application of time-temperature shift factors at a 0.005 strain level under uniaxial conditions	128
Figure 104. Graph. Stress-time curves for the Control mixture before the application of time-temperature shift factors at a 0.01 strain level under uniaxial conditions	129
Figure 105. Graph. Stress-time curves for the Control mixture before the application of time-temperature shift factors at a 0.015 strain level under uniaxial conditions	129
Figure 106. Graph. Stress-time curves for the Control mixture before the application of time-temperature shift factors at a 0.02 strain level under uniaxial conditions	130

Figure 107. Graph. Stress-time curves for the Control mixture before the application of time-temperature shift factors at a 0.0001 strain level under 500 kPa conditions.....	130
Figure 108. Graph. Stress-time curves for the Control mixture before the application of time-temperature shift factors at a 0.0005 strain level under 500 kPa conditions.....	131
Figure 109. Graph. Stress-time curves for the Control mixture before the application of time-temperature shift factors at a 0.001 strain level under 500 kPa conditions.....	131
Figure 110. Graph. Stress-time curves for the Control mixture before the application of time-temperature shift factors at a 0.003 strain level under 500 kPa conditions.....	132
Figure 111. Graph. Stress-time curves for the Control mixture before the application of time-temperature shift factors at a 0.005 strain level under 500 kPa conditions.....	132
Figure 112. Graph. Stress-time curves for the Control mixture before the application of time-temperature shift factors at a 0.01 strain level under 500 kPa conditions.....	133
Figure 113. Graph. Stress-time curves for the Control mixture before the application of time-temperature shift factors at a 0.015 strain level under 500 kPa conditions.....	133
Figure 114. Graph. Stress-time curves for the Control mixture before the application of time-temperature shift factors at a 0.02 strain level under 500 kPa conditions.....	134
Figure 115. Graph. Stress mastercurves for the Control mixture under uniaxial conditions.....	134
Figure 116. Graph. Stress mastercurves for the Control mixture under triaxial conditions (500 kPa).....	135
Figure 117. Graph. Variation of strain rate during unloading.....	135
Figure 118. Graph. Viscoplastic strain versus cumulative loading time (140 kPa confinement VT at 40 and 55 °C).....	136
Figure 119. Graph. Confining stress effect on the relaxation modulus.....	140
Figure 120. Graph. Comparison of zero-mean and zero-maximum deviatoric stress dynamic modulus mastercurves in semi-logarithmic scale.....	141
Figure 121. Graph. Comparison of zero-mean and zero-maximum deviatoric stress dynamic modulus mastercurves in logarithmic scale.....	141
Figure 122. Graph. Effect of test method on shift factor functions.....	142
Figure 123. Graph. Comparison of zero-mean and zero-maximum deviatoric stress phase angle mastercurves.....	142
Figure 124. Graph. Application of stress state-dependent model to zero-maximum deviatoric stress tests.....	143
Figure 125. Diagram. MVECD model characterization.....	144
Figure 126. Graph. C_{11} versus S for compression for Control mixture (5 °C reference).....	144
Figure 127. Graph. C_{12} versus S for compression for Control mixture (5 °C reference).....	145
Figure 128. Graph. C_{22} versus S for compression for Control mixture (5 °C reference).....	146
Figure 129. Graph. Comparison of tension and compression of C_{11} damage function.....	147
Figure 130. Graph. Comparison of tension and compression of C_{12} damage function.....	148
Figure 131. Graph. Comparison of tension and compression of C_{22} damage function.....	148
Figure 132. Graph. Incremental viscoplastic strain rate versus viscoplastic strain (500 kPa confinement, 2,000 kPa).....	151
Figure 133. Graph. Determined fitting results and coefficients of function $a(t_p)$	152
Figure 134. Graph. Determined fitting results and coefficients of function $D(t_p, \sigma)$	153
Figure 135. Graph. VT predictions.....	153
Figure 136. Graph. VL predictions.....	154
Figure 137. Graph. CLT predictions (2.0 MPa deviatoric stress—0.1-s pulse time).....	155

Figure 138. Graph. CLT predictions (2.0 MPa deviatoric stress—0.4-s pulse time)	155
Figure 139. Graph. CLT predictions (2.0 MPa deviatoric stress—1.6-s pulse time)	156
Figure 140. Graph. CLT predictions (2.0 MPa deviatoric stress—6.4-s pulse time)	156
Figure 141. Graph. CLT predictions (1.8 MPa deviatoric stress—1.6-s pulse time)	157
Figure 142. Graph. CLT predictions (2.2 MPa deviatoric stress—1.6-s pulse time)	157
Figure 143. Graph. Compressive and tensile peak stress in $\text{SQRT}(J_2) - I_1$ space.....	159
Figure 144. Graph. Determined γ_0 parameter function.....	160
Figure 145. Graph. Determined R parameter function	161
Figure 146. Graph. Determined n parameter function.....	161
Figure 147. Graph. Determined α_0 parameter function.....	162
Figure 148. Graph. Rate-dependent initial yield surface	162
Figure 149. Graph. Variation of α for 1,800 kPa CLT loading (500 kPa confinement).....	164
Figure 150. Graph. Viscoplastic strain predictions for VT tests (500 kPa confinement).....	164
Figure 151. Graph. Viscoplastic strain predictions for CLT tests (500 kPa confinement).....	165
Figure 152. Graph. Viscoplastic strain predictions for RVT tests (500 kPa confinement)	165
Figure 153. Illustration. Variation of yield stress (Standard Linear Solid model)	167
Figure 154. Graph. Stress histories for rest period analysis	169
Figure 155. Graph. Yield stress versus cumulative loading time (rest period analysis).....	170
Figure 156. Graph. Viscoplastic strain versus cumulative loading time (rest period analysis)..	170
Figure 157. Graph. Stress history for loading time analysis.....	171
Figure 158. Graph. Viscoplastic strain versus cumulative loading time (loading time analysis)	172
Figure 159. Graph. Viscoplastic strain versus cumulative loading time (140 kPa confinement VT).....	173
Figure 160. Graph. Viscoplastic strain versus cumulative loading time (140 kPa confinement VL).....	173
Figure 161. Graph. Viscoplastic strain versus cumulative loading time (500 kPa confinement VT).....	174
Figure 162. Graph. Viscoplastic strain versus cumulative loading time (500 kPa confinement VL).....	174
Figure 163. Graph. Viscoplastic strain versus cumulative loading time (140 kPa confinement VT).....	175
Figure 164. Graph. Viscoplastic strain versus cumulative loading time (140 kPa confinement VLT)	176
Figure 165. Graph. Viscoplastic strain versus cumulative loading time (140 kPa confinement VT).....	176
Figure 166. Graph. Viscoplastic strain versus cumulative loading time (140 kPa confinement VT + flow)	177
Figure 167. Graph. Viscoplastic strain versus cumulative loading time (500 kPa confinement 1,600 deviatoric VT).....	177
Figure 168. Graph. Viscoplastic strain versus cumulative loading time (500 kPa confinement 2,000 deviatoric VT).....	178
Figure 169. Graph. Viscoplastic strain versus cumulative loading time (500 kPa confinement 0.4 s CLT)	178
Figure 170. Graph. Viscoplastic strain versus cumulative loading time (500 kPa confinement 1.6 s CLT).....	179

Figure 171. Graph. Viscoplastic strain versus cumulative loading time (500 kPa confinement 6.4 s CLT)	179
Figure 172. Graph. Viscoplastic strain versus cumulative loading time (500 kPa confinement VLT)	180
Figure 173. Graph. Damage characteristic relationship used in the finite element implementation of one-dimensional VECD model.....	183
Figure 174. Graph. Layout of the numerical experiment specimen	183
Figure 175. Graph. Effect of continuum damage evolution on the vertical displacement of the test specimen at point <i>A</i> in the test simulation.....	184
Figure 176. Graph. Verification of strain prediction for monotonic uniaxial test using the new continuum damage material model	189
Figure 177. Graph. Evolution of damage parameter, <i>S</i> , for the monotonic test	190
Figure 178. Graph. Plot of function $C(S)$ with time	190
Figure 179. Diagram. Domain module	192
Figure 180. Illustration. Infinite elastic layer on a rigid base	193
Figure 181. Illustration. Finite element mesh required to model the physical problem with 1-percent accuracy without special elements.....	194
Figure 182. Illustration. Finite element mesh required to model the physical problem with 1-percent accuracy with special elements.....	194
Figure 183. Diagram. Analysis module	195
Figure 184. Screen capture. Main window of the preprocessor	196
Figure 185. Screen capture. Control panel.....	197
Figure 186. Screen capture. Mesh discretization	198
Figure 187. Screen capture. Zoom operation on a mesh.....	199
Figure 188. Diagram. Stages involved in an FEP++ analysis	200
Figure 189. Screen capture. Sample data entry window.....	201
Figure 190. Screen capture. Error dialog for a semantic error.....	202
Figure 191. Screen capture. Analysis run-time window.....	203
Figure 192. Graph. Temperature variations used for simulations	206
Figure 193. Illustration. Vertical strains in winter	207
Figure 194. Illustration. Vertical strains in summer	207
Figure 195. Illustration. Longitudinal strains in winter	208
Figure 196. Illustration. Longitudinal strains in summer	208
Figure 197. Illustration. Transverse strains in winter	209
Figure 198. Illustration. Transverse strains in summer.....	209
Figure 199. Illustration. Vertical strains for Control mixture.....	210
Figure 200. Illustration. Vertical strains for SBS mixture	211
Figure 201. Illustration. Longitudinal strains for Control mixture.....	211
Figure 202. Illustration. Longitudinal strains for SBS mixture	212
Figure 203. Illustration. Transverse strains for Control mixture	212
Figure 204. Illustration. Transverse strains for SBS mixture	213
Figure 205. Illustration. Vertical strains for a wheel speed of 13.41 m/s.....	214
Figure 206. Illustration. Vertical strains for a wheel speed of 26.82 m/s.....	215
Figure 207. Illustration. Longitudinal strains for a wheel speed of 13.41 m/s	215
Figure 208. Illustration. Longitudinal strains for a wheel speed of 26.82 m/s	216
Figure 209. Illustration. Transverse strains for a wheel speed of 13.41 m/s	216

Figure 210. Illustration. Transverse strains for a wheel speed of 26.82 m/s	217
Figure 211. Screen capture. General Information dialog.....	224
Figure 212. Screen capture. Material Properties dialog.....	225
Figure 213. Screen capture. Elastic material properties dialog	226
Figure 214. Screen capture. Viscoelastic material properties dialog.....	227
Figure 215. Screen capture. Prony Coefficients dialog	229
Figure 216. Screen capture. Layer properties dialog	230
Figure 217. Screen capture. Mesh properties dialog.....	232
Figure 218. Screen capture. Load properties dialog	234
Figure 219. Screen capture. Analysis Parameters dialog.....	236
Figure 220. Screen capture. Summary dialog.....	238
Figure 221. Screen capture. FEP++ analysis in progress	239

LIST OF TABLES

Table 1. Relevant asphalt binder information.....	37
Table 2. Summary of constructed lanes' air void and asphalt content	38
Table 3. Controlled crosshead testing matrix for Control-2006 in tension.....	42
Table 4. Controlled crosshead testing matrix for Control in compression	43
Table 5. Creep and recovery testing matrix for Control mixture in compression	44
Table 6. Test conditions for the VT and RVT tests	46
Table 7. Loading times for VLT test	48
Table 8. Linear viscoelastic characterization and variation for Control-2006 in unconfined state at selected frequencies and temperatures.....	51
Table 9. Linear viscoelastic characterization and variation for Control-2006 in 250 kPa confined state at selected frequencies and temperatures.....	52
Table 10. Linear viscoelastic characterization and variation for Control-2006 in 500 kPa confined state at selected frequencies and temperatures.....	53
Table 11. Effect of confining pressure on shift factor function coefficients for Control-2006 mixture	53
Table 12. Cyclic tests performed	99
Table 13. Summary of cyclic correction factors.....	99
Table 14. Summary of α values for refined model.....	104
Table 15. Cyclic tests performed for 9.5-mm Fine mixture	113
Table 16. Linear viscoelastic characterization and variation for the Control mixture in unconfined compression state at selected frequencies and temperatures	137
Table 17. Linear viscoelastic characterization and variation for the Control mixture in 140 kPa confined compression state at selected frequencies and temperatures	138
Table 18. Linear viscoelastic characterization and variation for the Control mixture in 500 kPa confined compression state at selected frequencies and temperatures	139
Table 19. Effect of confining pressure on shift factor function coefficients for the Control mixture in compression state	139
Table 20. Delft material model coefficients functions.....	159
Table 21. Material coefficients used for the developed model analysis.....	169
Table 22. Compression viscoplastic material model coefficients.....	172
Table 23. Properties of pavement	205
Table 24. Properties of moving wheel load	205

LIST OF ACRONYMS AND SYMBOLS

Abbreviations

2D	Two-dimensional
3D	Three-dimensional
ALF	Accelerated Load Facility
AMPT	Asphalt Mixture Performance Tester
CLT	Constant loading level and time test
CR-TB	Crumb Rubber Terminal Blend
CS	Controlled stress
CX	Controlled crosshead
EICM	Enhanced Integrated Climatic Model
FEM	Finite element method
FEP++	Finite element package (proper name)
FHWA	Federal Highway Administration
GUI	Graphical user interface
HISS	Hierarchical single surface
HMA	Hot mix asphalt
IDT	Indirect tension test
LVDT	Linear variable displacement transducers
LVE	Linear viscoelastic
MVECD	Multiaxial viscoelastic continuum damage
MVEPCD	Multiaxial viscoelastoplastic continuum damage
NCHRP	National Cooperative Highway Research Program
NCSU	North Carolina State University
NMSA	Nominal maximum size aggregate
RVT	Reversed variable loading time test
SBS	Styrene-butadiene-styrene
SHRP	Strategic Highway Research Program
SPT	Simple Performance Tester
t-TS	Time-temperature superposition
TFHRC	Turner-Fairbank Highway Research Center
TRS	Thermorheologically simple
UVECD	Uniaxial viscoelastic continuum damage
UVEPCD	Uniaxial viscoelastoplastic continuum damage
VECD	Viscoelastic continuum damage
VECD-FEP++	Viscoelastic continuum damage model included in finite element package
VEPCD	Viscoelastoplastic continuum damage
VP	Viscoplastic
VL	Variable loading level test
VLT	Variable loading level and time test
VT	Variable loading time test
VTK	Visualization Toolkit

Symbols

ε_{ij}^e	elastic strain
ε_{ij}^p	plastic strain
ε_{ij}^c	creep strain
ε_{ij}^{vp}	viscoplastic strain
ε_{ij}^{ve}	elastic plus linear viscoelastic strain due to damage
ε_{ve}	elastic plus linear viscoelastic strain due to damage
f_R	reduced physical frequency (Hz)
ω_R	reduced angular frequency ($=2\pi f_R \Delta t$)
a_T	time-temperature shift factor at specific temperature, T
π	3.141593
σ	stress
ε	strain
ε_x	strain in direction x
$\mu\varepsilon$	microstrain
$E(t)$	relaxation modulus
$D(t)$	creep compliance
τ	dummy integration variable
ρ_i	relaxation time (fitting coefficient)
τ_j	retardation time (fitting coefficient)
E_∞	relaxation modulus at infinite time
E_i	Prony coefficient for relaxation modulus
D_g	glassy compliance
D_j	Prony coefficient for creep compliance
E'	storage modulus
$ E^* $	dynamic modulus
ϕ	phase angle
t	time
ξ	reduced time
∂	partial derivative
ΔX	delta, finite difference in X
δX	delta, finite difference in X
ε^R	pseudo strain
E_R	reference modulus
C	normalized pseudo secant modulus
I	normalization parameter
S	damage
W	strain energy density

W_d^R	pseudo energy density
α	viscoelastic damage growth rate
C_{ijkl}	general stiffness matrix
ν	Poisson's ratio
E	elastic elongational modulus
G	elastic shear modulus
Z_{ij}	stiffness matrix for transversely isotropic material
E_3	modulus along axis of symmetry
E	modulus perpendicular to axis of symmetry
ν_{3132}	Poisson's ratio between axis of symmetry and perpendicular plane
ν_{1323}	Poisson's ratio between perpendicular plane and axis of symmetry
ν_{12}	Poisson's ratio on perpendicular plane
Υ	Poisson's ratio term
S_{ij}	compliance matrix for transversely isotropic material
A_{ij}	alterative stiffness matrix terms for transversely isotropic material
e_v	volumetric strain (dilation)
e_3	major deviatoric strain
e_2	strain difference
p	pressure
C_{11}	first material integrity term
C_{12}	second material integrity term
C_{22}	third material integrity term
ν	dilation
ν^R	pseudo dilation
Q_i	generalized loads
q_i	generalized displacements
U_e	complementary strain energy
$\dot{\epsilon}^{vp}$	viscoplastic strain rate
λ	positive scalar factor
g	plastic potential function (general viscoplasticity)
Φ	overstress function
η	viscosity
Γ	fluidity
I_1	first stress invariant
J_2	second deviatoric stress invariant
J_3	third deviatoric stress invariant
s_{ij}	deviatoric stress
δ_{ij}	Kroneker delta

κ	isotropic hardening parameter
α_{ij}	viscoplastic kinematic hardening parameter
g	stress function (strain hardening model specific)
P_a	atmospheric pressure
R	tensile strength parameter
n	yield stress shape parameter
β	parameter determining shape of yield stress in deviatoric stress space
$\dot{\varepsilon}^{in}$	inelastic strain rate
k	isotropic hardening function
α	viscoplastic back stress parameter (kinematic hardening)
D	drag stress
R	isotropic hardening function
H	kinematic hardening function
G	back stress (viscoplastic model)
ξ	viscoplastic strain trajectory
θ	angular direction in axisymmetric coordinate system
α_1	time-temperature shift factor function coefficient 1
α_2	time-temperature shift factor function coefficient 2
α_3	time-temperature shift factor function coefficient 3
θ	bulk stress
$\varepsilon_{pressure}^R$	pseudo strain due to pressure
$U_{pressure}^R$	pseudo dilation due to pressure
ε_e^R	effective pseudo strain
ε_s^R	permanent pseudo strain
ε_m^R	total maximum pseudo strain
ε_{me}^R	total effective pseudo strain at peak of loading
M	time change correction factor
t_p	pulse time
ξ_p	reduced pulse time
N	number of points in a calculation
F	pseudo strain slope function
G	pseudo strain hysteresis function
H	healing function
$\hat{\varepsilon}^R(t)$	analytical expression for pseudo strain as a function of time
Q	pseudo strain shape factor
Z	combined pseudo strain shape and pseudo stiffness time factor
$\varepsilon_{0,ta}^R$	pseudo strain tension amplitude only
$\sigma_{0,ta}$	stress tension amplitude only

σ_{pp}	peak-to-peak stress magnitude
β	factor quantifying time under tensile loading
σ_{peak}	maximum value of stress in a cycle
σ_{valley}	minimum value of stress in a cycle
ξ_i	reduced time within a cycle when tension loading begins
ξ_f	reduced time within a cycle when tension loading ends
R_k	form adjustment factor for characterization
K_1	form adjustment factor for prediction
$\varepsilon_{0,ta}$	strain tension amplitude only
$a(t_p)$	phenomenological viscoplastic model slope pulse time function
D	phenomenological viscoplastic model intercept function
γ	viscoplastic softening parameter
$I_{1,dilation}$	first stress invariant value at the beginning of dilation
$J_{2,dilation}$	second deviatoric stress invariant value at the beginning of dilation
$\dot{\varepsilon}_{reduced}$	reduced strain rate
D	viscosity parameter (final viscoplastic model)
G	orientation-dependent isotropic hardening function
G^{n+1}	value of hardening function at next time step
G^n	value of hardening function at current time step
ζ_0^n	value of elastic state variable at current time step
ζ_0^{n+1}	value of elastic state variable at next time step
ζ_i^n	value of state variable for element i at current time step
ζ_i^{n+1}	value of state variable for element i at next time step

EXECUTIVE SUMMARY

This report highlights findings from the FHWA DTFH61-05-H-00019 project, which focused on the development of the multiaxial viscoelastoplastic continuum damage (MVEPCD) model for asphalt concrete in both compression and tension. The MVEPCD model and finite element package (FEP++) have been developed for this purpose. The MVEPCD model combines elements of viscoelasticity, continuum damage mechanics, and viscoplasticity to model the material behavior. FEP++ is used to model the interaction of material and structure.

An introduction that outlines the research objectives and scope of the project is given in chapter 1 of this report. Chapter 2 provides a practical review of the underlying theories for the MVEPCD material model. Particular attention is paid to the concept of continuum damage mechanics and their implementation with viscoelastic materials. In addition, methodologies used to characterize the MVEPCD model are outlined in chapter 2. Details regarding specimen fabrication and testing protocols as well as background for the materials tested are in chapter 3.

Experimental results are categorized by loading direction, tension, or compression in chapter 4 and chapter 5, respectively. Specific comparisons of the effects of direction of loading are given in subsections 5.2.2 and 5.2.4. Each chapter provides the procedure for characterizing the viscoelastoplastic continuum damage (VEPCD), beginning with the linear viscoelastic characterization, proceeding to the viscoelastic damage characterization and viscoplastic characterization, and ending with the validation of the models. In addition, there is some discussion about the engineering properties of the materials in compression and tension, as well as verification of the time-temperature superposition (t-TS) principle with growing damage. Chapter 4 discusses the use of the VEPCD model for fatigue predictions. Because the rutting distress, a permanent deformation phenomenon, is related primarily to the compressive behavior of asphalt concrete, chapter 5 focuses on the viscoplastic behavior of the material in compression.

Chapter 6 presents the research efforts to enhance the finite element program with the viscoelastic continuum damage (VECD) model and the viscoelastic continuum damage model included in finite element package (VECD-FEP++). The resulting program is then used in chapter 7 to perform the three-dimensional (3D) finite element analysis to study the effects of temperature, material type, and vehicle speed on pavement responses. Chapter 8 summarizes the conclusions from both the experimental and computational work for this project. The future direction of the research at hand is provided at the end of chapter 8 as well.

CHAPTER 1. INTRODUCTION

1.1. PROBLEM STATEMENT

Asphalt concrete pavement, one of the largest infrastructure components in the United States, is a complex system that involves multiple layers of different materials, various combinations of irregular traffic loading, and various environmental conditions. Therefore, a realistic prediction of the long-term service life of asphalt pavements is one of the most challenging tasks for pavement engineers. The performance of asphalt concrete pavements is closely related to the performance of asphalt concrete. In order to predict the performance of asphalt concrete with reasonable accuracy, a better understanding of its deformation behavior under realistic conditions is urgently needed.

Asphalt concrete is a viscoelastic particulate composite that consists of aggregate particles and an asphalt binder matrix. When the asphalt-aggregate composite is subjected to repeated traffic loading at low temperatures, distributed microstructural damage occurs primarily in the forms of microcrack nucleation and growth due to the embrittled binder and high-stress concentrations along the aggregate-binder interfaces. Therefore, the role of the binder and the variables that influence the properties of the binder (e.g., aging, adhesion, etc.) become important to the study of this type of damage. At high temperatures, the asphalt binder becomes too soft to carry the load, and thus, the principal type of damage is permanent deformation due to volume change (i.e., densification) and rearrangement of aggregate particles. Therefore, a reliable performance prediction model should account for the effects of various constitutive factors that affect the aggregate-binder and aggregate-aggregate interactions.

With the goal of accurate pavement performance evaluation, researchers at North Carolina State University (NCSU) have been developing advanced models for asphalt concrete under complex loading conditions. Over the past decade, they have successfully developed material models that can accurately capture various critical phenomena such as microcrack-induced damage, which is critical in fatigue modeling, strain-rate temperature interdependence, and viscoplastic flow, which is critical for high-temperature modeling. The resulting model is termed the viscoelastic continuum damage (VEPCD) model. While the initial development of the VEPCD model focused on uniaxial tension behavior, the accurate performance prediction of an asphalt mixture in a pavement structure requires a multidimensional model.

To predict the performance of real pavement structures, it is also important to incorporate the material model in a pavement model that considers the vehicle and climatic loads as well as the boundary conditions. The finite element method is best suited for this purpose due to the nonlinear material behavior. The group has an in-house finite element code (FEP++) which can analyze general nonlinear dynamical systems. FEP++ is a research code and requires several modifications in order to be used for routine pavement modeling.

1.2. OBJECTIVES

The long-term goal of the asphalt pavement modeling research at NCSU is to develop a mechanistic asphalt pavement performance prediction methodology that can be used by State highway agencies. This research focuses on the following objectives to accomplish this goal:

1. To develop a multiaxial viscoelastoplastic continuum damage (MVEPCD) model for asphalt concrete in both compression and tension.
2. To enhance FEP++ so that nonlinear analysis of pavements can be easily conducted.

1.3. RESEARCH SCOPE

This research includes four of the mixtures used in the Federal Highway Administration's (FHWA) Accelerated Load Facility (ALF) current study that is funded through the pooled-fund study, TPF-5(019). Three of the mixtures contain asphalt binders modified with polymeric additives; the remaining mixture contains an unmodified asphalt binder. Material behavior under both tension and compression is addressed in this research. For the current research in multiaxial model development, only the unmodified mixture is being used.

CHAPTER 2. CONSTITUTIVE MODELING WITH A MULTIAXIAL VISCOELASTOPLASTIC CONTINUUM DAMAGE MODEL

2.1. HISTORICAL PERSPECTIVE

The foundation for the work presented in this report was laid by researchers at Texas A&M University almost two decades ago.⁽¹⁾ These researchers successfully applied Schapery's nonlinear viscoelastic constitutive theory for materials with distributed damage to describe the behavior of sand asphalt under controlled strain cyclic loading. Later research shows that this theory can also describe the behavior of asphalt concrete under both controlled stress and controlled strain cyclic loading.⁽²⁻⁴⁾ Later research shows that the damage characteristics of a material are independent of the mode of loading and can be determined using simpler tests.⁽⁵⁾ Further, verification of the t-TS principle at high levels of damage is an equally significant discovery.⁽⁶⁾ These two findings significantly reduce the required testing protocol while simultaneously extending the realm of application for the model. Work by Chehab et al. utilizes Schapery's theory, along with strain decomposition, to account for both viscoelastic and viscoplastic strains. (See references 7 through 11.) The most recent work applies this theory to mixtures tested at the FHWA ALF in Mclean, VA,⁽¹²⁾ and successfully demonstrates the application of the modeling principles to both modified and unmodified asphalt concrete mixtures. This work is the basis for the current research.

2.2. MODELING APPROACH

The MVEPCD model is a theoretical and phenomenological extension of the uniaxial VEPCD model presented in previous work and briefly reviewed here. These modeling approaches share many of the same principles, such as linear viscoelasticity, elastic-viscoelastic correspondence principle, continuum damage, and strain-hardening plasticity. A complete review of these principles in the uniaxial sense is given elsewhere, and a brief review is given in the following sections.⁽¹³⁾ For a more rigorous treatment of the subject, the reader is referred to previous work and to the work of Schapery for linear viscoelasticity and continuum damage mechanics. (See references 1 through 10.) For a detailed review of strain-hardening viscoplasticity, the reader is directed to the work of others.^(7,10,14)

Linear viscoelastic materials exhibit time- and temperature-dependent properties that make them dependent upon the history of loading, unlike elastic materials. This issue complicates the analysis since many continuum theories have been developed assuming an elastic material. In this report, the elastic-viscoelastic correspondence principle is used so that these elastic theories can be applied to the viscoelastic asphalt concrete mixtures. The correspondence principle uses pseudo strains, a quantity calculated from the actual time-dependent strains, in place of the actual strains. It is a general theory in so much that for purely elastic materials, the pseudo strains may be equal to the physical strains. Many damage theories exist, and in this report Schapery's theory based on energy principles is used. For this theory, consideration is given for both the time-dependent nature of energy availability as well as the time dependence of damage resistance. These arguments are considered within a thermodynamic framework. Finally, strain-hardening plasticity is found to be simple to model and commonly observed viscoplastic phenomenon.

A well-known assumption, founded in the theory of plasticity, is that total strain can be decomposed into elastic and plastic strains. Likewise, total strain can be decomposed into elastic strain, plastic strain, and creep strain, according to the theory of viscoplasticity, to account for the rate-dependent plastic strain of materials, as shown equation 1. In some studies that involve such rate-dependent materials, the rate-independent plastic strain and the rate-dependent creep strain are defined as viscoplastic strain because it is difficult to distinguish the plastic deformation from creep deformation. The theoretical background for the viscoplastic strain concept was first discussed by Perzyna, and since then more complicated models have been developed to explain the behavior of a material due to plasticity-creep interaction.⁽¹⁵⁾

$$\varepsilon_{ij}^{total} = \varepsilon_{ij}^e + \varepsilon_{ij}^p + \varepsilon_{ij}^c = \varepsilon_{ij}^e + \varepsilon_{ij}^{vp} \quad (1)$$

Where:

ε_{ij}^e = Elastic strain.

ε_{ij}^p = Plastic strain.

ε_{ij}^c = Creep strain.

ε_{ij}^{vp} = Viscoplastic strain.

From a similar perspective, Schapery suggests that total strain may be separated into several components, such as elastic, viscoelastic, and viscoplastic strains.⁽¹⁰⁾ For the MVEPCD model, elastic, linear viscoelastic, and strains due to microcracking damage are combined into a single term, and plastic and viscoplastic strains are combined into another, as shown in equation 2.

$$\varepsilon_{ij}^{total} = \varepsilon_{ij}^{ve} + \varepsilon_{ij}^{vp} \quad (2)$$

Where:

ε_{ij}^{ve} = Elastic plus linear viscoelastic strain due to damage.

ε_{ij}^{vp} = Viscoplastic strain.

2.2.1. Linear Viscoelasticity

Linear viscoelastic (LVE) materials exhibit time- and temperature-dependent behavior—the current response is dependent on both the current input and all past input (i.e., the input history). By contrast, the response of an elastic material is only dependent on the current input. Constitutive relationships for LVE materials are typically expressed in the convolution integral form, as follows:

$$\sigma = \int_0^t E(t-\tau) \frac{d\varepsilon}{d\tau} d\tau \quad (3)$$

$$\varepsilon = \int_0^t D(t-\tau) \frac{d\sigma}{d\tau} d\tau \quad (4)$$

Where:

$E(t)$ and $D(t)$ are the relaxation modulus and creep compliance, respectively. In this report, the analytical forms for these functions are given by the common Prony series formulation shown in equation 5 and equation 6. Note that the characterization of LVE behavior is undertaken by performing temperature and frequency sweep tests which are then processed to obtain the coefficients for these functions.⁽¹³⁾

$$E(t) = E_{\infty} + \sum_{i=1}^m E_i e^{-t/\rho_i} \quad (5)$$

$$D(t) = D_g + \sum_{j=1}^n D_j \left(1 - e^{-t/\tau_j}\right) \quad (6)$$

2.2.1.1. Linear Viscoelastic Interconversion

The unit response functions presented in equation 3 and equation 4 are often measured in the frequency domain using the complex modulus test because it is often difficult to obtain measurements in the time domain due to limitations of the testing machine's capacity for testing time. The complex modulus provides the constitutive relationship between the stress and strain amplitudes of a material loaded in a steady-state sinusoidal manner. Then, the storage modulus can be determined from the complex modulus and converted to a time-dependent property, such as $E(t)$ and $D(t)$, according to the theory of linear viscoelasticity. When the storage modulus is expressed in terms of reduced angular frequency, ω_R , as shown in equation 7, it can be expressed using the Prony series representation given in equation 8.^(16,17)

$$E'(\omega_R) = |E^*(\omega_R)| \sin(\phi(\omega_R)) \quad (7)$$

$$E'(\omega_R) = E_{\infty} + \sum_{i=1}^m \frac{\omega_R^2 \rho_i E_i}{\omega_R^2 \rho_i^2 + 1} \quad (8)$$

Where:

E_{∞} = Elastic modulus.

ω_R = Angular frequency ($=2\pi f_R \Delta t$).

Δt = Time lag between stress and strain.

E_i = Modulus of i^{th} Maxwell element (fitting coefficient).

ρ_i = Relaxation time (fitting coefficient).

The coefficients determined from this process are then used with equation 5 to find the relaxation modulus. Using the theory of viscoelasticity, the exact relationship between the creep compliance and relaxation modulus is given by equation 9.

$$\int_0^t E(t-\tau) \frac{dD(\tau)}{d\tau} d\tau = 1 \quad (9)$$

If the creep compliance, written in terms of the Prony representation (equation 10), is substituted into equation 9 along with equation 5 and simplified, then the result can be expressed as a linear algebraic system, shown as equation 11. The coefficients $\{D\}$ are solved by any proper numerical method.

$$D(t) = D_g + \sum_{j=1}^n D_j \left(1 - e^{-t/\tau_j}\right) \quad (10)$$

$$[A]\{D\} = [B] \quad (11)$$

Where:

$$[A] = \sum_{j=1}^M \left[\sum_{m=1}^N \frac{\rho_m E_m}{\rho_m - \tau_j} \left(e^{\frac{-t}{\rho_m}} - e^{\frac{-t}{\tau_j}} \right) + E_\infty \left(1 - e^{\frac{-t}{\tau_j}} \right) \right] \quad (12)$$

$$\{D\} = D_j \quad (13)$$

$$[B] = 1 - \frac{1}{E_\infty + \sum_{m=1}^N E_m} \left(E_\infty + \sum_{m=1}^N E_m e^{\frac{-t}{\rho_m}} \right) \quad (14)$$

Once the coefficients D_j are determined, they are substituted into equation 10 to find the creep compliance.

2.2.1.2. Linear Viscoelastic Characterization Methodology

Numerous research efforts by the authors have led to a methodology for assessing and analyzing LVE properties through the dynamic modulus. Explicit details of the experimental method are given in subsection 3.4.1; however, it should be known that the test applies cyclic sinusoidal loading at several combinations of frequency and temperature either with or without confining pressure. Load and axial deformations measured at four locations separated by 90-degree intervals are recorded for each combination of frequency and temperature. From these measurements, stresses and strains are calculated based on the specimen area and gauge length of the deformation measurements, respectively. The analysis procedure is the same for both confined and unconfined tests and is given in detail elsewhere.^(13,18)

Asphalt concrete in the LVE range is known to be thermorheologically simple (TRS) and, as such, the effects of time and temperature can be combined into a joint parameter, reduced time/frequency, through the time-temperature shift factor (a_T) using equation 15.

$$f_R = f \times a_T \quad (15)$$

In practical terms, this behavior allows for the horizontal shifting of the processed data to form a single curve, the mastercurve, for describing the constitutive behavior of asphalt concrete. The amount of horizontal shift is known as the t-TS shift factor, and the relationship between this factor and temperature is known as the t-TS shift factor function. When combined with the mastercurve, these two functions allow for the prediction of the LVE behavior over a wide range of conditions. The process is shown schematically in figure 1 through figure 3.

2.2.2. Correspondence Principle

The damage theory used in this research, which was originally developed for elastic materials, is generalized for viscoelastic materials using the elastic-viscoelastic correspondence principle.⁽⁸⁾ In short, this principle states that viscoelastic problems can be solved with elastic solutions when physical strains are replaced by pseudo strains.

$$\epsilon^R = \frac{1}{E_R} \int_0^t E(t-\tau) \frac{d\epsilon}{d\tau} d\tau \quad (16)$$

Where:

E_R is a particular reference modulus, typically taken as one. Using pseudo strain in place of physical strain, the uniaxial constitutive relationship presented in equation 3 can be rewritten as follows:

$$\sigma = E_R \epsilon^R \quad (17)$$

As equation 17 shows, for the uniaxial condition, a form corresponding to that of a linear elastic material (Hooke's Law) is taken when strains are replaced by pseudo strains. Additional theoretical details of this concept can be found elsewhere.^(8,19,20) In a practical sense, pseudo strains are simply the LVE stress response to a particular strain input. The most important effect of pseudo strains is seen when plotting with stress, as the time effects are removed from the resulting graph. This property allows the direct quantification of damage independent of any time effects. The results of two typical monotonic tests are presented in figure 4 and figure 5 in both stress strain space and stress-pseudo strain space. The behavior during initial loading is shown as an inset in these figures. In stress-strain space, as seen in figure 4, nonlinearity appears in the initial stage of loading, which might suggest that damage commences from the outset. However, the nonlinearity in this zone is related only to the time effects of the material. When these time effects are removed, as seen in figure 5, it is clear that damage does not commence at the outset of loading and does not begin until the stress level reaches approximately 500 kPa.

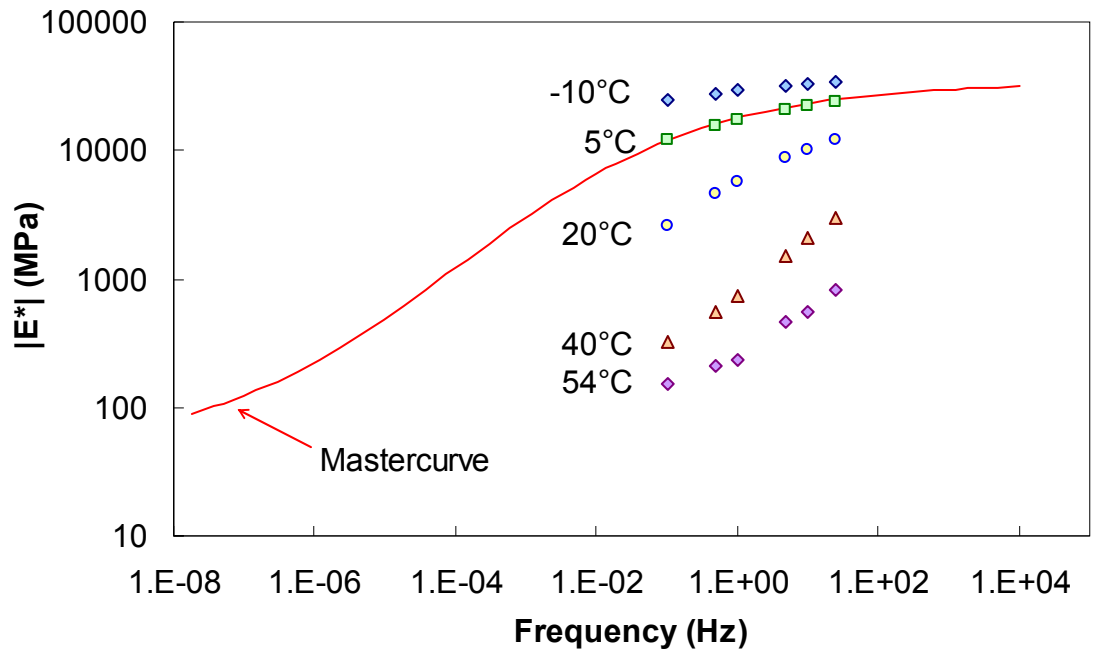


Figure 1. Graph. Schematic representation of dynamic modulus shifting process with unshifted data.

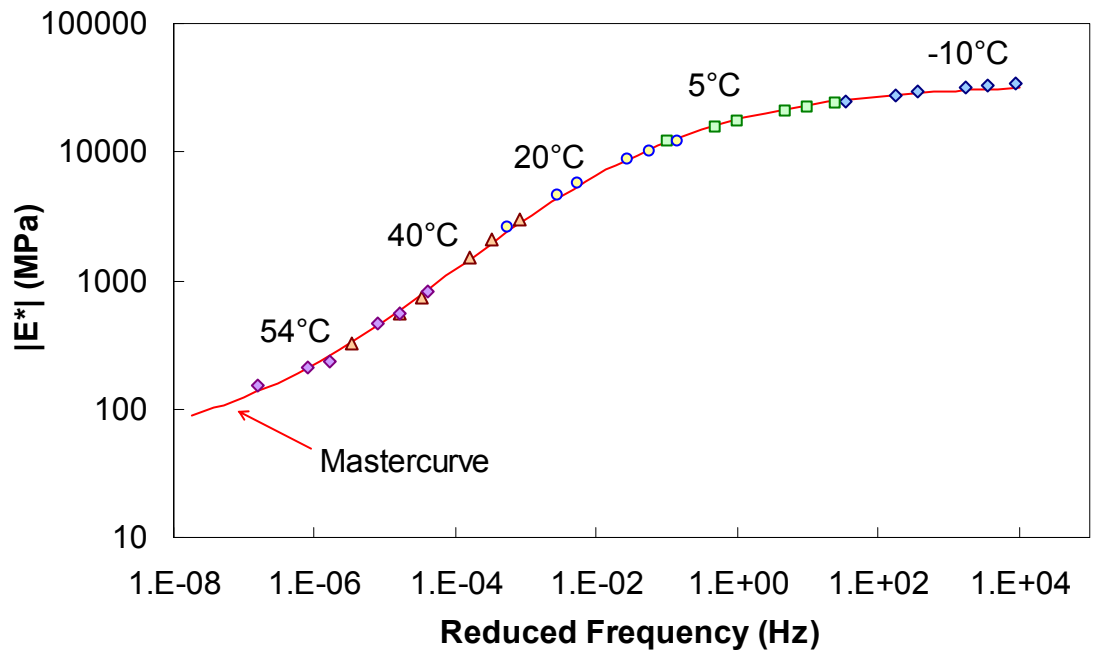


Figure 2. Graph. Schematic representation of dynamic modulus shifting process with shifted data.

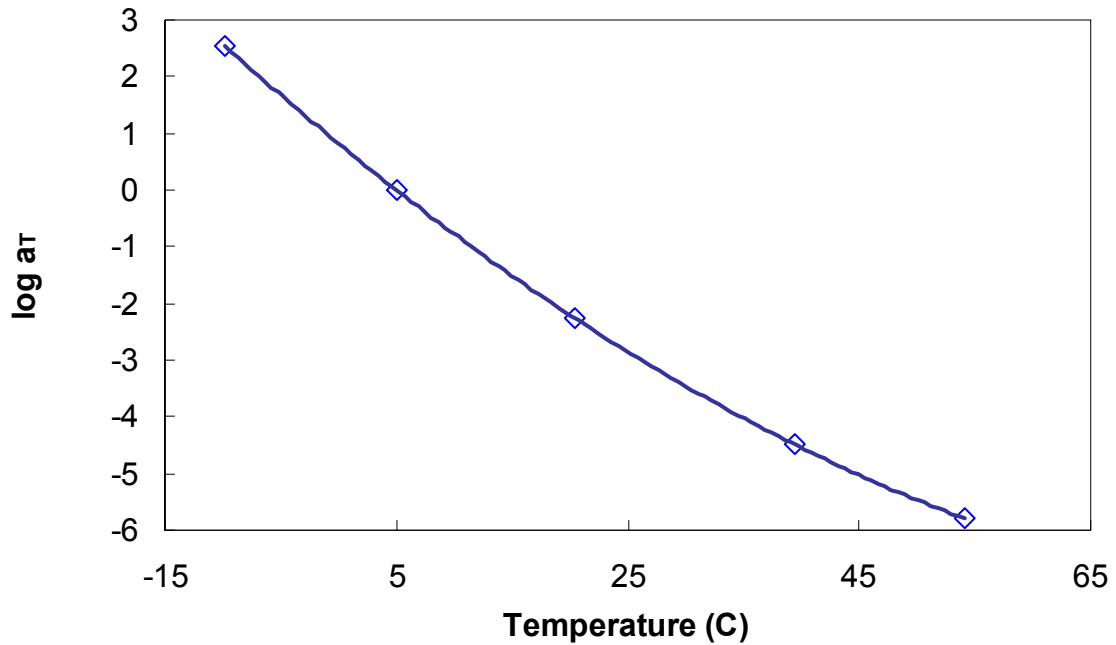


Figure 3. Graph. Schematic representation of dynamic modulus shifting process with time-temperature shift factor.

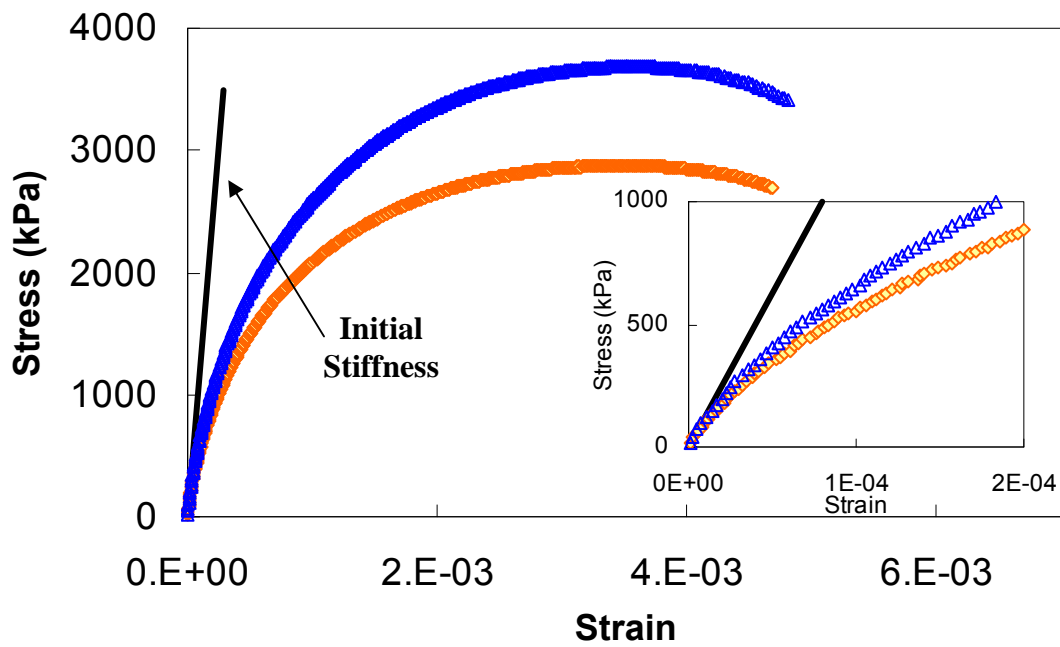


Figure 4. Graph. Constant crosshead test results in stress-strain space.

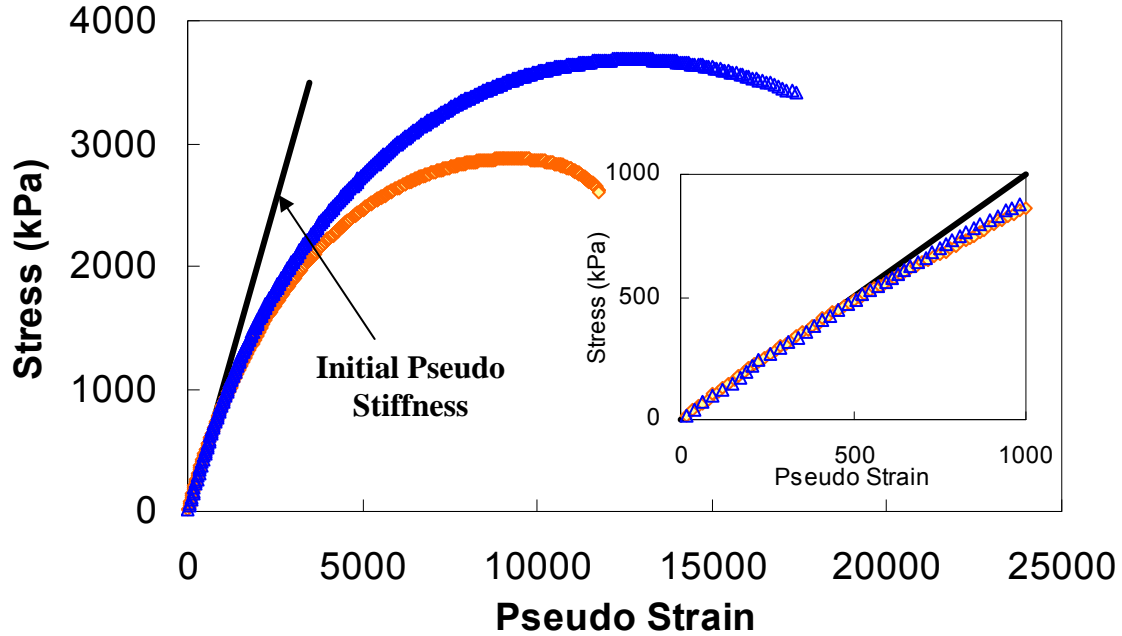


Figure 5. Graph. Constant crosshead test results in stress-pseudo strain space.

2.2.3. Continuum Damage

On the simplest level, continuum damage mechanics considers a damaged body with some stiffness as an undamaged body with reduced stiffness. Continuum damage theories thus attempt to quantify two values: damage and effective stiffness. Further, these theories ignore specific microscale behaviors and instead characterize a material using macroscale observations (i.e., the net effect of microstructural changes on observable properties). The most convenient method to assess the effective stiffness in the macro sense is the instantaneous secant modulus. On the other hand, damage is oftentimes more difficult to quantify and generally relies on macroscale measurements combined with rigorous theoretical considerations. For the model at hand, Schapery's work potential theory, based on thermodynamic principles, is appropriate for the purpose of quantifying damage. Within Schapery's theory, damage is quantified by an internal state variable, S , that accounts for microstructural changes in the material. (See references 8 through 11.)

2.2.4. Viscoelastic Continuum Damage Theory

The uniaxial viscoelastic continuum damage (UVECD) model combines elements from the preceding sections to arrive at the constitutive relationship. From continuum damage, the stiffness reduction is defined by the pseudo secant modulus (pseudo stiffness). This quantity is typically normalized for specimen-to-specimen variability by the factor I and denoted as C .

$$C = \frac{\sigma}{\varepsilon^R \times I} \quad (18)$$

The relationship between damage, S , and the normalized pseudo secant modulus, C , is known as the damage characteristic relationship and is a material function independent of loading conditions.⁽¹⁹⁾ With these considerations, the nonlinear constitutive relationships used for this research are given by equation 19 for stresses and equation 20 for strains.

$$\sigma = C(S) \varepsilon^R \quad (19)$$

$$\varepsilon_{ve} = E_R \int_0^{\xi} D(t-\tau) \frac{d\left(\frac{\sigma}{C(S)}\right)}{d\tau} d\tau \quad (20)$$

In comparing equation 20 to equation 4, a striking similarity is observed. Equation 4 is the constitutive relationship for linear viscoelasticity with a stress input. The modeling approach uses the given input (σ) to determine the input if no damage has occurred (ε^R) and then utilizes the LVE constitutive relationships to find the response. Equation 20 is solved in this research using the same state variable type of approach used for solving equation 16. These formulations are presented elsewhere.⁽¹³⁾

2.2.4.1. Refinement of Damage Characteristic Relationship

The work potential theory specifies an internal state variable, S , to quantify damage. This internal state variable quantifies any microstructural changes that result in the observed stiffness reduction. For asphalt concrete in tension, this variable is related primarily to the microcracking phenomenon. This report highlights only components new to this research, as significant theoretical work has been done by others. (See references 2, 7, 20, and 21.)

The derivation of the UVECD model begins with an assumption of damage behavior (equation 21) or damage evolution law.

$$\frac{dS}{dt} = \left(-\frac{\partial W_d^R}{\partial S} \right)^\alpha \quad (21)$$

The method used to solve the damage evolution law is a matter of preference; therefore, two different solutions are proposed for solving equation 21. The first transforms the original form of the equation into an integral form, assumes $\alpha \gg 1$, and defines a new parameter, \hat{S} .⁽²¹⁾ Equation 22 presents this method in discrete form.

$$S = \left[\hat{S} \left(1 + \frac{1}{\alpha} \right) \right]^{1+\frac{1}{\alpha}} \quad (22)$$

Where:

\hat{S} is given by equation 22, as follows:

$$\hat{S}_{i+1} = \hat{S}_i - \frac{1}{2}(\Delta C)_i (\varepsilon_i^R)^2 t^{\frac{1}{\alpha}} \quad (23)$$

The second possible solution shown in equation 24 utilizes the chain rule and makes no assumption regarding α .⁽³⁾ Both methods have been successfully applied in asphalt concrete research.^(7,20,21)

$$S_{i+1} = S_i + \left[-\frac{1}{2}(\Delta C)_i (\varepsilon_i^R)^2 \right]^{\frac{\alpha}{1+\alpha}} \Delta t^{\frac{1}{1+\alpha}} \quad (24)$$

To reconcile the approximations of these methods, an iterative refinement technique is incorporated into this research. In short, this method assumes that the change in material integrity is sufficiently small over some discrete time step. The rate of change of the material integrity with respect to damage is determined at a point near the current value of damage, $S_i + \delta S$, where the extrapolation error is minimized.

This refinement process begins with an initial calculation of S by either of the approximate methods, both of which require results from constant crosshead rate tests for the stress-pseudo strain relationship. The initial S values are plotted with the pseudo stiffness values, C , to obtain the damage characteristic curve. This relationship is then fitted to some analytical form, as shown in equation 25.

$$C = e^{aS^b} \quad (25)$$

Returning to equation 21 and noting that the increments of time are generally small, the rate of change in damage can be written as follows:

$$\frac{dS}{dt} = \frac{\Delta S}{\Delta t} \quad (26)$$

By substituting this expression into equation 21 and rearranging and writing in the discrete form, equation 27 is established:

$$S_{i+1} = S_i + \Delta t \left(-\frac{\delta W_i^R}{\delta S} \right)^\alpha \quad (27)$$

For the uniaxial case, the work function, W^R , is given by equation 28.⁽¹⁹⁾

$$W_d^R = \frac{1}{2} C(S) \varepsilon^R \quad (28)$$

By substituting equation 28 into equation 27 and then simplifying, equation 29 is reached.

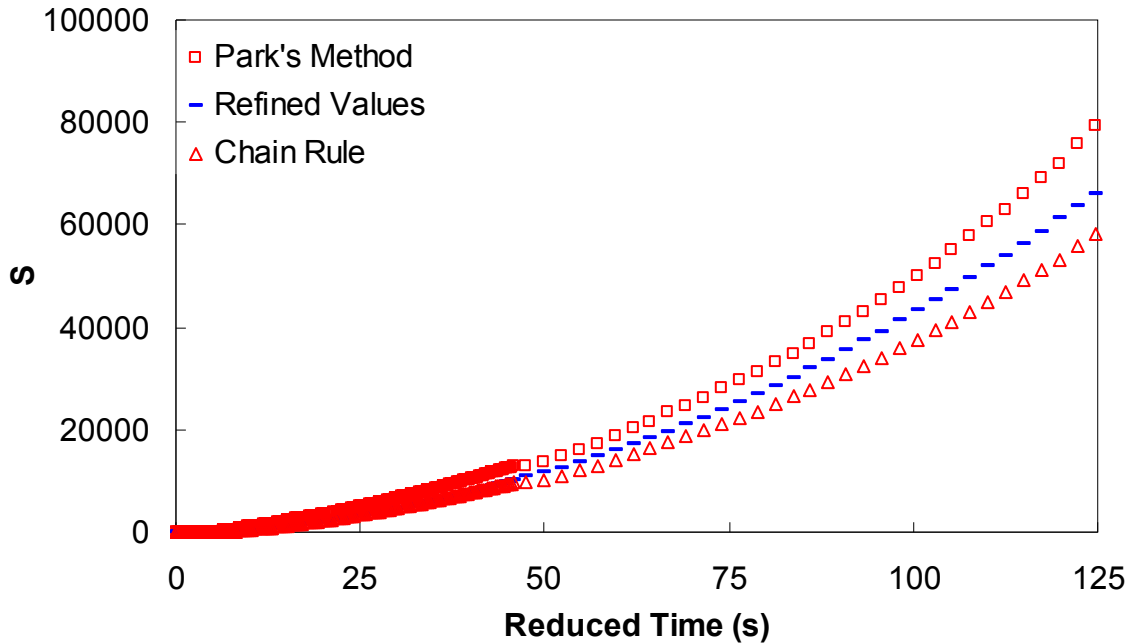
$$S_{i+1} = S_i + \Delta t \left(-\frac{1}{2} (\varepsilon^R)^2 \frac{(\delta C)_i}{\delta S} \right)^\alpha \quad (29)$$

In equation 29, it is assumed that before loading occurs, S and C are zero and 1, respectively. Furthermore, δS must be specified and should be significantly less than the change in damage over a time step (typically, 0.1 is used). After calculating the value of damage, S_i , and the incremental damage, $S_i + \delta S$, at a given time step, the corresponding values of C are found by equation 25. The difference between these values (δC) is then used to calculate damage at the next time step. The process is repeated until all data points are processed.

After completing this first iteration, the new values of S are plotted against the original pseudo stiffness values, and a new analytical relationship is found. The entire process is repeated until the change in successive iterations is small. In this research, eight such iterations were performed, but very little improvement was made after the third or fourth iteration.

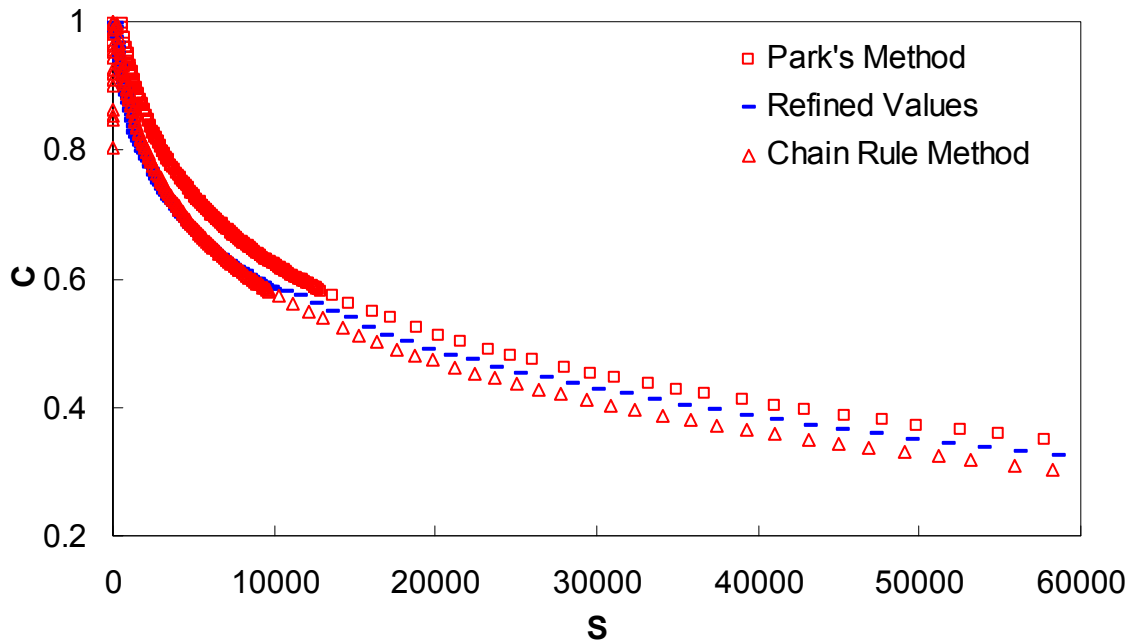
Figure 6 and figure 7 present the initial S calculated by both approximate techniques along with results from the refinement process. From these figures, it is seen that the refinement process results in S values that fall between the two approximate methods. In these figures, the seed values for the refinement process are obtained by the chain rule method. However, trials show that regardless of the method used to find the seed values, iterations collapse to the same curve. Details regarding this refinement process can be found elsewhere.⁽²²⁾

The final refined values of S are plotted with C to obtain the true damage characteristic curve. As noted before, the benefit of this curve is its mode-of-loading independence; the curve represents a fundamental behavior of the material. From equation 16 and equation 19, if this fundamental relationship is known and the relaxation modulus is given, then the stresses can be directly calculated. Conversely, if this fundamental relationship is known and the creep compliance is given, the strain response can be directly calculated for any stress input using equation 20.



Transportation Research Board, National Academy of Science. From *Appendixes to National Cooperative Highway Research Program (NCHRP) Report 547: Sample Performance Tests and Advanced Materials Characterization Models* (2005)

Figure 6. Graph. Comparison of refined and approximate damage calculation techniques.⁽²²⁾



Transportation Research Board, National Academy of Science. From *Appendixes to NCHRP Report 547: Sample Performance Tests and Advanced Materials Characterization Models* (2005)

Figure 7. Graph. Comparison of refined and approximate damage characteristic relationship.⁽²²⁾

2.2.4.2. Calculation of Damage

In a typical application, the user wants to predict strain from only stress and time using equation 20. However, from the preceding discussion, the user must know the strain to compute S and C . To bypass this requirement, it is first assumed that S and C are initially zero and 1, respectively. Then, at some incremental amount of damage (δS), C can be computed by the functional relationship found through the refinement process. Finally, using the relationship in equation 19, equation 29 can be rewritten as follows:

$$S_{i+1} = S_i + \Delta t \left(-\frac{1}{2} \left(\frac{\sigma_i}{C_i} \right)^2 \frac{(\delta C)_i}{\delta S} \right)^\alpha \quad (30)$$

Through equation 30, damage may be incrementally calculated using a technique similar to that used to refine S using only stress and time.

2.2.4.3. Viscoelastic Damage Characterization Methodology

Viscoelastic damage characterization refers to the development of the characteristic damage relationship (i.e., the C versus S relationship). Although such characterization can be performed under any loading condition, the simplest method is the constant crosshead rate test.⁽²⁰⁾ For MVEPCD characterization, both confined and unconfined constant crosshead rate tests are performed. The only requirement for this test is that viscoelastic damage mechanisms dominate the material behavior, such as when the material is at a low temperature or when it is loaded at a very fast rate. In this study, characterization is performed at 5 °C. This temperature is convenient because it allows for moderate strain rates and does not require consideration of any dynamic effects that might be related to extremely high strain rates. In practice, at least three different rates are tested at 5 °C, and if the resulting C versus S curves collapse, it is known that viscoelastic damage mechanisms dominate. The appropriate strain rates are material-dependent.

For both VEPCD and MVEPCD characterization, the first step is the calculation of the pseudo strains by equation 16 for the constant rate tests. These values are used along with equation 18 and equation 24 to calculate the initial damage, S , values. The relationship between C and these initial S values are fitted to equation 25 and refined through the aforementioned procedure. The true C versus S relationship is obtained by refitting equation 25 to these refined S values. Results from the tests at different rates are finally averaged to obtain the C versus S relationship for modeling. Typically, each test is sampled at different intervals, which complicates this averaging process. To overcome this difficulty, a common list of C values is compiled, and the corresponding S values are interpolated from the respective test. Averaging can then be easily performed because each test has common C values.

2.3. MULTIAXIAL VISCOELASTIC CONTINUUM DAMAGE MODEL

2.3.1. Review of Mechanistic Principles

The arguments presented in this section focus on general stress-strain relationships. For notational simplicity, the derivations in this section are given for linear elasticity; however, the

arguments remain valid for viscoelastic materials through the elastic-viscoelastic correspondence principle. Much information about this principle has been provided elsewhere; the form given by Schapery is adopted here.⁽⁸⁾

For linear elastic materials, the most general constitutive relationship is given by the following:

$$\sigma_{ij} = C_{ijkl} \varepsilon_{kl} \quad (31)$$

C_{ijkl} is a fourth-order tensor with 81 constants. Through symmetry arguments, this number is reduced to 21. In matrix form, equation 31 can be viewed as equation 32.

$$\mathbf{C} = \begin{bmatrix} C_{11} & C_{12} & C_{13} & C_{14} & C_{15} & C_{16} \\ C_{12} & C_{22} & C_{23} & C_{24} & C_{25} & C_{26} \\ C_{13} & C_{23} & C_{33} & C_{34} & C_{35} & C_{36} \\ C_{14} & C_{24} & C_{25} & C_{44} & C_{45} & C_{46} \\ C_{15} & C_{25} & C_{35} & C_{45} & C_{55} & C_{56} \\ C_{16} & C_{26} & C_{36} & C_{46} & C_{56} & C_{66} \end{bmatrix} \quad (32)$$

If further assumptions such as orthotropic isotropy, transverse isotropy, and cubical isotropy are assumed, these numbers reduce further. The simplest of these cases is full isotropy, which assumes no directional dependence on the material properties. In this case, two material constants are necessary to describe the constitutive relationship between stress and strain. In general terms, these are called Lamé's constants and together define the more commonly recognized fundamental parameters: Poisson's ratio (ν), shear modulus (G), Young's modulus (E), and bulk modulus (K). In terms of compliances, these constants define the shear compliance (J), longitudinal compliance (D), and bulk compliance (B).

For a general isotropic case, it can be shown that C_{11} , C_{22} , and C_{33} are equal; C_{12} , C_{13} , and C_{23} are equal; and C_{44} , C_{55} , and C_{66} equal either half of the shear modulus or just the shear modulus depending on the definition used for shear strain. All other terms become zero. Written in full, assuming the shear strain in equation 31 is given as the total angle form, the stiffness matrix for the general isotropic case becomes equation 33.

$$\mathbf{C} = \frac{E}{(1+\nu)(1-2\nu)} \begin{bmatrix} (1-\nu) & \nu & \nu & 0 & 0 & 0 \\ \nu & (1-\nu) & \nu & 0 & 0 & 0 \\ \nu & \nu & (1-\nu) & 0 & 0 & 0 \\ 0 & 0 & 0 & \frac{(1-2\nu)}{2} & 0 & 0 \\ 0 & 0 & 0 & 0 & \frac{(1-2\nu)}{2} & 0 \\ 0 & 0 & 0 & 0 & 0 & \frac{(1-2\nu)}{2} \end{bmatrix} \quad (33)$$

It is seen from equation 31 that the use of equation 33 recovers the common form of Hooke's law.⁽²³⁾ For the problem at hand, however, isotropy is of less concern than transverse isotropy. For this case, it can be shown that the stiffness matrix is given by equation 34. A change in nomenclature from C_{ij} to Z_{ij} for general stiffness is made to avoid confusion with later terminology. Also, axis three is assumed to be the axis of symmetry.

$$\mathbf{Z} = \begin{bmatrix} Z_{11} & Z_{12} & Z_{13} & 0 & 0 & 0 \\ & Z_{11} & Z_{13} & 0 & 0 & 0 \\ & & Z_{33} & 0 & 0 & 0 \\ & sym & & Z_{44} & 0 & 0 \\ & & & & Z_{44} & 0 \\ & & & & & Z_{66} \end{bmatrix} \quad (34)$$

For isotropy, it is seen that the stiffness matrix terms are related to the engineering parameters, Young's modulus and Poisson's ratio. Using similar terminology, transverse isotropy can be considered to have two Young's moduli and three Poisson's ratios. The nomenclature used in this report for these parameters is as follows:

$E = E_1 = E_2 =$ Stiffness on isotropy plane.

$E_3 =$ Stiffness along axis of symmetry.

$\nu_{12} =$ Poisson's ratio on isotropy plane.

$$\nu_{3132} = -\frac{\epsilon_{11}}{\epsilon_{33}} = -\frac{\epsilon_{22}}{\epsilon_{33}}.$$

$$\nu_{1323} = -\frac{\epsilon_{33}}{\epsilon_{11}} = -\frac{\epsilon_{33}}{\epsilon_{22}}.$$

$G_{13} = G_{23} =$ Shear modulus between transverse plane and axis of symmetry.

$G_{12} =$ Shear modulus on transverse isotropy plane. (35)

Where:

ν_{1323} is not equal to ν_{3132} ; however, for symmetry, $\nu_{3132}/E_3 = \nu_{1323}/E$.

The relationships between Z_{ij} and the values defined in equation 35 are as follows:

$$\begin{aligned}
Z_{11} &= E(1 - \nu_{1323}\nu_{3132})\Upsilon \\
Z_{33} &= E_3(1 - \nu_{12})\Upsilon \\
Z_{12} &= E(\nu_{12} + \nu_{1323}\nu_{3132})\Upsilon \\
Z_{13} &= E(\nu_{3132} + \nu_{12}\nu_{3132})\Upsilon = E_3(\nu_{1323} + \nu_{12}\nu_{1323})\Upsilon \\
Z_{44} &= G_{23} = G_{13} \\
Z_{66} &= G_{12} \\
\Upsilon &= \frac{1}{1 - \nu_{12}^2 - 2\nu_{3132}\nu_{1323} - 2\nu_{12}\nu_{3132}\nu_{1323}}
\end{aligned} \tag{36}$$

Or, solving for the engineering parameters, the relationships are as follows:

$$\begin{aligned}
E &= \frac{(Z_{11}^2 Z_{33} + 2 * Z_{13}^2 Z_{12} - 2 * Z_{13}^2 Z_{11} - Z_{33} Z_{12}^2)}{(Z_{11} Z_{33} - Z_{13}^2)} \\
E_3 &= \frac{(Z_{11}^2 Z_{33} + 2 * Z_{13}^2 Z_{12} - 2 * Z_{13}^2 Z_{11} - Z_{33} Z_{12}^2)}{(Z_{11}^2 - Z_{12}^2)} \\
\nu_{12} &= \frac{(Z_{12} Z_{33} - Z_{13}^2)}{(Z_{11} Z_{33} - Z_{13}^2)} \\
\nu_{3132} &= \frac{(Z_{13} Z_{11} - Z_{12} Z_{13})}{(Z_{11}^2 - Z_{12}^2)} \\
\nu_{1323} &= \frac{(Z_{13} Z_{11} - Z_{12} Z_{13})}{(Z_{11} Z_{33} - Z_{13}^2)} \\
G_{23} &= G_{13} = Z_{44} \\
G_{12} &= Z_{66}
\end{aligned} \tag{37}$$

If the compliance matrix with generalized compliances, S_{ij} , is considered, then the resulting relationships are as shown in equation 38.

$$S = \begin{bmatrix} 1/E & -\nu_{12}/E & -\nu_{3132}/E_3 & 0 & 0 & 0 \\ -\nu_{12}/E & 1/E & -\nu_{3132}/E_3 & 0 & 0 & 0 \\ -\nu_{1323}/E & -\nu_{1323}/E & 1/E_3 & 0 & 0 & 0 \\ 0 & 0 & 0 & 1/G_{23} & 0 & 0 \\ 0 & 0 & 0 & 0 & 1/G_{23} & 0 \\ 0 & 0 & 0 & 0 & 0 & 1/G_{12} \end{bmatrix} \quad (38)$$

The compliance matrix is considered here for completeness. Also, the constitutive relationships are more compact and easier to present.

2.3.2. Application of Schapery's Work Potential Theory

Schapery's work potential theory model contains parameters that characterize the material integrity with damage growth.^(22,11) To clarify the issue of the physical significance of these parameters, a step-by-step process is followed to link the damage functions to the engineering parameters defined in equation 37.

In terms of principal strains, the strain energy density function as defined by the terms found in equation 34 is shown in equation 39:

$$W = \frac{1}{2} \left[Z_{11}\varepsilon_1^2 + Z_{11}\varepsilon_2^2 + Z_{33}\varepsilon_3^2 + 2*Z_{12}\varepsilon_1\varepsilon_2 + 2*Z_{13}\varepsilon_1\varepsilon_3 + 2*Z_{23}\varepsilon_2\varepsilon_3 \right] \quad (39)$$

Schapery shows that a more convenient way to express the strain energy density function for transversely isotropic materials is as follows:

$$W = \frac{1}{2} \left[A_{11}e_v^2 + A_{22}e_3^2 + 2*A_{12}e_3e_v + A_{66}e_2^2 \right] \quad (40)$$

Where:

$$e_v = \varepsilon_1 + \varepsilon_2 + \varepsilon_3, \quad e_3 = \varepsilon_3 - e_v/3 \text{ and } e_2 = \varepsilon_2 - \varepsilon_1 \quad (41)$$

The stiffness values, A_{ij} , in equation 40 can be damage dependent for both the elastic and viscoelastic case. Through an expansion of equation 40, the A_{ij} values correspond to the more recognizable forms in equation 39, thusly:

$$\begin{aligned}
Z_{11} = Z_{22} &= A_{11} + \frac{1}{9}A_{22} - \frac{2}{3}A_{12} + A_{66} \\
Z_{33} &= A_{11} + \frac{4}{9}A_{22} + \frac{4}{3}A_{12} \\
Z_{12} &= A_{11} + \frac{1}{9}A_{22} - \frac{2}{3}A_{12} - A_{66} \\
Z_{23} = Z_{13} &= A_{11} - \frac{2}{9}A_{22} + \frac{1}{3}A_{12}
\end{aligned} \tag{42}$$

Schapery presents the energy density function as a dual energy density function so that the damage characteristics of a cylindrical body subjected to confining pressure, p , and axial deformation can be more easily characterized. This dual energy density function, as derived by Schapery, is presented in equation 43. To arrive at the relationship presented in equation 43, Schapery assumes that work potential exists and uses the principle of virtual work on a cylindrical specimen subjected to axial loading and confining pressure.⁽¹¹⁾ Then, he defines a general work potential theory and expands it into a power series, canceling terms to satisfy the initial conditions. The relationships between the A_{ij} terms and the damage-dependent variables, C_{ij} , are presented in equation 44. These relationships must be satisfied for consistency between equation 40 and equation 43. The C_{ij} terms in equation 43 and equation 44 are not the same as those defined in equation 32.

$$W_d = \frac{1}{2}C_{11}\varepsilon^2 + C_{12}\varepsilon p + \frac{1}{2}C_{22}p^2 \tag{43}$$

$$\begin{aligned}
A_{11} &= \frac{1}{9} \left[C_{11} - \frac{(C_{12} - 3)^2}{C_{22}} \right] \\
A_{12} &= \frac{C_{11}}{3} + \frac{C_{12}}{C_{22}} \left(1 - \frac{C_{12}}{3} \right) \\
A_{22} &= C_{11} - \frac{C_{12}^2}{C_{22}} \\
A_{44} = A_{66} &\cong G_0
\end{aligned} \tag{44}$$

Making substitutions and canceling terms, the engineering parameters in equation 37 are expressed as a function of C_{ij} :

$$\begin{aligned}
E_3 &= C_{11} \\
E &= \frac{4G_0 C_{11}}{C_{11} + G_0 (1 + C_{12}^2 - 2C_{12} - C_{22} C_{11})} \\
\nu_{3132} &= \frac{1}{2}(1 - C_{12}) \\
\nu_{1323} &= \frac{2(C_{12} - 1)G_0}{C_{11} + G_0 (1 + C_{12}^2 - 2C_{12} - C_{22} C_{11})} \\
\nu_{12} &= \frac{C_{11} - G_0 (1 + C_{12}^2 - 2C_{12} - C_{22} C_{11})}{C_{11} + G_0 (1 + C_{12}^2 - 2C_{12} - C_{22} C_{11})}
\end{aligned} \tag{45}$$

For the compliance matrix, the following can be seen:

$$\mathbf{S} = \begin{bmatrix} \frac{C_{11} + G_0 (1 + C_{12}^2 - 2C_{12} - C_{22} C_{11})}{4G_0 C_{11}} & \frac{-C_{11} + G_0 (1 + C_{12}^2 - 2C_{12} - C_{22} C_{11})}{4G_0 C_{11}} & \frac{-(1 - C_{12})}{2C_{11}} & 0 & 0 & 0 \\ \frac{-C_{11} + G_0 (1 + C_{12}^2 - 2C_{12} - C_{22} C_{11})}{4G_0 C_{11}} & \frac{C_{11} + G_0 (1 + C_{12}^2 - 2C_{12} - C_{22} C_{11})}{4G_0 C_{11}} & \frac{-(1 - C_{12})}{2C_{11}} & 0 & 0 & 0 \\ \frac{-(1 - C_{12})}{2C_{11}} & \frac{-(1 - C_{12})}{2C_{11}} & \frac{1}{C_{11}} & 0 & 0 & 0 \\ 0 & 0 & 0 & \frac{1}{G_0} & 0 & 0 \\ 0 & 0 & 0 & 0 & \frac{1}{G_0} & 0 \\ 0 & 0 & 0 & 0 & 0 & \frac{1}{G_0} \end{bmatrix} \tag{46}$$

It is worthwhile to consider the definitions of stress and strain used in equation 43. Stress is defined as the stress above stress due to pressure (i.e., the deviator stress). According to the definition of strain given in the formulation of the work potential theory presented in the Park dissertation, strain includes all changes in length, even those associated with volume change.⁽²⁴⁾ In an earlier paper, strain is defined clearly as the change in axial displacement due to load divided by the initial length.⁽¹¹⁾ To clarify the confusion, virtual work is defined by the following:

$$\delta(\text{Work}) = \sum_{i=1}^N Q_i dq_i \tag{47}$$

In equation 47, Q_i are the generalized loads, and q_i are the generalized displacements. Whether the strain is defined as the total strain, the evaluated value of equation 47 does not change because the derivative of the strain is independent of these two definitions. Still, the issue does present some consequences in the characterization stage, and so, equation 40 and the

relationships in equation 44 will be used to clarify the issue. For a transversely isotropic axial specimen subjected to confining pressure and axial elongation along the axis of symmetry, the following can be shown:

$$\frac{\partial W}{\partial \varepsilon_3} = \sigma_3 = \varepsilon_3 \left(A_{11} + \frac{4}{3} A_{12} + \frac{4}{9} A_{22} \right) + 2\varepsilon_1 \left(A_{11} + \frac{1}{3} A_{12} - \frac{2}{9} A_{22} \right) \quad (48)$$

Using the relationships in equation 44, equation 48 can be recast with ν defined the same way as e_ν from equation 40 as the following:

$$\sigma_3 = \varepsilon_3 C_{11} + \frac{(C_{12} - 1)}{C_{22}} [\nu - C_{12} \varepsilon_3] \quad (49)$$

From equation 43, C_{22} and C_{12} are related by the following:

$$C_{22} = \frac{\nu - C_{12} \varepsilon}{p} \quad (50)$$

If it is assumed that the strain in equation 50 is the total strain, ε_3 , and that equation 50 is substituted into equation 49 and rearranged, then the following occurs:

$$\sigma_3 + p = \varepsilon_3 C_{11} + C_{12} p \quad (51)$$

Equation 51 is compared to the similar form obtained from equation 43 to achieve equation 52:

$$\frac{\partial W_d}{\partial \varepsilon} = \sigma = C_{11} \varepsilon + C_{12} p \quad (52)$$

Observing that the sign convention for pressure is opposite that of stress above pressure, a comparison of equation 51 and equation 52 indicates that the stress in equation 43 is the deviator stress, and the strain is the total strain.

2.4. THEORY OF VISCOPLASTICITY

The hot mix asphalt (HMA) mixture is a pavement material that exhibits both viscoelastic and viscoplastic behavior and therefore shows complicated rate-dependent behavior for repetitive traffic loadings. Rutting, one of the major distress types in HMA pavements, is directly related to the rate-dependent permanent deformation behavior of HMA. To predict the rutting performance of HMA, much effort has been made to develop constitutive models capable of describing the rate-dependent permanent strain development in HMA. Some researchers suggest a viscoplastic model with strain-hardening features.⁽²⁵⁾ As the simplest model, it is also able to describe monotonic behavior in tension, as shown by researchers.^(7,10) Others have presented a viscoplastic model for HMA that incorporates Perzyna's flow rule with Desai's yield function.^(26,27) While still others suggest a simplified hierarchical single surface (HISS)-Perzyna model that shows a reasonable viscoplastic strain prediction.⁽²⁸⁾ However, the difficulty in developing a constitutive model for HMA is that hardening rules based on the behavior of metals

or soils are not necessarily appropriate to describe both viscoplastic and viscoelastic behaviors of HMA. That is, models developed for metals and soils describe only elastic recovery during unloading, whereas HMA shows nonlinear strain recovery during unloading due to the viscoelastic property of the material. An important observation supporting this phenomenon was made by Saadeh.⁽²⁹⁾

2.4.1. Flow Rule

The general concepts behind the constitutive equations for plastic deformation were proposed by Von Mises based on the theory of elasticity.⁽³⁰⁾ As such, the strain tensor is related to the stress through an elastic potential function, the complementary strain energy, U_e .

$$\varepsilon_{ij}^e = \frac{\partial U_e}{\partial \sigma_{ij}} \quad (53)$$

Where:

ε_{ij}^e = Elastic strain tensor.

U_e = Elastic complementary strain energy.

σ_{ij} = Stress tensor.

The plasticity theory based on the above flow rule is called the *plastic potential theory*. When the state of stress reaches the yield criterion, f , plastic strain develops; this mechanism is called *plastic flow*. To generalize this concept to the plasticity theory, Von Mises proposes that a plastic potential function, $g(\sigma_{ij})$, exists.⁽³⁰⁾ The plastic strain rate, $d\varepsilon_{ij}^p$, can then be derived from the following flow rule:

$$d\varepsilon_{ij}^p = \lambda \frac{\partial g}{\partial \sigma_{ij}} \quad (54)$$

Where:

$d\varepsilon_{ij}^p$ = Plastic strain rate.

λ = Positive scalar factor.

$\frac{\partial g}{\partial \sigma_{ij}}$ = Gradient of the plastic potential, $g(\sigma_{ij})$.

In equation 54, λ is a proportional positive scalar factor that can be determined from the yield criterion. For some materials, the plastic potential function, g , and the yield function, f , can be assumed to be the same. These kinds of materials are considered to follow the associative flow rule of plasticity. In other words, the normality rule for this material is associated with the yield criterion, f . However, for other materials, the plastic potential function, g , and the yield function, f , are different. These materials are considered to follow the nonassociative flow rule of plasticity, and the flow rule of the material is derived from a plastic potential, g . In this case, $\partial g / \partial \sigma_{ij}$ is not proportional to $\partial f / \partial \sigma_{ij}$, and therefore, the plastic strain direction is not normal to the yield surface, f . Basically, the viscoplastic flow rule takes a similar form to the plastic flow rule except

that it takes advantage of the over-stress function as a replacement for λ , as shown in equation 55.

$$\dot{\varepsilon}_{ij}^{vp} = \lambda \frac{\partial f}{\partial \sigma_{ij}} = \frac{\Phi}{\eta_0} \frac{\partial f}{\partial \sigma_{ij}} = \Gamma \Phi \frac{\partial f}{\partial \sigma_{ij}} \quad (55)$$

Where:

Φ = Overstress function.

η_0 = Viscosity.

Figure 8 represents the viscoplastic flow rule using a mechanical analog, which combines a dashpot and a slip element in parallel.⁽³¹⁾ In this case, the overstress function in equation 55 is represented by the difference from the applied stress (σ) and the yield stress (G) to the viscosity (η_0) in this model.

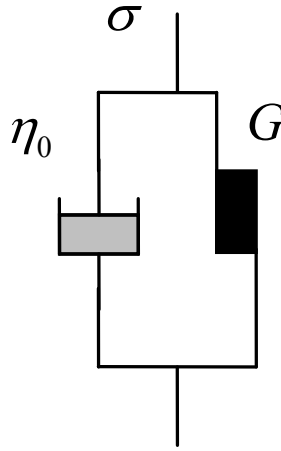


Figure 8. Illustration. Mechanical analog for the viscoplastic model.

2.4.2. Yield Criterion

In conventional viscoplasticity, the elastic limit of the material can be defined by a surface-in-stress space. Mathematically, the yield surface for general anisotropic materials is expressed as equation 56.

$$f(\sigma_{ij}) = 0 \quad (56)$$

For an isotropic material, the orientation of the principal axis is immaterial, and the principal stresses, σ_{11} , σ_{22} , and σ_{33} , are sufficient to describe the state of stress. The principal stresses form the integrity basis; it is common to use I_1 , J_2 , and J_3 as the integrity basis. Therefore, the yield function becomes equation 57 for the isotropic material.

$$f(\sigma_{11}, \sigma_{22}, \sigma_{33}) = f(I_1, J_2, J_3) = 0 \quad (57)$$

Where:

$$I_1 = \sigma_{11} + \sigma_{22} + \sigma_{33} \quad (58)$$

$$J_2 = \frac{1}{2} s_{ij} s_{ij} \quad (59)$$

$$J_3 = \frac{1}{3} s_{ij} s_{jk} s_{ki} \quad (60)$$

$$s_{ij} = \sigma_{ij} - \frac{1}{3} \sigma_{kk} \delta_{ij} \quad (61)$$

δ_{ij} = Kronecker delta.

Physically, I_1 represents the hydrostatic pressure, and J_2 represents the distortional energy in the material; no clear physical meaning is related to J_3 . Generally, yield criteria can be classified into two subgroups according to their dependence on hydrostatic stress. The isotropic hardening model is the simplest hardening model and is based on the assumption that the yield surface expands isotropically as the plastic strain develops. The typical isotropic hardening model is presented in equation 62 and figure 9. Because the loading surface expands uniformly, it cannot account for the Bauschinger effect observed in various materials, which describes the reduction of compressive yield strength due to a previously applied tensile stress, or vice versa. Therefore, using only the isotropic hardening model frequently limits the characterization of the material behavior when both tension and compression loads are applied.

$$f(\sigma_{ij}, K) = f(s_{ij}) - \kappa = 0 \quad (62)$$

Where:

s_{ij} = Deviatoric stresses.

κ = Isotropic hardening parameter.

The kinematic hardening model assumes that during plastic deformation the yield surface translates as a rigid body in the stress space and has the same shape and size as the initial yield surface. The kinematic hardening model is represented by equation 63 and figure 10.

$$f(\sigma_{ij}, a) = f(s_{ij} - \alpha_{ij}) = 0 \quad (63)$$

Where:

s_{ij} = Deviatoric stresses.

α_{ij} = Kinematic hardening parameters (i.e., coordinates of the center of the yield surface in the deviatoric stress space).

Equation 64 and equation 65 conceptually represent the classic kinematic hardening rules suggested by Prager, Armstrong-Frederick, and Chaboche, respectively.⁽³²⁻³⁴⁾ The kinematic hardening rate is a function of the viscoplastic strain rate in these equations, and the hardening rate is always zero when there is no change in viscoplastic strain. Therefore, when a material is subjected to one-directional loading, such as a constant strain-rate test and a repetitive creep and recovery test, the yield stress increases only in the direction of the developed viscoplastic strain and never decreases.

$$\dot{\alpha} = g(\dot{\epsilon}^{vp}) \quad (64)$$

$$\dot{\alpha} = g(\dot{\epsilon}^{vp}, \alpha) \quad (65)$$

Where:

α = Kinematic hardening stress.

$\dot{\epsilon}^{vp}$ = Viscoplastic strain rate.

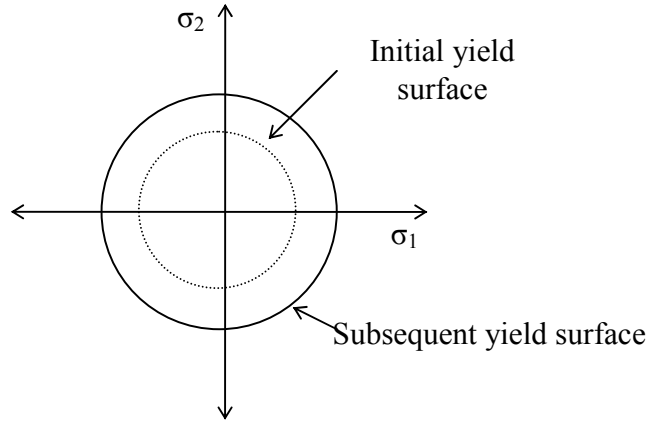


Figure 9. Illustration. Isotropic hardening diagram.

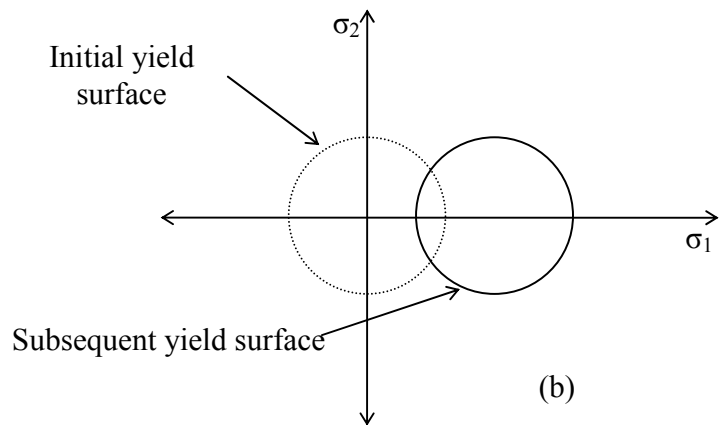


Figure 10. Illustration. Kinematic hardening diagram.

2.5. VISCOPLASTIC MODELS

2.5.1. Simple Strain-Hardening Model

A simple strain-hardening model has been suggested and is shown in equation 66, which assumes that viscosity obeys a power law in viscoplasticity. Researchers have shown that the model is applicable to monotonic behavior in tension.^(7,10,25)

$$\dot{\varepsilon}_{vp} = \frac{g(\sigma)}{\eta(\varepsilon_{vp})} \quad (66)$$

Where:

$g(\sigma)$ = Stress function.

η = Viscosity.

Assuming that η is a power law in the viscoplastic strain, equation 67 becomes the following:

$$\dot{\varepsilon}_{vp} = \frac{g(\sigma)}{A\varepsilon_{vp}^p} \quad (67)$$

Where:

A and p are model coefficients. Rearranging and integrating yield the following:

$$\varepsilon_{vp}^p d\varepsilon_{vp} = \frac{g(\sigma) dt}{A} \quad (68)$$

$$\varepsilon_{vp}^{p+1} = \frac{p+1}{A} \int_0^t g(\sigma) dt \quad (69)$$

Raising both sides of equation 69 to the $1/(p+1)$ power yields the following:

$$\varepsilon_{vp} = \left(\frac{p+1}{A} \right)^{\frac{1}{p+1}} \left(\int_0^t g(\sigma) dt \right)^{\frac{1}{p+1}} \quad (70)$$

Letting $g(\sigma) = B\sigma^q$ and coupling coefficients A and B into coefficient Y , equation 70 becomes the following:

$$\varepsilon_{vp} = \left(\frac{p+1}{Y} \right)^{\frac{1}{p+1}} \left(\int_0^t \sigma^q dt \right)^{\frac{1}{p+1}} \quad (71)$$

In the current work, the coefficients, p , q , and Y , are pressure-dependent quantities.

Typically, viscoplastic models are characterized using creep and recovery tests. These tests allow relatively easy separation of the viscoplastic and viscoelastic components, as shown in figure 11. However, it is difficult (if not impossible in some machines) to maintain zero load during the recovery period of the creep and recovery test in tension. Therefore, in tension, viscoplastic characterization uses constant rate tests in which the VECD model is used to first predict the viscoelastic strains. These viscoelastic strains are then subtracted from the measured strains to provide the viscoplastic strains that are needed for curve fitting to equation 71.

The advantage of this model is that it is easy to implement and does not consume much computational time. This model's ability to predict the HMA behavior under complex loading histories in tension is reported by Underwood et al.⁽¹²⁾ However, this model's major weakness is its one-dimensional nature, which is not sufficient to describe the behavior of HMA in pavements. This deficiency is particularly troublesome in compression where the confinement is known to play a major role in permanent deformation behavior of HMA. In the following subsections, more general viscoplastic models are presented.

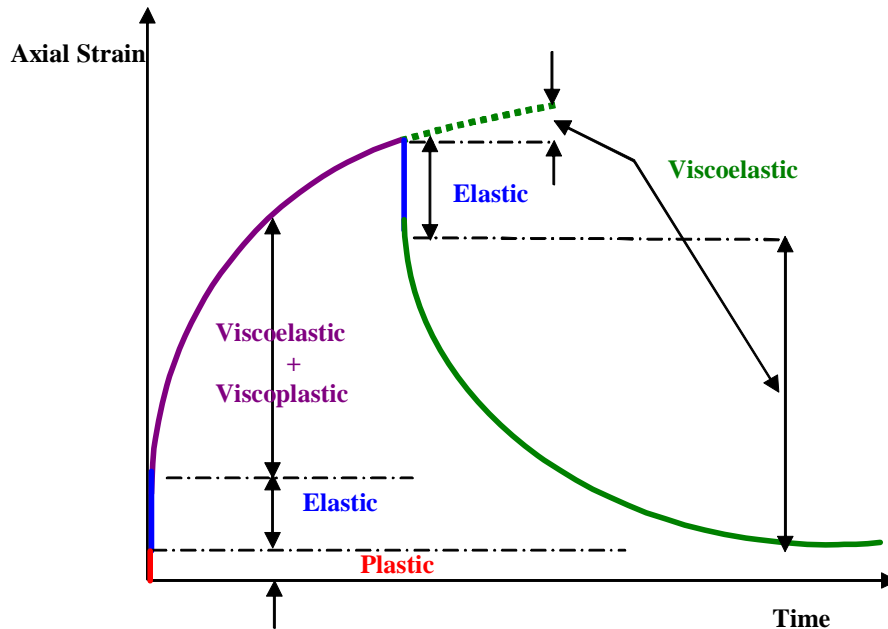


Figure 11. Illustration. Strain decomposition from creep and recovery testing.

2.5.2. HISS-Perzyna Model

The HISS plasticity model provides a general formulation for the elastoplastic characterization of material behavior. This model, which is potentially able to incorporate isotropic and kinematic hardening and associated and nonassociated plasticity characterizations, can be used to represent a material response based on the continuum plasticity theory. Therefore, the HISS model allows the selection of a more appropriate derivative model for a given material in a specific engineering application. Various well-known plasticity models, such as the Von Mises, Mohr-Coulomb, Drucker-Prager, continuous yielding critical-state, and capped models, can be derived as special cases of the HISS model.^(30,32,35)

2.5.2.1. HISS Model Implemented by Delft University of Technology

Equation 72 represents the HISS criterion.⁽³⁵⁾ In the criterion, n and α determine the shape of the yield stress in deviatoric-hydrostatic stress space, and γ represents ultimate yield stress. R represents the cohesion of the material and determines the position of the yield stress with respect to the hydrostatic stress axis. Because the yield stress of the HISS criterion varies depending on the first stress invariant, I_1 , the model exhibits a spindle shape of its yield surface

when the shape of the yield surface is assumed to be circular ($\beta=0$) in the deviatoric stress space, as shown in figure 12.

$$f = \frac{J_2}{P_a^2} - \frac{\left[\gamma \left(\frac{I_1 - R}{P_a} \right)^2 - \alpha \left(\frac{I_1 - R}{P_a} \right)^n \right]}{\sqrt{\left(1 - \beta \frac{3\sqrt{3}J_3}{2(J_2)^{\frac{3}{2}}} \right)}} = 0 \quad (72)$$

Where:

γ = Softening parameter.

α = Hardening parameter.

R = Tensile strength of material when deviatoric stress is zero.

n = Parameter determining shape of yield stress.

β = Parameter determining shape of yield stress in deviatoric stress space.

P_a = Atmosphere pressure.

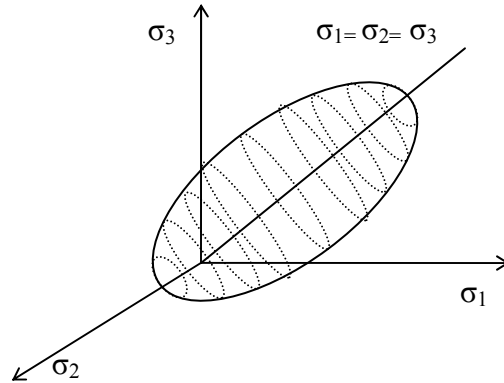


Figure 12. Illustration. Typical yield surface of HISS model.

Researchers using this model suggest an HISS criterion whose parameters are the strain rate-dependent functions for a given HMA mixture.⁽³⁶⁾ For the characterization, a series of constant strain-rate tests in tension and in compression are performed at several strain rates and temperatures. Then, predictions are made for indirect tension (IDT) specimens subjected to constant strain-rate loading. Because this model requires constant strain-rate testing using several different strain rates and temperatures for characterization, it is important to determine the appropriate range of the strain rates and temperatures to minimize the amount of experimental effort. Although it appears that the model can successfully explain the viscoplastic behavior when subjected to monotonic loading, numerical issues related to parameter determination and prediction still remain. In addition, because the model is characterized using constant strain-rate tests, it cannot fully explain the behavior of HMA under discontinuous loading, such as repetitive creep and recovery loading.

2.5.2.2. HISS Model Implemented by the University of Maryland

A viscoplastic model based on the simplified HISS model and using Perzyna's flow rule has also been suggested.⁽²⁸⁾ Repetitive creep and recovery tests are used for both calibration and prediction, and numerical optimization techniques are adapted for calibrations, unlike Erkens' model.⁽³⁶⁾ As shown in equation 73, γ , which represents both the ultimate yield stress and the softening of the material, is considered a constant, and R is a function of the viscoplastic strain. In Erkens' study, however, γ and R are functions of the viscoplastic strain rate and temperature.⁽³⁶⁾

$$F = J_2 - \left[\gamma (I_1 - R(\xi))^2 - \alpha(\xi) (I_1 - R(\xi))^n \right] \quad (73)$$

Where:

- ξ = Viscoplastic strain trajectory.
- γ = Softening parameter (constant).
- α = Hardening parameter (function of viscoplastic strain).
- R = Tensile strength of material when the deviatoric stress is zero.

The main contribution of this research is to apply the t-TS principle to a conventional viscoplastic constitutive model and confirm the validity of the superposition principle.

2.5.3. Unified Model

In theory of viscoplasticity, the term *unified constitutive model* refers to models that describe the rate-dependent viscoplastic strain for steel or polymer. However, in other disciplines, the unified constitutive model is used to represent not only viscoplastic strain but also viscoelastic strain. Because this type of model takes a more flexible form of hardening equations than other viscoplastic models, it is worth reviewing the approaches used in the unified model.

2.5.3.1. Linear Kinematic Hardening Model

The simplest unified constitutive model is the linear kinematic hardening model shown in equation 74 and equation 75.⁽³⁷⁾ The inelastic strain rate has a linear relationship with the overstress, $\sigma - \alpha$. The back stress rate is a function of the back stress in the previous time step and the strain rate in the current time step. Because the model is designed to explain inelastic strain, which is the summation of viscoelastic strain, plastic strain, and viscoplastic strain, the inelastic strain rate can be negative depending on the stress history. The back stress rate, $\dot{\alpha}$, is another representation of the Maxwell model of mechanical analog.⁽⁵⁰⁾

$$\dot{\varepsilon}^{in} = C(\sigma - \alpha) \quad (74)$$

$$\dot{\alpha} = A\varepsilon^{in} - B\alpha \quad (75)$$

Where:

$\dot{\varepsilon}^{in}$ = Inelastic strain.

α = Back stress.

A, B, C = Material constants.

2.5.3.2. *Chaboche Model*

In general, the viscoplastic strain of a material obeys a power law, and the hardening of the material can be represented by kinematic and isotropic hardening, as shown in equation 76.

$$\dot{\varepsilon}_{ij}^{vp} = \Phi(\sigma, \alpha, k) \frac{\partial F}{\partial \sigma_{ij}} = \left\langle \frac{F(\sigma - \alpha) - k}{D} \right\rangle^n \frac{\partial F}{\partial \sigma_{ij}} \quad (76)$$

Where:

Φ = Magnitude of strain rate.

α = Kinematic hardening function (back stress function).

k = Isotropic hardening function.

The Chaboche model is a viscoplastic model consisting of the above flow rule and hardening function represented by a summation form of back stress.⁽³⁴⁾ By using decomposed back stress, the model is capable of describing nonlinear hardening with enhanced accuracy for a wider range of viscoplastic strain. Equation 77 shows the back stress function in the Chaboche model; it becomes the Armstrong-Frederick model when $n = 1$.

$$\alpha = \sum_{i=1}^n \alpha_i(\varepsilon_{vp}) \quad (77)$$

Where:

$\alpha_i(\varepsilon_{vp}) = i^{\text{th}}$ back stress, which is a function of the viscoplastic strain.

2.5.3.3. *Krempl and Ho Models*

As an advanced and recent form of the linear kinematic hardening model, some researchers have proposed a viscoplastic model based on the overstress concept.^(38,39) The constitutive model also includes a description of the time-dependent recoverable strain of the materials. It begins with the assumption that the coefficients of viscoelasticity are nonlinear functions. Equation 78 is the differential equation used to derive the model.

$$m(\sigma - g(\varepsilon)) \times \dot{\varepsilon} + g(\varepsilon) = \sigma + k(\sigma - g(\varepsilon)) \times \dot{\sigma} \quad (78)$$

Where:

$m(\sigma - g(\varepsilon))$ = Positive, bounded and even function.

$k(\sigma - g(\varepsilon))$ = Positive, bounded and even function.

$g(\varepsilon)$ = Odd function of strain.

$\sigma - g(\varepsilon)$ = Overstress.

When the functions $m(\sigma - g(\varepsilon))$ and $k(\sigma - g(\varepsilon))$ become constant and when $g(\varepsilon)$ is linear in ε , equation 78 reduces to the differential equation of a standard linear solid model that represents viscoelastic behavior. The equation can then be expanded to the regular convolution integrals of linear viscoelasticity. Because equation 79 holds true for slow loading, the relationship between the strain rate and stress can be expressed as equation 80, the simplest form of the viscoplastic model.⁽⁴⁰⁾

$$E = \frac{m(\sigma - g(\varepsilon))}{k(\sigma - g(\varepsilon))} \quad (79)$$

Where:

E = Material elastic modulus.

$$\dot{\varepsilon} = \frac{\sigma}{E} + \frac{\sigma - g(\varepsilon)}{E \times k(\sigma - g(\varepsilon))} \quad (80)$$

More complicated model forms are available for describing hardening, dynamic and static softening, and relaxing, as well as negative and positive rate sensitivities. However, as shown in equation 80, Krempl's constitutive models have neither loading or unloading conditions nor the concept of yield stress because they are derived from the concept of general viscoelasticity. Therefore, it is not appropriate to describe only the viscoplastic behavior of HMA, even though the model gives an idea of the rate dependency of viscoplastic properties under unloading conditions. This potential shortcoming is overcome by introducing Macauley's bracket into the second term of equation 80.⁽⁴¹⁾ Because the model is based on equation 80, the back stress function is related to the kinematic stress function, as shown in equation 83.

$$\dot{\varepsilon}^{in} = B \left\langle \frac{|\sigma - H| - R}{D} \right\rangle^m \frac{(\sigma - G)}{|\sigma - G|} \quad (81)$$

Where:

D = Drag stress.

R = Isotropic hardening function.

H = Kinematic stress function ($\dot{H} = E \dot{\varepsilon}^{in}$) (82)

G = Back stress.

$$\dot{G} = \psi \left[\dot{\varepsilon}^{in} - \frac{(G-H)}{R} |\dot{\varepsilon}^{in}| \right] + \dot{H} \quad (83)$$

Where:

B , m , and ψ = Material constants characterized from experimental results.

In contrast to Krempl's model, this model does not allow a change in the material state during unloading because the state of the material is a function only of the viscoplastic strain rate.

2.6. VISCOELASTOPLASTIC CONTINUUM DAMAGE MODEL

In the previous sections, the viscoelastic and viscoplastic models are developed separately. It has been shown by using a thermodynamic formulation that the total strain is the sum of the viscoelastic and viscoplastic components even in the non-small strain region.⁽¹⁰⁾ Thus, the viscoelastic and viscoplastic models can now be integrated to form the VEPCD model in which the predicted viscoelastic and viscoplastic responses are combined to obtain the total response for a given stress history.

The resulting equation from combining equation 20 and equation 71 predicts the total strain history for a general loading history at a reference temperature.

$$\varepsilon_T = E_R \int_0^{\xi} D(\xi - \xi') \frac{d \left(\frac{\sigma - C_{12}(S)p}{C_{11}(S)} \right)}{d\xi'} d\xi' + \left(\frac{p+1}{Y} \right)^{1/p+1} \left(\int_0^{\xi} \sigma^q d\xi \right)^{1/p+1} \quad (84)$$

Equation 84 is presented in terms of reduced time, (ξ), due to the verification of the t-TS principle with growing damage. Stated simply, this principle allows the use of time-temperature shift factors determined from LVE characterization to combine the effects of time and temperature at higher levels of damage. This simplification significantly reduces the required testing protocols while simultaneously expanding the realm of application for the model. Section 4.5 and subsection 5.1.3 present the methodology and experimental work used to verify this principle for both tension and compression modes of loading, respectively.

CHAPTER 3. SPECIMEN FABRICATION AND TESTING PROTOCOLS

3.1. MATERIALS

Component materials used in this study were obtained from FHWA's Turner-Fairbank Highway Research Center (TFHRC). Two options for materials acquisition were available to the researchers at the outset of the project. The first option was to acquire already mixed asphalt concrete that was available and used for construction of the ALF testing lanes. The second option was to have the component materials sampled and transported to NCSU for fabrication of appropriate asphalt concrete mixtures. Based on the availability and desired consistency of the materials, the latter option was chosen, and component materials were obtained from TFHRC. Four stockpiles, #68, #78, #10, and Sand (FHWA Designation B-6265, B-6264, B-6306, and B-6263, respectively), were sampled and transported to NCSU for fabrication. For the ALF lanes, hydrated lime was first mixed with the #10 stockpile before mixing it with the asphalt binder. The decision was made to not use this stockpile for fabrication; instead, hydrated lime was added separately on a specimen by specimen basis at NCSU. In addition to acquiring aggregates, four asphalt binders, PG 70-22 (B-6298), Crumb Rubber Terminal Blend (B-6286), Styrene-Butadiene-Styrene (B-6295), and Ethylene Terpolymer (B-6289), were also acquired.

The aggregate structure for each of the mixtures was constant and was a coarse 12.5-mm nominal maximum size aggregate (NMSA) mixture comprised of 18.0 percent #68 stone, 36.4 percent #78 stone, 17.1 percent #10 stone, 27.5 percent sand, and 1.0 percent lime. For the multiaxial tension work, a slightly modified mixture was used. This mixture contained the same binder and gradation as the Control mixture; however, the #78 aggregate for this mixture was obtained almost 4 years after the original aggregate was obtained. To reflect the later date of aggregate acquisition, this mixture is referred to as Control-2006. The blended gradation is shown in figure 13. Four asphalt binders, three polymer-modified and one unmodified, of similar performance grade were used for this study. Table 1 summarizes the relevant information for each of these binders. The asphalt content for each mixture was set at 5.3 percent by total mixture mass based on the mix design values.

Table 1. Relevant asphalt binder information.

Binder	Designation	PG Grade	Cont. PG Grade
Unmodified	Control/Control-2006	70-22	72-23
Crumb Rubber Term. Blend	CR-TB	76-28	79-28
Styrene-Butadiene-Styrene	SBS	70-28	74-28
Ethylene Terpolymer	Terpolymer	70-28	74-31

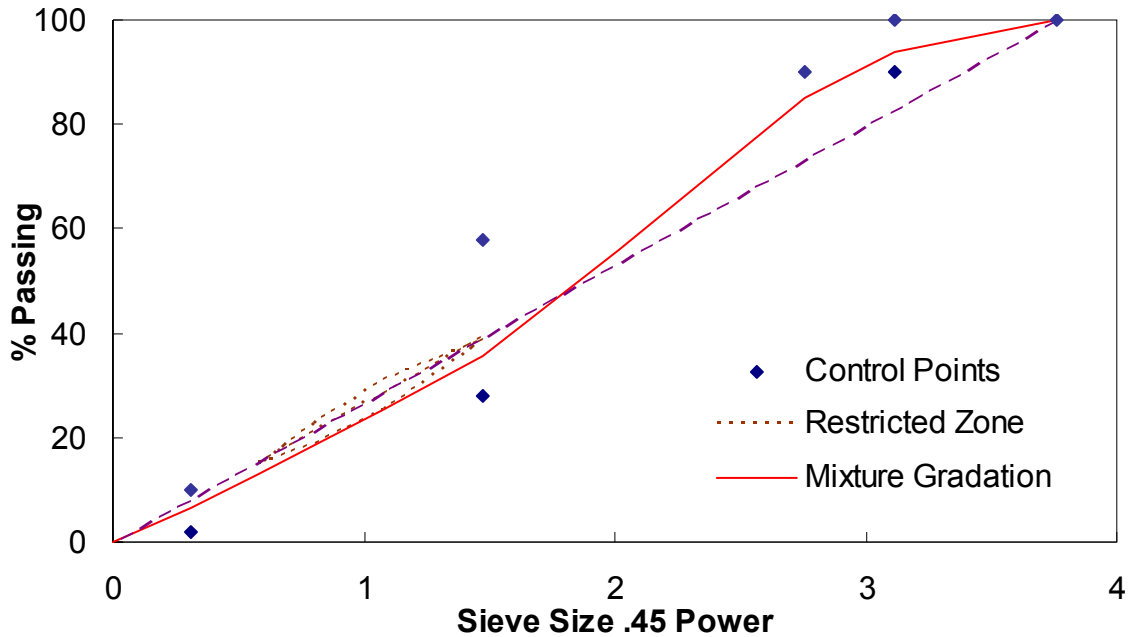


Figure 13. Graph. Mixture gradation chart.

The laboratory materials were similar to those found in the field with the following exceptions:

- Differences between the laboratory air voids and the constructed air voids.
- Differences in internal structures (not quantified) between the compaction techniques used—gyratory in the lab and roller in the field.
- Small differences in the mixture gradations due to construction factors.

The actual field mixture conditions are summarized in table 2 and figure 14.

Table 2. Summary of constructed lanes' air void and asphalt content.

Mixture	Laboratory		Test Lanes		
	Percent Air Voids	Percent Asphalt ¹	Percent Air Voids	Percent Asphalt ¹ Ignition	Percent Asphalt ¹ Nuclear
Control	4.0	5.3	7.8	5.23	4.82
CR-TB			6.8	5.48	5.09
SBS			6.0	5.28	5.05
Terpolymer			6.5	5.52	5.25

¹ By percent mass.

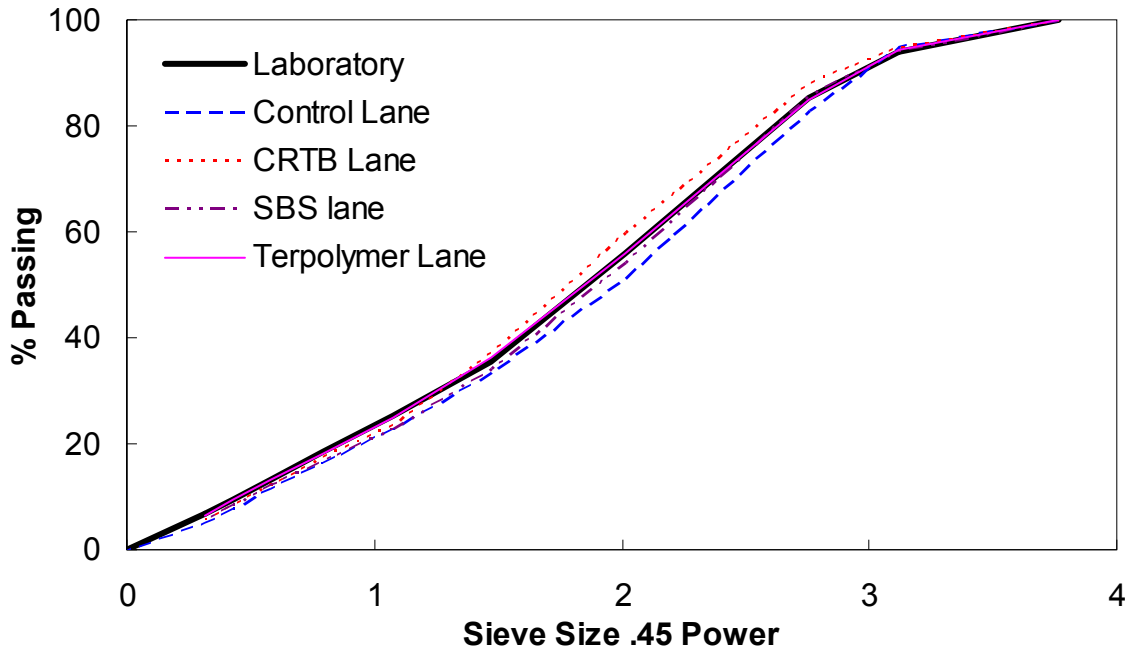


Figure 14. Graph. Comparison of test lane and laboratory gradations.

3.2. SPECIMEN FABRICATION

All specimens were compacted by the Superpave Gyrotory Compactor to a height of 178 mm and a diameter of 150 mm. To obtain specimens of uniform air void distribution, these samples were cored and cut to a height of 150 mm with a diameter of either 75 mm for tension testing or a diameter of 100 mm for compression testing. Details can be found elsewhere.^(19,20)

After obtaining specimens of the appropriate dimensions, air void measurements were taken via the CoreLok method, and specimens were stored until testing. The air voids for all tests in this study were between 3.5 and 4.5 percent. During storage, specimens were sealed in bags and placed in an unlit cabinet to reduce aging effects. Furthermore, no test specimens were stored for longer than 2 weeks before testing.

3.3. TEST SETUP

A closed-loop servo-hydraulic loading frame was used for all the tests. Depending on the nature of the test, either an 8.9- or a 25-kN load cell was used. An environmental chamber, equipped with liquid nitrogen coolant and a feedback system, was used to control and maintain the test temperature.

Measurements of axial and, in some instances, radial deformations were taken during loading. Axial measurements were taken at 90-degree intervals over the middle 100 mm of the specimen with loose-core linear variable displacement transducers (LVDTs). When taken, radial deformations were measured at 90-degree intervals with spring-loaded LVDTs. These measurements were taken on the central plane of the specimen. Load, crosshead movement, triaxial cell pressure (when appropriate) and deformation data for the specimen were acquired with National Instruments® hardware and collected with LabView™ software.

Prior to all tension testing, steel end plates were glued to the specimen with Devcon[®] steel putty. Extreme care was taken to completely clean both the end plates and the specimen ends before each application. It was observed early in the testing that failure to do so could result in the premature failure of the test. To ensure that the specimens were properly aligned, a special gluing jig was employed to ensure that the end plates were parallel, minimizing any eccentricity that might occur during the test. The triaxial tension end-plates had holes drilled specifically so that after the end plate glue had cured, a drill could create another hole through the glue at the center of the bottom end of the specimens to allow them to drain excess pore pressure during testing.

For the uniaxial constant crosshead rate compression tests, a circular hole that was 3 mm in depth and 14 mm in diameter was made at the center of the top surface of the specimen. The top plate had a key with the same dimensions in its center. The key and the hole were used to prevent the specimen from sliding during the test. For the creep and recovery test specimens, an aluminum end plate was used to minimize the creep due to the weight of the end plate. A 0.3048-mm thick rubber membrane with a 100-mm diameter and lubricant were used to avoid the end effect caused by friction between the end plate and the surface of the specimen.

Tests performed under confining pressure were the most difficult to prepare. The preparation protocols for confined tests are similar to those of an unconfined setup, except that before testing the specimen is encased in a latex membrane. To ensure proper drainage during the compression tests, the bottom lubricated membrane was punctured with a hole approximately 25 mm in diameter. This drainage ensured that no excess pore pressure developed during testing.

Following the protocol presented elsewhere, the specimen was encased in a latex membrane after attaching LVDT mounting studs.⁽⁴²⁾ Early observations showed that extreme care had to be taken when attaching LVDTs and that failure to remove all air pockets between the membrane and specimen, particularly around the LVDT studs, resulted in unusual and inconsistent results. In this study, a hole in the membrane approximately 2.5 mm in diameter was punctured at the center of each LVDT mounting stud. This hole was then stretched around the LVDT studs, and all surrounding air pockets were removed. Studs were mounted and prepared similarly for radial measurements. Mounts were prepared for radial measurements instead of directly measuring the membrane-encased specimen because it was found that deformation of the membrane was significant during pressurization. Finally, after all LVDT mounting brackets were attached, acrylic latex caulk was used to seal the areas around the mounts.

3.4. TEST PROTOCOLS

The laboratory testing was divided into four phases. The objective of the first phase was to determine the temperature and loading frequency dependence of the four mixtures. Temperature and frequency sweep complex modulus testing, either under confinement or not, were performed during this phase.

The second phase was intended to verify the t-TS principle with growing damage under confinement. This phase was important because the positive verification of the t-TS principle with growing damage under confinement significantly reduced the testing program for MVEPCD model development. Due to the limitation of time and resources, only the constant crosshead rate tests were performed for validation of the t-TS principle.

The third phase of laboratory testing was designed to determine the MVEPCD model coefficients of the mixtures. The testing program required for this phase consisted of the following:

- Constant crosshead rate tests at low temperatures and fast loading rates under both confined and unconfined conditions for the development of the viscoelastic continuum damage model.
- Constant crosshead rate tests at high temperatures with a range of loading rates or creep and recovery tests for the development of the viscoplastic model. The creep and recovery tests required a constant loading time with varying load amplitudes and constant loading amplitude with varying loading times.

The final phase of the experimental program was designed to validate the developed model. In this phase, constant rate tests under conditions not used in model development were used.

The four phases of testing applied both to tension and compression testing. For the tension testing, 75-mm diameter, 150-mm tall specimens were used, whereas 100-mm diameter, 150-mm tall specimens were used for the compression testing.

3.4.1. Complex Modulus Test

The complex modulus test was performed in the load-controlled mode in axial tension-compression (zero-mean deviatoric stress) or in compression only (zero-maximum deviatoric stress) according to American Association of State Highway and Transportation Officials (AASHTO) TP62-03. For the zero-mean deviatoric stress condition, confining pressures of 0, 250, and 500 kPa were tested, whereas the zero-maximum deviatoric stress tests were performed for confining pressures of 0, 140, and 500 kPa. Load levels for these tests were determined by a trial and error process so that the resulting strain amplitudes were between 50 and 70 $\mu\epsilon$. Based on the work of other researchers, it was assumed that this criterion ensured an accurate viscoelastic characterization.^(7,42) Under both confined and unconfined conditions, tests were performed at five temperatures (-10, 5, 20, 40, and 54 °C) and six frequencies (25, 10, 5, 1, 0.5, and 0.1 Hz) or in compression at four temperatures (-10, 10, 35, and 54 °C) and eight frequencies (25, 10, 5, 1, 0.5, 0.1, 0.05, and 0.01 Hz).

3.4.2. Constant Crosshead Rate Tests

Constant crosshead rate tests were performed with the application of a constant rate of deformation over the complete loading train. Because each component of the loading train (machine ram, load cell, etc.) deformed slightly, the on-specimen displacement rate or strain rate was not constant.⁽²⁰⁾ Prior to the confined tension test, a constant confining pressure was applied for 2 hours before testing. This 2-hour period ensured that bulk creep could not affect the analysis. To simplify the discussion of these results for the reader, a test identification (ID) system (e.g., 55-1, 55-2, etc.) has been used to describe the data for the remainder of this report. The first number in the test ID is the test temperature, and the second number indicates the ranking of the strain rate, with 1 being the fastest. For tension tests, the test ID is followed by a “T” (e.g., 55-1-T, 55-2-T).

Tests in tension were performed at three temperatures (5, 25, and 40 °C) and at multiple rates. These tests were used for the following:

- Viscoelastic (Multiaxial viscoelastic continuum damage (MVECD)) damage characterization (5 °C tests).
- Viscoplastic (VP) characterization (40 °C tests).
- MVEPCD model validation.
- t-TS principle with growing damage verification.

Table 3. Controlled crosshead testing matrix for Control-2006 in tension.

Test ID	Confining Pressure (kPa)		Temp. (°C)	Crosshead Strain Rate	Purpose
	0	500			
5-1-T	X	X	5	5.50E-05	MVECD characterization
5-2-T	X	X		3.00E-05	
5-3-T	X	X		2.20E-05	
5-4-T		X		2.15E-05	
5-5-T		X		1.50E-05	
5-6-T	X			1.05E-05	
25-1-T		X	25	5.00E-04	MVEPCD and t-TS verification
25-2-T		X		1.50E-03	
25-3-T		X		4.50E-03	
25-4-T		X		1.35E-02	
40-1-T	X	X	40	3.00E-02	VP characterization
40-2-T	X	X		1.00E-02	
40-3-T	X	X		3.00E-03	
40-4-T	X	X		1.00E-03	
40-5-T	X	X		3.00E-04	

Table 3 presents the strain rates calculated from the crosshead displacement rates over the 150-mm specimen height that were used for each phase. Tension tests were performed at 5, 25, and 40 °C at 0 and 500 kPa.

Tests in compression were performed at 5, 25, 40, and 55 °C at 0 and 500 kPa. For compression modeling purposes, these tests were used for the following:

- Viscoelastic damage characterization (5 °C tests).
- t-TS principle with growing damage verification.

To conserve materials while still covering a wide range of material behavior, it was decided that the best course of action would be to conduct tests at several different combinations of temperatures and rates with one replicate test for each combination. The strain rates used for testing at each temperature were selected so that an overlap would occur in the reduced strain rates between adjacent temperatures. The relevant information for the compression tests is presented in table 4.

Table 4. Controlled crosshead testing matrix for Control in compression.

Test ID	Confining Pressure (kPa)		Temp. (°C)	Crosshead Strain Rate	Purpose
	0	500			
5-1	X	X	5	5.75E-05	MVECD characterization
5-2	X	X		3.83E-05	
5-3	X	X		1.92E-05	
5-4	X	X		9.60E-06	
25-1	X	X	25	1.35E-02	t-TS verification
25-2	X	X		4.50E-03	
25-3	X	X		1.50E-03	
25-4	X	X		5.00E-04	
40-1	X	X	40	3.01E-02	
40-2	X	X		1.00E-02	
40-3	X	X		3.00E-03	
40-4	X	X		1.00E-03	
55-1	X	X	55	2.99E-02	
55-2	X	X		1.00E-02	
55-3	X			3.00E-03	
55-4	X			1.00E-03	

3.4.3. Repetitive Creep and Recovery Tests

Repetitive creep and recovery tests were conducted in uniaxial and multiaxial compression up to failure at 55 °C. These tests consisted of the repeated application of creep and recovery cycles. For characterization, two different conditions were applied: one with the loading time fixed and the stress magnitude increasing in each cycle (i.e., a variable loading (VL) test) and the other with a fixed-stress level and increasing loading time as the loading cycle increases (i.e., a variable time (VT) test). To gain insight into the material behavior with respect to sequence of

loading, a VT test was performed in the reverse order of the characterization VT test (i.e., a reverse VT (RVT)). For model verification, three different conditions were used:

1. A test with constant load and constant time (CLT).
2. A variable load and variable time test (VLT).
3. A VT test that was followed by a flow number test.

A summary of the test methods and the confining pressures used with each is shown in table 5. The following sections provide a brief summary of each test method used.

3.4.3.1. VL Test

The repetitive creep and recovery test with a variable load level was performed for the calibration of the developed viscoplastic model. In this VL test, the loading time remained constant until the end of the test, whereas the load level was varied. One loading block consisted of eight increasing loading pulses. The deviatoric stress of the first loading in the loading group was the same as that of the third loading in the preceding loading group. For testing with an unconfined and confining pressure of 140 kPa, the first deviatoric stress was 137.9 kPa and was stepped by $1.2^{(n-1)}$ as the number of loads, n , increased, as shown in figure 15. The confined testing began with a deviatoric stress of 300 kPa for the 500 kPa confining pressure test, as shown in figure 16. For both cases, the loading time was set to 0.4 s, and the loading was repeated until the specimens failed.

Table 5. Creep and recovery testing matrix for Control mixture in compression.

		Confining Pressure (kPa)		
		0	140	500
VT		X	X	X
RVT			X	X
VL		X	X	X
VLT			X	X
CLT	0.4 s			X
	1.6 s			X
	6.4 s			X
VT + Flow Number			X	

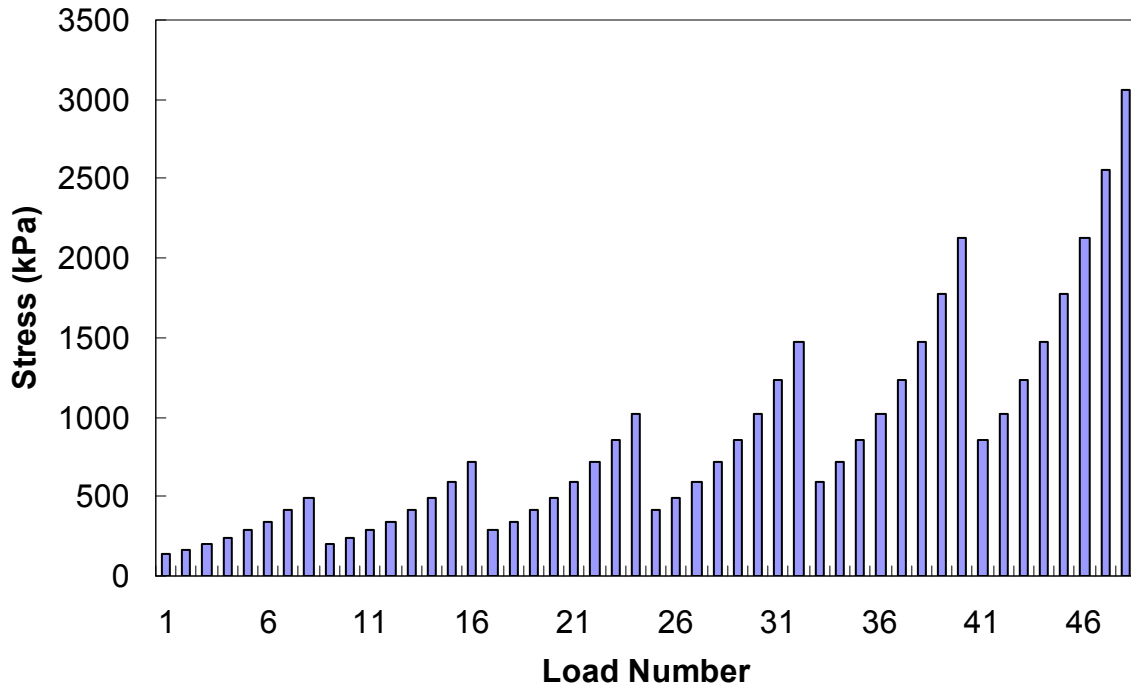


Figure 15. Graph. Stress history of VL testing (unconfined and 140 kPa confinement VL).

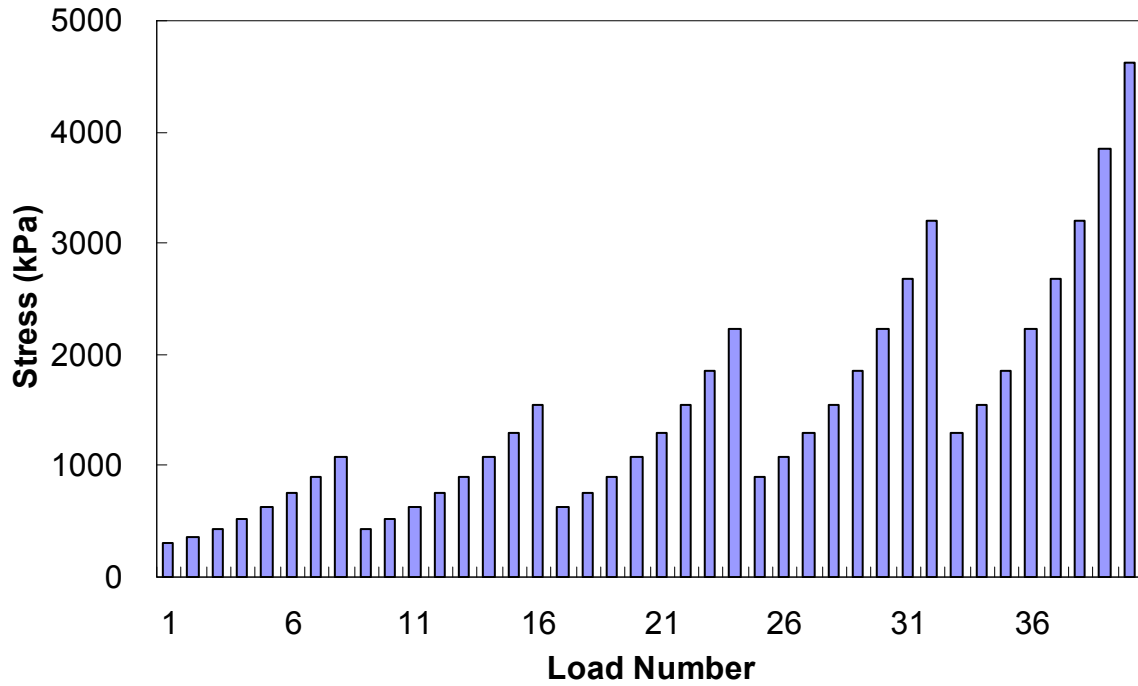


Figure 16. Graph. Stress history of VL testing (500 kPa confinement VL).

3.4.3.2. VT and RVT Test

The repetitive creep and recovery tests with variable loading times were performed to achieve three major goals:

1. Identify the effect of loading time (pulse time) on viscoplastic strain development.
2. Verify the t-TS principle.
3. Characterize the viscoplastic model.

For the VT tests, the level of deviatoric stress remained the same until the end of the test, but the duration of the load was varied. As with the VL testing, these tests consisted of the repeated application of load pulses in groups or blocks. The first loading block started with a 0.05-s loading pulse followed by 200 s of rest. Longer loading pulses with 200 s of rest were applied subsequently until the loading block ended, as shown in table 6. This loading block was repeated depending on the deviatoric stress and confining pressure of the test.

Table 6. Test conditions for the VT and RVT tests.

Confining Pressure (kPa)	Deviatoric Stress (kPa)	Pulse Time (rest period) (s, physical time at the testing temperature)						
		0.05 (200)	0.1 (200)	0.2 (200)	0.4 (200)	1.6 (200)	6.4 (200)	—
0	827	0.05 (200)	0.1 (200)	0.2 (200)	0.4 (200)	1.6 (200)	6.4 (200)	—
140	552, 827	0.05 (200)	0.1 (200)	0.2 (200)	0.4 (200)	1.6 (200)	6.4 (200)	—
		0.82 *(40)	1.63 *(40)	3.27 *(40)	6.53 *(40)	26.12 *(50)	104.49 *(60)	—
500	1600, 1800, 2000	0.05 (200)	0.1 (200)	0.25 (200)	0.4 (200)	1.6 (200)	2.0 (200)	6.4 (200)

* Physical time at 40 °C, which is equivalent in reduced time to physical time at 55 °C.

— No measurement taken.

Note from table 6 that at a confining pressure of 140 kPa two different pulse times and rest period histories are given. Tests at this confining pressure were performed for t-TS verification with damage, and the second history was performed at 40 °C for this verification. In RVT testing, the loading conditions were the same as for VT testing except for the sequence of loading, which was exactly opposite to that in the VT tests.

3.4.3.3. CLT Test

CLT testing was conducted to confirm the effects of loading time (or pulse time) on the viscoplastic strain development. During CLT testing, the loading time, rest period, and load level were kept constant. These tests were performed only at the 500 kPa confining pressure, and only a single deviatoric stress level of 1,800 kPa was used. Three different loading times of 0.4, 1.6, and 6.4 s were used.

3.4.3.4. VLT Test

VLT testing incorporated the combined loading histories of the VT and VL testing. The test started with a deviatoric stress of 100 kPa and a loading time of 0.05 s, as shown in figure 17, figure 18, and table 7. After 200 s of rest following the first loading, another loading followed by 200 s of rest using the same deviatoric stress but with an increased loading time, similar to the VT testing. Following the rest period, the deviatoric stress increased to the next stress level, as shown in figure 17 and figure 18. This sequence was repeated until the specimen failed.

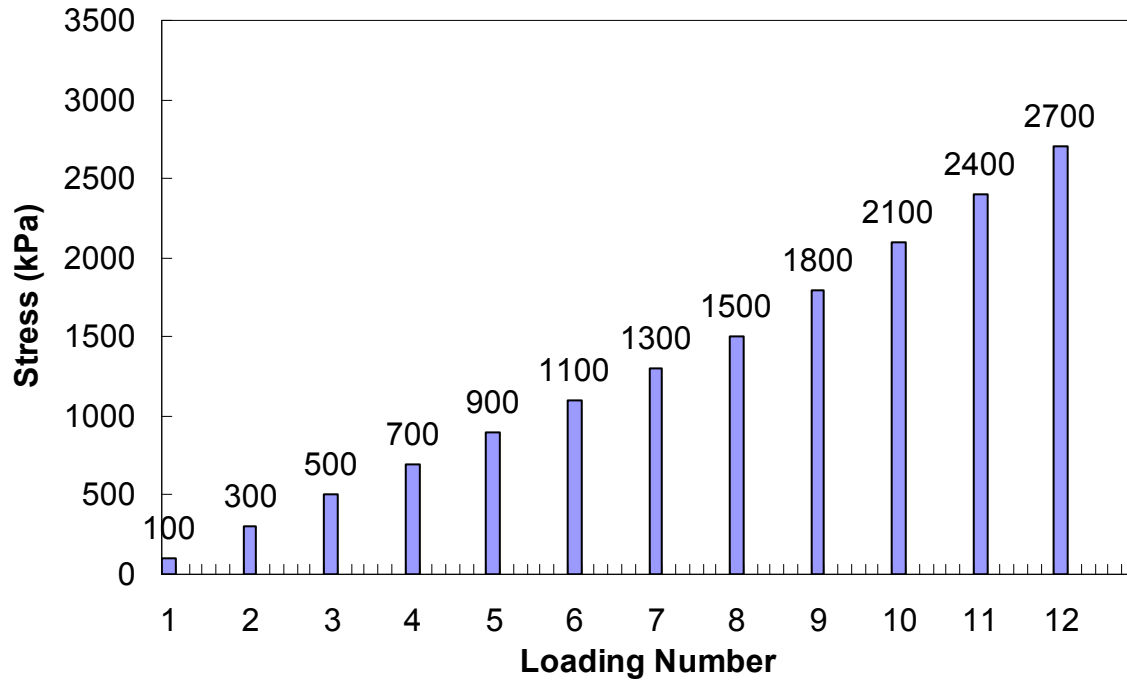


Figure 17. Graph. Stress history of VLT testing (140 kPa confinement).

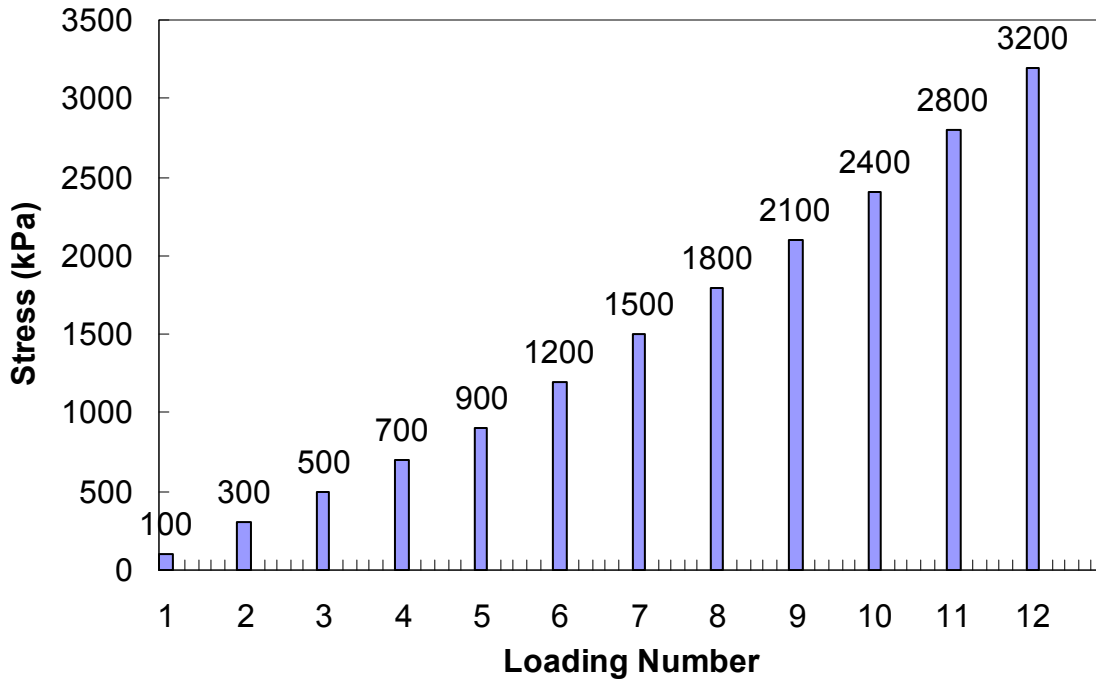


Figure 18. Graph. Stress history of VLT testing (500 kPa confinement).

Table 7. Loading times for VLT test.

Confining Pressure (kPa)	Pulse Time (s)					
	0.05	0.1	0.2	0.4	1.6	6.4
140	0.05	0.1	0.2	0.4	1.6	6.4
500	0.05	0.1	0.25	0.4	1.6	6.4

3.5. DATA ANALYSIS

Various data analysis methods were evaluated in this research. The major objective in the data analysis was to determine the MVEPCD model coefficients. The time-temperature shift factors were determined from the frequency and temperature sweep dynamic modulus test. These factors were also used to check if the mixtures exhibited t-TS with growing damage. Dynamic modulus mastercurves were used for the determination of MVECD characteristics.

The viscoelastic model development involved the determination of pseudo strain and the damage parameter, S . The constant crosshead rate monotonic tests at 5 °C were used to develop the damage characteristic curve for each mixture. The viscoplastic model coefficients were determined from either constant crosshead rate tests at high temperatures or creep and recovery tests with varying loading times and stress levels.

The MVEPCD model, developed with the above mentioned testing program, was used to calculate the viscoelastic and viscoplastic strains under random cyclic loading. A comparison of the calculated and the measured strains revealed the accuracy of the MVEPCD model under realistic loading conditions. All of the analysis techniques presented were performed with analysis software developed at NCSU.

CHAPTER 4. MVEPCD CHARACTERIZATION AND VERIFICATION IN TENSION

4.1. INTRODUCTION

Fatigue cracking of asphalt pavements, along with permanent deformation, is known to be a major form of pavement distress in the United States. Such cracking occurs due to extensive cyclic applications of loads and/or variations in temperature. The typical understanding of this cracking phenomenon suggests that these cycles create areas of tensile strain at the bottom of the pavement layer, leading to the initiation of microcracks. Under repeated loadings, these microcracks densify, coalesce, propagate, and eventually develop into more visible macrocracks on the pavement surface. Further research in recent years also suggests that under certain conditions cracking can begin at the top of the pavement and progress downward.^(43–45)

Traditional fatigue testing and performance prediction are based on empirical methods that are developed from the “bottom-up” understanding of fatigue cracking. For fatigue assessment, these methods rely on the simulation of field conditions in the laboratory. As such, typical methods apply cyclic bending stresses to asphalt beams of a particular dimension and support condition.⁽⁴⁶⁾ Tests are performed under either controlled stress or controlled strain conditions. Using such methods alone can lead to gross errors in performance prediction when field conditions vary considerably from those used in the laboratory. Further complications with these methods are evidenced by the combined effects of the elements of both material and structure. This shortcoming can be bypassed, however, by separating these two behaviors and focusing on the material separately from the structure.

Results of the Strategic Highway Research Program (SHRP) A-003 project acknowledged the need to combine material and structural components in some way.^(46,47) Researchers on this project concluded that experimental work should be performed to extract fatigue properties and that mechanistic analysis should be performed to calculate stresses and strains in the pavement structure. Although these researchers made considerable advances in beam fatigue testing—an ever-present shortfall of these tests—the inability of the test to truly separate the material from the structure could not be overcome.

A fundamental purpose of this report is to show that material behavior can be accurately described using a simplified laboratory program by using constitutive models that make rigorous theoretical considerations. The benefits of such an approach lie in the constitutive model’s use of the fundamental properties that govern material behavior. That is, changes in external conditions, such as temperature and loading level, are easily taken into account without the need for additional experimentation. When combined with a structural model, such as finite elements, this approach can then account for any combination of pavement structure, traffic, and environmental condition.

In a previous report, a VEPCD model was characterized using the FHWA ALF mixtures.⁽¹³⁾ However, this model was limited because in-service asphalt concrete undergoes a more complicated state of stress than that which was simulated in the laboratory. With this in mind, a possible drawback to the current VEPCD model formulation is the exclusion of stress state

dependence. In this chapter, the multiaxial extension, first derived by Ha and Schapery, is characterized and verified using the Control-2006 mixture.⁽⁴⁸⁾

As part of the characterization process, results were obtained that allowed further verification of the t-TS principle with growing damage, and these results are presented here. The final section of this chapter presents findings from a study of the uniaxial VEPCD model as it relates to the prediction of cyclic fatigue test results. This section of the report is particularly important because it relates directly to potential test protocols that are to be included in the Simple Performance Tester (SPT)/Asphalt Mixture Performance Tester (AMPT).

4.2. MVECD CHARACTERIZATION IN TENSION

4.2.1. Linear Viscoelastic Characterization

Characterization of the MVEPCD model began with the development of a stress state dependent linear viscoelastic model. Following the test protocols presented in chapter 3, frequency-temperature sweep tests were conducted in both the unconfined and confined state. The results of this characterization are shown for the unconfined stress state in table 8, a confining pressure of 250 kPa in table 9, and a confining pressure of 500 kPa in table 10. Generally, higher variability was observed in the confined tests relative to the ones performed under unconfined conditions. However, the variability in both was generally small, on the order of 5 percent. It is also observed from table 8 through table 10 that the confinement effect became more prominent as the temperature increased or the frequency decreased.

Table 8. Linear viscoelastic characterization and variation for Control-2006 in unconfined state at selected frequencies and temperatures.

Temp. (°C)	Frequency (Hz)	Average E* (MPa)	Average Phase Angle (°)	E* Coefficient of Variation (%)	Phase Angle Coefficient of Variation (%)
-10	25	32,290	4.9	2.8	34.8
	10	31,260	5.4	2.9	31.4
	5	30,416	5.7	3.1	28.4
	1	27,905	6.7	3.1	30.4
	0.5	26,771	7.1	3.0	26.2
	0.1	23,694	8.8	4.0	8.0
5	25	23,184	9.7	2.9	17.1
	10	21,243	10.7	3.0	17.2
	5	19,713	11.3	2.8	16.2
	1	16,286	13.7	3.2	12.5
	0.5	14,831	14.8	3.3	13.3
	0.1	11,439	18.3	3.8	13.6
20	25	12,305	18.2	2.1	6.6
	10	10,384	20.4	1.7	8.5
	5	8,834	22.8	2.2	5.8
	1	5,732	29.0	3.7	5.6
	0.5	4,701	31.3	3.2	5.1
	0.1	2,736	38.9	2.1	3.4
40	25	2,713	38.4	4.0	4.0
	10	1,856	43.2	3.5	2.0
	5	1,358	44.2	3.8	2.6
	1	705	44.5	5.1	2.7
	0.5	527	42.4	5.7	3.5
	0.1	294	34.3	5.2	4.4
54	25	764	45.1	8.9	4.1
	10	523	42.8	6.8	2.8
	5	419	38.7	8.7	1.5
	1	229	30.9	9.7	6.6
	0.5	204	25.6	9.5	11.0
	0.1	151	18.2	10.2	34.3

Table 9. Linear viscoelastic characterization and variation for Control-2006 in 250 kPa confined state at selected frequencies and temperatures.

Temp. (°C)	Frequency (Hz)	Average E* (MPa)	Average Phase Angle (°)	E* Coefficient of Variation (%)	Phase Angle Coefficient of Variation (%)
-10	25	31,769	2.2	—	—
	10	30,490	2.5	—	—
	5	29,595	2.3	—	—
	1	27,011	3.2	—	—
	0.5	25,884	3.6	—	—
	0.1	22,966	4.6	—	—
5	25	22,775	6.5	—	—
	10	21,065	7.5	—	—
	5	19,555	7.5	—	—
	1	16,143	9.5	—	—
	0.5	14,661	10.9	—	—
	0.1	11,312	14.3	—	—
20	25	12,538	15.0	—	—
	10	10,525	16.7	—	—
	5	9,173	18.2	—	—
	1	6,119	22.8	—	—
	0.5	5,069	24.8	—	—
	0.1	2,974	29.3	—	—
40	25	3,801	26.1	—	—
	10	2,841	25.8	—	—
	5	2,408	24.0	—	—
	1	1,554	20.5	—	—
	0.5	1,434	18.1	—	—
	0.1	1,088	14.0	—	—
54	25	1,905	22.8	—	—
	10	1,555	20.0	—	—
	5	1,363	17.4	—	—
	1	1,156	13.7	—	—
	0.5	1,031	11.2	—	—
	0.1	925	8.1	—	—

— Data based on a single test thus variational analysis is not possible.

Table 10. Linear viscoelastic characterization and variation for Control-2006 in 500 kPa confined state at selected frequencies and temperatures.

Temp. (°C)	Frequency (Hz)	Average E* (MPa)	Average Phase Angle (°)	E* Coefficient of Variation (%)	Phase Angle Coefficient of Variation (%)
-10	25	31,031	4.3	1.9	22.6
	10	30,093	4.7	2.7	24.1
	5	29,207	4.9	2.9	26.3
	1	26,480	5.8	3.0	26.4
	0.5	25,203	6.4	2.9	25.7
	0.1	22,112	7.9	3.1	20.1
5	25	22,380	8.3	2.3	18.1
	10	20,573	9.3	3.4	13.9
	5	19,043	9.7	4.0	15.2
	1	15,601	12.1	4.0	13.5
	0.5	14,177	13.4	4.0	10.8
	0.1	10,879	16.8	5.0	9.6
20	25	12,628	16.0	5.4	6.4
	10	10,815	17.4	6.3	5.4
	5	9,408	19.1	7.8	2.3
	1	6,561	22.6	10.8	1.7
	0.5	5,623	22.9	12.4	0.5
	0.1	3,994	24.0	6.4	7.0
40	25	4,430	24.2	6.5	7.0
	10	3,528	22.9	1.6	6.6
	5	3,049	21.6	2.8	7.0
	1	2,268	18.7	5.8	8.7
	0.5	2,103	17.4	4.6	11.7
	0.1	1,731	14.4	4.6	16.3
54	25	2,550	20.1	5.6	9.4
	10	2,154	18.0	4.6	10.7
	5	1,981	16.3	5.5	14.9
	1	1,658	12.8	5.2	20.4
	0.5	1,575	11.6	5.2	24.1
	0.1	1,463	9.5	4.4	29.9

Table 11. Effect of confining pressure on shift factor function coefficients for Control-2006 mixture.

Parameters	0 kPa	250 kPa	500 kPa
α_1	0.00069	0.00079	0.00063
α_2	-0.16245	-0.15411	-0.14816
α_3	0.79489	0.75076	0.72512

The data presented in table 8 and table 10 have been shifted to form a continuous mastercurve. The results are plotted for the three conditions in figure 19, figure 21, and figure 22. The shift factor function coefficients are shown in table 11. For all cases, zero-mean deviatoric stress conditions (i.e., tension compression) were applied. From figure 19 through figure 21, it is observed that at high reduced frequencies, stiffness and phase angle values were insensitive to confining pressure, but they diverged as the reduced frequency decreased. Furthermore, it is seen from figure 19 and figure 20 that the slope of the confined mastercurve was not as steep as the slope of the unconfined mastercurve, thus suggesting reduced time dependence in the material under confined stress. In addition, by examining the phase angle mastercurves in figure 21, it is seen that at lower reduced frequencies, the material behaved more elastically under confining pressure than it did in the uniaxial state. This effect was not significantly dependent on the confining stress level. The same observation can be made with regards to the t-TS shift factors from figure 22.

These observations are consistent with those made by other researchers for asphalt concrete.^(22,49) This finding may have implications on the simple performance test protocols since it is known that in the pavement structure complicated stress states do exist. Time and resources do not allow for an indepth investigation into the effects of this phenomenon, and it is unclear exactly what factors influence the phenomenon's magnitude. Care should be taken in using the findings shown in these figures to justify the confined protocol for simple performance testing until the necessary analysis has been completed and further testing is performed. Performing confined dynamic modulus testing, even in the compression mode, is considerably more complex and time-consuming than uniaxial tests. In the end, this effort may be wasteful if, through careful study, the overall impacts of this behavior are similar across mixtures and would be indirectly considered through any mechanistic-empirical analysis calibration process.

These observations are also the same as those found from unbound paving materials (i.e., higher stiffness increases the confining pressure). Therefore, the behavior appears to be related to the ability of the asphalt cement to resist dilation of the aggregate skeleton. However the deformation that was applied in these tests was generally small, on the order of $60 \mu\epsilon$, which was not large enough to introduce significant aggregate reorientation. Nevertheless, it seems reasonable to assume that the mechanisms responsible for the increased stiffness under confining pressure were at least similar to those of unbound materials. This hypothesis may also suggest that confining pressure effects can be considered without the need to significantly reconsider the LVE properties of the material. Support for this hypothesis is given in figure 23 where the relaxation spectrum for the confined and unconfined tests is plotted. The relaxation spectrum was the crossplot of the Prony coefficients, E_i , and their active or relaxation times, ρ_i , from equation 5. This plot provides an indication of molecular processes occurring in the material and the times at which they occurred under fixed displacement.^(50,51) Stated more simply, this plot provides a snapshot of the LVE processes that occurred in the material. Figure 23 shows that the spectrum obtained from collocation for the unconfined test was very similar to that for the confined test. The reason for the differences shown in figure 19 can be largely attributed to differences in the equilibrium or long-time elastic modulus of the material. In fact, figure 24 presents the effect of using the uniaxial relaxation spectrum with the confined equilibrium modulus, and the overall effect was small.

One may also question whether the differences observed at low reduced frequencies were related to a permanent hardening of the material, recoverable hardening, or some other mechanism. To examine the possibility of permanent hardening, the frequency sweep test was rerun with no confining pressure approximately 1 hour after decompressing from the first 500 kPa test. Results of this test are presented in figure 25 along with the average from the original uniaxial characterization tests at 54 °C. Similar results were obtained for the two sets of tests, with the test performed after the confined test showing slightly higher values. The slightly higher values could be related to membrane effects but were more likely due to the relative magnitudes of the friction and applied stress levels. The loading rod for the uniaxial tests was not subjected to friction, whereas, in the tests run after the confined test (labeled “unconfined” in figure 25), friction was present where the rod passes through the triaxial cell lid. Regardless of the influence of the friction on the measured modulus, figure 25 shows that the increased stiffness at low reduced frequencies was a mostly recoverable phenomenon at the very least.

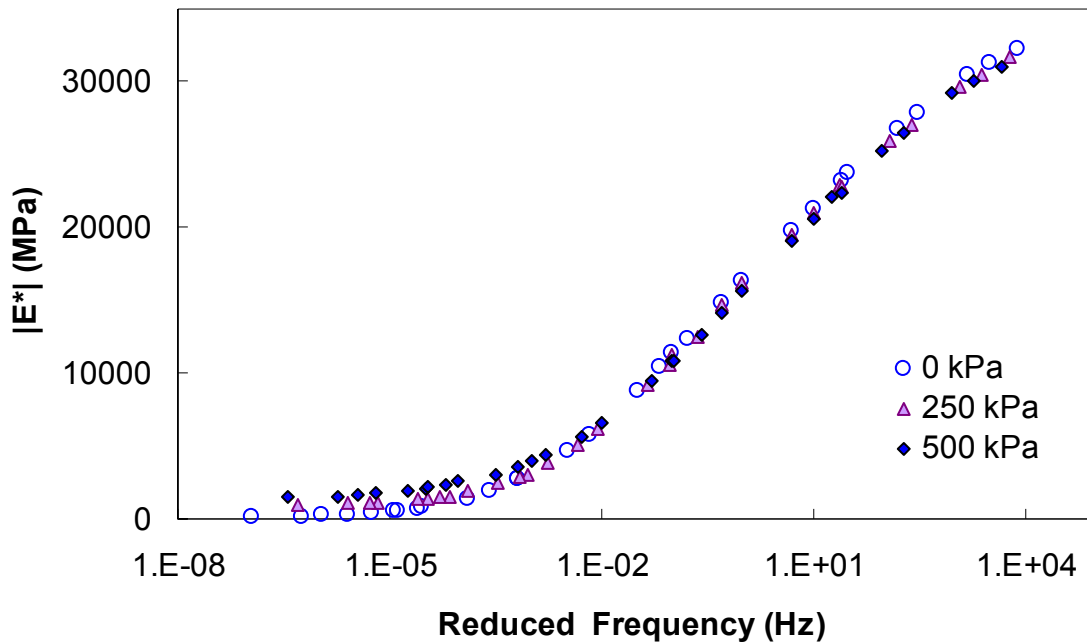


Figure 19. Graph. Effect of 500 kPa confining pressure on the dynamic modulus in semi-log space.

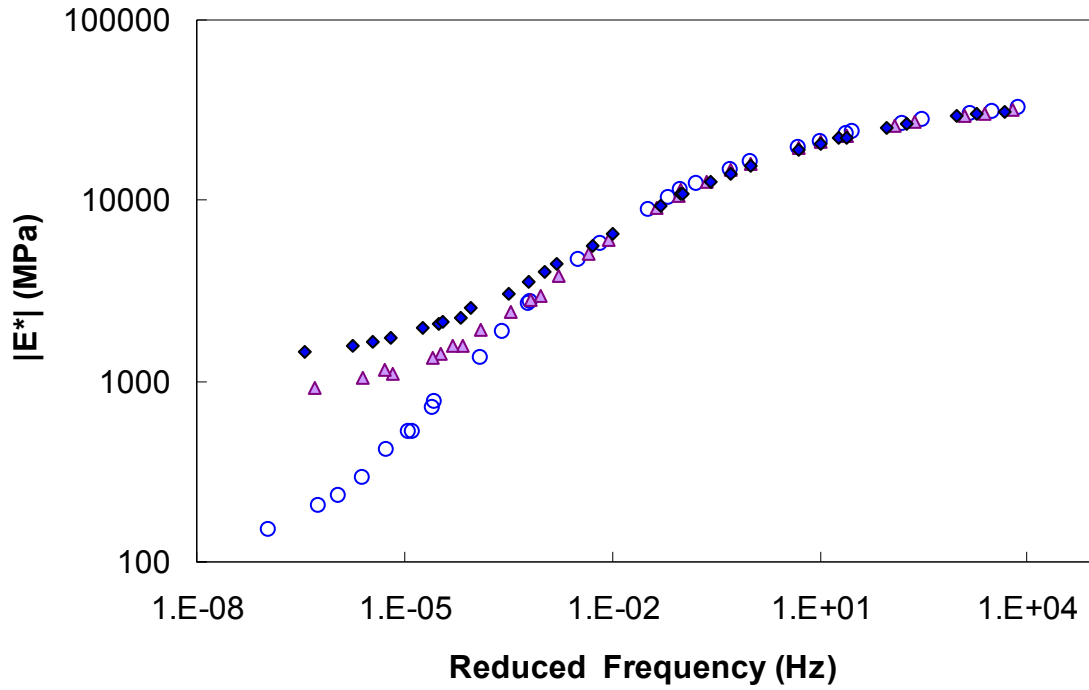


Figure 20. Graph. Effect of 500 kPa confining pressure on the dynamic modulus in log-log space.

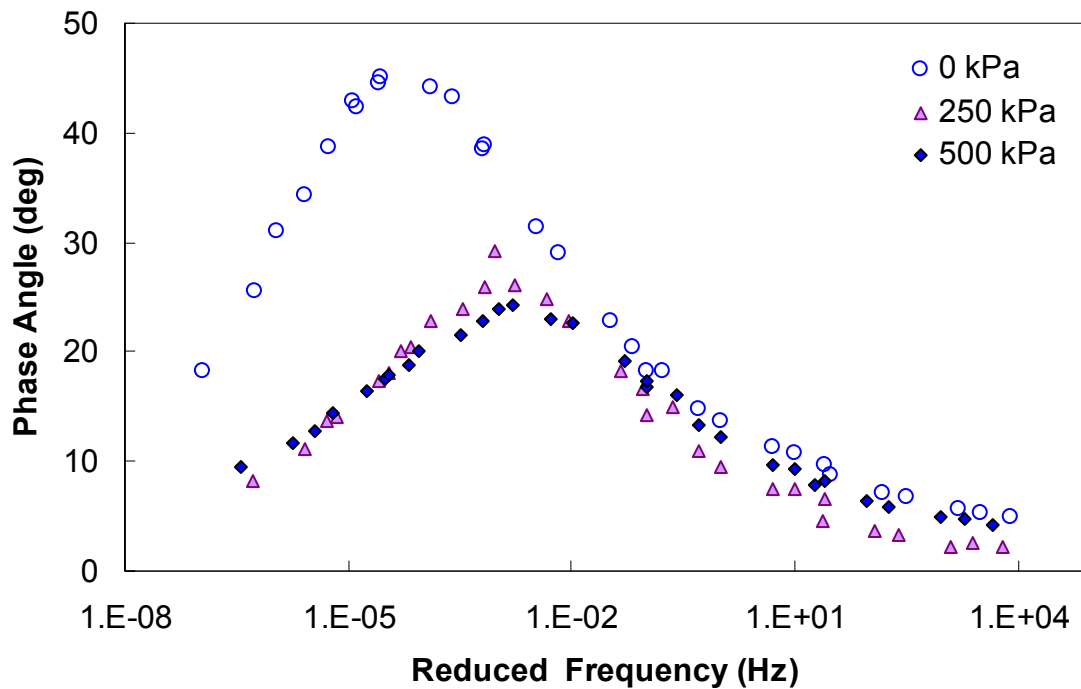


Figure 21. Graph. Effect of 500 kPa confining pressure on observed elasticity in the Control mixture.

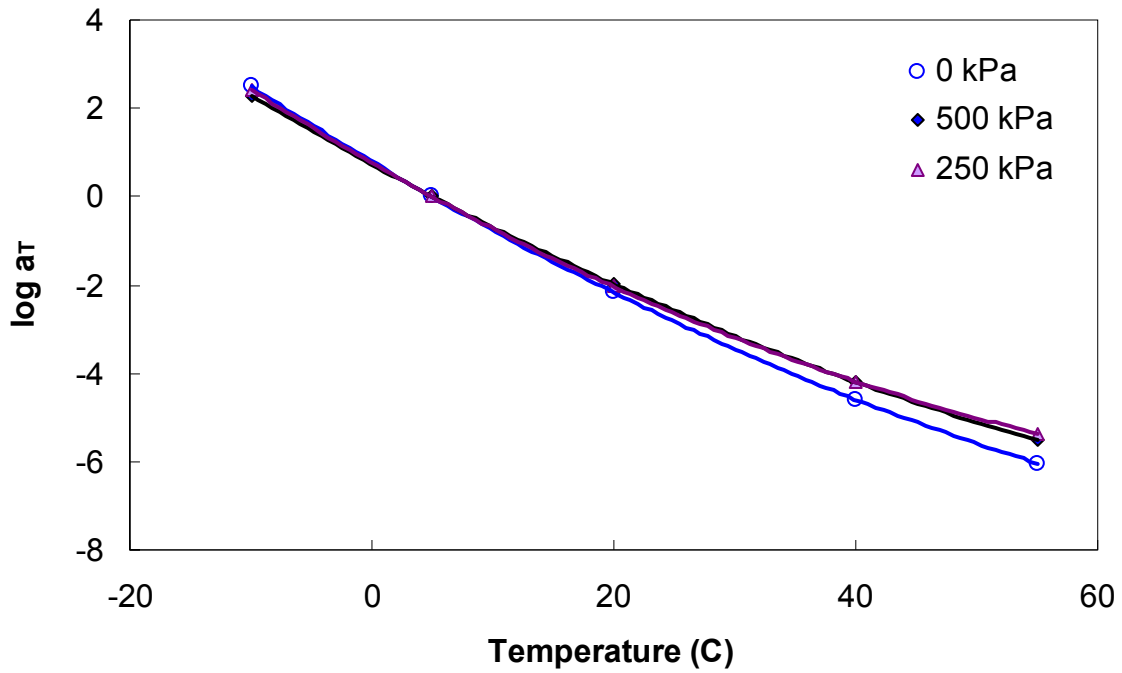


Figure 22. Graph. Effect of 500 kPa confining pressure on the log shift factor function.

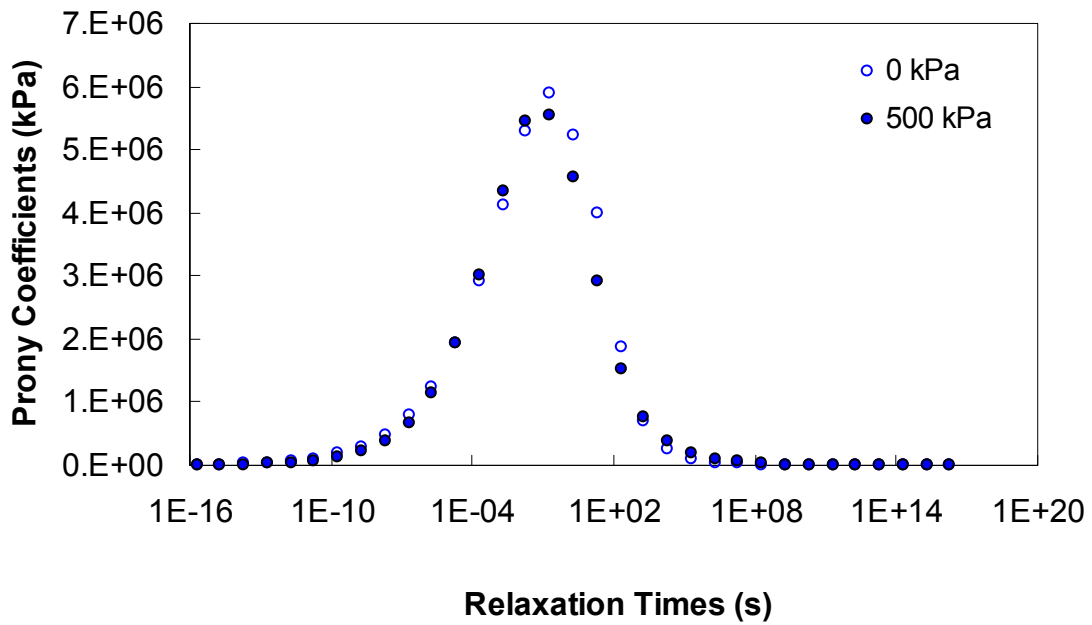


Figure 23. Graph. Effect of confining pressure on the relaxation spectrum.

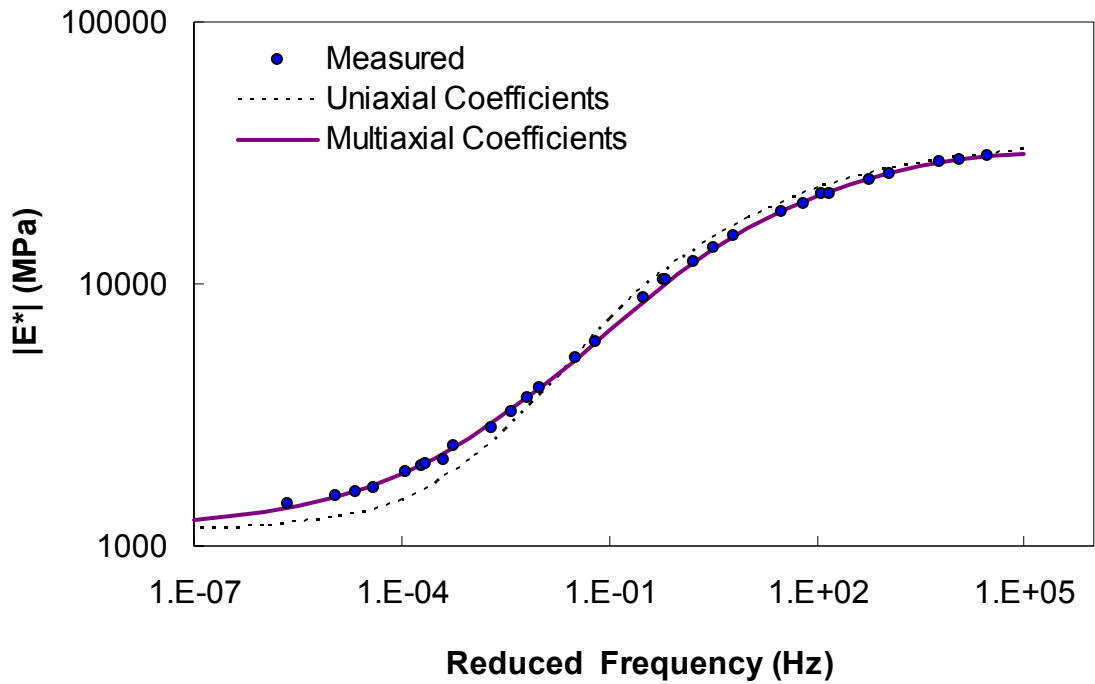


Figure 24. Graph. Use of the uniaxial relaxation spectrum for multiaxial test results.

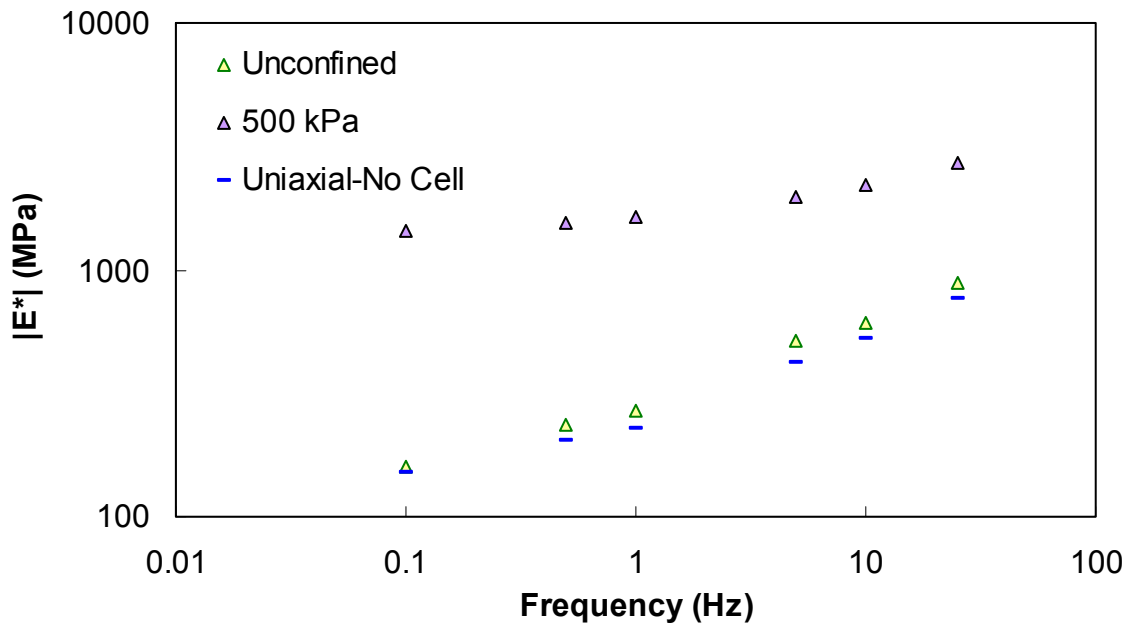


Figure 25. Graph. Effect of performing confined temperature/frequency sweep testing on the unconfined dynamic modulus.

4.2.2. Modeling Stress State Dependence of the $|E^*|$

To model the stress state dependence of the $|E^*|$ of asphalt concrete, a phenomenological model similar to that used for unbound material moduli was utilized. For the purposes of this report, the modulus mastercurves determined from 0, 250, and 500 kPa were used along with the observations given in figure 19 through figure 25. The relaxation spectrum from the uniaxial test was assumed to be independent of confining pressure, and all pressure effects were combined into the long-time equilibrium modulus (E_∞ from equation 5). The model used for the equilibrium modulus is shown in equation 85. The characterization results for this model are shown in figure 26, and it was found that $k_1 = -1,859$, $k_2 = 0.681$, and $k_3 = 10.01$. The degree to which these models agreed with the measured responses is shown for the storage modulus in figure 27. Note that the MVEPCD model verification efforts in section 4.4 employ the modulus predicted from equation 85 instead of the measured modulus.

$$E_\infty = k_1 P_a \left[\frac{\theta - 3k_6}{P_a} \right]^{k_2} \quad (85)$$

Where:

θ = Bulk stress, $\sigma_{11} + \sigma_{22} + \sigma_{33}$.

P_a = Atmospheric pressure.

k_1, k_2, k_3 = Fitting coefficients.

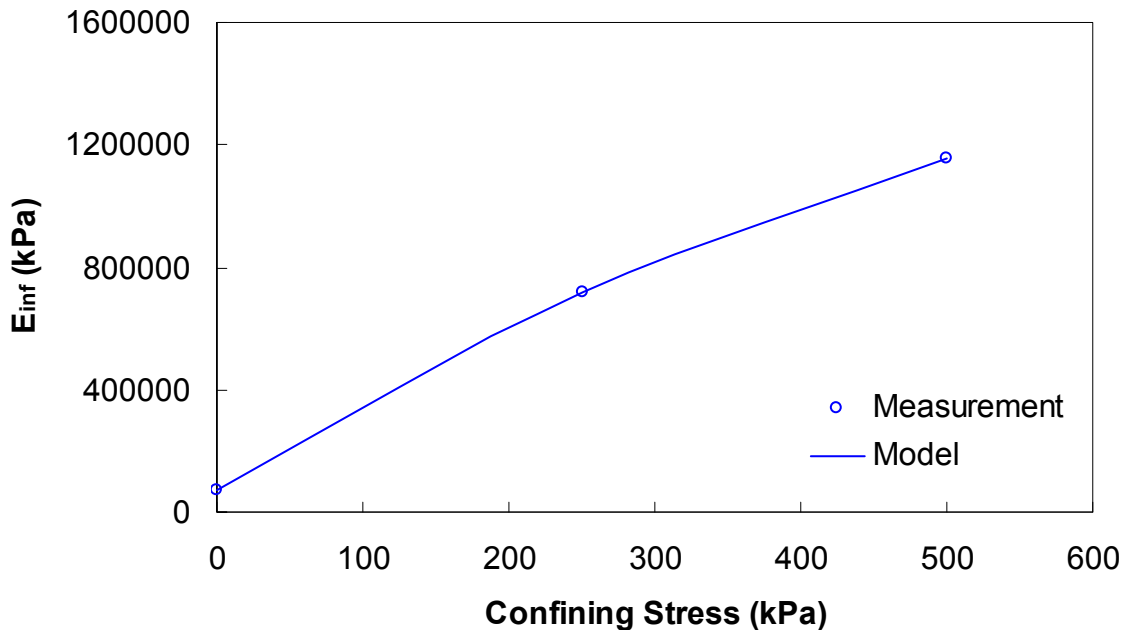


Figure 26. Graph. Multiaxial equilibrium characterization results.

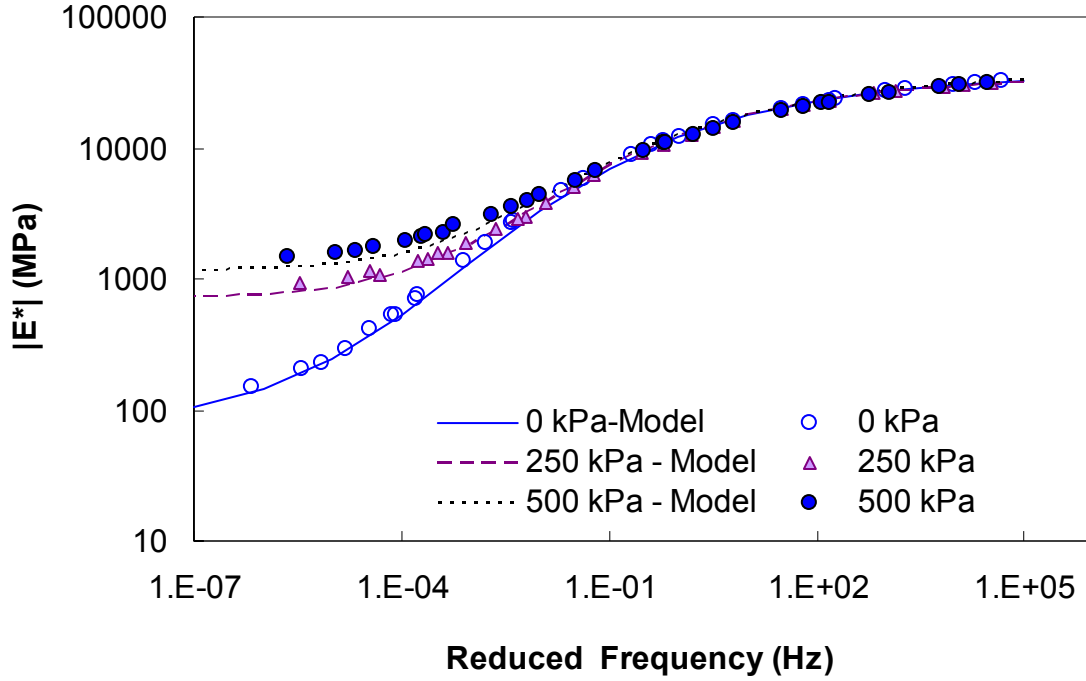


Figure 27. Graph. Multiaxial dynamic modulus model strength.

4.2.3. MVECD Damage Function Characterization

Characterization of the MVECD model involves developing the functional relationship of C_{11} , C_{12} , and C_{22} with damage, S . It is recalled that the general strain energy density function is given as such:

$$W_d^R = \frac{1}{2} C_{11}(S) (\varepsilon^R)^2 + C_{12}(S) \varepsilon^R p + \frac{1}{2} C_{22}(S) p^2 \quad (86)$$

From this equation, the stress and pseudo dilation can be shown as follows:

$$\sigma = C_{11}(S) \varepsilon^R + C_{12}(S) p \quad (87)$$

$$v^R = C_{12}(S) \varepsilon^R + C_{22}(S) p \quad (88)$$

From equation 87 and equation 88, C_{11} and C_{12} may be characterized using uniaxial constant crosshead rate tests under conditions where viscoelastic damage mechanisms dominate the material behavior. C_{22} , however, must be characterized using multiaxial constant crosshead rate tests.

4.2.3.1. Characterization of $C_{11}(S)$

Under uniaxial conditions in equation 87, the pressure is zero, and C_{11} may be solved at any time as shown in equation 89.

$$(C_{11})_i = \frac{\sigma_i}{\varepsilon_i^R} \quad (89)$$

To find the relationship between C_{11} and S , the damage is first calculated using the chain rule method, equation 90, with C denoting C_{11} for notational simplicity.

$$S_i = S_{i-1} + \left(-\frac{1}{2} (\varepsilon^R)^2 (C_i - C_{i-1}) \right)^{\alpha/1+\alpha} (t_i - t_{i-1})^{1/\alpha} \quad (90)$$

These S values are then refined using the method outlined in the NCHRP 9-19 Final Report.⁽²²⁾ Finally, the functional relationship between C_{11} and the refined S is determined for each replicate test and averaged to obtain the representative C_{11} - S relationship. This relationship is shown for the mixture under consideration in figure 28. This figure is constructed at a reference temperature of 5 °C and applies only to the material under tensile loading. For this given mixture, it is found that $a = -0.00157$ and $b = 0.5320$.

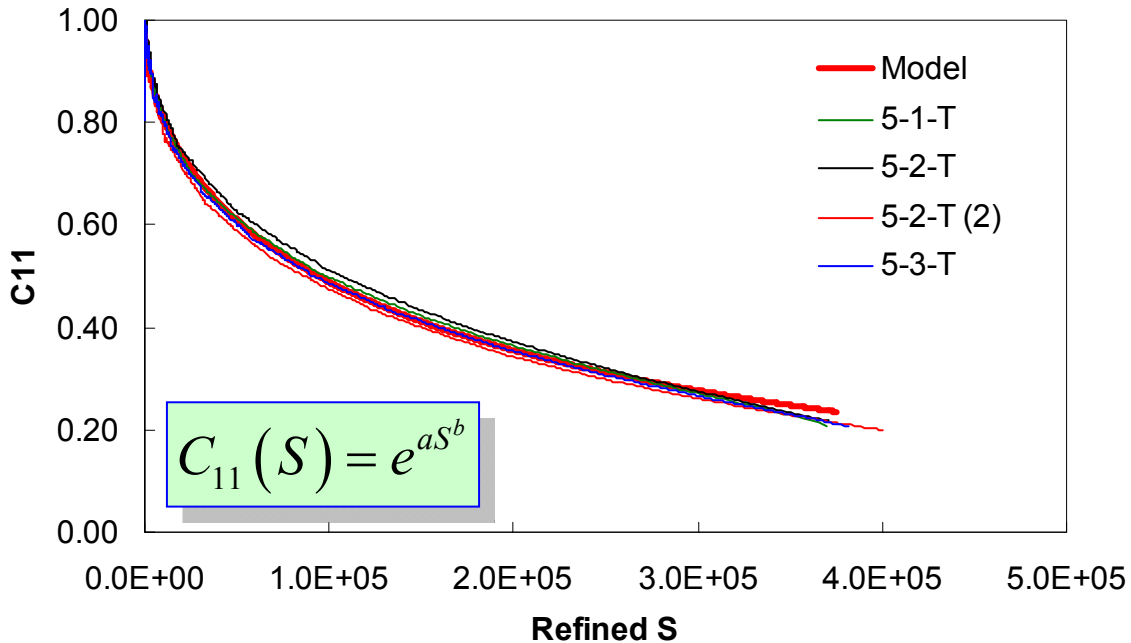


Figure 28. Graph. C_{11} versus S for tension for Control-2006 mixture (5 °C reference).

4.2.3.2. Characterization of $C_{12}(S)$

Under uniaxial conditions in equation 88, the pressure is zero, and C_{12} may be solved at any time, as shown in equation 91.

$$(C_{12})_i = \frac{\nu_i^R}{\varepsilon_i^R} \quad (91)$$

Where:

The pseudo dilation is calculated using the convolution of the relaxation modulus and the sum of the axial and radial strain components.

Complications arose in C_{12} characterization due to the differences in time dependence of the axial and radial strains (i.e., the time dependence of Poisson's ratio). The generalized correspondence principle did not account for such time dependence in Poisson's ratio. Instead, the correspondence principle placed all of the time dependence with the relaxation modulus or creep compliance.

Through the definitions of pseudo strain and pseudo dilation, it can be observed that $C_{12} = (1 - 2\nu)$. Thus, C_{12} defined, in a way, the change in Poisson's ratio with damage. The initial value of C_{12} was related to the undamaged Poisson's ratio of the material, and any change in this value was assumed to be related to damage effects alone. When the material of interest did not have a constant Poisson's ratio, the same could be claimed because time effects caused C_{12} to change as well. The data shown in figure 29 demonstrate this effect. Here, a LVE prediction of strains has been performed for the axial and radial strains. These predicted strains were then used to calculate pseudo strain and pseudo dilation. In turn, these values were used to calculate C_{12} , which was plotted against time. Two predictions were performed, one utilizing the time-independent Poisson's ratio and one using the time-dependent Poisson's ratio. Figure 29 shows that the prediction utilizing a time-dependent Poisson's ratio incorporated changes in the values, whereas the values from a time-independent Poisson's ratio did not change with time.

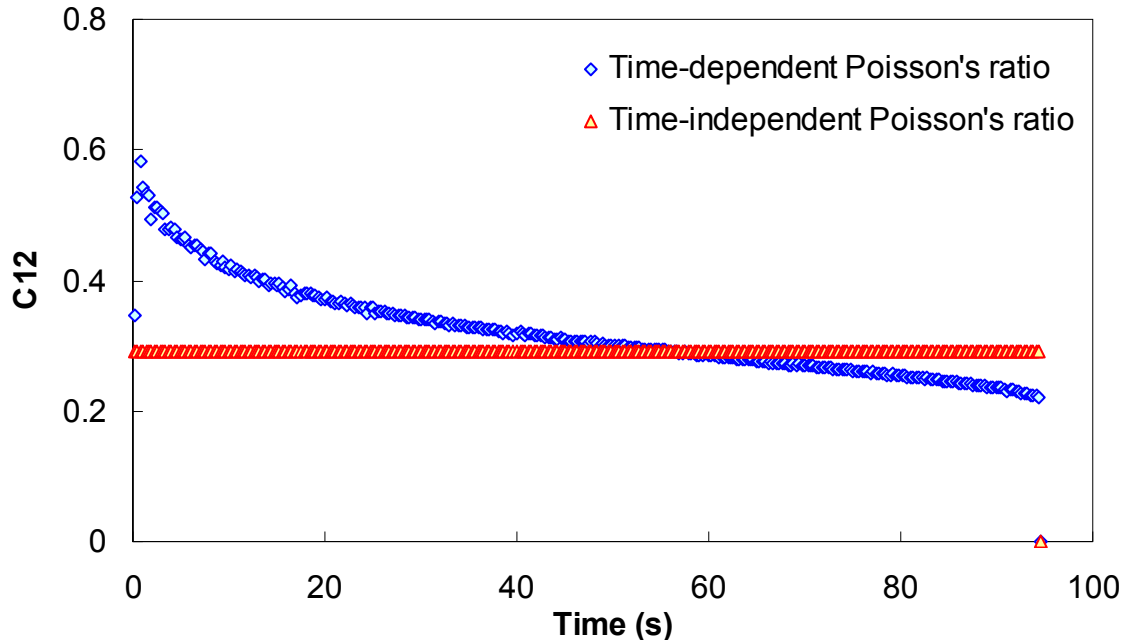


Figure 29. Graph. Effect of time-dependent Poisson's ratio on C_{12} calculation.

To begin, the calculated C_{12} versus S curves for the asphalt concrete mixture of interest are presented in figure 30. This figure shows that C_{12} decreased drastically at first and then increased, suggesting that at small damage levels Poisson's ratio increased, and then decreased at some

critical damage level. From measurements of the axial and radial strains taken during small strain dynamic loading tests and dynamic modulus tests, it was known that the short-time elastic Poisson's ratio for the material of interest was approximately 0.137. When the data in figure 30 were plotted in semilogarithmic scale, as shown in figure 31, it was observed that at the smallest S values, it was not unreasonable to assume an average C_{12} value of 0.726. This value of C_{12} corresponded to a Poisson's ratio of 0.137 and supported the findings from the dynamic modulus tests. The reasons for complications in the characterization of C_{12} became clear. Any change in the C_{12} value was assumed to be due to damage alone. However, because the measurements were subject to the time dependence of Poisson's ratio, a change in C_{12} could be due either to damage growth or time dependence (figure 29).

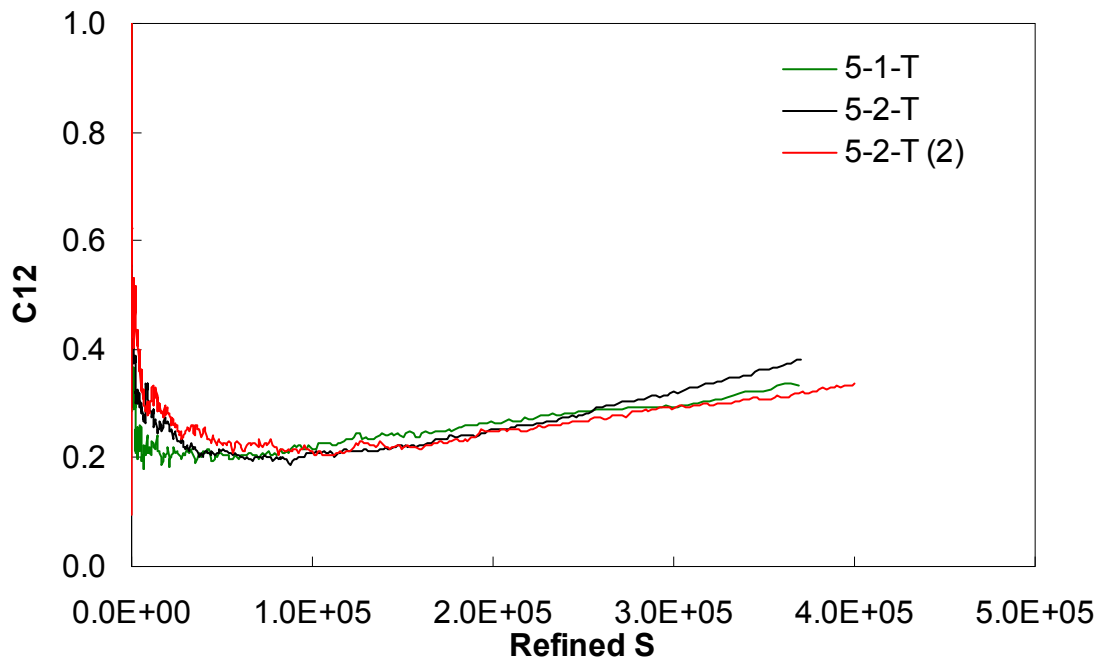
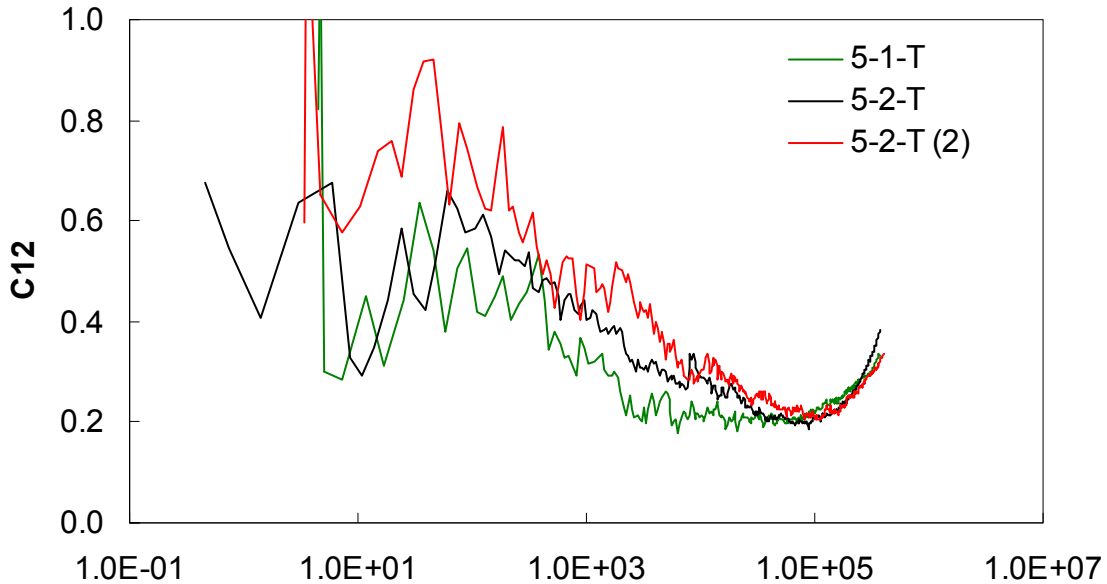


Figure 30. Graph. C_{12} characteristic curve for Control-2006 mixture.



Refined S

Figure 31. Graph. C_{12} characteristic curve for Control-2006 mixture in semi-logarithmic space.

Because damage affects both axial strains and radial strains, eliminating the time effects from the measurements was not possible. Further, it was not possible to separate the time effects from the true damage effects seen in figure 30. This situation left only a third possibility, which was to assume a constant Poisson's ratio that was overall representative of the material behavior. With this in mind, it was reasonable to assume that the change in curvature of the C_{12} curves in figure 30 occurred because the effects of damage overwhelmed those of time. To then characterize the material behavior, the value of C_{12} at the curvature point was averaged for the three replicates (approximately 0.23) and was taken as the initial undamaged C_{12} value. If this operation was performed, Poisson's ratios at points to the left of the curvature point were all overstated.

To clarify the influence of this error, a series of numerical simulations using LVE analysis were performed for tests in the same reduced time range as the characterization tests. In these simulations, the value of radial strains calculated using the time-dependent Poisson's ratio was assumed to be correct (the standard). Then, different time-independent Poisson's ratio values were assumed, and comparisons were drawn between these constant Poisson's ratio predictions and the standard. Numerical simulations were performed in lieu of VECD model predictions because other errors could be introduced in the prediction process otherwise, and the LVE simulation scheme allowed for a more accurate assessment of only the constant Poisson's ratio assumption. Results of the calculations with various assumptions of a constant Poisson's ratio are presented in figure 32. As the figure shows, amongst the values tested, a constant Poisson's ratio of 0.4 performed best. This value was very similar to the point of curvature in the C_{12} plots shown in figure 30. The error in assuming that Poisson's ratio was equal to the low-bound elastic ratio is demonstrated.

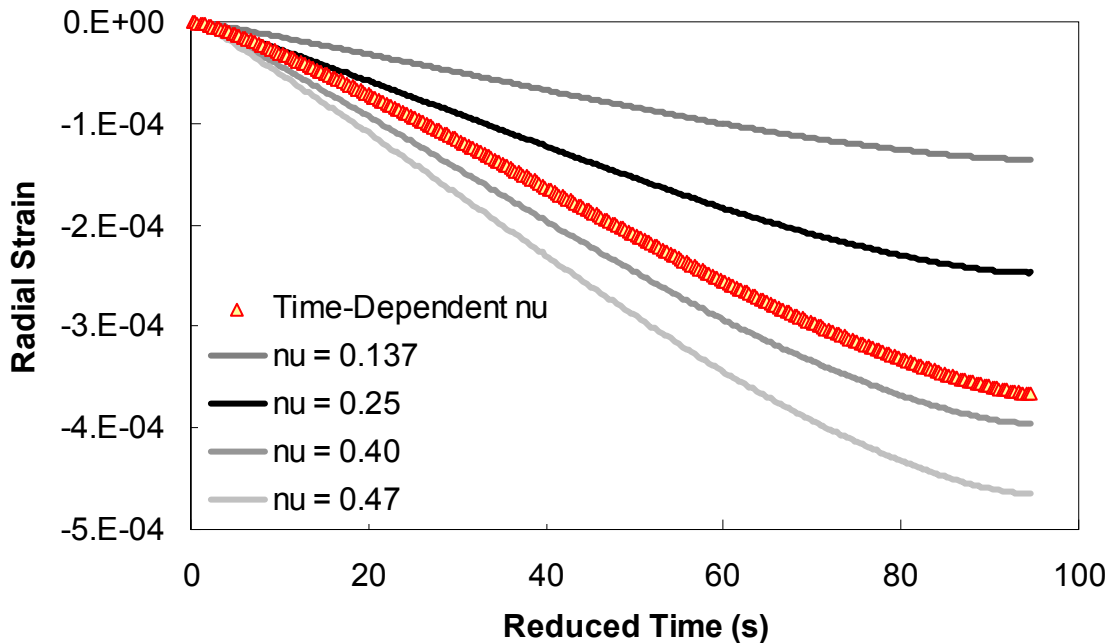


Figure 32. Graph. Effect of different time-independent Poisson's ratio values on radial strain predictions.

An assumption of 0.25 for Poisson's ratio did not provide a good prediction. This observation was interesting because the generally accepted value for Poisson's ratio at 5 °C was 0.25. However, this acceptance was based on experience with the resilient modulus test, which applied a much shorter time of loading than these tests. In brief, this observation further emphasized the importance of a reduced time of loading when considering the fundamental behavior of asphalt concrete. From the results of the analytical simulations, the assumed lower bound value for C_{12} appeared to work well for the tests used in characterization. However, each of these tests covered a similar range in reduced time. The implication for tests that occurred in a more limited range of time, e.g., cyclic tests, was less clear. These tests, when performed at a constant frequency, did not display any time dependence in Poisson's ratio over a given cycle. A cyclic test performed at 25 Hz and 5 °C, for example, might be represented well by a Poisson's ratio of 0.25, but the model would assume it to be 0.386, thus leading to more erroneous predictions than were currently observed in the constant crosshead rate tests. It is unclear exactly how this issue will be addressed. It is hoped that the C_{12} curve can be scaled appropriately depending on the input conditions, but more experimental data and theoretical development are needed to determine the proper course of action.

The form taken for C_{12} as a function of damage is shown with the data in figure 30 and figure 33. It was observed that at early damage stages, Poisson's ratio changed very little, but generally, as damage increased, Poisson's ratio reduced, as indicated by an increase in C_{12} . For this mixture, it was found that $K_1 = 0.228558$, $K_2 = -6.9785 \times 10^{-6}$, $K_3 = 0.960065$, and $K_4 = 7.81989 \times 10^{-7}$.

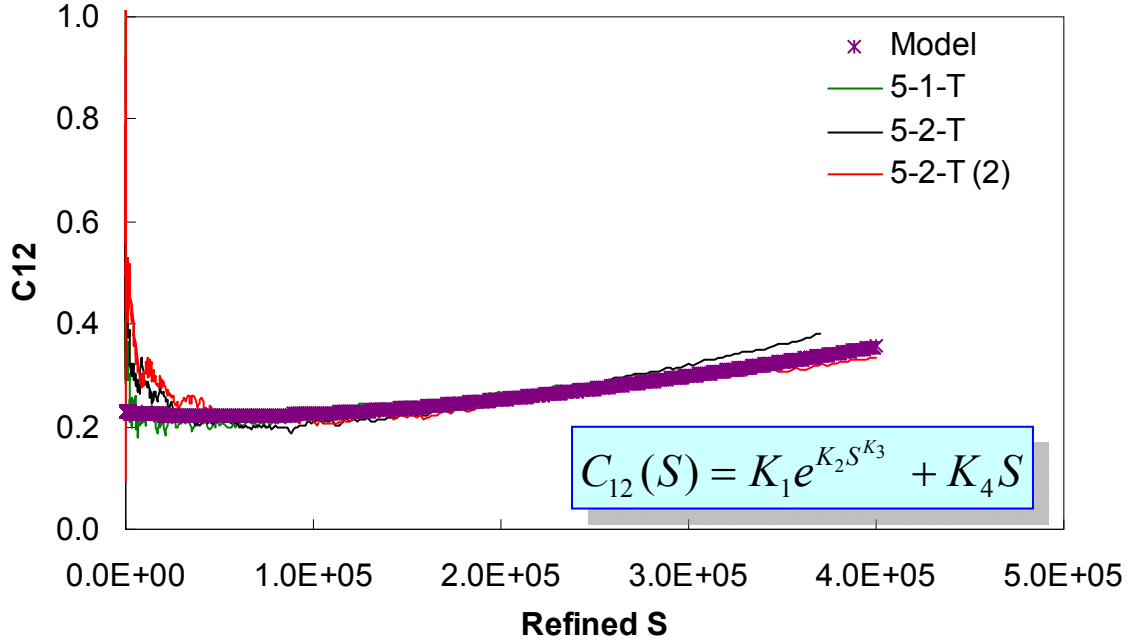


Figure 33. Graph. C_{12} versus S for tensile loading for Control-2006 mixture (5 °C reference).

4.2.3.3. Characterization of $C_{22}(S)$

Characterization of C_{22} was not as straightforward as the C_{11} and C_{12} characterization. For multiaxial loading all three relationships, C_{11} , C_{12} , and C_{22} , had to be used to calculate S , but C_{22} was not yet known. To compensate for this problem, researchers in the NCHRP 9-19 project developed an iterative technique whereby C_{22} was substituted, as follows:⁽²²⁾

$$C_{22}(S) = \frac{\nu^R - C_{12}(S)\varepsilon^R}{p} \quad (92)$$

Where:

ν^R and ε^R are calculated from the measured strains based on the relaxation modulus determined at the pressure of interest p .

However, there were some concerns over the NCHRP 9-19 interpretation of the problem.⁽²²⁾ As a result of such concern, three methods were examined for the S calculation when the pressure was greater than zero, and the C_{11} and C_{12} versus S relationships were known. The first method was based on the NCHRP 9-19 derivation with only slight differences;⁽²²⁾ the second was based on discussions with Schapery; and the third was based on an optimization technique of equation 87. In these methodologies, the pseudo strain and pseudo dilation due to pressure were assumed to have the following equalities:

$$\varepsilon_{pressure}^R = -p(1 - 2 * 0.386) \quad (93)$$

$$\nu_{pressure}^R = -3p(1 - 2 * 0.386) \quad (94)$$

This assumption was necessary to make equation 87 accurate when no load was applied and to make equation 88 consistent with the terms in equation 87. In a similar manner, the initial value of C_{22} had to be specified for the consistent transformation from isotropy to transverse isotropy. Because C_{11} equaled 1 when damage was zero, the initial condition of C_{22} is given as follows:

$$C_{22} = -2(1-2\nu)(1+\nu) \quad (95)$$

4.2.3.3.1. Characterization by NCHRP 9-19 Methodology:⁽²²⁾

By inserting the expression of dual strain energy, equation 86, in the damage evolution law the following was found:

$$\frac{dS}{d\xi} = \left(\frac{\partial \left(\frac{1}{2} C_{11}(S) (\varepsilon^R)^2 + C_{12}(S) \varepsilon^R p + \frac{1}{2} C_{22}(S) p^2 \right)}{\partial S} \right)^\alpha \quad (96)$$

$$\frac{dS}{d\xi} = \left[- \left(\frac{1}{2} \frac{dC_{11}}{dS} (\varepsilon^R)^2 + \frac{dC_{12}}{dS} \varepsilon^R p + \frac{1}{2} \frac{dC_{22}}{dS} p^2 \right) \right]^\alpha \quad (97)$$

From equation 92, the following was found:

$$\frac{dC_{22}}{dS} = - \left(\frac{dC_{12}}{dS} \right) \frac{\varepsilon^R}{p} \quad (98)$$

Equation 98 assumed that ν^R was either a weak function of S or independent of S . Inserting equation 98 into equation 97 yielded the following:

$$\frac{dS}{d\xi} = \left[- \left(\frac{1}{2} \frac{dC_{11}}{dS} (\varepsilon^R)^2 + \frac{dC_{12}}{dS} \varepsilon^R p - \frac{1}{2} \frac{dC_{12}}{dS} \varepsilon^R p \right) \right]^\alpha \quad (99)$$

For small $\Delta \xi$, the result was as follows:

$$\Delta S = \Delta \xi \left[- \left(\frac{1}{2} \frac{(dC_{11})_i}{dS} (\varepsilon_i^R)^2 + \frac{1}{2} \frac{(dC_{12})_i}{dS} \varepsilon_i^R p \right) \right]^\alpha \quad (100)$$

With change in notation, it appeared as follows:

$$S_{i+1} = S_i + \Delta \xi \left[- \left(\frac{1}{2} \frac{(dC_{11})_i}{dS} (\varepsilon_i^R)^2 + \frac{1}{2} \frac{(dC_{12})_i}{dS} \varepsilon_i^R p \right) \right]^\alpha \quad (101)$$

Where:

$$S_I = 0.$$

δS is an increment smaller than $\Delta S = S_{i+1} - S_i$, for example, 0.1.

$$\delta C_i = C(S_i + \delta S) - C(S_i).$$

These values of S were then used to calculate C_{12} at a given time step. Because pressure was constant and pseudo dilation and pseudo strain were known as functions of time, equation 88 may be used to directly calculate C_{22} . These values were then plotted against the values of S found from the first step, and the C_{22} - S relationship was developed. Due to some numerical complications, a condition was set such that if the term inside the parenthesis of equation 101 was less than zero, the term was replaced by zero.

4.2.3.3.2. Characterization with Schapery's Approach:

Equation 88 was rearranged to solve for C_{22} (equation 102):

$$C_{22} = \frac{\nu^R}{p} - \frac{C_{12}\varepsilon^R}{p} \quad (102)$$

Then, taking the derivative of equation 102 with respect to time and applying the chain rule achieved the following:

$$\frac{dC_{22}}{dt} = \frac{dC_{22}}{dS} \frac{dS}{dt} = \frac{1}{p} \frac{d\nu^R}{dt} - \frac{d\varepsilon^R}{dt} \frac{dC_{12}}{dS} \frac{dS}{dt} - \frac{C_{12}}{p} \frac{d\varepsilon^R}{dt} \quad (103)$$

Solving equation 103 for the damage rate resulted in equation 104:

$$\frac{dS}{dt} = \frac{1}{p} \left[\frac{\dot{\nu}^R - C_{12}\dot{\varepsilon}^R}{\frac{dC_{22}}{dS} + \frac{\varepsilon^R}{p} \frac{dC_{12}}{dS}} \right] \quad (104)$$

Similarly, using equation 87 resulted in equation 105:

$$\frac{dS}{dt} = \frac{1}{p} \left[\frac{\dot{\sigma} - C_{11}\dot{\varepsilon}^R}{\frac{dC_{12}}{dS} + \frac{\varepsilon^R}{p} \frac{dC_{11}}{dS}} \right] \quad (105)$$

Because equation 104 must equal equation 105, the following can be shown:

$$\frac{dC_{22}}{dS} = \frac{1}{p} \left[\frac{\dot{\nu}^R - C_{12}\dot{\varepsilon}^R}{\dot{\sigma} - C_{11}\dot{\varepsilon}^R} \right] \left(\frac{dC_{12}}{dS} + \frac{\varepsilon^R}{p} \frac{dC_{11}}{dS} \right) - \frac{\varepsilon^R}{p} \frac{dC_{12}}{dS} \quad (106)$$

Substituting equation 106 into equation 97 and simplifying found the following:

$$\frac{dS}{dt} = \left[- \left(\frac{1}{2} \frac{dC_{11}}{dS} \varepsilon^R \left(\varepsilon^R + \frac{\lambda}{p} \right) + \frac{dC_{12}}{dS} \left(p \varepsilon^R + \frac{\lambda}{2} - \frac{\varepsilon^R}{2p} \right) \right) \right]^\alpha \quad (107)$$

Where:

λ = A function of C_{11} , C_{12} , and the pseudo dilation, pseudo strain, and stress rates.

Equation 88 may be used to directly calculate C_{22} . These values were then plotted against the values of S found from the first step, and the C_{22} - S relationship was developed. Due to some numerical complications, a condition was set such that if the term inside the parenthesis of equation 101 was less than zero, the term is replaced by zero.

4.2.3.3.3. Characterization by Optimization:

From the triaxial constant crosshead rate tests, it was found that pressure was constant, stress was measured, and pseudo strain may be calculated using the measured strains and the relaxation modulus. Then, from equation 87, the only unknown was S . In this methodology, S was solved for by numeric optimization to minimize the error between measured stress and the stress calculated from equation 87. These values of S were then used to calculate C_{12} at a given time step. Because pressure was constant, and pseudo dilation and pseudo strain were known as functions of time, equation 88 may be used to directly calculate C_{22} . These values were then plotted against the values of S found from the first step, and the C_{22} - S relationship was developed.

4.2.3.3.4. Comparison of Methodologies:

Each of the above methods has been used to characterize S . Comparisons were made first with the S values as functions of time for a single test. Figure 34 through figure 37 and figure 38 through figure 41 show the S calculated from each of the methods in both arithmetic and logarithmic scales. Figure 42 through figure 45 present the stress calculated using the characterized S and equation 87. Method three used optimization; thus, the predicted stress and measured stress agree exactly. Figure 46 through figure 49 show the damage characteristic relationship by each technique for the four tests. The final representative $C_{22}(S)$ function is shown in figure 50. The initial conditions required H_1 to be equal to equation 95. Explicitly, the coefficients for $C_{22}(S)$ are $H_1 = -0.633435$, $H_2 = 3.0834 \times 10^{-5}$, and $H_3 = 0.83682$.

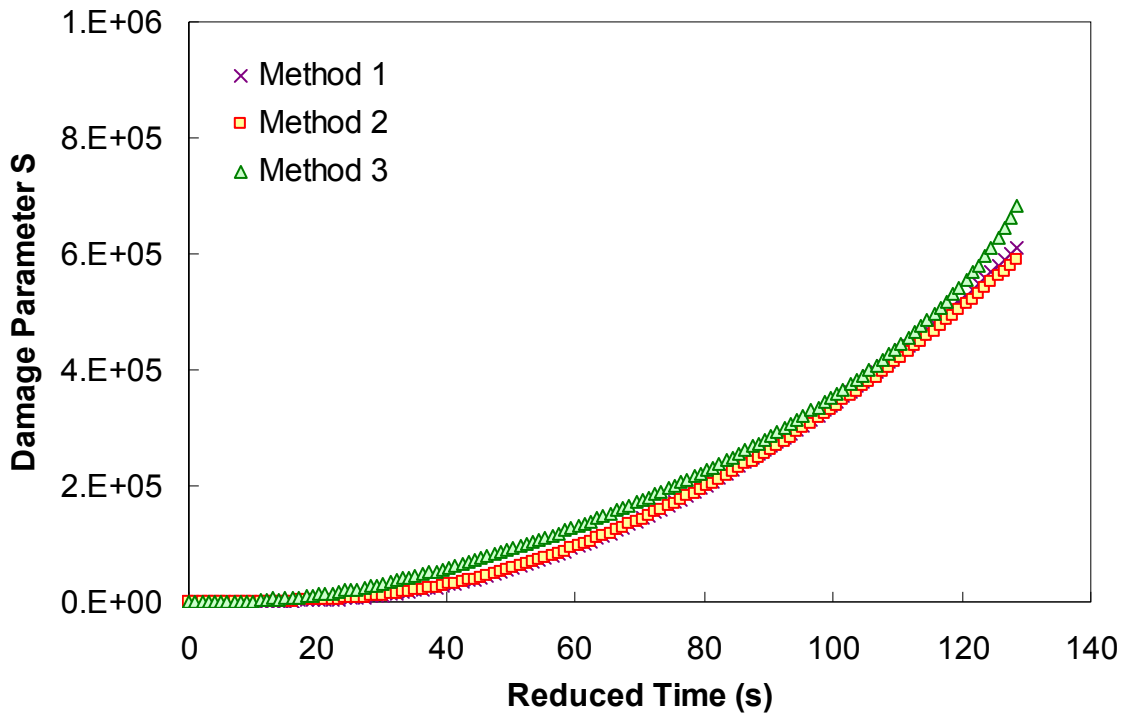


Figure 34. Graph. S as a function of reduced time calculated by three different methodologies in arithmetic space for 5-1-T.

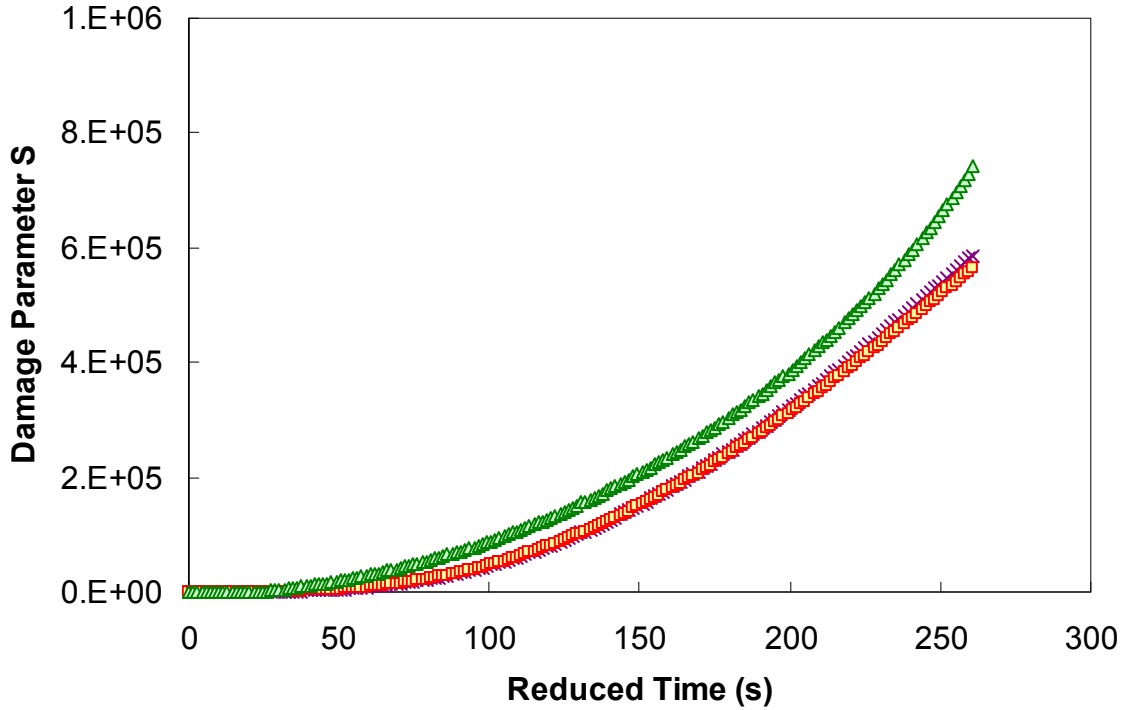


Figure 35. Graph. S as a function of reduced time calculated by three different methodologies in arithmetic space for 5-3-T.

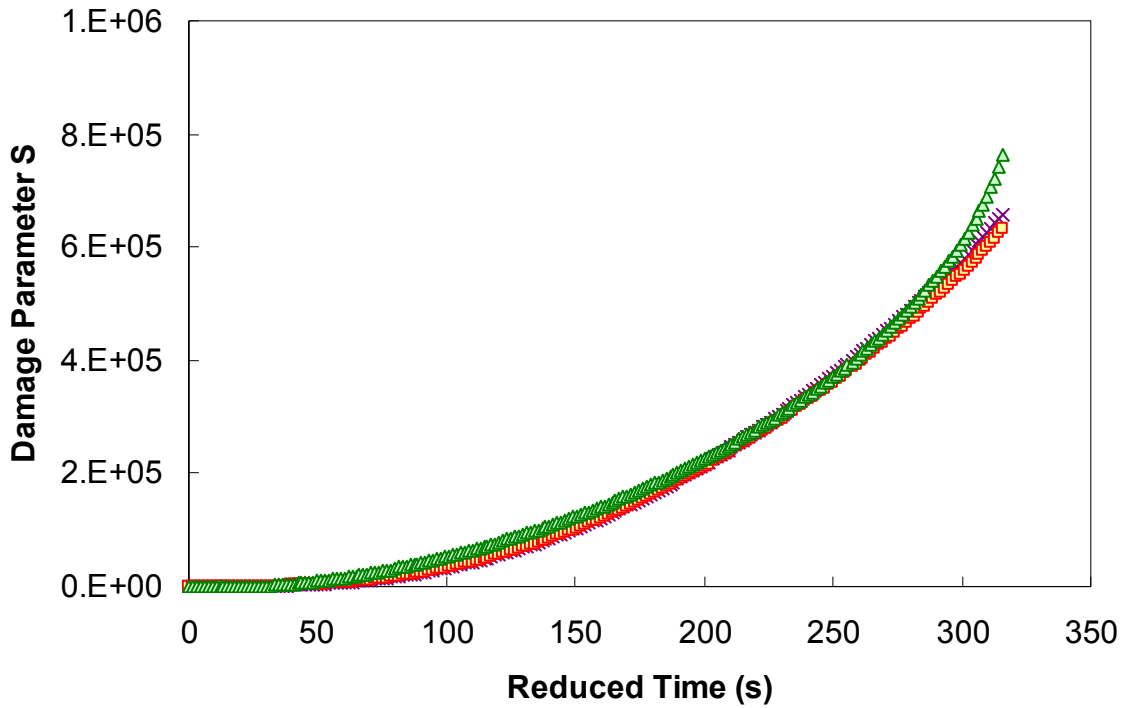


Figure 36. Graph. S as a function of reduced time calculated by three different methodologies in arithmetic space for 5-4-T.

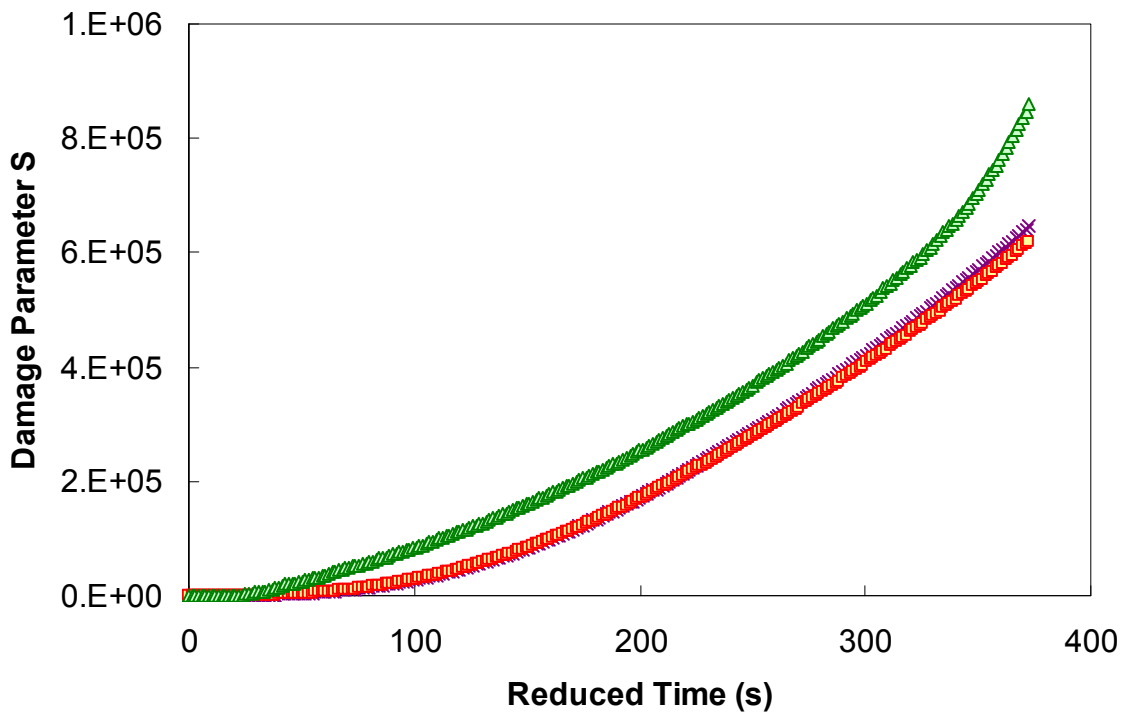


Figure 37. Graph. S as a function of reduced time calculated by three different methodologies in arithmetic space for 5-5-T.

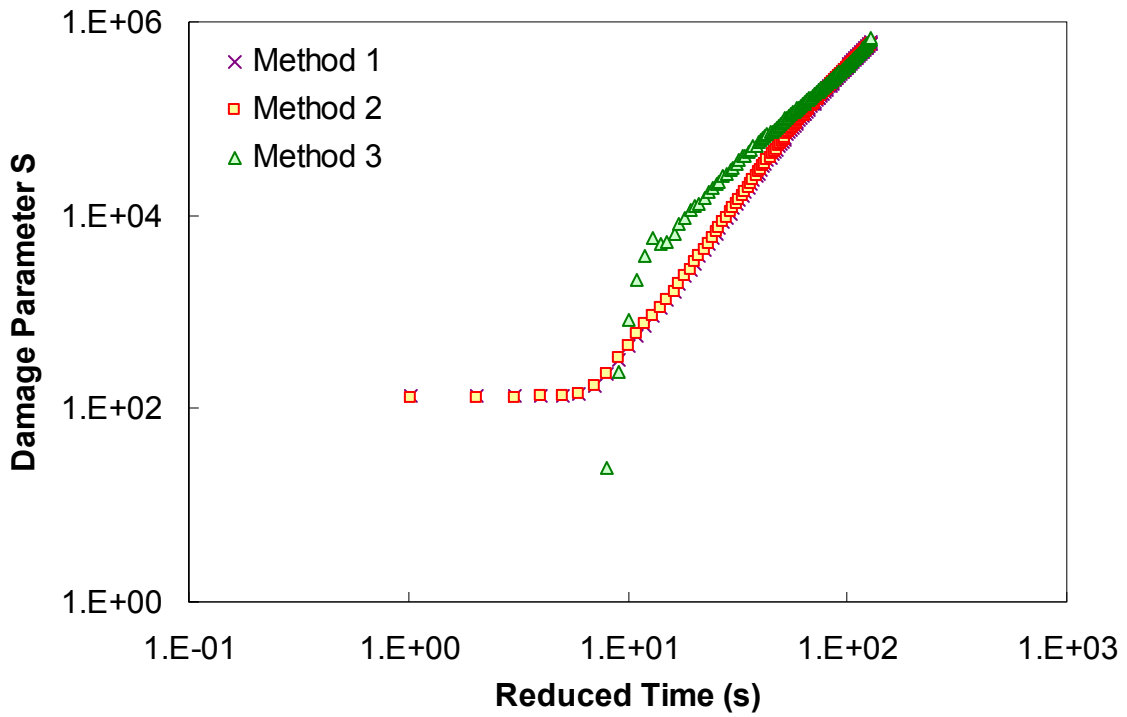


Figure 38. Graph. S as a function of reduced time calculated by three different methodologies in logarithmic space for 5-1-T.

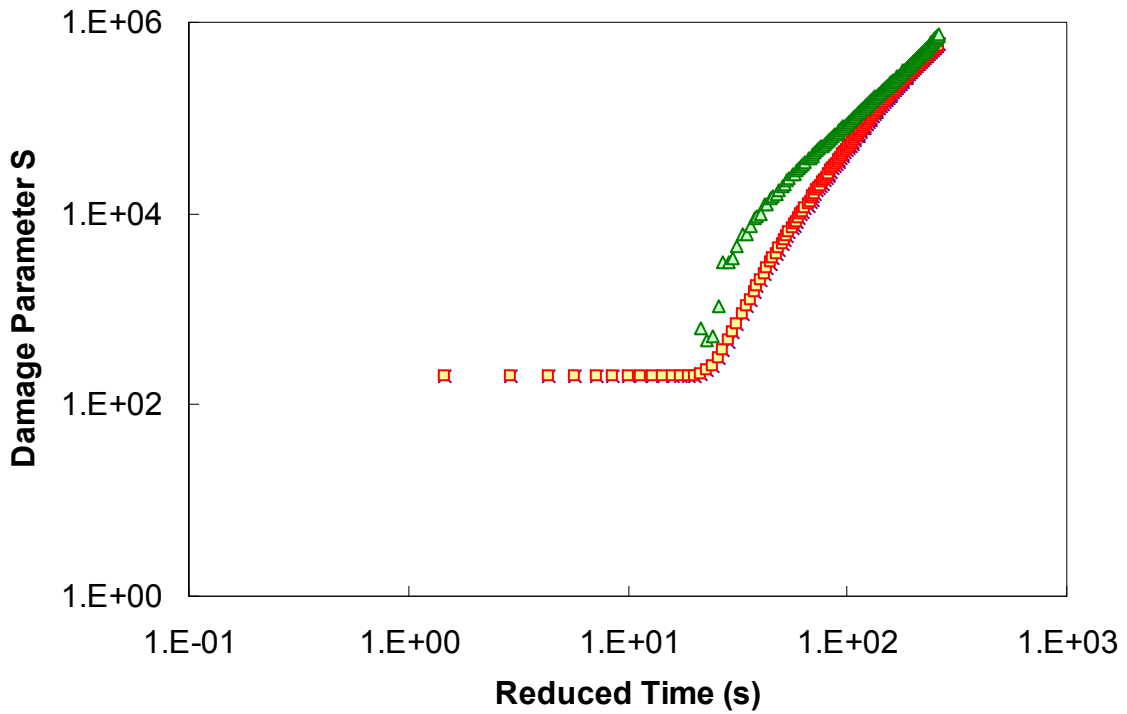


Figure 39. Graph. S as a function of reduced time calculated by three different methodologies in logarithmic space for 5-3-T.

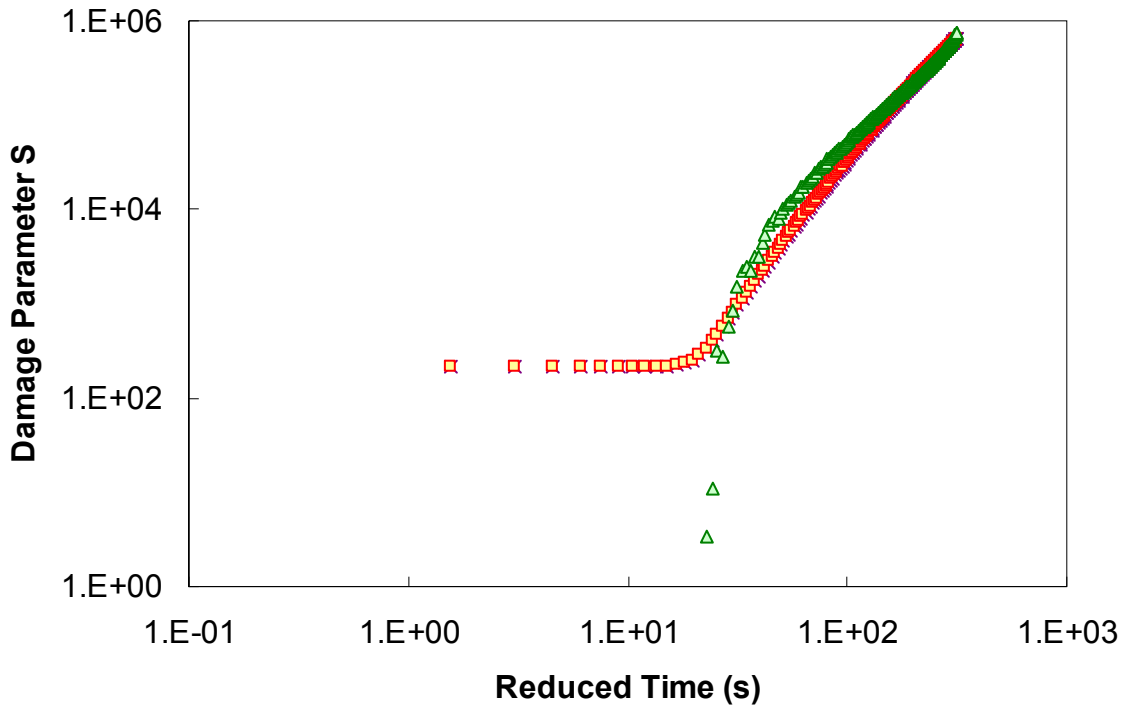


Figure 40. Graph. S as a function of reduced time calculated by three different methodologies in logarithmic space for 5-4-T.

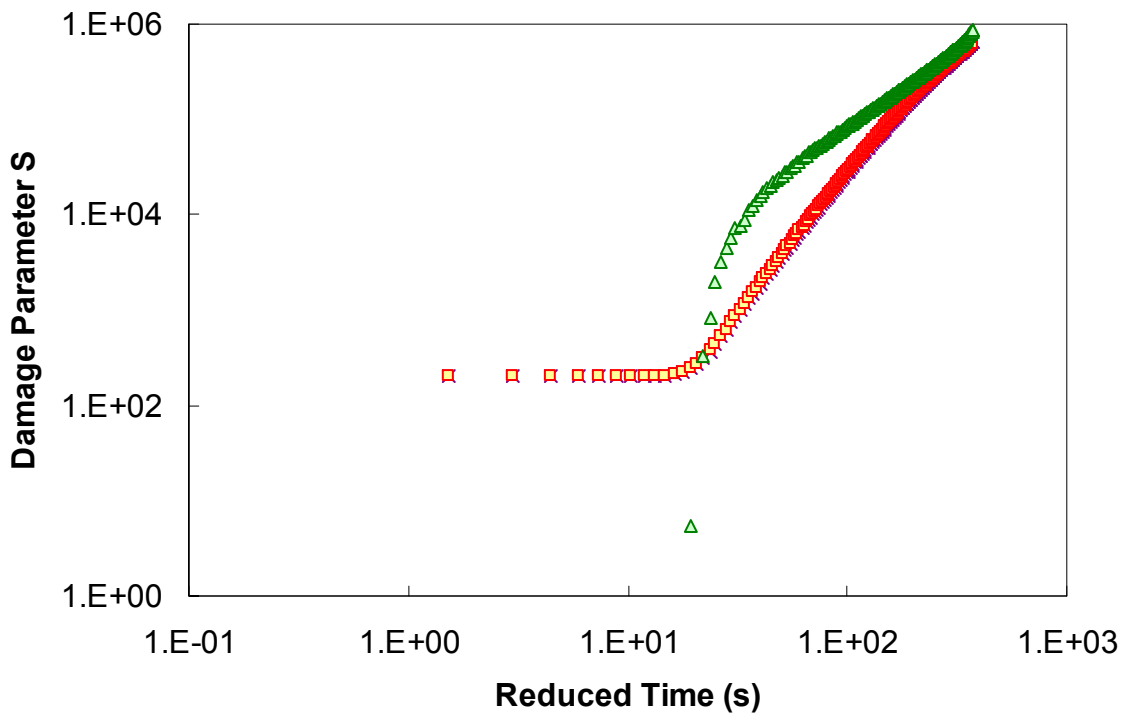


Figure 41. Graph. S as a function of reduced time calculated by three different methodologies in logarithmic space for 5-5-T.

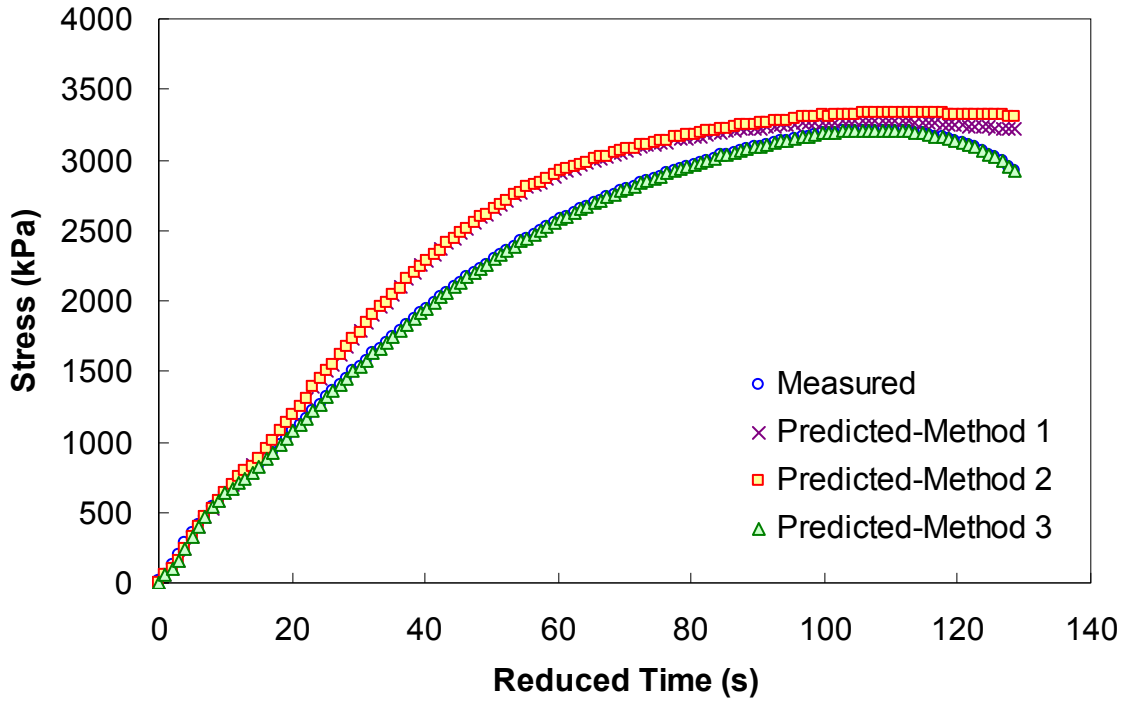


Figure 42. Graph. Predicted and measured stress as a function of reduced time for different S calculation methodologies for 5-1-T.

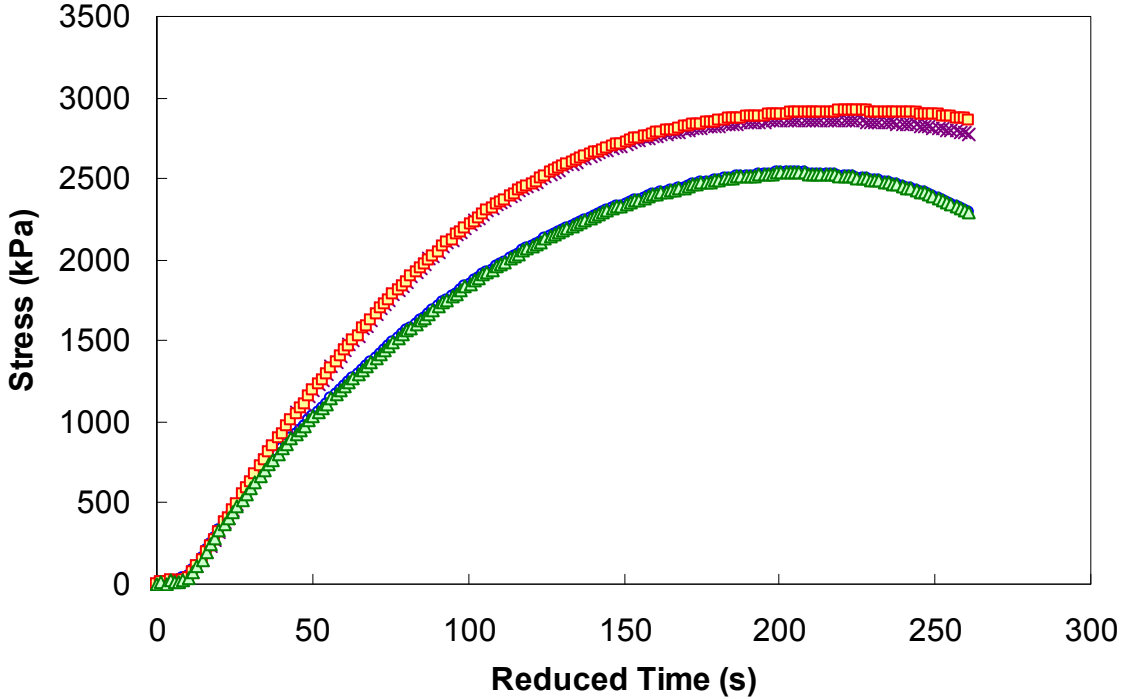


Figure 43. Graph. Predicted and measured stress as a function of reduced time for different S calculation methodologies for 5-3-T.

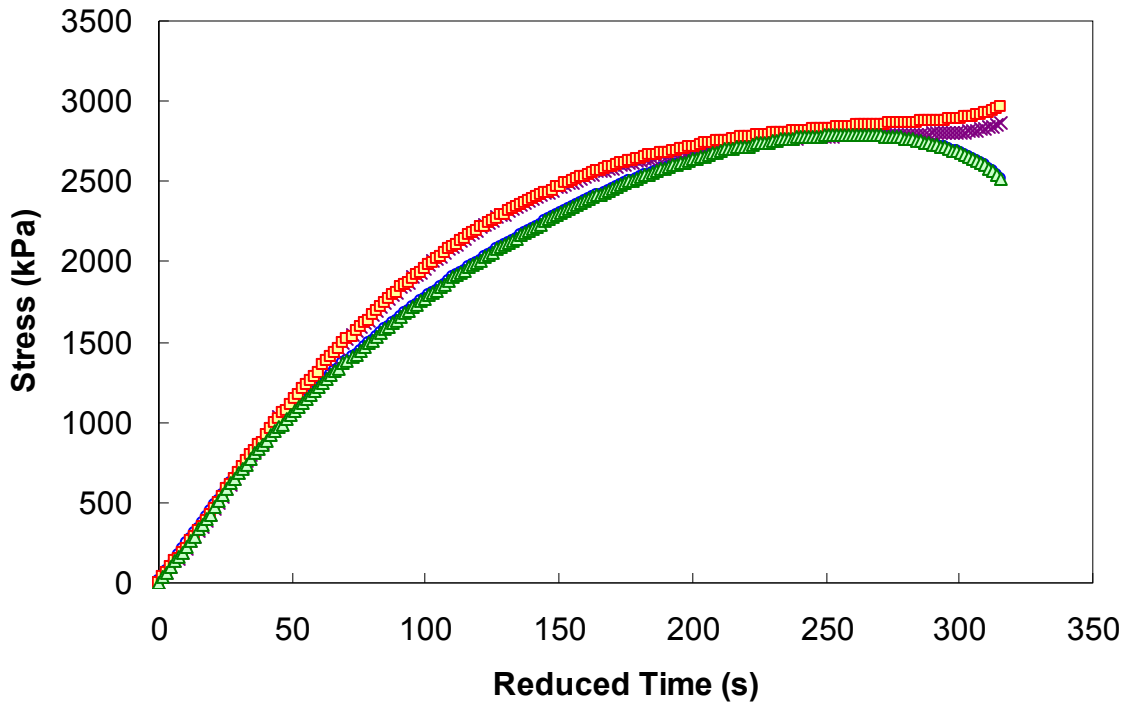


Figure 44. Graph. Predicted and measured stress as a function of reduced time for different S calculation methodologies for 5-4-T.

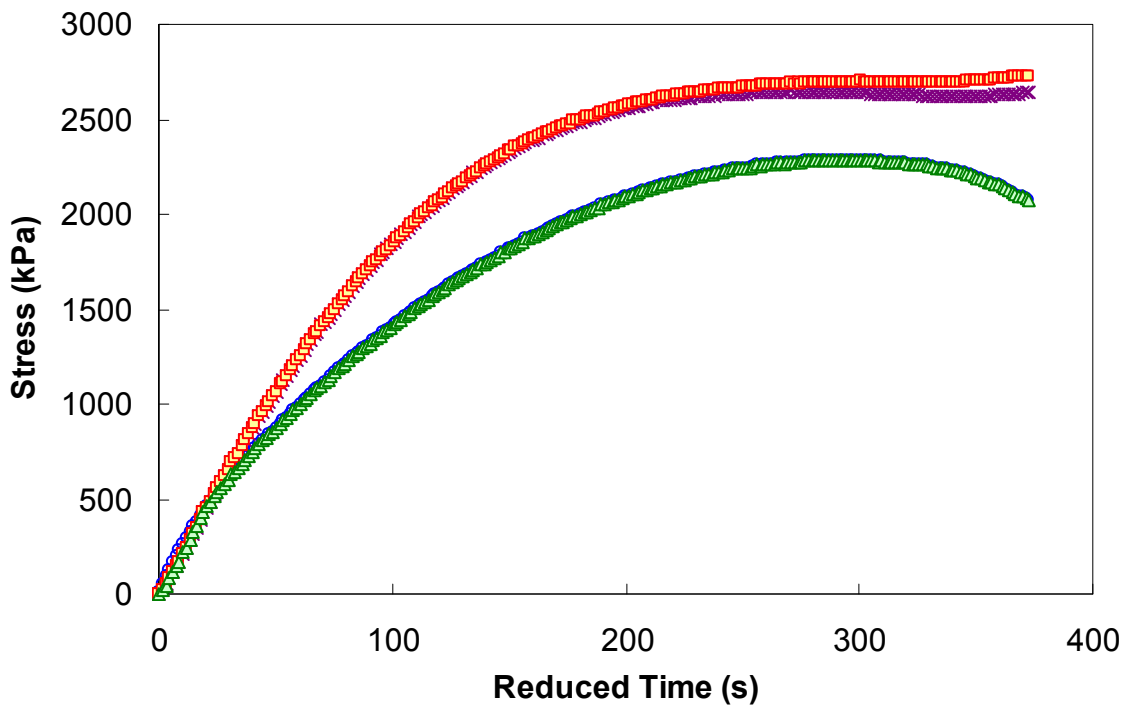


Figure 45. Graph. Predicted and measured stress as a function of reduced time for different S calculation methodologies for 5-5-T.

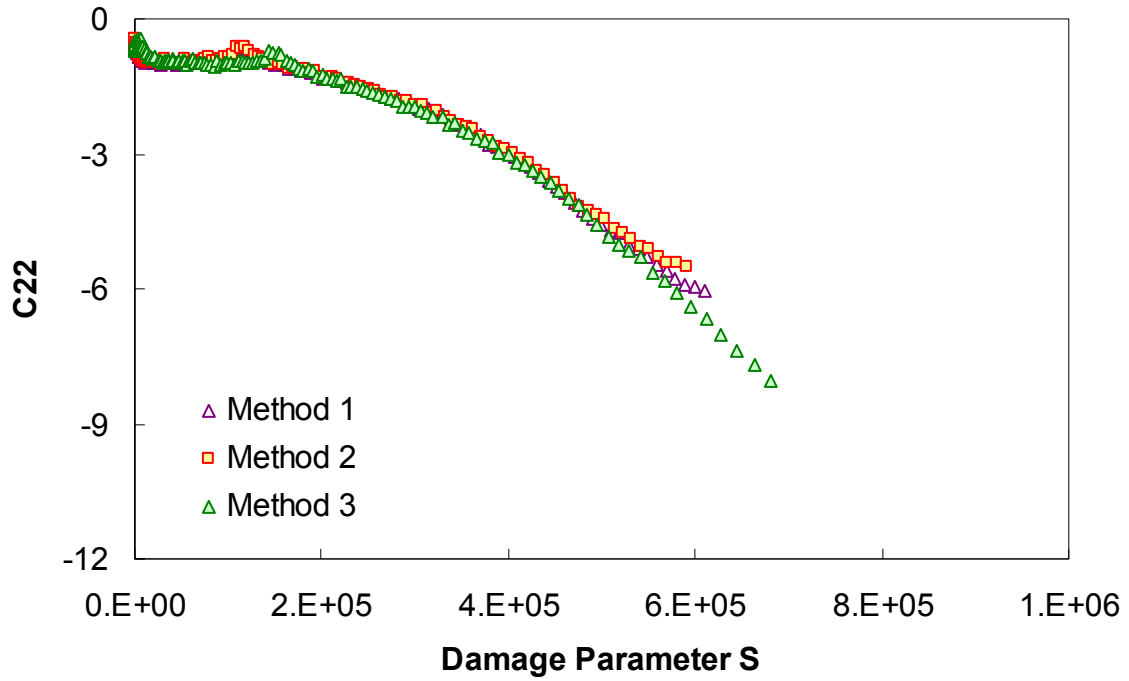


Figure 46. Graph. C_{22} as a function of S calculated by different methodologies for 5-1-T.

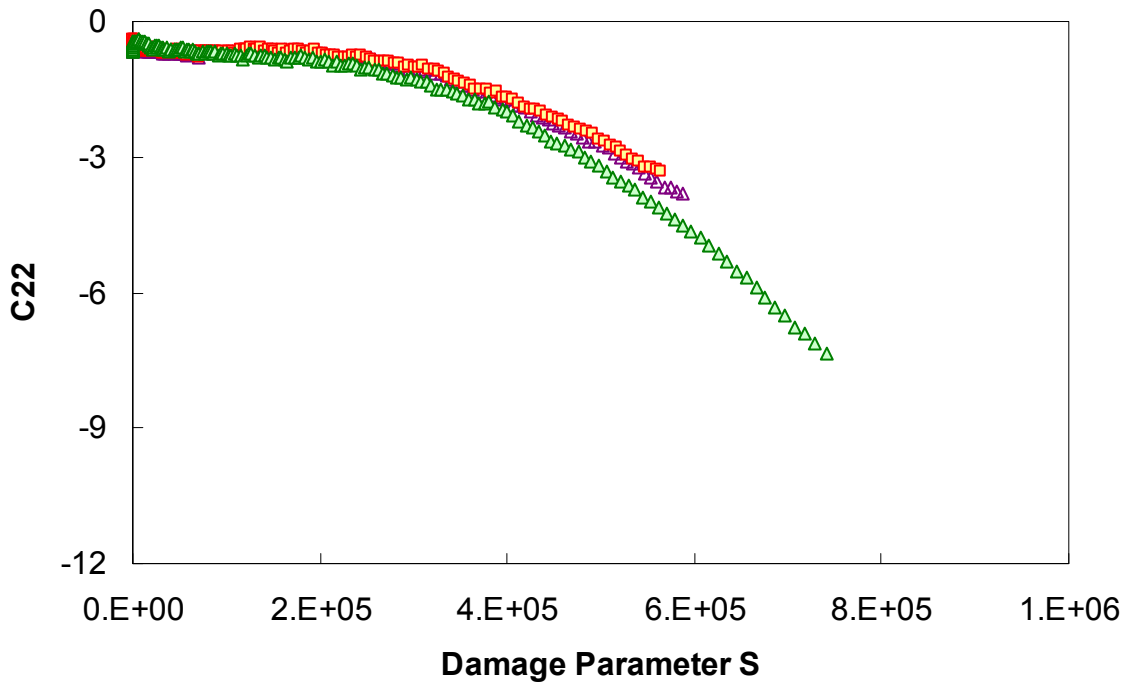


Figure 47. Graph. C_{22} as a function of S calculated by different methodologies for 5-3-T.

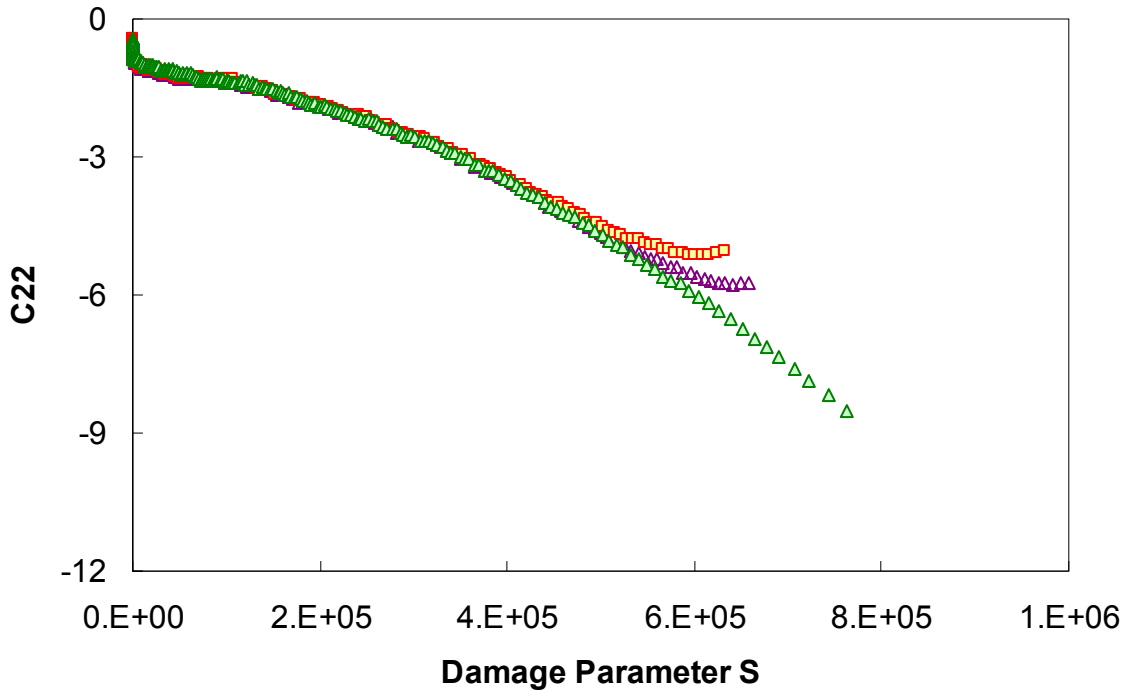


Figure 48. Graph. C_{22} as a function of S calculated by different methodologies for 5-4-T.

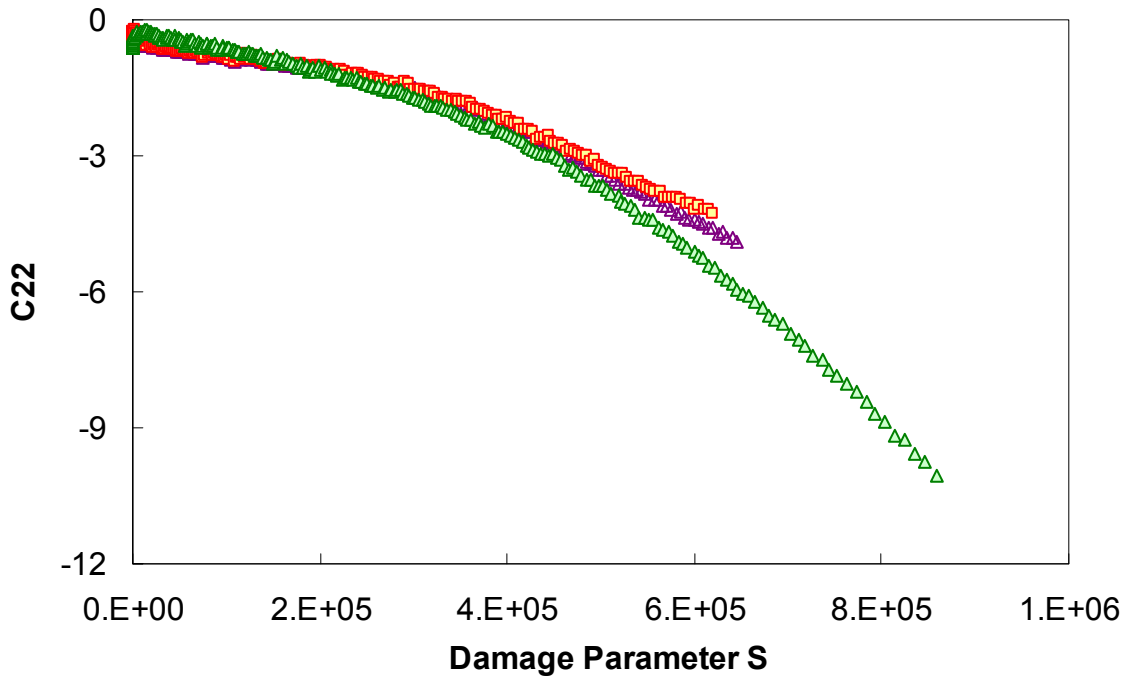


Figure 49. Graph. C_{22} as a function of S calculated by different methodologies for 5-5-T.

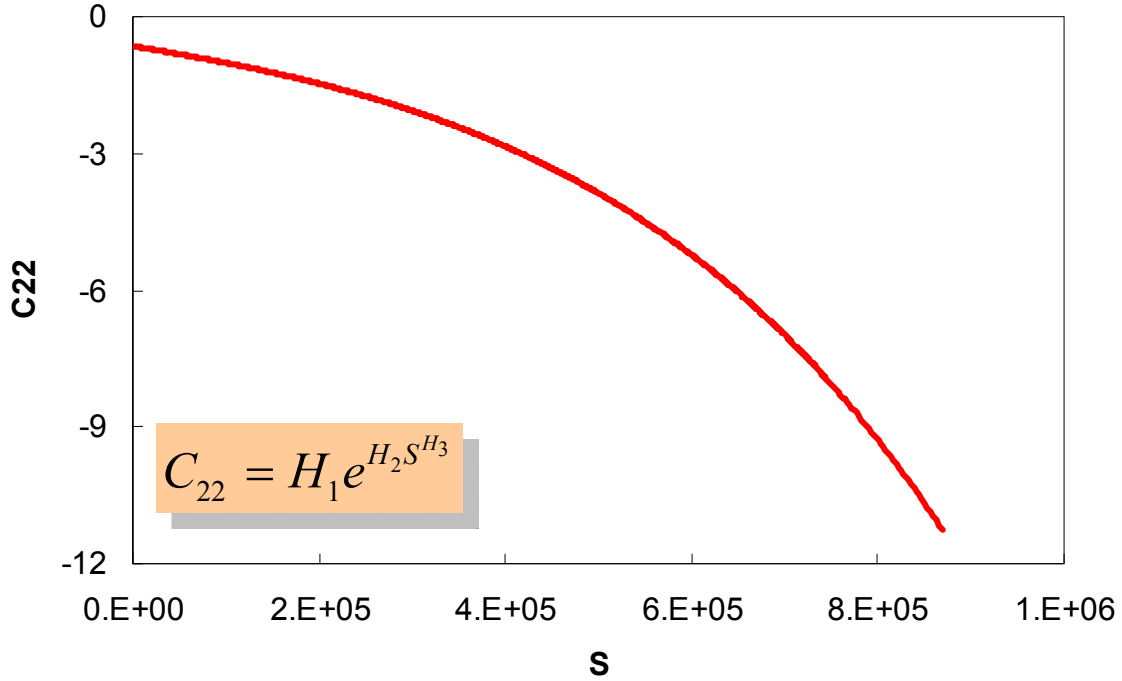


Figure 50. Graph. Representative C_{22} versus S for tension using optimization methodology (5 °C reference).

4.3. VISCOPLASTIC MODELING OF ASPHALT CONCRETE IN TENSION

With the damage characteristic functions thus characterized, it was possible to predict the material behavior under conditions where viscoelastic damage mechanisms dominate. However, it was known that viscoplastic effects may have been significant factors governing the overall behavior of asphalt concrete in tension. Currently, viscoplastic effects are considered using an empirical strain-hardening model. Because details of this model have been presented previously and elsewhere, only the integrated form of the constitutive equation is shown here in equation 108.^(12,13,25)

$$\varepsilon_{vp} = \left(\frac{p+1}{Y} \right)^{\frac{1}{p+1}} \left(\int_0^t \sigma^q dt \right)^{\frac{1}{p+1}} \quad (108)$$

As with the MVECD model, the characterization of equation 108 utilized constant crosshead rate tests under confining pressure. The procedure first required prediction of the VECD related strains of such tests at high temperatures. Viscoplastic strains were then backcalculated by subtracting the predicted MVECD strains from the measured values. This process was repeated in multiple tests where viscoplastic strains were considered to be significant. The backcalculated values for these tests were then presented to the model, and the coefficients were determined by optimization using a genetic algorithm.

For the prediction of viscoplastic behavior under various confining states, a phenomenological observation was utilized. From the characterization, it was found that the coefficients p and q are

not strongly affected by confining states, but the coefficient Y was found to depend heavily on confining pressure. This relationship, along with the stress dependent model, is shown in figure 51.

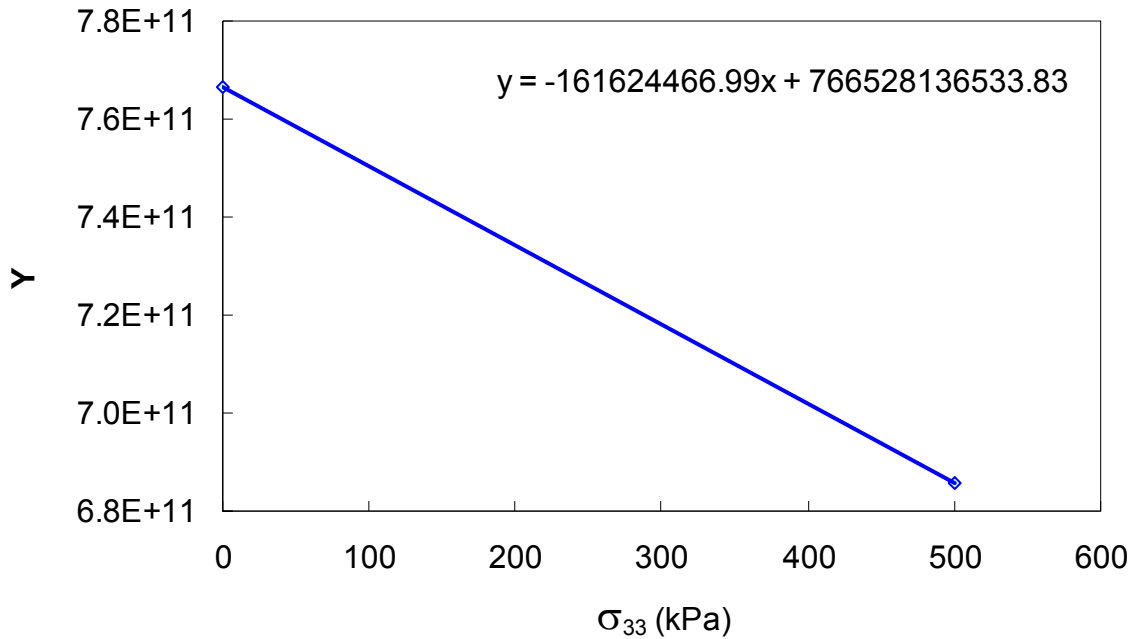


Figure 51. Graph. Effect of confining pressure on coefficient Y .

4.4. MVEPCD MODEL VERIFICATION

Verification tests for the MVEPCD model were similar to those used for characterization (i.e., constant crosshead rate tests under a constant confining pressure). Some of the tests were performed at the same confining pressure as characterization tests, but at a different temperature (25 °C). A second verification test was performed at the same temperatures as characterization but at a different confining pressure (250 kPa). Results of the first verification data set are shown in figure 52. Both axial and radial strain predictions are shown in this figure. Although not shown here, the agreement observed in figure 52 was approximately the same as that observed in the verification of the uniaxial VEPCD model. This agreement was considered a good match with the measurements. The results of the second verification data set are shown in figure 53 for 40 °C and in figure 54 for 5 °C. Although this data set did not show as good an agreement with the measured response, the fitting was considered reasonable.

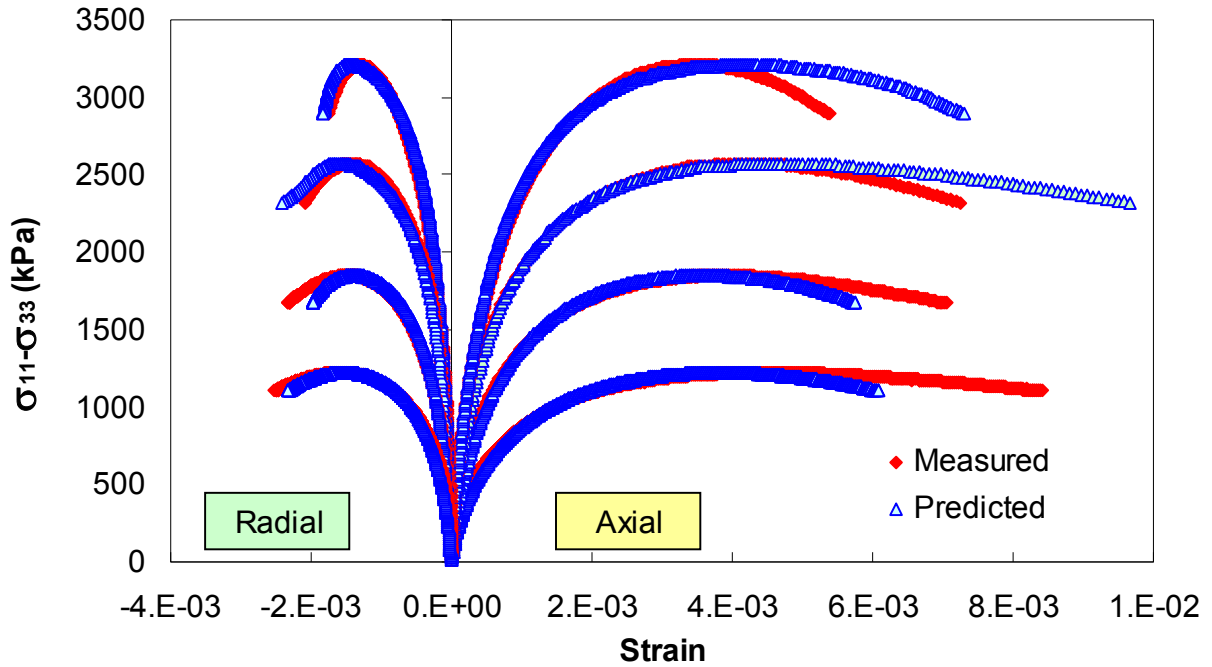


Figure 52. Graph. Results of MVEPCD model simple verification for constant crosshead rate tests under 500 kPa confinement at 25 °C.

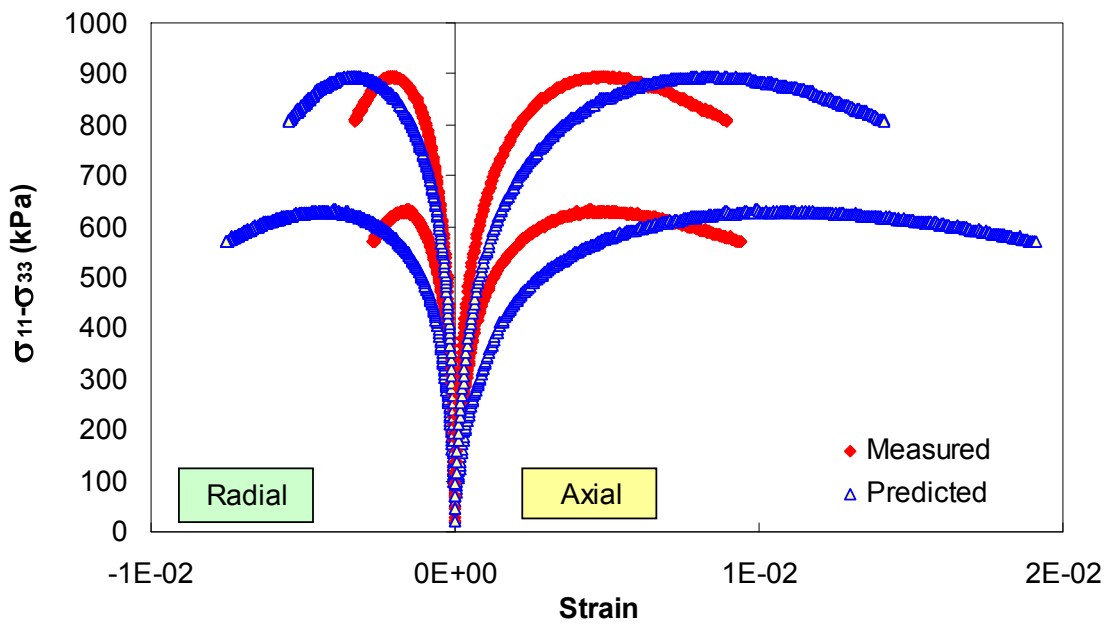


Figure 53. Graph. Results of MVEPCD model verification for constant crosshead rate tests under 250 kPa confinement at 40 °C.

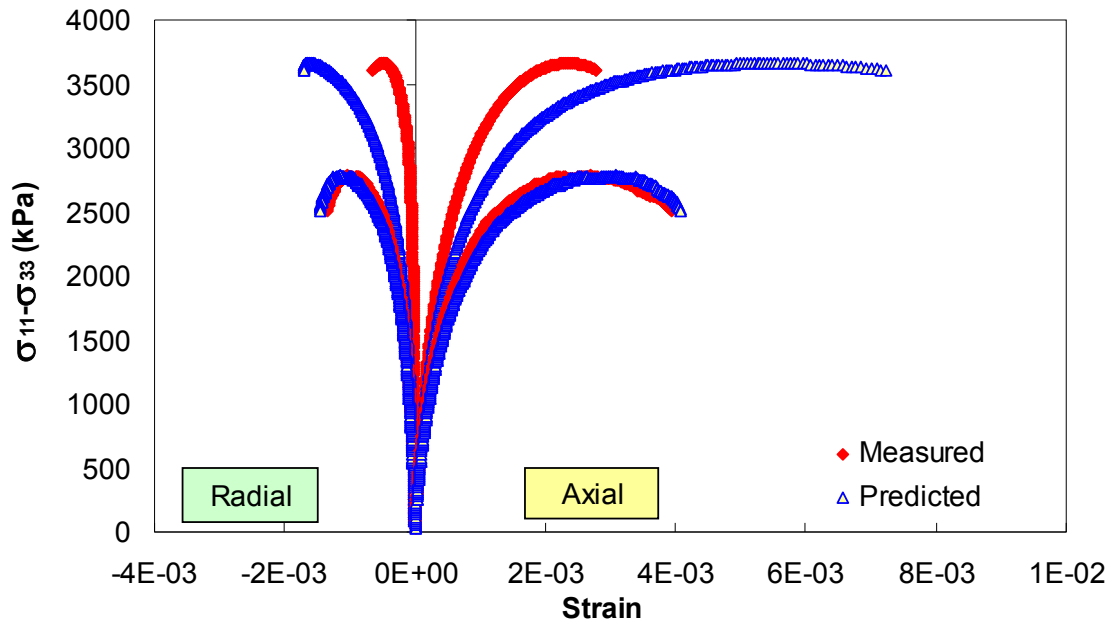


Figure 54. Graph. Results of MVEPCD model verification for constant crosshead rate tests under 250 kPa confinement at 5 °C.

4.5. t-TS WITH GROWING DAMAGE IN TENSION

It has been shown repeatedly that dense-graded asphalt concrete, including that with modified binders, exhibits t-TS under growing damage in the uniaxial stress state. Less conclusive results are available for the behavior of mixtures under confining pressure. Therefore, it was necessary to verify the principle of t-TS under confining pressure. Verification was performed following the method presented in Chehab.⁽²⁰⁾ The advantage of utilizing this method was that tests used for validation of t-TS may also have utilized in the characterization procedure, thus reducing excessive testing. A brief schematic representation of the process is presented in figure 55 through figure 57. In short, stress as a function of reduced time for constant crosshead rate tests performed at different rates and temperatures was plotted for a given strain level. Therefore, each test produced a single point in the respective plot. This process was repeated for several strain levels covering a broad range in material behavior. If t-TS with growing damage was valid, then the resulting plots would appear to be continuous.

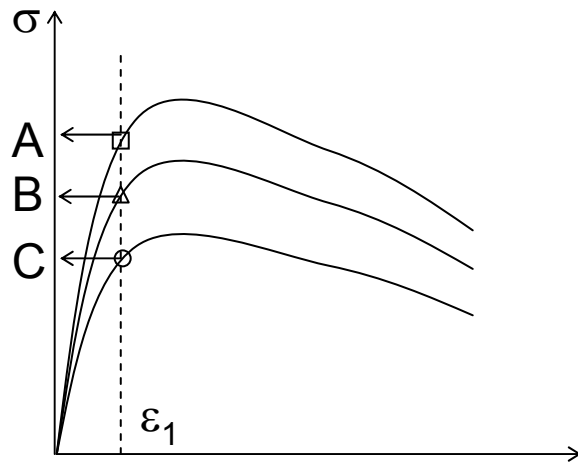


Figure 55. Illustration. Schematic representation of first step for verifying the t-TS principle under growing damage, finding stress for different tests at a consistent strain level.

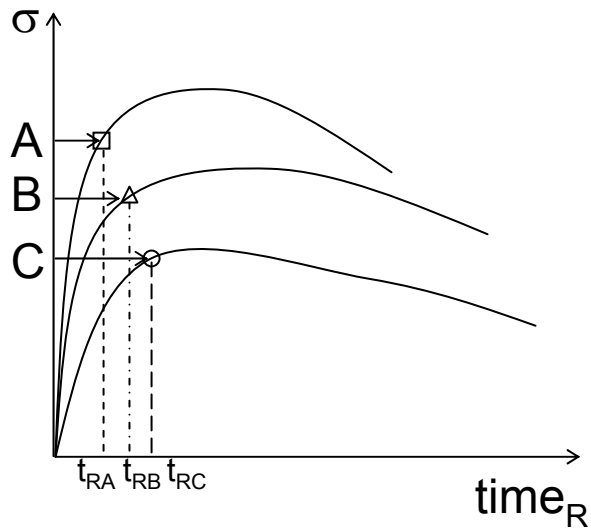


Figure 56. Illustration. Schematic representation of the second step for verifying the t-TS principle under growing damage, finding reduced time for the stress found in the first step for each test.

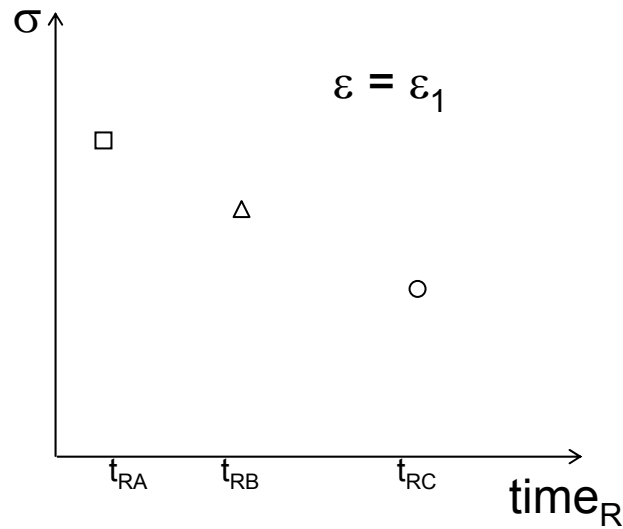


Figure 57. Illustration. Schematic representation of the third step for verifying the t-TS principle under growing damage, plotting the stress from the first step against the reduced time from the second step.

The strain levels examined for t-TS analysis are shown graphically along with the stress-strain curves in figure 58. The stress-strain curves in figure 58 represented all the tests noted in table 3, and the examined strain levels covered both low damage (low strain levels) and high damage (high strain levels) ranges. The resulting stress versus reduced time curves at these strain levels are presented in figure 59 through figure 64. At all strain levels examined, the curves appeared continuous, and thus, t-TS under deviatoric tension conditions was satisfactorily verified. In figure 63 and figure 64, data for 5 °C were not presented due to localization of the strain prior to reaching the given strain levels. This observation is also apparent in figure 58, in which the tests with the highest strength were performed at 5 °C.

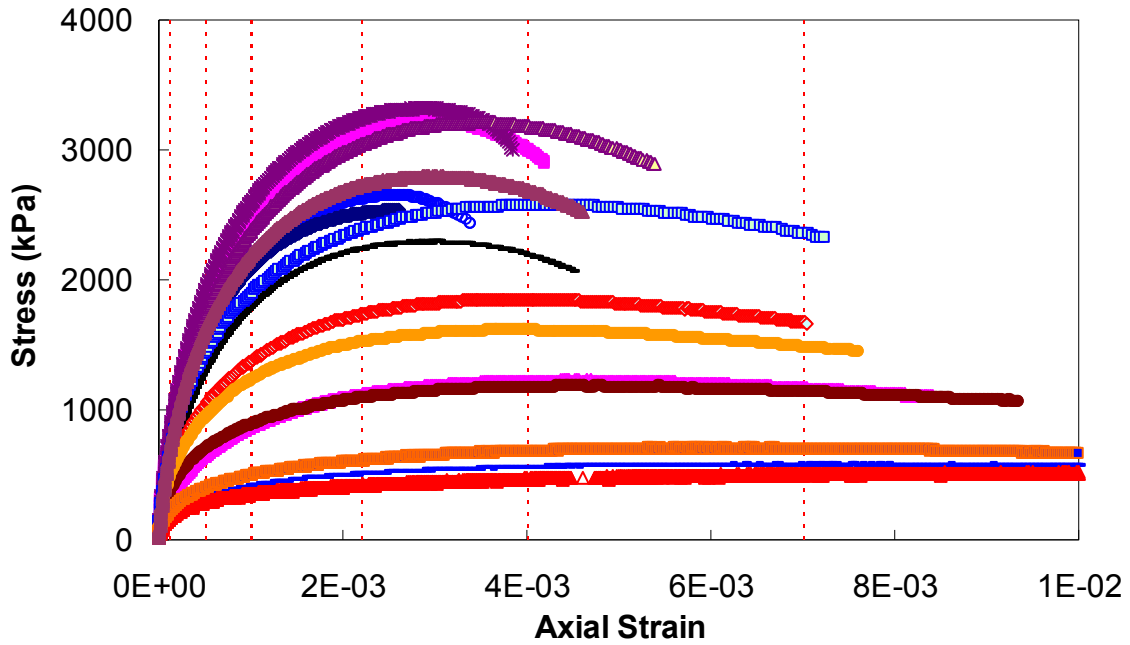


Figure 58. Graph. Strain levels examined for verifying the t-TS principle under growing damage and confining pressure for the Control-2006 mixture.

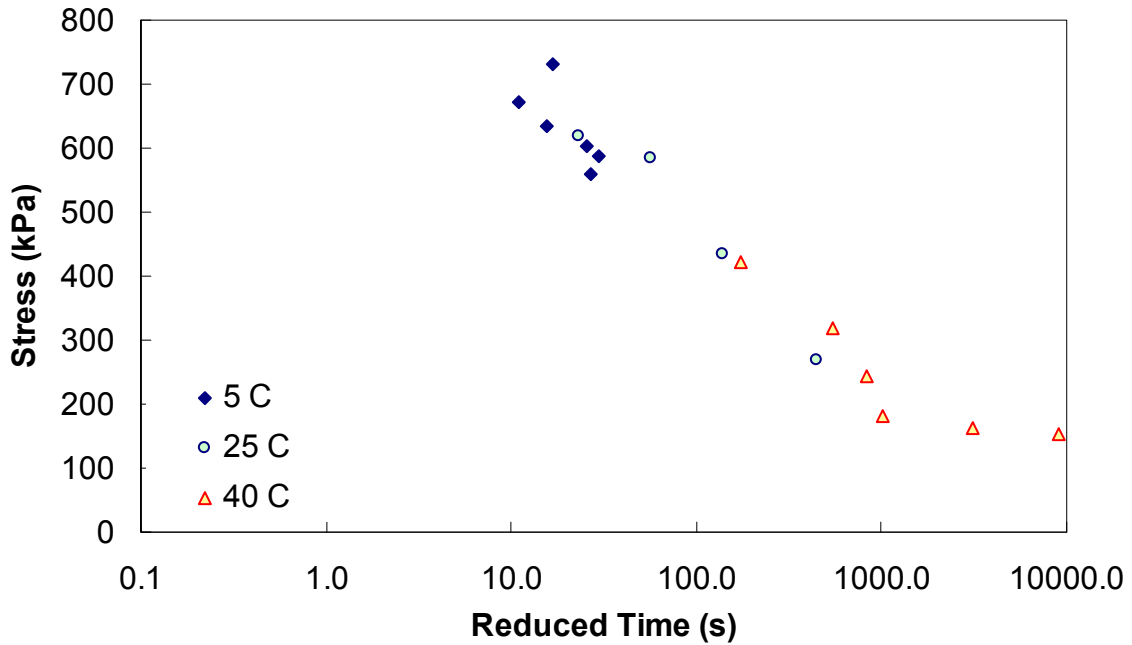


Figure 59. Graph. t-TS with growing damage under confinement verification at a 0.0001ϵ level.

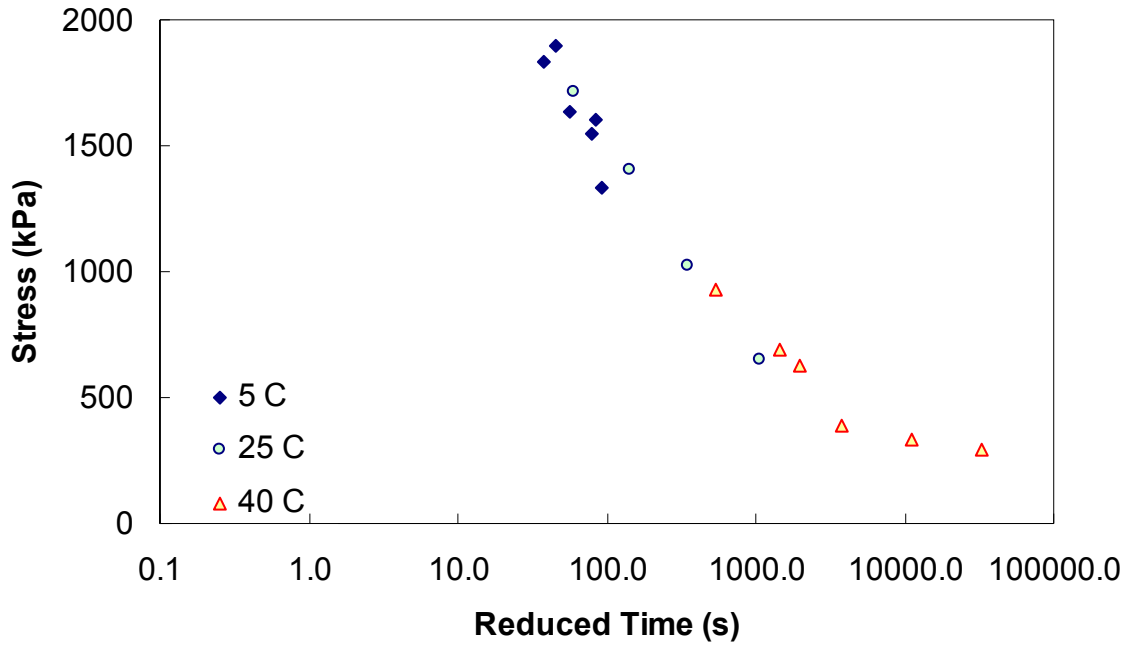


Figure 60. Graph. t-TS with growing damage under confinement verification at a 0.0005ε level.

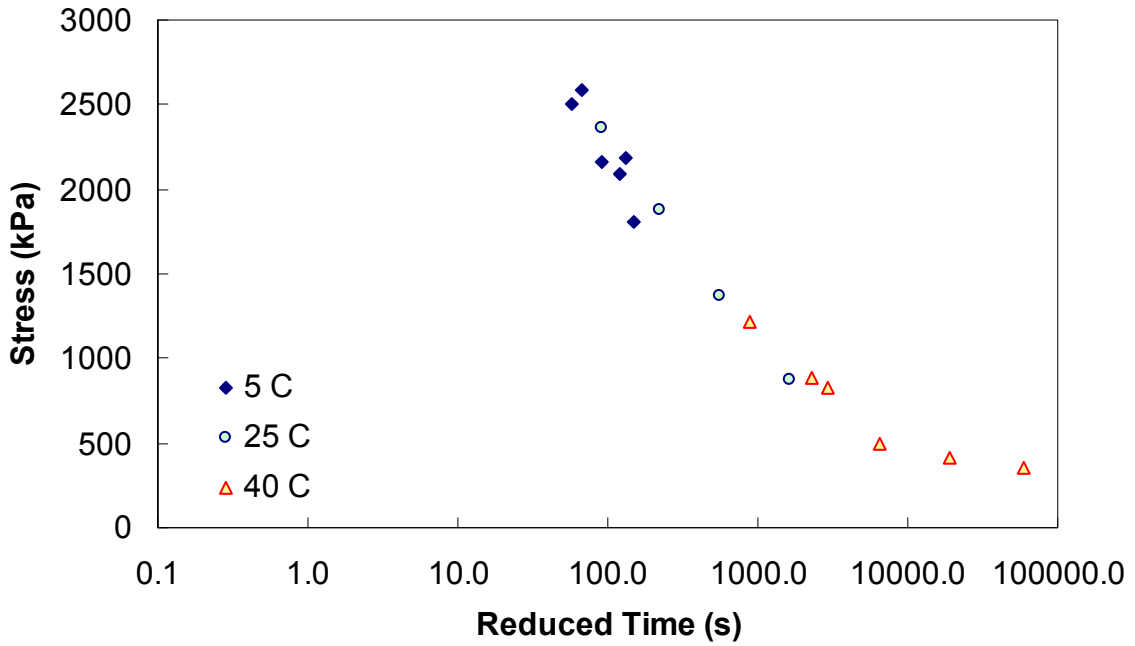


Figure 61. Graph. t-TS with growing damage under confinement verification at a 0.001ε level.

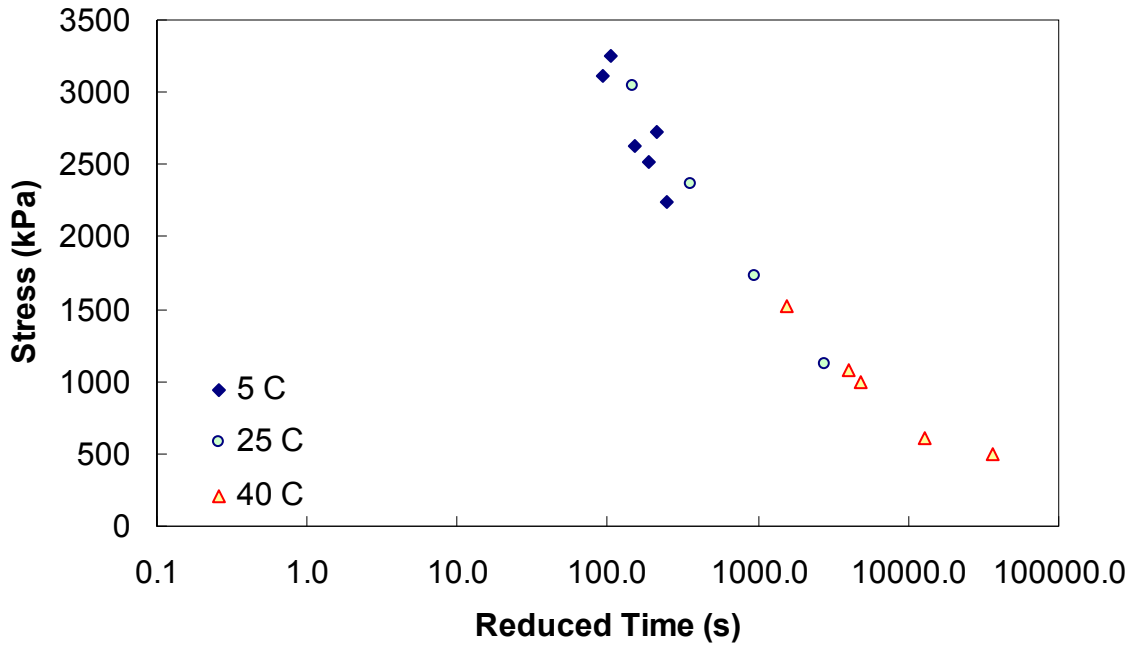


Figure 62. Graph. t-TS with growing damage under confinement verification at a 0.0022ε level.

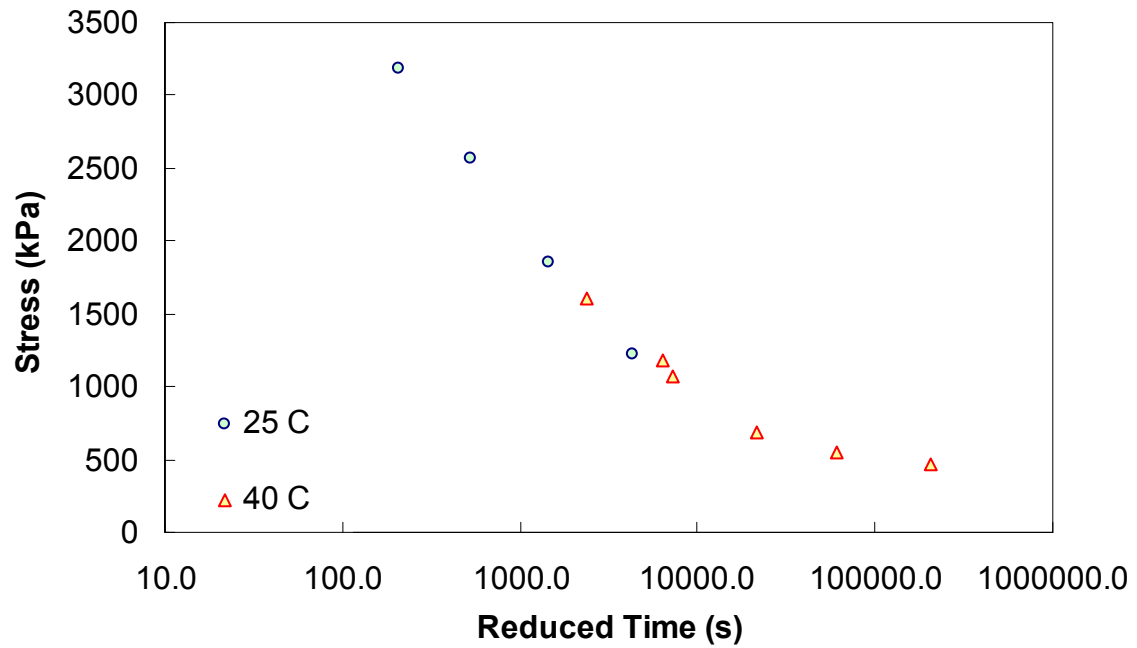


Figure 63. Graph. t-TS with growing damage under confinement verification at a 0.004ε level.

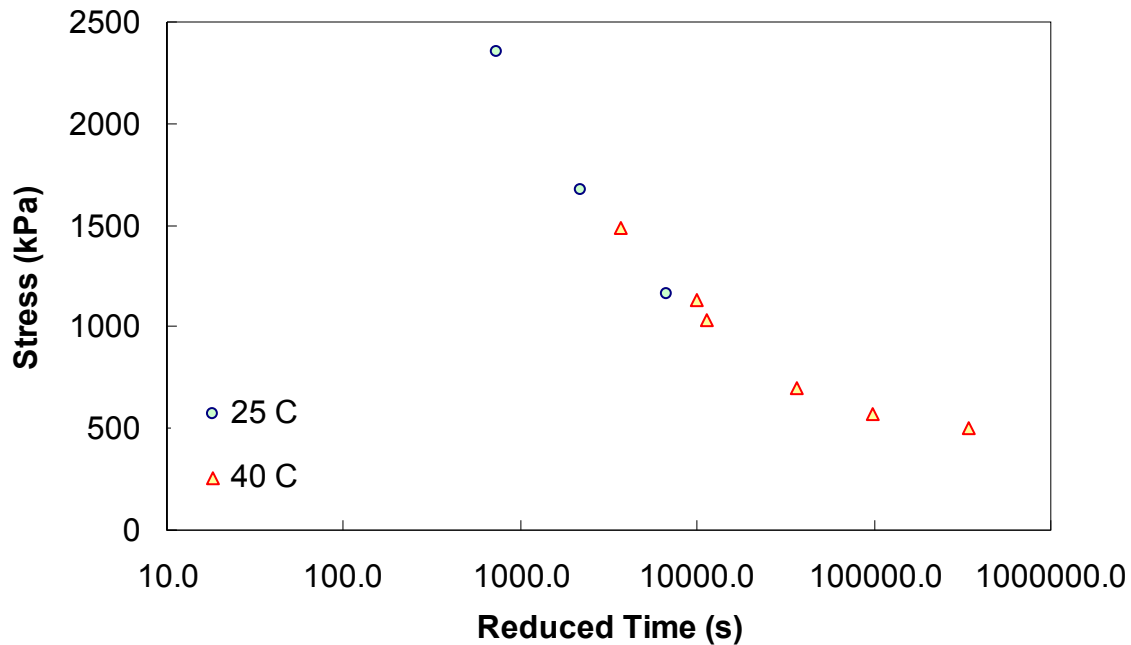


Figure 64. Graph. t-TS with growing damage under confinement verification at a 0.007ε level.

4.6. ENGINEERING BEHAVIOR IN CONFINED TENSION

Verification of t-TS with growing damage under confining stress permitted the development of mastercurves for various engineering parameters. Such curves were created in much the same way as LVE mastercurves (refer to subsection 2.2.1). In this case, the reduced variable of interest was the reduced strain rate. This value was calculated for a given test by multiplying the physically observed strain rate by the time-temperature shift factor for that test. The time-temperature shift factor was determined by using the test temperature with the time-temperature shift factor function shown in figure 22.

One such curve of particular interest was the strength mastercurve, which is shown for both the confined and unconfined conditions in figure 65. Each point in these curves reflected the result from a single test. When examining this figure, the tests performed at higher temperatures resulted in lower reduced strain rates, and tests performed at lower temperatures resulted in higher reduced strain rates. No tests were performed at intermediate temperatures in the unconfined condition, and thus, no data were available in the middle reduced rates for this stress condition. From figure 65, results similar to those observed in LVE characterization were seen. Specifically, strength did not appear to be a function of confining pressure at high reduced rates but did appear to be a strong function of confining pressure at lower reduced rates. Also, less rate dependence was observed in the confined test at lower reduced rates. Another similar curve of interest was the strain at failure mastercurve. This curve provided a glimpse of the effect of temperature and rate on ductility. Plots of the strain at failure mastercurves under both the confined and unconfined conditions are shown in figure 66. Given the variability in these measurements, it was difficult to find any certain conclusive differences in the ductility with pressure. However, the data seemed to indicate an increase in ductility under all conditions, particularly at low reduced rates (i.e., high temperatures). The observation regarding asymptotic

behavior of both stiffness and strength at the low reduced frequencies/rates did not seem to transfer to the ductility.

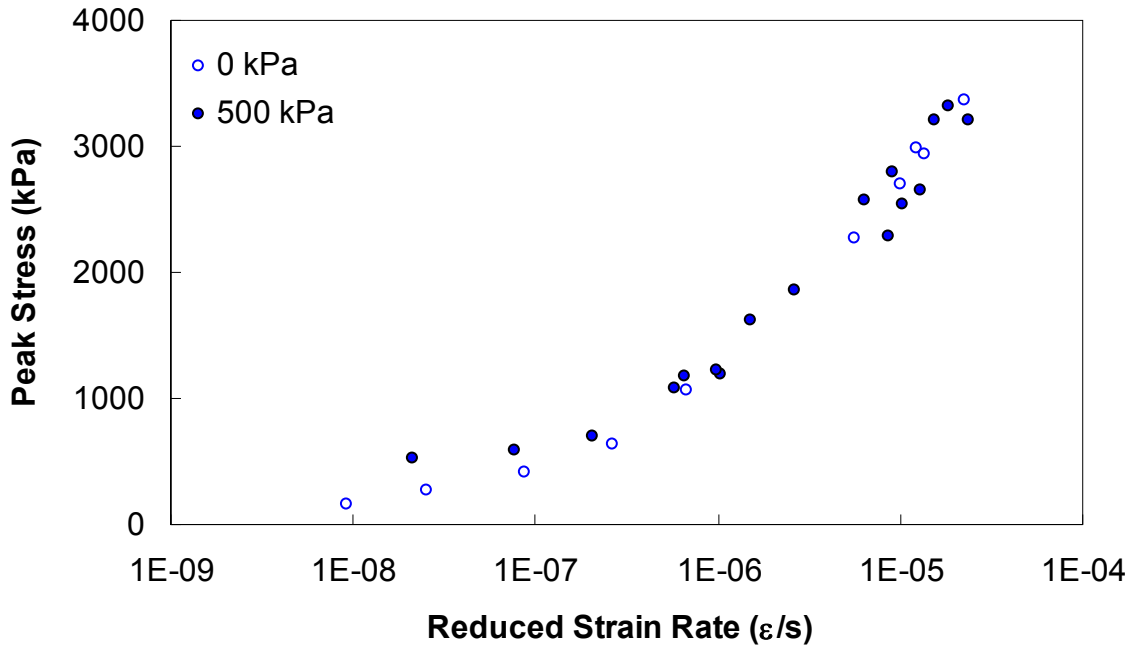


Figure 65. Graph. Effect of 500 kPa confining pressure on strength mastercurves.

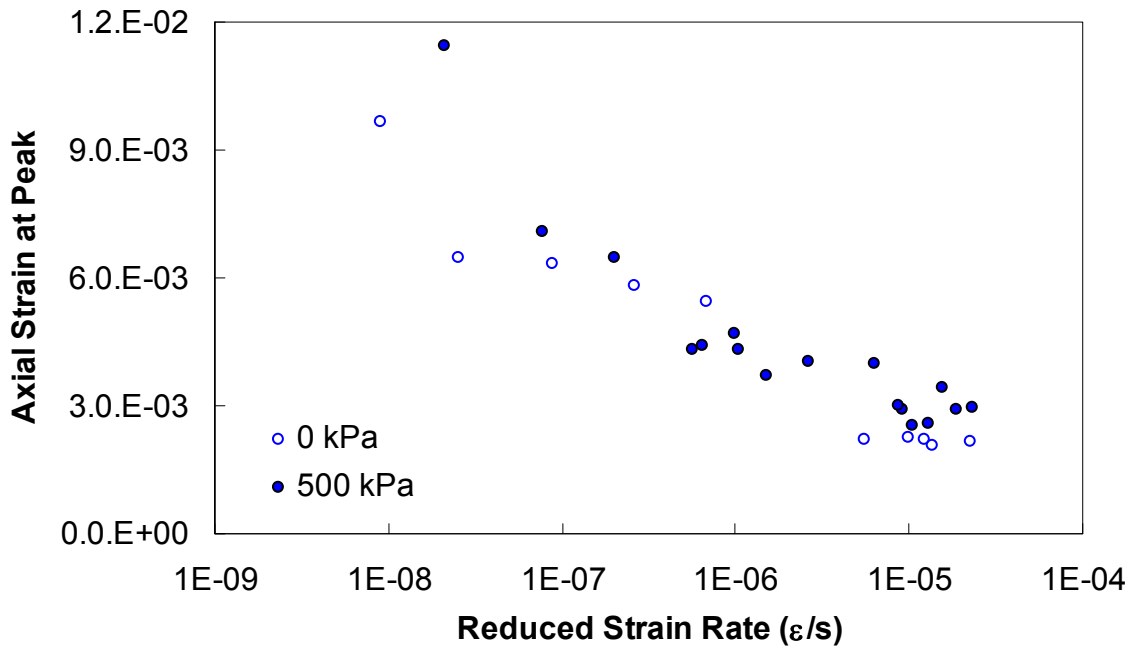


Figure 66. Graph. Effect of 500 kPa confining pressure on ductility in constant crosshead rate tests.

4.7. FATIGUE ANALYSIS WITH VECD MODEL

4.7.1. VECD Integrated Formulation Summary

Formulas relating to the existing formulation of the VEPCD model are shown in equation 109 through equation 116. The damage evolution law is given by the following:

$$\frac{dS}{dt} = \left(\frac{\partial W_d^R}{\partial S} \right)^\alpha \quad (109)$$

Where:

The dual energy density function for uniaxial loading was as follows:

$$W_d^R = \frac{1}{2} C(S) (\varepsilon^R)^2 \quad (110)$$

This leads to the constitutive relationship, which is shown in equation 111.

$$\sigma = C(S) \varepsilon^R \quad (111)$$

Noting that increments of time are generally small, the following can be assumed.

$$\frac{dS}{dt} = \frac{\Delta S}{\Delta t} , \quad (112)$$

Thus,

$$S_i \cong S_{i-1} + \Delta t \left(-\frac{\delta W_i^R}{\delta S} \right)^\alpha \quad (113)$$

Because only C was a function of damage, equation 113 simplified to the following:

$$S_i \cong S_{i-1} + \Delta t \left(-\frac{1}{2} (\varepsilon_i^R)^2 * \frac{(\delta C)_i}{\delta S} \right)^\alpha \quad (114)$$

However, in the case where only stress and time were given, it was convenient to observe that the following:

$$\varepsilon^R = \frac{\sigma}{C} \quad (115)$$

Assuming that pseudo strain was constant over a given increment of time, equation 114 can be recast as follows:

$$S_i \cong S_{i-1} + \Delta t \left(-\frac{1}{2} \left(\frac{\sigma_i}{C_i} \right)^2 * \frac{(\delta C)_i}{\delta S} \right)^\alpha \quad (116)$$

For solving equation 116, either an iterative technique or the analytical representation of $\delta C / \delta S$ can be used.

The important aspects of this formulation as they relate to this report are as follows:

- Damage grew whenever loading was imposed although it did not necessarily grow at an almost zero rate.
- Pseudo strain (true pseudo strain) must also equal zero when stress equaled zero.
- The time dependence of the material was assumed constant regardless of the damage level.
- Damage was irreversible.
- Damage was predicted to grow equally during tension and compression.
- The LVE characteristics of the material were related to the damage characteristics using a single variable, C .
- Damage growth was a function of α true pseudo strain (or stress and pseudo stiffness) and the current value of damage only.

4.7.2. Formulation of Lee, Daniel, and Kim

Formulas relating to the previous formulation as they have been applied in the past are shown in equation 117 through equation 123.

$$\sigma = I \varepsilon_e^R (F + G + H) \quad (117)$$

Where:

I = Normalization factor.

ε_e^R = Effective pseudo strain = $\varepsilon^R - \varepsilon_s^R$.

ε_s^R = Permanent pseudo strain.

F = Function representing the slope of an individual stress-pseudo strain loop.

G = Hysteresis function.

H = Healing function.

It was observed that the damage function, C , is not explicit in equation 117; rather, C enters through the function, F , as follows:

$$F = \left(\frac{\varepsilon_m^R}{\varepsilon_m^R - \varepsilon_s^R} \right) C(S) \quad (118)$$

Equation 117 led to the pseudo energy density function shown in equation 119:

$$W^R = \left[\frac{1}{2} \left(\frac{\varepsilon_m^R}{\varepsilon_m^R - \varepsilon_s^R} \right) C(S) + \frac{1}{2} G + \frac{1}{2} H \right] (\varepsilon_e^R)^2 \quad (119)$$

The damage evolution law was the same for this approach and the current approach. Because G and H were not functions of damage, the damage growth equation became the following:

$$\frac{dS}{dt} = \left(-\frac{1}{2} * \frac{\varepsilon_m^R}{\varepsilon_m^R - \varepsilon_s^R} * (\varepsilon_e^R)^2 * \frac{\partial C}{\partial S} \right)^\alpha \quad (120)$$

Previous researchers further simplified this equation by taking only the pseudo strain values at the peak and then performing the chain rule operation as follows:

$$S_i \cong S_{i-1} + \left(\frac{1}{2} * (\varepsilon_m^R)_i (\varepsilon_{me}^R)_i * (C_{i-1} - C_i) \right)^{\alpha/\alpha+1} * \Delta t^{1/\alpha+1} \quad (121)$$

Where:

- $\varepsilon_{m,i}^R$ = Peak pseudo strain of cycle i .
- $\varepsilon_{me,i}^R$ = Effective pseudo strain at the peak of cycle i .
- C_i = Pseudo stiffness at the $\varepsilon_{m,i}^R$.
- C_{i-1} = Pseudo stiffness at $\varepsilon_{m,i-1}^R$.
- Δt = Cycle pulse time times the number of cycles occurring between observation i and observation $i - 1$.

If it is assumed that the permanent pseudo strain at the beginning of the cycle was approximately equal to the permanent pseudo strain at the peak of the cycle and if it is assumed that the permanent pseudo strain was much smaller than the maximum pseudo strain, then equation 121 can be recast as follows:

$$S_i \cong S_{i-1} + \left(\frac{1}{2} * (\varepsilon_m^R)_i^2 * (C_{i-1} - C_i) \right)^{\alpha/\alpha+1} * \Delta t^{1/\alpha+1} \quad (122)$$

In terms of the iterative approach currently used, the following was the case:

$$S_i \cong S_{i-1} + \Delta t \left(-\frac{1}{2} (\varepsilon_m^R)_i^2 * \frac{\partial C}{\partial S} \right)^\alpha \quad (123)$$

The important aspects of this formulation as they relate to this report are as follows:

- The effect of damage was only a reduction in stiffness.
- Other nonlinear aspects were considered but not physically justified using other functions (G and H).
- Damage growth was independent of other nonlinear effects.
- The pseudo stiffness at the peak value was assumed sufficient for characterization and prediction purposes.
- Damage growth was a function of α , maximum apparent pseudo strain, the current value of damage, and permanent pseudo strain levels at the beginning of a cycle.
- A correction factor was necessary. Rationalization for this factor was provided by the assumption that damage only grew when pseudo strain was positive and increasing to collapse damage curves for cyclic and monotonic data.

4.8. SIMPLIFIED ANALYSIS OF CYCLIC FATIGUE DATA

4.8.1. Correction Factor in Formulation of Lee, Daniel, and Kim

To make cyclic and monotonic data agree in the previous formulation, it was necessary to introduce a pseudo stiffness time change correction factor, M , into the damage calculation function.

$$S_i \cong S_{i-1} + \left(\frac{1}{2} (\varepsilon_m^R)_i^2 * (C_{i-1} - C_i) \right)^{\alpha/1+\alpha} * \left(\frac{\Delta t}{M} \right)^{1/\alpha} \quad (124)$$

To examine the significance of equation 124, it must be returned to its base form before the introduction of factor, M , to equation 121. Undoing the final simplification step for this equation is as follows:

$$S_i \cong S_{i-1} + \left(\frac{1}{2} (\varepsilon_m^R)_i^2 * \frac{(C_{i-1} - C_i)}{\Delta t} \right)^{\alpha/1+\alpha} * \Delta t \quad (125)$$

In order to make equation 125 agree with equation 124, it was necessary to introduce the correction factor, M , as shown in equation 126.

$$S_i \cong S_{i-1} + \left(\frac{1}{2} (\varepsilon_m^R)_i^2 * \frac{(C_{i-1} - C_i)}{\Delta t} \right)^{\alpha/1+\alpha} * \frac{\Delta t}{M} \quad (126)$$

From this equation, it was observed that a factor, M (taken as 4 in previous research), introduced in the manner shown in equation 124, implied that the pseudo stiffness decreased at a rate of M

times the observed cycle averaged rate for a period of $1/M * t_p$ (figure 67). Mathematically, this approach can be schematically represented in figure 69. This figure indicates that the problem was simplified from that of a cyclic load application with magnitude ε^R_m to a square wave form of duration $1/M * t_p$ and a magnitude equal to ε^R_m . Although the square waveform is shown centered about the pulse, no real consideration was given to it when the equivalent square pulse was located during the cyclic pulse.

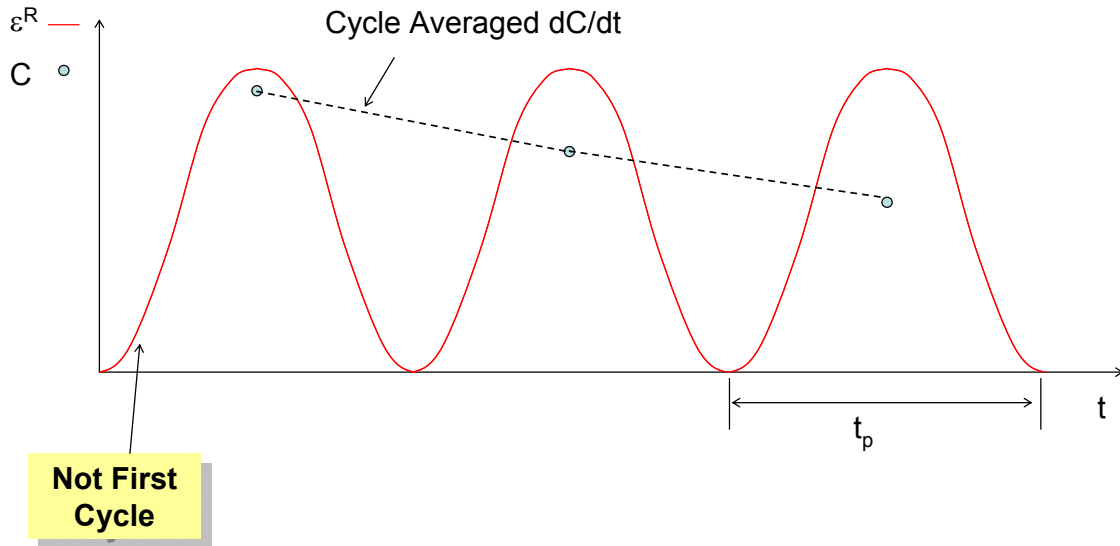


Figure 67. Illustration. A schematic representation of the concept of average dC/dt .

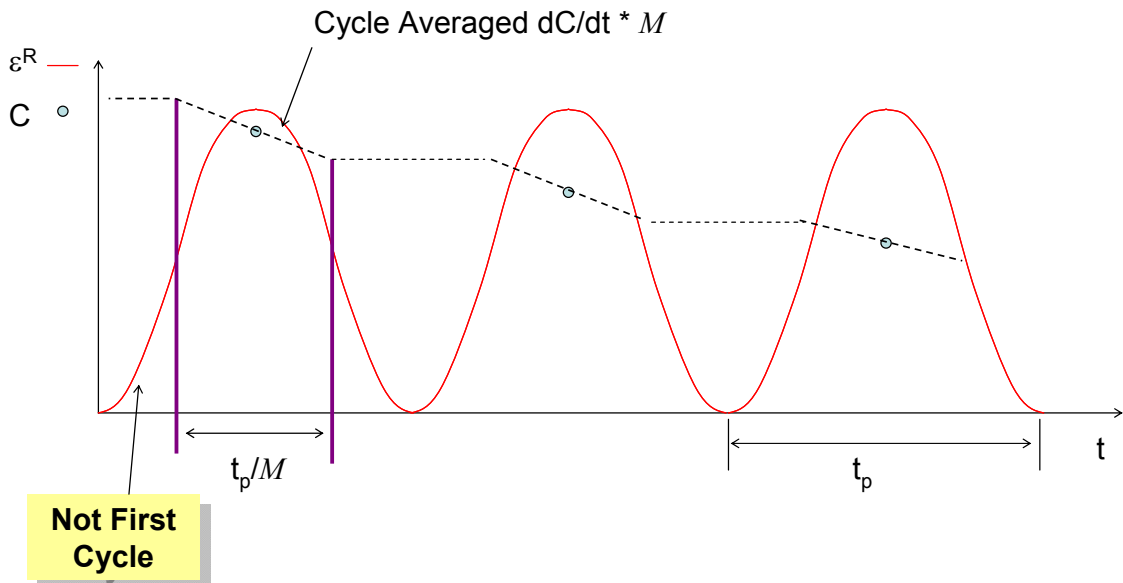
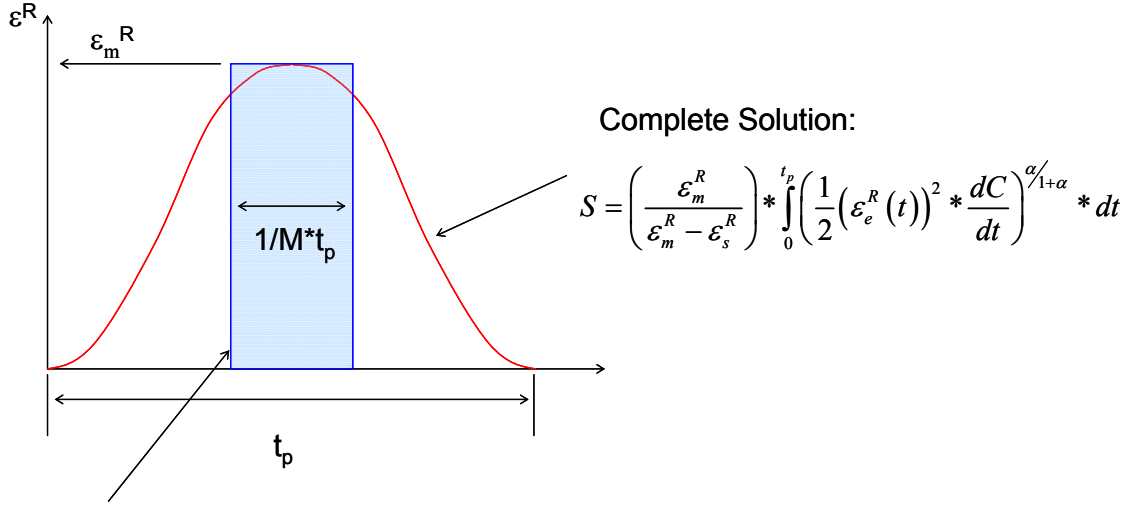


Figure 68. Illustration. A schematic representation of the effect of the M factor on dC/dt used in calculation.



Complete Solution:

$$S = \left(\frac{1}{2} (\varepsilon_m^R)^2 \frac{dC}{dt} \right)^{\alpha/1+\alpha} * \frac{t_p}{M}$$

Figure 69. Illustration. Mathematical equivalence of the formulation used by Lee, Daniel, and Kim.^(3,4,5)

4.8.2. Rigorous Analysis of Pseudo Strain History Effects

The primary complication was that pseudo stiffness values were taken only at the peak. However, in order to have a net reduction in pseudo stiffness over a cycle, the damage must evolve during loading. Some assumptions had to be made regarding how damage grew between the peak values to more rigorously apply equation 120. Ideally, it should be possible to use the measured data to determine exactly when damage seems to grow, but complications in the analysis of full-time data in cyclic tests prevented such an approach.

Because the integration was so well defined and repeatable (constant cyclic loading, for example), the correction factor could be simplified and applied in a way similar to the previous formulation by introducing another derivable factor, Q , as shown in equation 127. This factor was known as the pseudo strain shape factor and accounted for the time-varying pseudo strain history.

It was hypothesized that the more rigorously accurate solution to equation 120 is given by equation 127 (in contrast to equation 124).

$$\begin{aligned} S_i &\cong S_{i-1} + \left(\frac{1}{2} (\varepsilon_m^R)_i^2 * Q * (C_{i-1} - C_i) \right)^{\alpha/1+\alpha} * \left(\frac{\Delta t}{M} \right)^{1/\alpha} \\ &= S_{i-1} + \left(\frac{1}{2} (\varepsilon_m^R)_i^2 * Q * \Delta C_{\text{betweenpeaks}} \right)^{\alpha/1+\alpha} * \left(\frac{\Delta t}{M} \right)^{1/\alpha} \end{aligned} \quad (127)$$

To derive the factor, Q , the G and H functions in equation 119 had to be ignored and substituted with an analytical expression for total pseudo strain as a function of time. This expression was denoted by $\hat{\varepsilon}^R(t)$. Then this function was introduced into the damage evolution law, and the chain rule to arrive at an equation for the amount of damage occurring within a single cycle applied.

$$\Delta S_{withincycle} \cong \sum_{i=1}^N \left[\left(-\frac{1}{2} (\hat{\varepsilon}^R)_i^2 \frac{\Delta C}{\Delta t} \right)^{\alpha/1+\alpha} * \Delta t \right] \quad (128)$$

Equation 128 implies a different form for the constitutive relationship. In particular, the factor, $\varepsilon_m^R / (\varepsilon_m^R - \varepsilon_s^R)$, was lumped in with the effective pseudo strain. This particular factor did not affect equation 127; however, it did imply arrival at equation 127 somewhat differently than was done previously (equation 120 through equation 122). During the cycle, damage grew over only a certain portion of the cycle pulse time, t_p . Furthermore, during this time, pseudo stiffness reduced linearly at a rate such that the total reduction in pseudo stiffness that occurred over this reduced portion was equal to the experimentally observed reduction in pseudo stiffness between peaks. Mathematically this phenomenon is as follows:

$$\frac{\Delta C}{\Delta t} = \frac{\Delta C_{betweenpeaks}}{t_p} * M \quad (129)$$

$$\Delta t = \frac{t_p}{M * N} \quad (130)$$

$$(\hat{\varepsilon}^R)_i = \hat{\varepsilon}^R(t_i) \quad (131)$$

Where:

M = Factor denoting the inverse of the proportion of total pulse time when damage occurs (i.e., if it is assumed that damage occurs during only a quarter of the pulse time, then $M = 4$).

t_p = Cycle pulse time (1/f).

N = Number of discrete points used in the numerical calculation.

Substituting equation 129 and equation 130 into equation 128 and then simplifying found the following:

$$\Delta S_{withincycle} \cong \left(-\frac{1}{2} \frac{\Delta C_{betweenpeaks}}{t_p} * M \right)^{\alpha/1+\alpha} * \sum_{i=1}^N \left[(\hat{\varepsilon}^R)_i^{2\alpha/1+\alpha} \right] * \frac{t_p}{M * N} \quad (132)$$

$$\Delta S_{withincycle} \cong \left(-\frac{1}{2} \frac{\Delta C_{betweenpeaks}}{t_p} \right)^{\alpha/1+\alpha} * \sum_{i=1}^N \left[(\hat{\varepsilon}^R)_i^{2\alpha/1+\alpha} \right] * \frac{1}{N} * \left(\frac{t_p}{M} \right)^{1/\alpha+1} \quad (133)$$

A comparison of equation 133 and equation 127 illustrated that the factor, Q , could be solved as follows:

$$Q = \frac{\left(\sum_{i=1}^N \left[(\hat{\varepsilon}^R)_i^{2\alpha/1+\alpha} \right] * \frac{1}{N} \right)^{1+\alpha/\alpha}}{(\varepsilon_m^R)^2} \quad (134)$$

It was then necessary to assume over which range of t_p damage would occur. For controlled stress testing, it was assumed that damage growth occurred over only half of the loading cycle and was centered over the peak stress. It was important to specify the proportion of loading where damage occurred and when damage occurred in the loading cycle. The functional form of $\hat{\varepsilon}^R(t)$ also had to be assumed. For controlled stress loading, this function is represented by equation 135:

$$\hat{\varepsilon}^R(t)_{stress} = \left(\frac{\varepsilon_m^R}{\varepsilon_m^R - \varepsilon_s^R} \right) \left[(\varepsilon_m^R - \varepsilon_s^R) \sin^2(\omega t/2) \right] = \varepsilon_m^R \sin^2(\omega t/2) \quad (135)$$

A schematic view of the assumptions made for controlled stress loading conditions is shown in figure 70. The shaded region the figure represents the portion of the loading pulse where it was assumed that damage was occurring.

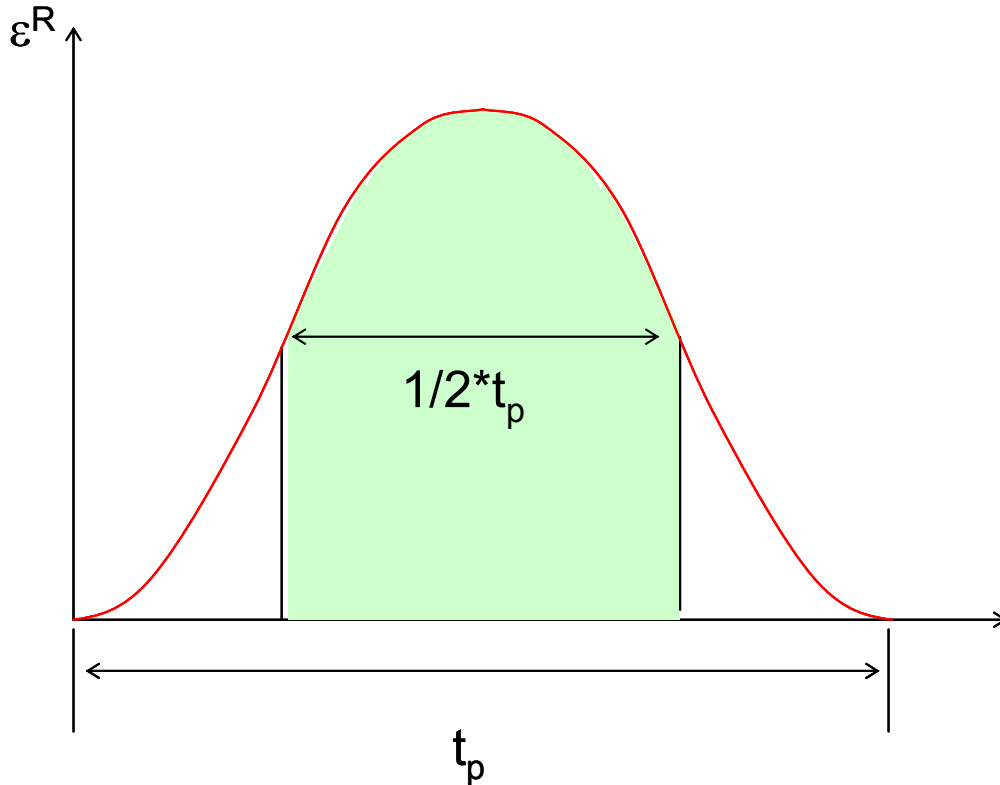


Figure 70. Illustration. Schematic representation of assumptions made for controlled stress cyclic loading to develop Q and M factors.

In the case of controlled crosshead loading, the functional form for $\hat{\varepsilon}^R(t)$ is given by equation 136.

$$\hat{\varepsilon}^R(t)_{Xhd} = \left(\frac{\varepsilon_m^R}{\varepsilon_m^R - \varepsilon_s^R} \right) \left[(\varepsilon_m^R - \varepsilon_s^R) \cos(\omega t) \right] = \varepsilon_m^R \cos(\omega t) \quad (136)$$

A schematic view of the assumptions made for controlled crosshead loading is shown in figure 71. Again, the shaded region represents the portion of the load pulse where it was assumed that damage was occurring.

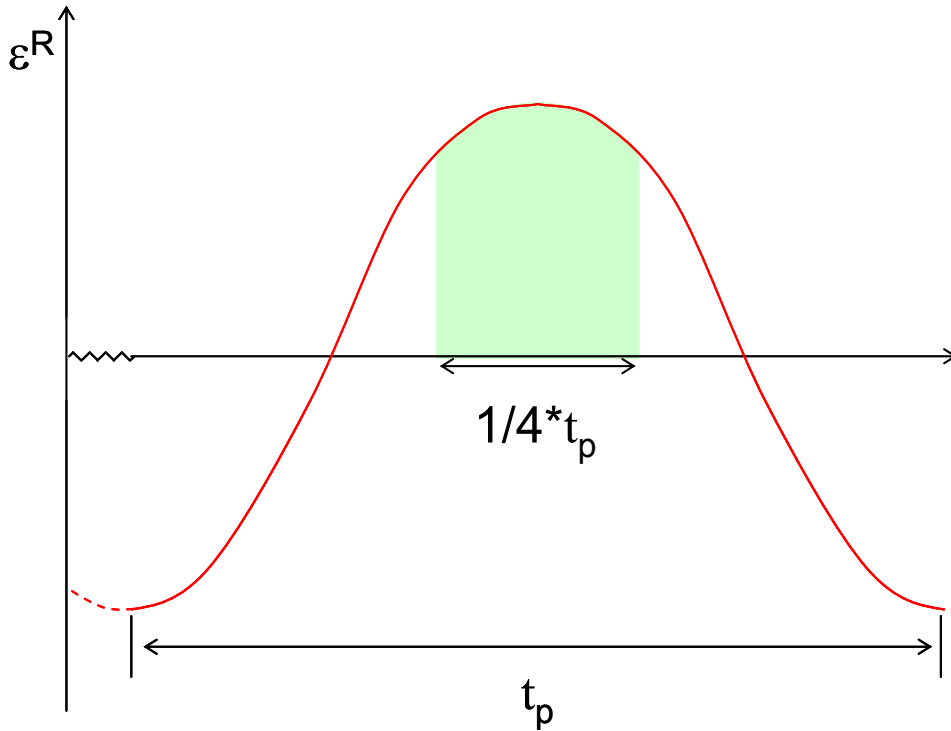


Figure 71. Illustration. Schematic representation of assumptions made for controlled crosshead cyclic loading to develop Q and M factors.

Finally, combining the pseudo strain shape factor and the pseudo stiffness time factor into a single parameter, Z , resulted in the following relationship:

$$dS_{cycle} = \left(-\frac{1}{2} (\varepsilon_m^R)^2 (C_{cycle,i} - C_{cycle,i-1}) \right)^{\alpha/1+\alpha} * (t_p)^{1/1+\alpha} * Z \quad (137)$$

Where:

Z factor was given by the following equation 138.

$$Z = Q^{\alpha/1+\alpha} * \left(\frac{1}{M}\right)^{1/1+\alpha} \quad (138)$$

In the work of Lee, Daniel, and Kim, the Z factor was given by equation 139.⁽³⁻⁵⁾

$$Z = \left(\frac{1}{4}\right)^{1/1+\alpha} \quad (139)$$

The tests used to verify the above derivation are summarized in table 12. The four ALF mixtures used in the VEPCD model verification and discussed in detail elsewhere were used here.^(12,13) Table 12 shows that each of the mixtures had both controlled stress (CS) and controlled crosshead (CX) tests and different combinations of levels and temperatures. The Q and Z factors for each of these mixtures are summarized in table 13 for both the CS and CX conditions.

Table 12. Cyclic tests performed.

Material	Specimen Name	Test Type	Test Designation	Level (kPa/ $\mu\epsilon$)	Freq. (Hz)	Temp. (°C)	N _f
Control	FHWA 101	CS	5-CS-H	1,500/42	4	5	32,000
	FHWA 99	CS	19-CS-H	750/52	4	19	4,700
	FHWA 100	CS	19-CS-L	250/16	4	19	108,720
	FHWA 96	CX	19-CX-L	—/262	4	19	14,800
	FHWA 97	CX	19-CX-L(2)	—/273	4	19	17,800
	FHWA 98	CX	19-CX-H	—/327	4	19	7,900
	FHWA 85	CX	5-CX-H	—/89	10	5	51,170
	FHWA 87	CX	5-CX-H(2)	—/83	10	5	48,190
	FHWA 88	CX	5-CX-L	—/73	10	5	135,000
CRTB	CRTB 30	CS	5-CS-H	1,500/90	4	5	4,400
	CRTB 28	CS	19-CS-H	750/90	4	19	2,360
	CRTB 29	CS	19-CS-L	250/25	4	19	106,700
	CRTB 26	CX	19-CX-H	—/333	4	19	27,500
	CRTB 27	CX	19-CX-L	—/442	4	19	48,762
SBS	SBS 28	CS	5-CS-H	1,500/70	4	5	4,100
	SBS 26	CS	19-CS-H	750/110	4	19	670
	SBS 27	CS	19-CS-L	250/30	4	19	54,240
	SBS 25	CX	19-CX-L	—/300	4	19	>120,000
	SBS 24	CX	19-CX-H	—/523	4	19	> 90,000
Terpolymer	EVY 28	CS	5-CS-H	1,500/70	4	5	5,500
	EVY 26	CS	19-CS-H	750/140	4	19	740
	EVY 27	CS	19-CS-L	250/50	4	19	56,230
	EVY 24	CX	19-CX-L	—/428	4	19	> 138,000
	EVY 25	CX	19-CX-H	—/579	4	19	75,000

— Initial stress level in CX tests are not reported,

Table 13. Summary of cyclic correction factors.

Mixture	α	Test Type	Q	Z
PG 70-22	2.12	CS	0.669	0.609
		CX	0.814	0.558
CRTB	2.96	CS	0.672	0.624
		CX	0.815	0.605
SBS	2.62	CS	0.671	0.619
		CX	0.814	0.588
Terpolymer	2.44	CS	0.670	0.622
		CX	0.815	0.605

The comparisons of the C versus S curves characterized from the monotonic tests and from cyclic tests are shown in figure 72 through figure 75. The loading portions of the first cycle in all of the tests shown in figure 72 were calculated using the formulation shown in equation 29.

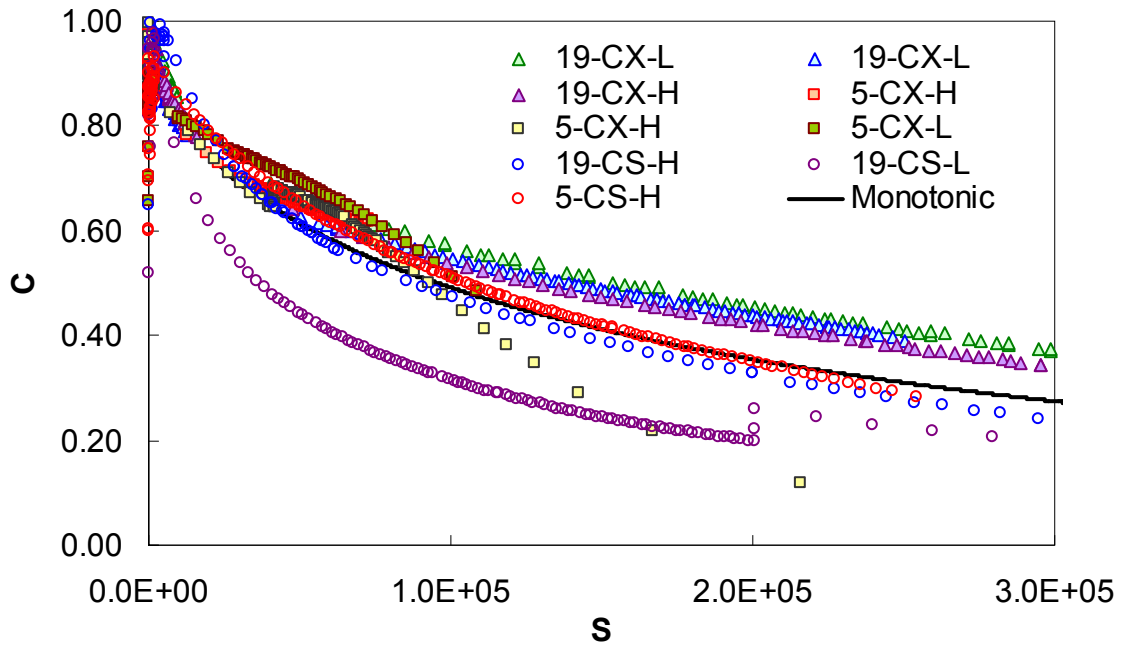


Figure 72. Graph. Damage characteristic comparison, cyclic to monotonic using equation 127 Control mixture.

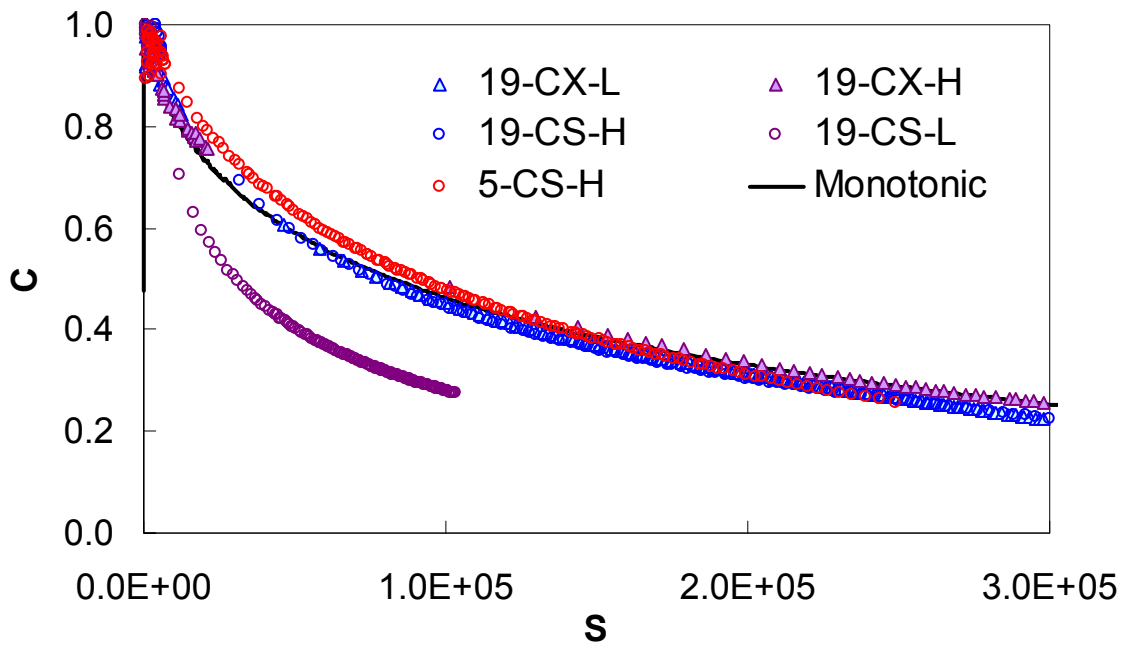


Figure 73. Graph. Damage characteristic comparison, cyclic to monotonic using equation 127 CRTB mixture.

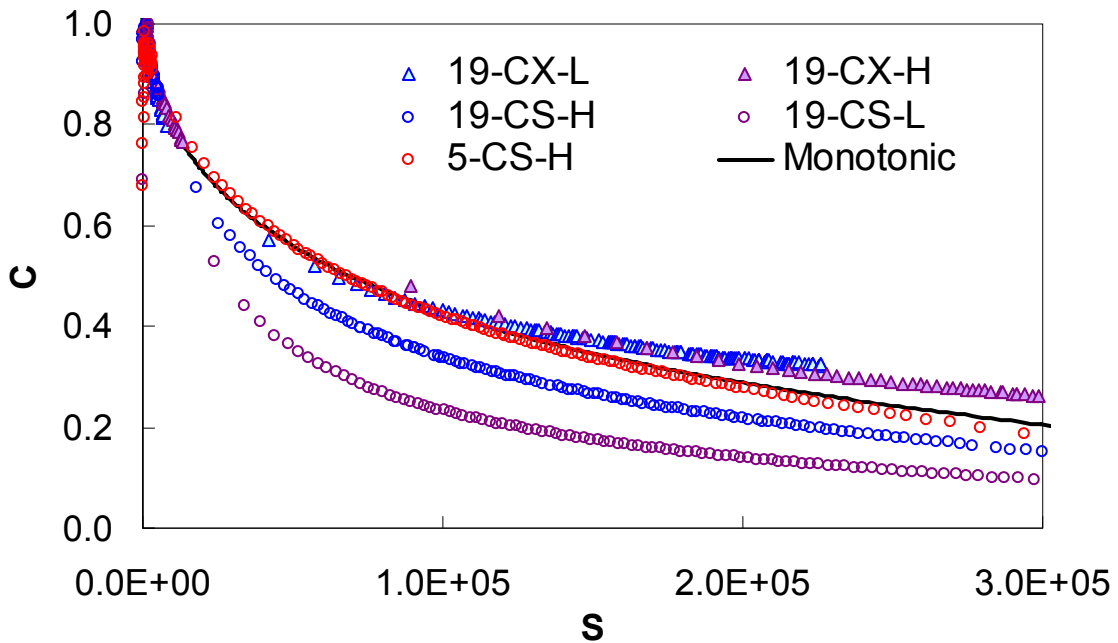


Figure 74. Graph. Damage characteristic comparison, cyclic to monotonic using equation 127 SBS mixture.

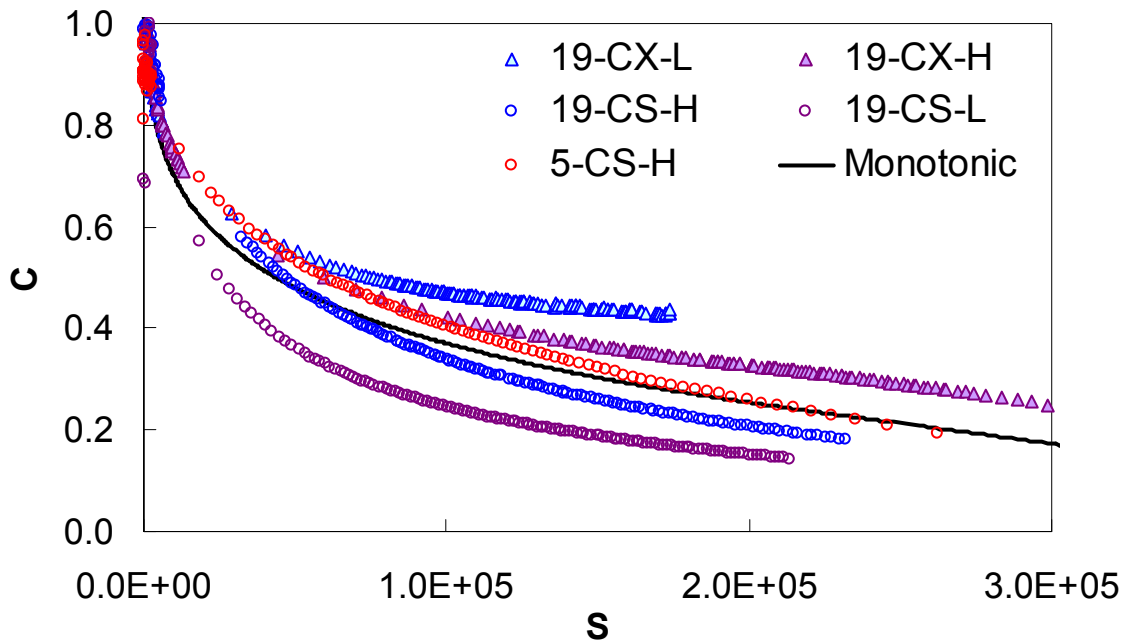


Figure 75. Graph. Damage characteristic comparison, cyclic to monotonic using equation 127 Terpolymer mixture.

4.8.3. Discussion of Simplified Model Approach

Figure 72 through figure 75 show that the collapse of the damage characteristic curve between cyclic and monotonic data depended on both the mixture and test conditions. The Control and

CRTB mixtures showed the most favorable overall collapse, whereas the SBS and terpolymer mixtures showed the least favorable collapse. For each of the mixtures, the degree of collapse appeared to reduce as the amount of permanent strain developing in the test increases. In general, such permanent strains were significantly higher in the CS tests than they were in the CX tests. These strains also tended to increase as a percentage of the total with lower input amplitudes or higher temperatures. These results appeared to become significant for only the 19-CS-L test for the Control and CRTB mixtures. The SBS mixture showed the effects under both of the 19 °C CS test conditions, whereas the terpolymer mixture showed major effects under only the 19-CS-L and the CX conditions.

In addition to the effects of permanent strain, the collapse may have been affected by errors in some of the aforementioned assumptions made for the calculation of damage. Unfortunately, the direct verification of these assumptions was not possible due to uncontrollable data analysis and acquisition errors. Additionally, in cyclic loading, it was possible that other mechanisms, such as nonlinear viscoelasticity and microcrack healing, may have occurred. If this was the case, these mechanisms may not have been triggered by constant rate tension testing. Therefore, it was not expected that the curves would collapse until the model was appropriately formulated. Another potential source of error lay with the α variable in the VEPCD model. Two different physical interpretations of the α variable were used in the literature. However, these interpretations were based on the physical consequences for a single macrocrack (i.e., fracture process zone characteristics, which may have had no relation to the physical realities of a continuum damage problem). In addition, the interpretation of α as a constant value independent of test conditions was based on certain LVE characteristics. These particular characteristics were not observed for asphalt concrete under every condition. In addition, because α was an exponent in the model, its impact was complicated and could have caused an increase or decrease in the damage prediction, depending on temperature, mode of loading, and amplitude of loading.

4.9. REFINED DERIVATION OF SIMPLIFIED FATIGUE MODEL

The previous formulations had some obvious problems either in the rigor of their derivations or in the assumptions made. To address this problem, a new formulation was proposed. In the following subsections this refined formulation is given. Then, the refined formulation is further simplified into a form which can be easily programmed into a spreadsheet for fatigue life predictions. To be clear, the definition used for pseudo stiffness with this formulation is shown in equation 140. Notice that pseudo stiffness is given by the variable F to differentiate it from the definition used in the previous formulations. Qualitative the meaning of F and C are the same even though they differ slightly quantitatively.

$$F = \frac{\sigma_{0,ta}}{\epsilon_{0,ta}^R * I} \quad (140)$$

Where:

$\sigma_{0,ta}$ = The stress tension amplitude.

$\epsilon_{0,ta}^R$ = The pseudo strain tension amplitude.

I = The normalization factor (0.9–1.1).

4.9.1. Identification of Tensile Loading Time

To quickly analyze the cyclic data in the simplified mechanics model, it was important to identify the actual time that a given cycle was under tensile loading. This time was important because it was assumed that fatigue damage occurred only under such conditions. To determine this time, it was assumed that regardless of the input condition the following analytical function was descriptive of the stress history of any given cycle for the tests used in this study:

$$\frac{\sigma(\xi)}{\sigma_{0,ta}} = (\beta - \cos(\omega_R \xi)) \frac{1}{\beta + 1} \quad (141)$$

Where:

$\sigma_{0,ta}$ = The tension stress amplitude and for generality time was given as reduced time, ξ .

The β term, defined by equation 142, was a factor that allowed direct quantification of the duration that a given stress history was tensile. In equation 142, $(\sigma_{peak})_i$ was the largest value within cycle i , and $(\sigma_{valley})_i$ was the smallest value within cycle i .

$$\beta_i = \frac{(\sigma_{peak})_i + (\sigma_{valley})_i}{|\sigma_{peak}|_i + |\sigma_{valley}|_i} \quad (142)$$

When $\beta = 1$, the entire stress (and therefore the pseudo strain minus permanent pseudo strain) history for the given cycle was tensile; when $\beta = 0$, half of the history was tensile; and when $\beta = -1$, the entire history was compressive. This last condition was not used for any of the tests in this study.

Noting that the total pulse time was $\omega_R/(2\pi)$ and using the definition of stress shown in equation 141, the factor M used in the previous formulation can now be rigorously calculated using equation 143.

$$\frac{1}{M} = \frac{1}{2} \left(1 - \frac{\cos^{-1}(\beta)}{\pi} \right) \quad (143)$$

With the definition of total stress history and β in equation 141 and equation 142 respectively, it can be shown that the tensile amplitude can be calculated from the peak-to-peak values if β is known by equation 144. Although equation 144 is shown for stress, it can also be applied to pseudo strain.

$$\sigma_{0,ta} = \frac{\beta + 1}{2} \sigma_{0,pp} \quad (144)$$

Finally, it can be shown that the times during the load pulse at which tensile loading begins and ends for any given cycle are, in terms of the coefficient, β , and the reduced loading frequency, ω_R , given by equation 145 and equation 146.

$$\xi_i = \frac{\pi}{\omega_R} - \frac{\pi - \cos^{-1}(\beta)}{\omega_R} \quad (145)$$

$$\xi_f = \frac{\pi}{\omega_R} + \frac{\pi - \cos^{-1}(\beta)}{\omega_R} \quad (146)$$

4.9.2. Defining Alpha

The power, α , in the VECD model has been discussed previously. In the reformulated model, the power was defined more clearly. Through theoretical arguments that use the macrocracking phenomenon, this power was found to relate to linear viscoelastic time dependence.⁽⁹⁾ Motivated by earlier work on this subject, the maximum absolute value of the log-log slope of the relaxation modulus, m , was taken to represent the linear viscoelastic response. (See references 4, 5, 7, and 8.) According to the theory, if the material's fracture energy and failure stress are constant, then $\alpha = 1/m + 1$, but if the fracture process zone size and fracture energy are constant, then $\alpha = 1/m$. A review of the literature shows that different researchers have used differing α values. Some researchers suggest that it is most appropriate to use $\alpha = 1/m$ for the type of CS tests that were performed in this current study and $\alpha = 1/m + 1$ for the CX tests.^(3,4) This approach is supported by the work of other researchers that uses the constant failure stress and energy criteria for the CX tests and by separate studies which have used CS-type tests and $\alpha = 1/m$.^(5,7,12) Therefore, this study used $\alpha = 1/m + 1$ for the CX tests, and $\alpha = 1/m$ for the CS tests. No attempt was made in this work to calibrate these relationships further. A summary of the α values used for the mixtures of interest is given in table 14.

Table 14. Summary of α values for refined model.

Mixture	Test Type	α
PG 70-22	CS	2.40539
	CX and Monotonic	3.40539
CRTB	CS	3.31787
	CX and Monotonic	4.31787
SBS	CS	2.92686
	CX and Monotonic	3.92686
Terpolymer	CS	2.72093
	CX and Monotonic	3.72093
9.5 Fine	CS	3.12658
	CX and Monotonic	4.12658

4.9.3. Failure in Cyclic Mode of Loading

Two criteria were adopted to define the cycle at which data could be used in the VECD characterization/verification process. Two different criteria were necessary because the CS and CX tests failed in quite different patterns and because each criterion captured one of the two possible reasons that it was inappropriate to use a given test result: (1) localization of damage at the point of a single macrocrack, or (2) the onset of additional dominating mechanisms that were not related to microdamage. To identify the point of macrocrack localization in these tests, the

method suggested in the literature, whereby the cycle at which the phase angle showed a sharp decrease, was taken as N_f .⁽⁵⁸⁾ This cycle was identified graphically by plotting the phase angle versus cycle number. During the test, the phase angle tended to increase steadily until a point at which it dropped rapidly. The cycle where this rapid drop occurred was N_f .

When processes other than damage mechanisms, such as viscoplasticity, began to have significant effect, then a test could no longer be used directly for characterization. Although at this time rigorous identification of this occurrence was not possible, it was assumed that the onset of other mechanisms was closely related to the total amount of permanent strain experienced by the specimen. It was known from experience that the constant crosshead rate tests at 5 °C and strain rates above 1×10^{-5} for unmodified mixtures and 1×10^{-4} for polymer-modified mixtures were dominated by the viscoelastic damage mechanisms.^(7,12) It was also known that for any given mixture the tests performed at these rates showed similar strain levels at the peak stress. These mixture-dependent strain levels represented a known level below which VECD mechanisms dominate. The cycle in the fatigue tests at which the permanent strain exceeded this threshold was taken as the point after which data could not be used for VECD characterization. To find the permanent strain during the cyclic test, the permanent pseudo strain was tracked by cycle. Then these permanent pseudo strain values were compiled as a function of reduced time, where reduced time was taken at the end of the beginning of the respective cycle where the permanent pseudo strain was known. It was then assumed that the permanent pseudo strain varied linearly within the cycle (the final value for cycle i was equivalent to the initial value for cycle $i + 1$). With this assumption, equation 16 could be inverted and used with the state variable formulation to solve for permanent strain. Note that while the effect of assuming a linear pseudo strain growth is not explored here, the effect of this assumption was small since the amount of permanent pseudo strain within a cycle is generally very small.

When either of these two conditions was met, failure was said to have occurred, and all data gathered afterward were ignored. Thus, all of the data shown in any of the subsequent graphs represent the data prior to this failure point. It is worth noting that in this study all tests in the CX mode failed due to the rapid change in phase angle, while all tests performed in the CS mode failed due to exceeding the strain limit.

4.9.4. Refined Simplified Model Derivation

The basic concept of the refined model is to separate the damage calculation into two components: damage occurring in the first loading path and damage occurring due to the repeated loading. These two components were referred to as the transient and cyclic portions respectively. The mathematical implications are given in equation 147.

$$dS = \begin{cases} dS_{Transient} & \xi \leq \xi_p \\ dS_{Cyclic} & \xi > \xi_p \end{cases} \quad (147)$$

Where:

ξ_p = Reduced cycle pulse time.

This refined method assumed that all of the effects of damage were shown through a reduction of the cyclic pseudo stiffness, F . This assumption did not mean that damage affected only the cyclic pseudo stiffness but rather that this pseudo stiffness wholly reflected damage effects. It was also assumed that damage growth within a given cycle was small. The test data were still normalized for specimen-to-specimen variability by the correction factor, I , defined earlier. The transient calculation was the same as the rigorous calculation shown in equation 114, but the form of the cyclic portion was given by equation 148 where the variable R was a form adjustment factor. The subscript k was only a placeholder to represent the fact that the factor R could vary from cycle to cycle depending on the particular loading history. During real experiments this might occur due to slight deviations in machine control. In general, though, the value of R varied only slightly throughout loading. However, the refined model was capable, by including the form adjustment factor, to explicitly account for any load form shape (i.e., square, saw-tooth, sinusoidal, etc.), or combinations of shapes, as long as that load history did not violate the assumptions made in the following paragraphs.

$$dS_{cyclic,k} = \left(-\frac{I}{2} (\varepsilon_{0,ta}^R)^2 \Delta F \right)^{\alpha/1+\alpha} * (\xi_p)^{1/\alpha} * (R_k) \quad (148)$$

This adjustment factor was found by assuming that equation 150 could be used to simplify the more rigorous equation 149.

$$\Delta S = \int_{\xi_i}^{\xi_f} \left(-\frac{I}{2} * (\varepsilon_e^R)^2 \frac{\partial C}{\partial S} \right)^{\alpha} * d\xi \quad (149)$$

$$\Delta S = \left(-\frac{I}{2} * (\varepsilon_{0,ta}^R)^2 \frac{\partial F}{\partial S} \right)^{\alpha} * (\xi_f - \xi_i) * K_1 \quad (150)$$

$$\varepsilon_e^R(\xi) = (\varepsilon_m^R - \varepsilon_s^R) * f(\xi) = \varepsilon_{0,ta}^R * f(\xi) \quad (151)$$

Setting equation 149 equal to equation 150 and noting that (equation 152):

$$\frac{\partial C}{\partial S} \cong \frac{\partial F}{\partial S} \quad (152)$$

gave the following (equation 153):

$$\int_{\xi_i}^{\xi_f} \left(-\frac{I}{2} * (\varepsilon_e^R)^2 \frac{\partial F}{\partial S} \right)^{\alpha} * d\xi = \left(-\frac{I}{2} * (\varepsilon_{0,ta}^R)^2 \frac{\partial F}{\partial S} \right)^{\alpha} * (\xi_f - \xi_i) * K_1 \quad (153)$$

Finally, if it was assumed that within a cycle, $\partial F/\partial S$ was nearly constant and if it is recalled that the effective pseudo strain history is given by equation 151, then (equation 154):

$$\left(\varepsilon_{0,ta}^R\right)^{2\alpha} * \int_{\xi_i}^{\xi_f} \left(f(\xi)\right)^{2\alpha} * d\xi = \left(\varepsilon_{0,ta}^R\right)^{2\alpha} * \left(\xi_f - \xi_i\right) * K_1, \quad (154)$$

which simplifies to (equation 155):

$$K_1 = \frac{1}{\xi_f - \xi_i} * \int_{\xi_i}^{\xi_f} \left(f(\xi)\right)^{2\alpha} * d\xi \quad (155)$$

The implication of assuming that $\partial F/\partial S$ was nearly constant was not explored for this study. However, in the context of fatigue where failure often required thousands to millions of cycles, it was assumed that such an assumption was valid. It can be shown that the R factor was equal to K_1 raised to a power that was a function of α as shown in equation 156, where the times for the integral in this equation were defined by equation 145 and equation 146. The values for this adjustment factor were approximately equal to 0.77 for the CX tests (nearly sinusoidal loading) and 0.70 for the CS tests (purely haversine loading) for most mixtures. Should the loading form be something other than these two types, the value of R would be different but could be calculated using equation 156.

$$R = \left(\frac{1}{\xi_f - \xi_i} * \int_{\xi_i}^{\xi_f} \left(f(\xi)\right)^{2\alpha} * d\xi \right)^{1/(1+\alpha)} \quad (156)$$

4.9.5. Model Application

The refined model was applied to the tests given in table 12, and the comparison of the damage characteristic curves from the cyclic and monotonic tests are shown in figure 76 through figure 79. Comparing these figures to the results shown in figure 72 through figure 75, it was seen that the refined method did a much better job in collapsing the damage characteristic curves, suggesting that the mathematical rigor and assumptions made in this refined method were more appropriate for describing the behavior of asphalt concrete materials.

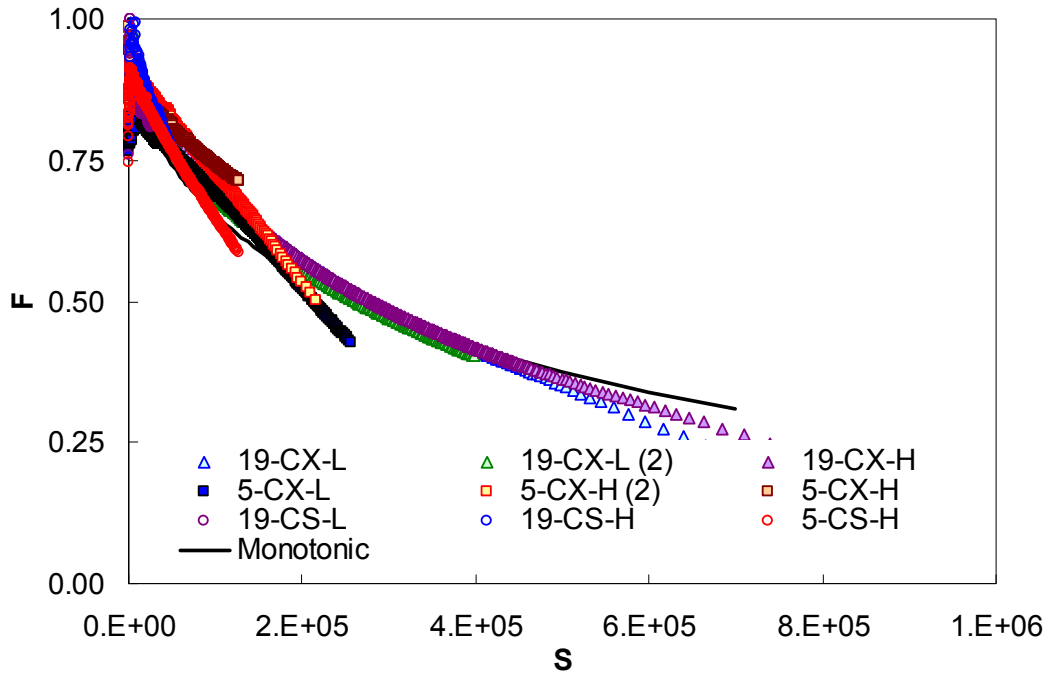


Figure 76. Graph. Damage characteristic comparison, cyclic to monotonic using refined model Control mixture.

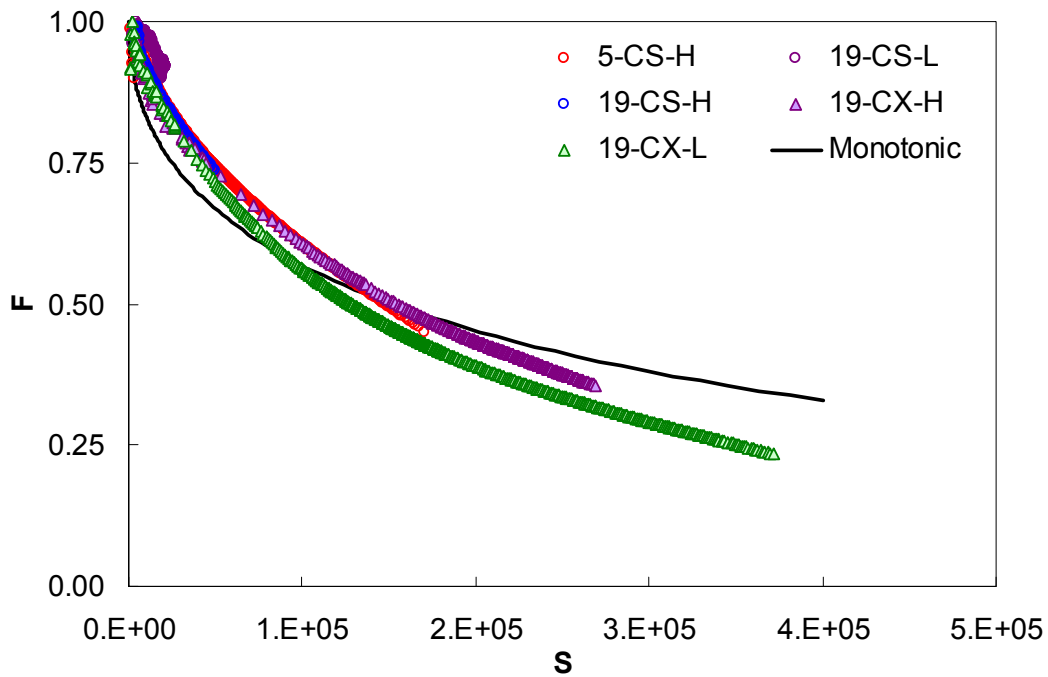


Figure 77. Graph. Damage characteristic comparison, cyclic to monotonic using refined model CRTB mixture.

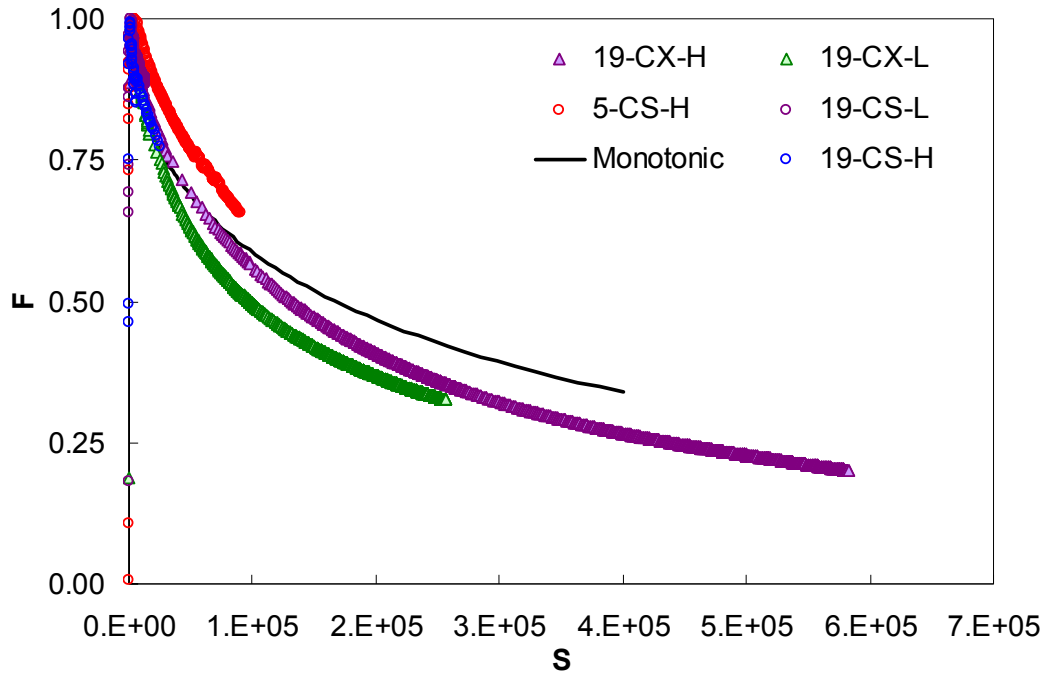


Figure 78. Graph. Damage characteristic comparison, cyclic to monotonic using refined model SBS mixture.

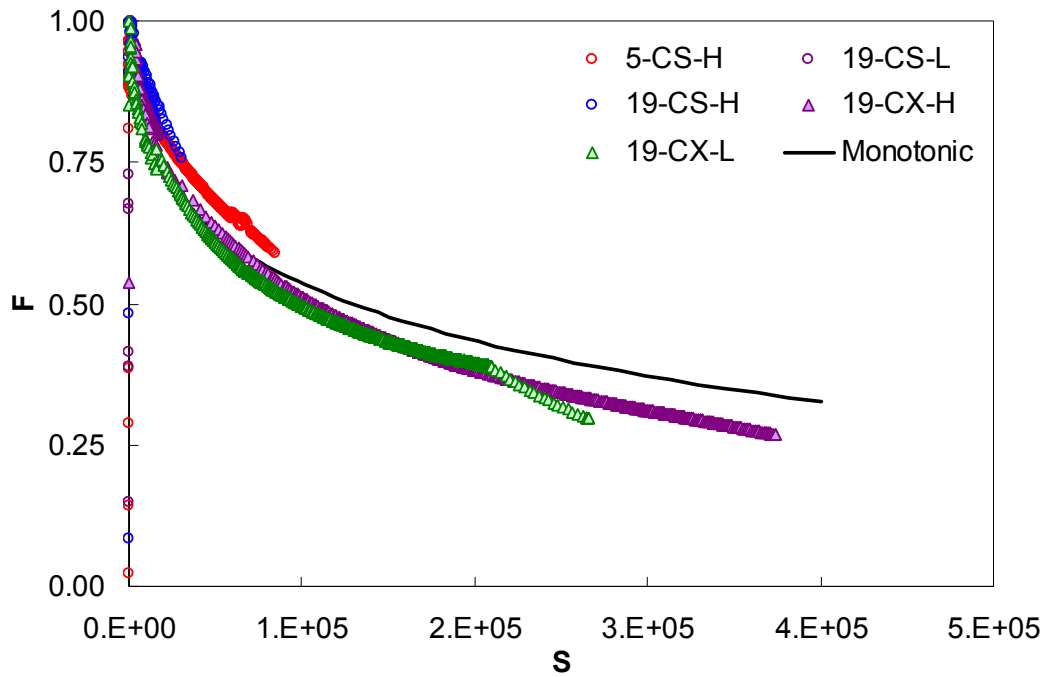


Figure 79. Graph. Damage characteristic comparison, cyclic to monotonic using refined model Terpolymer mixture.

4.9.6. Simplifications to Refined Model

Compared to the rigorous modeling, the refined model was simple to use. However, the method still required the complete calculation of pseudo strain for the entire loading history, e.g., evaluation of the integral in equation 16. This process could have been time consuming, so it was worthwhile to examine simplifications to the calculation. The easiest simplification was referred to as the steady-state assumption because it was rigorously accurate only under steady-state loading. This condition was only approximately true for the cyclic portion of loading and is mathematically shown in equation 157.

$$\left(\varepsilon_{0,ta}^R\right)_{cycle\ i} = \frac{1}{E_R} \left(\varepsilon_{0,ta}\right)_i * |E^*|_{LVE} = \frac{1}{E_R} * \frac{\beta + 1}{2} \left(\left(\varepsilon_{0,pp}\right)_i * |E^*|_{LVE}\right) \quad (157)$$

Replacing the pseudo strain amplitude in equation 148 with that in equation 157 greatly simplified the calculation and made a spreadsheet solution a possibility. The consequences of this simplification are shown in figure 80 through figure 84. Note that an additional mixture was included in this group of graphs. The test summary for only this mixture is given in table 15; a summary of the other mixtures has already been given in table 12. Due to the change in definition for pseudo stress, the pseudo stiffness is now referred to as C^* to indicate that it was computed using the steady-state assumption. Also, recall the definitions of failure in these tests have been provided in subsection 4.9.3.

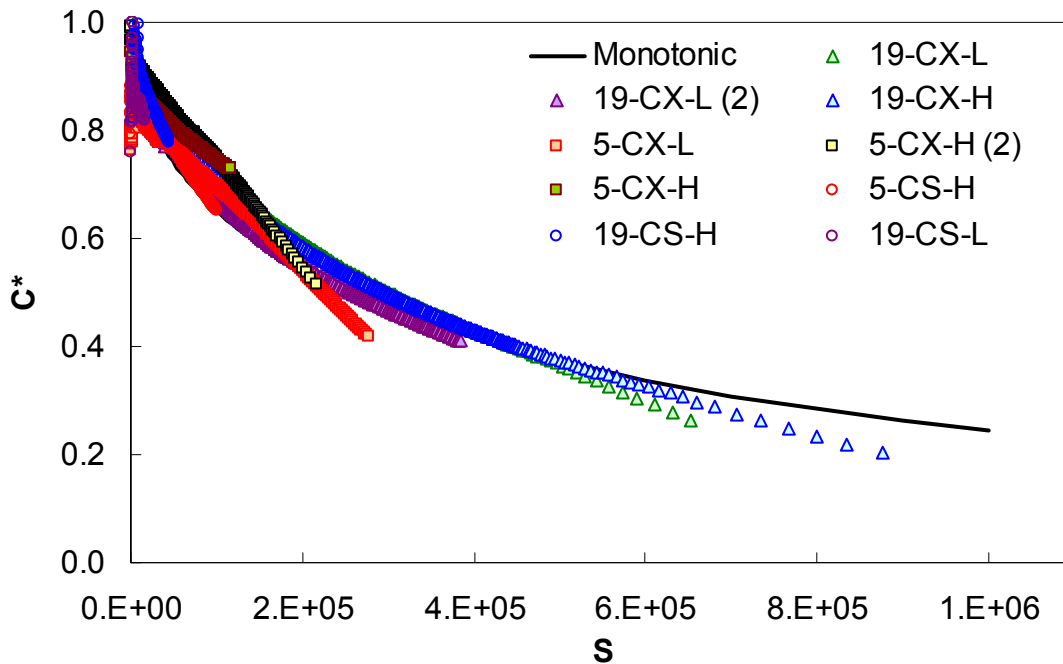


Figure 80. Graph. Damage characteristic comparison, cyclic to monotonic using refined simplified model Control mixture.

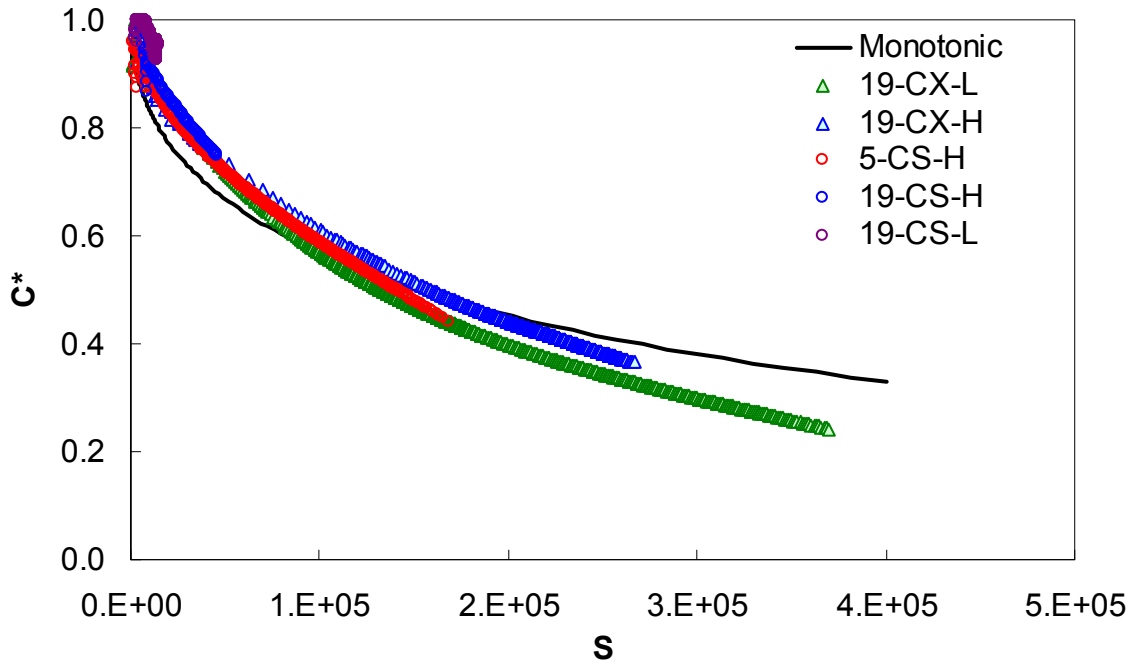


Figure 81. Graph. Damage characteristic comparison, cyclic to monotonic using refined simplified model CRTB mixture.

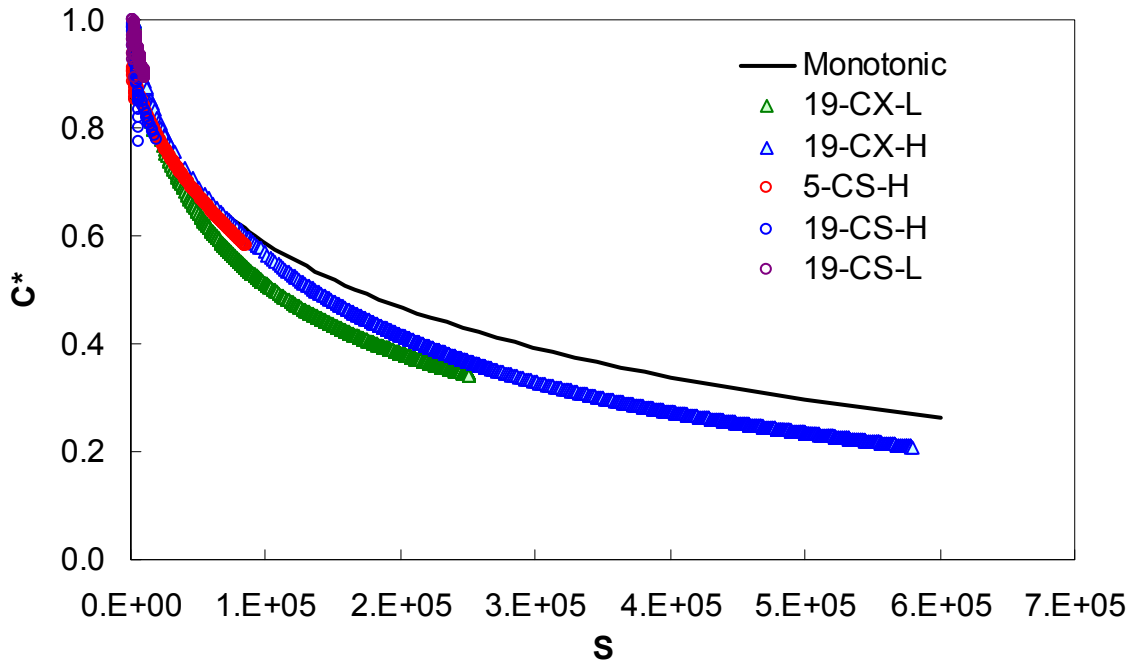


Figure 82. Graph. Damage characteristic comparison, cyclic to monotonic using refined simplified model SBS mixture.

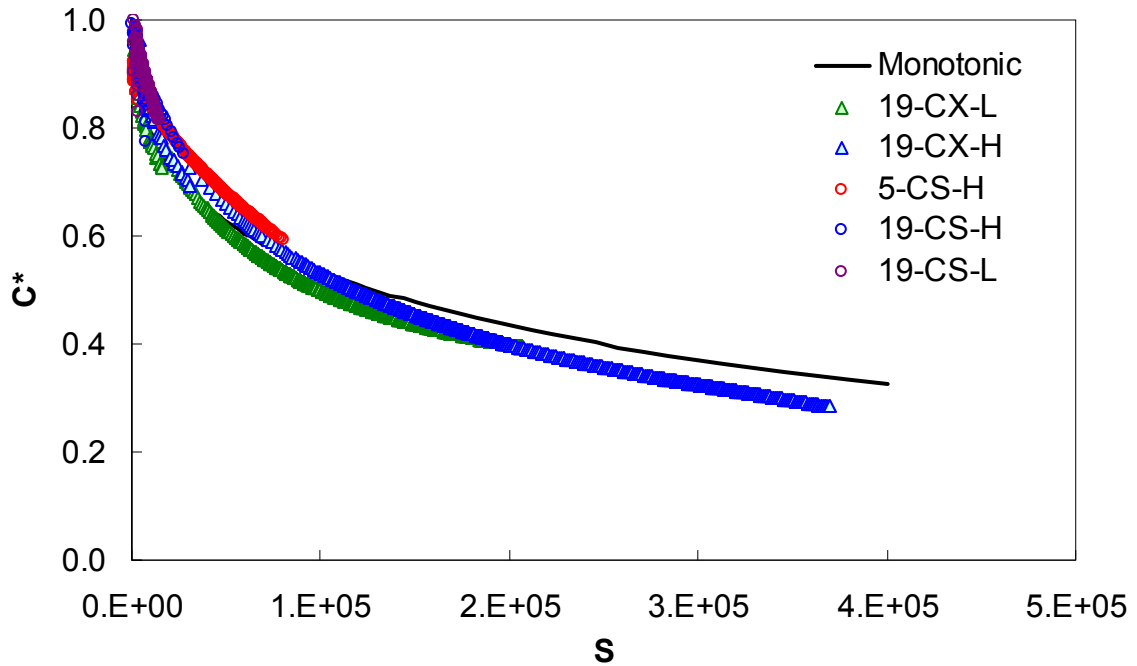


Figure 83. Graph. Damage characteristic comparison, cyclic to monotonic using refined simplified model Terpolymer mixture.

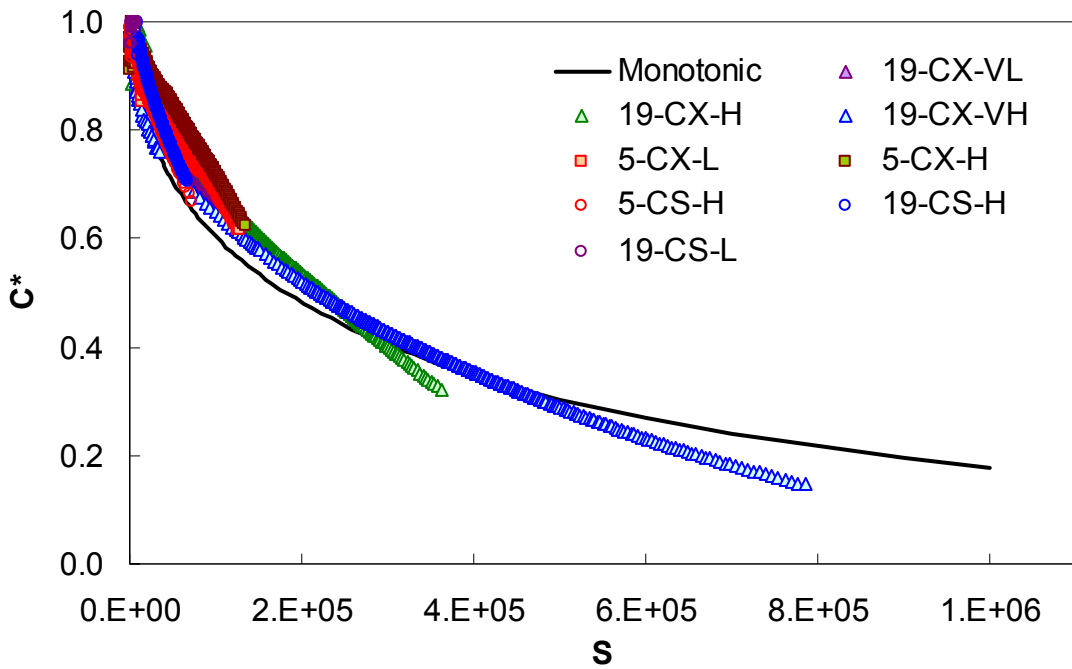


Figure 84. Graph. Damage characteristic comparison, cyclic to monotonic using refined simplified model 9.5-mm Fine mixture.

Table 15. Cyclic tests performed for 9.5-mm Fine mixture

Material	Test Type	Test Designation	Level (kPa / $\mu\epsilon$)	Freq. (Hz)	Temp. ($^{\circ}\text{C}$)	N_f
9.5 Fine	CS	5-CS-H	1,500/115	10	5	5,900
	CS	5-CS-L	750/40	10	5	29,6450
	CS	19-CS-H	750/108	10	19	2,950
	CS	19-CS-L	250/35	10	19	105,480
	CX	19-CX-H	—/240	10	19	46,389
	CX	19-CX-VL	—/190	10	19	311,170
	CX	19-CX-VH	—/402	10	19	2,670
	CX	5-CX-H	—/150	10	5	70,140
	CX	5-CX-L	—/126	10	5	145,410

— Initial stress level in CXH tests is not reported.

4.10. SUMMARY

Various interpretations of the work potential/pseudo strain class of continuum damage models have been explored, and a final refined version is suggested. The two methods shown in this report represented a simplification of a more rigorous theory so that it can be easily and accurately applied to cyclic fatigue testing and characterized using cyclic fatigue tests that are performed in the AMPT. The final suggested version is also further simplified so that it can be implemented as a software solution. The earlier versions of this model contained certain shortcomings in the rigor of their derivations. The rigorously accurate VECD model has been used to gain understanding of, and improve upon, these earlier models. The resulting refined formulation unified the results of CS, CX, and monotonic testing and supported earlier findings that the damage characteristic curve was a material property independent of temperature and test type. In addition, this model allowed rapid characterization and/or prediction of the material fatigue response. Coupled with either a structural model or a predictive scheme similar to that used in the NCHRP 1-37A *Mechanistic Empirical Pavement Design Guide*, this model could also be used to predict the fatigue response of asphalt concrete pavements.⁽⁵⁹⁾ This topic is the subject to ongoing efforts by the research team.

CHAPTER 5. MVEPCD CHARACTERIZATION AND VERIFICATION IN COMPRESSION

The permanent deformation in HMA is affected by several mixture factors, such as the resistance of the binder to flow, aggregate angularity and gradation, the amount of asphalt, the air void content, etc. A significant amount of research has been conducted to develop laboratory test methods, analysis techniques, and models to study the permanent deformation growth of HMA. The nature of the permanent deformation models available in the literature ranges from empirical to mechanistic-empirical to completely mechanistic. Further attempts have been made in recent years to develop a mechanistic permanent deformation model that involves fundamental material characterization.^(20,52,53)

The objective of this research was to develop a constitutive model of HMA in compression that could predict HMA behavior under loading conditions and temperatures encountered in the field. The following sections present theories used in the modeling, the experimental program, the characterization process, and predictions for various loading histories. For this effort only, the ALF Control mixture has been used, and it should be understood that all figures in this chapter are related to this mixture.

5.1. ENGINEERING BEHAVIOR OF ASPHALT CONCRETE IN COMPRESSION

5.1.1. Constant Rate Compression

Figure 85 and figure 86 show the rate-dependent stress-strain curves of HMA at the confining pressures of 0 and 500 kPa, respectively. As observed from figure 85 and figure 86, the gross trends in stress-strain curves with 500 kPa confinement were quite similar to those with 0 kPa confining pressure; the overall strength of the material decreased with increasing temperature and with decreasing strain rates. Directly comparing the curves at different temperatures (figure 87 through figure 90), it was found that at 5 and 25 °C, the response was not sensitive to confining pressure. The strengths began to deviate during the 40 °C tests and were significantly different at 55 °C, with the confined tests showing higher strengths. This trend was similar to that observed in the confined dynamic modulus tests, which was described for tension-compression loading in subsection 4.2.2 and for compression loading in section 5.2. This finding suggests that when the material was very stiff, the effects of confinement were negligible.

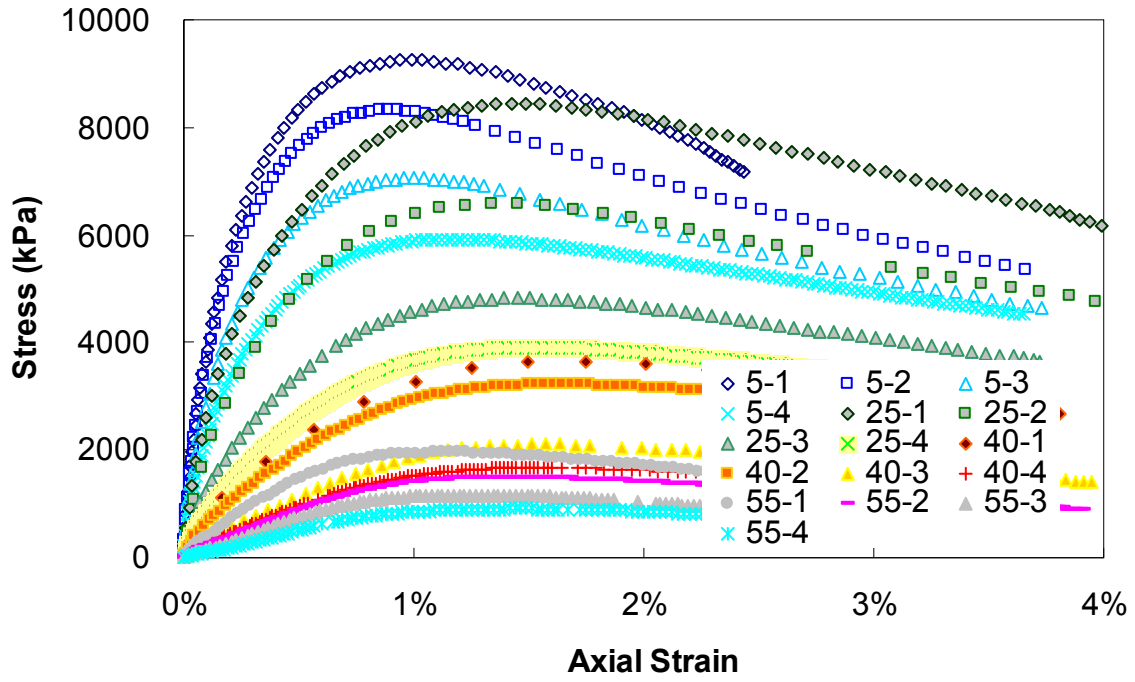


Figure 85. Graph. Stress-strain curves for unconfined constant strain-rate tests.

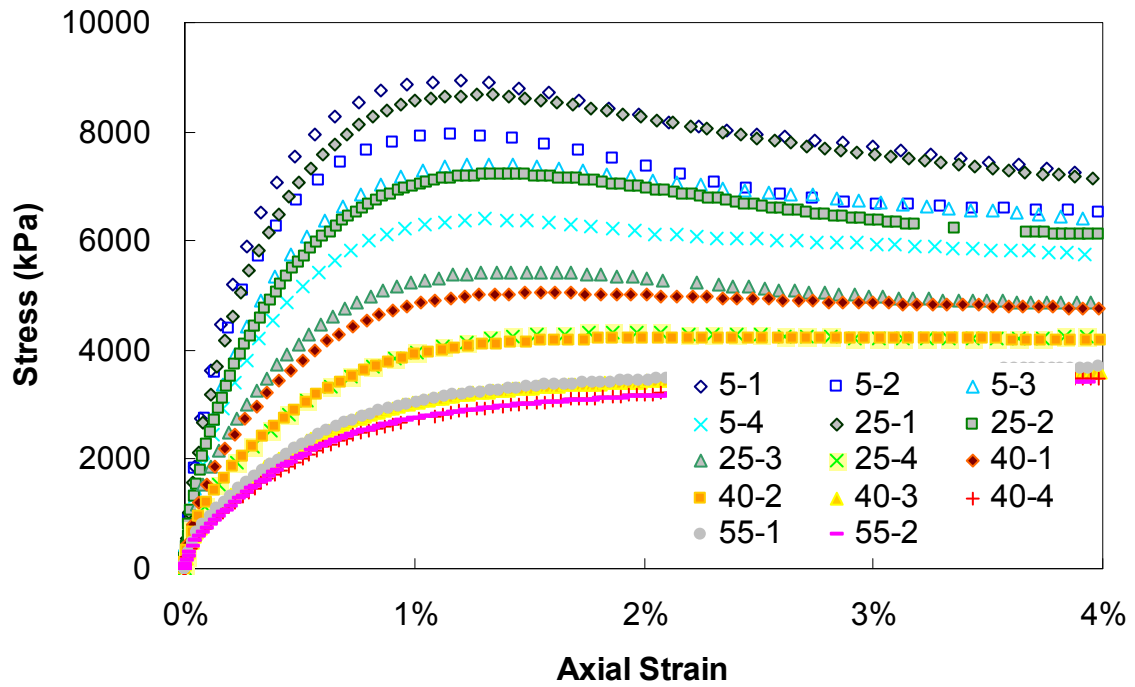


Figure 86. Graph. Stress-strain curves for 500 kPa confinement constant strain-rate tests.

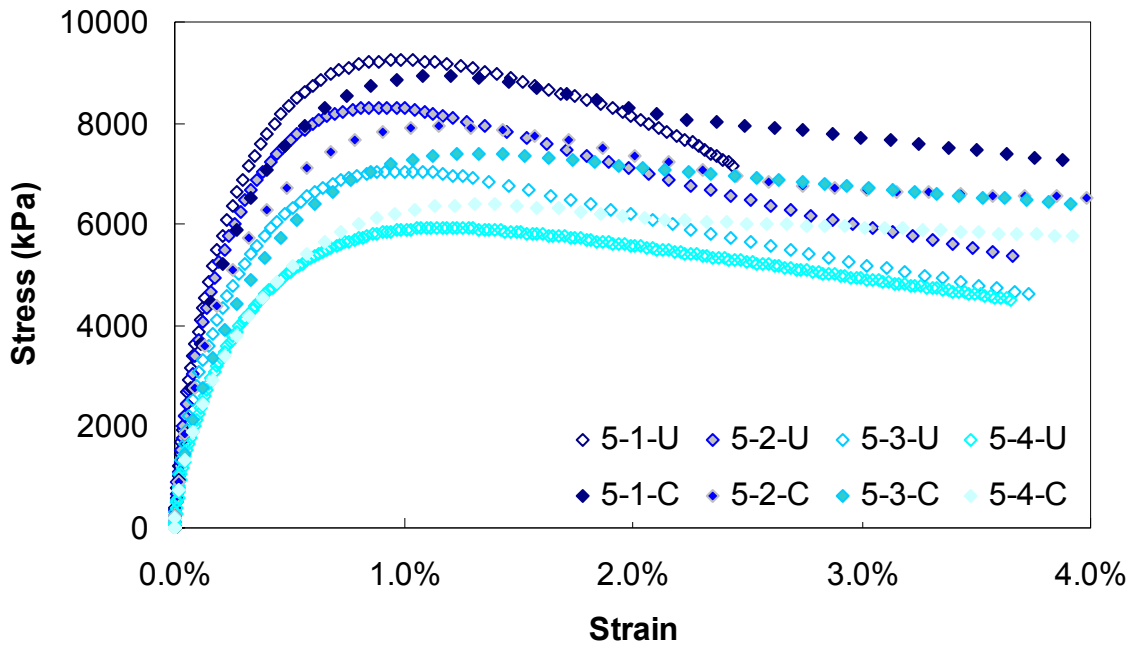


Figure 87. Graph. Comparison of 500 kPa confinement and unconfined constant rate tests for 5 °C.

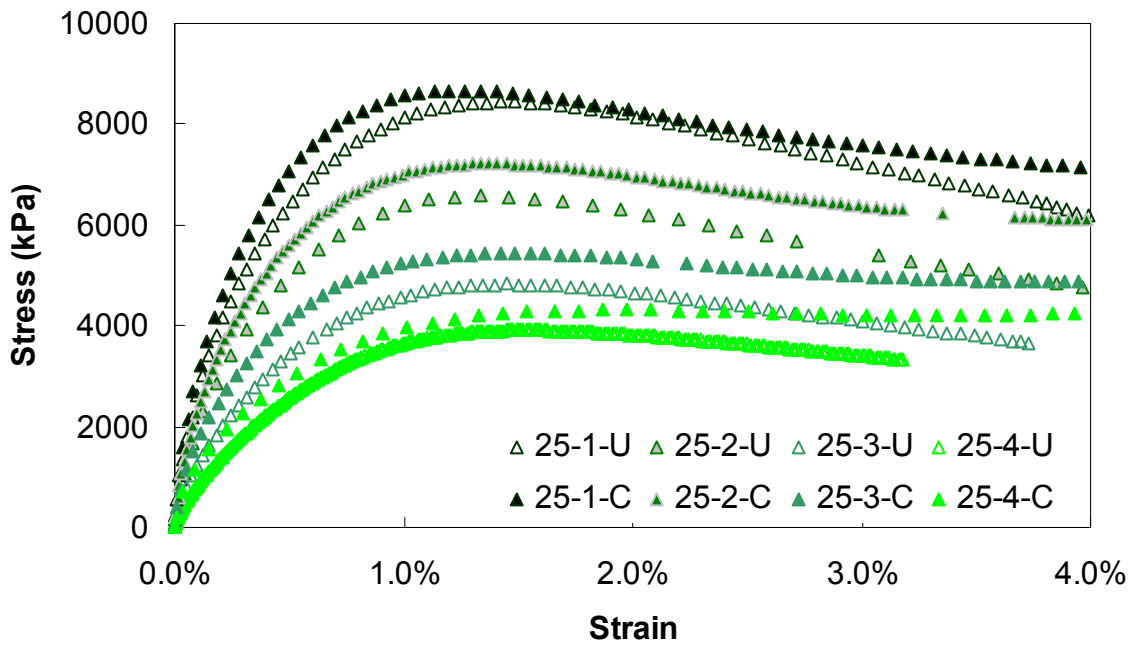


Figure 88. Graph. Comparison of 500 kPa confinement and unconfined constant rate tests for 25 °C.

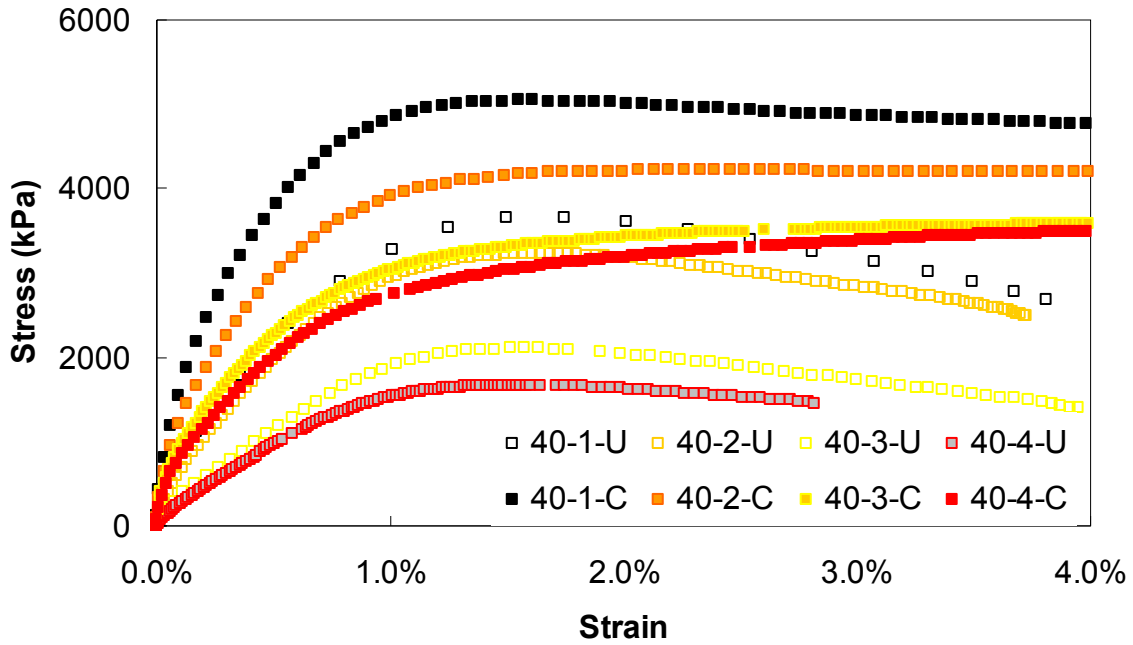


Figure 89. Graph. Comparison of 500 kPa confinement and unconfined constant rate tests for 40 °C.

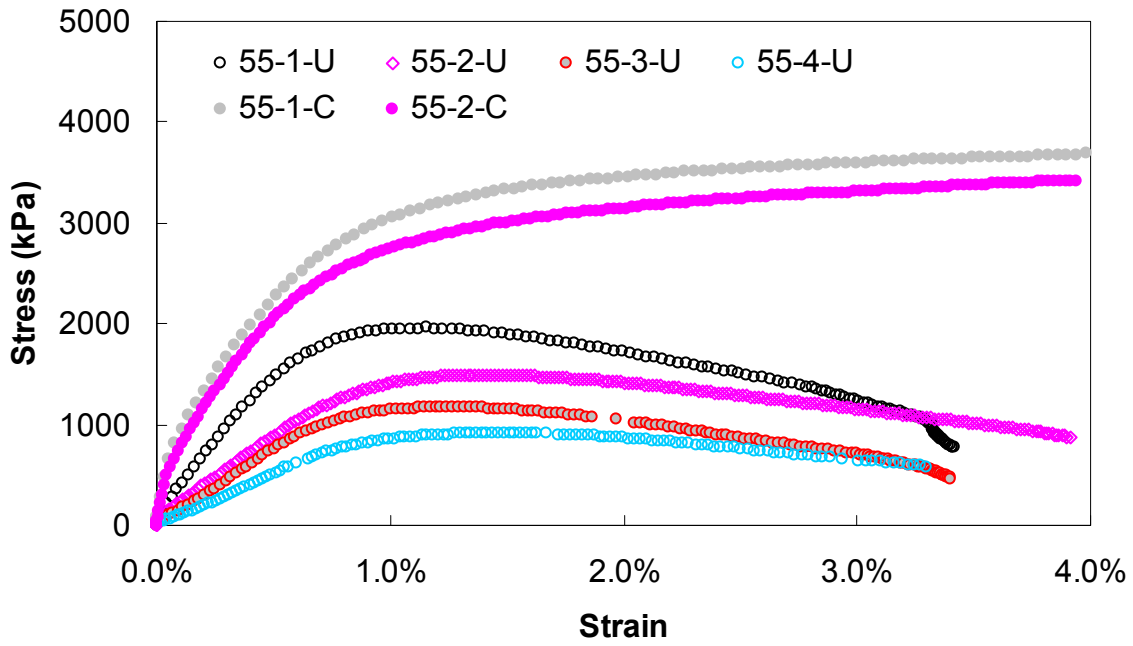


Figure 90. Graph. Comparison of 500 kPa confinement and unconfined constant rate tests for 55 °C.

5.1.2. Repetitive Creep and Recovery Test

5.1.2.1. Creep and Recovery Test with VL

Figure 91 through figure 93 present the viscoplastic strains for the given VL stress histories. The viscoplastic strains caused by the first loading in each group, except for the first loading group, were close to zero or were at least very small because the deviatoric stress that caused the viscoplastic strains was quite small compared to that of previous loadings.

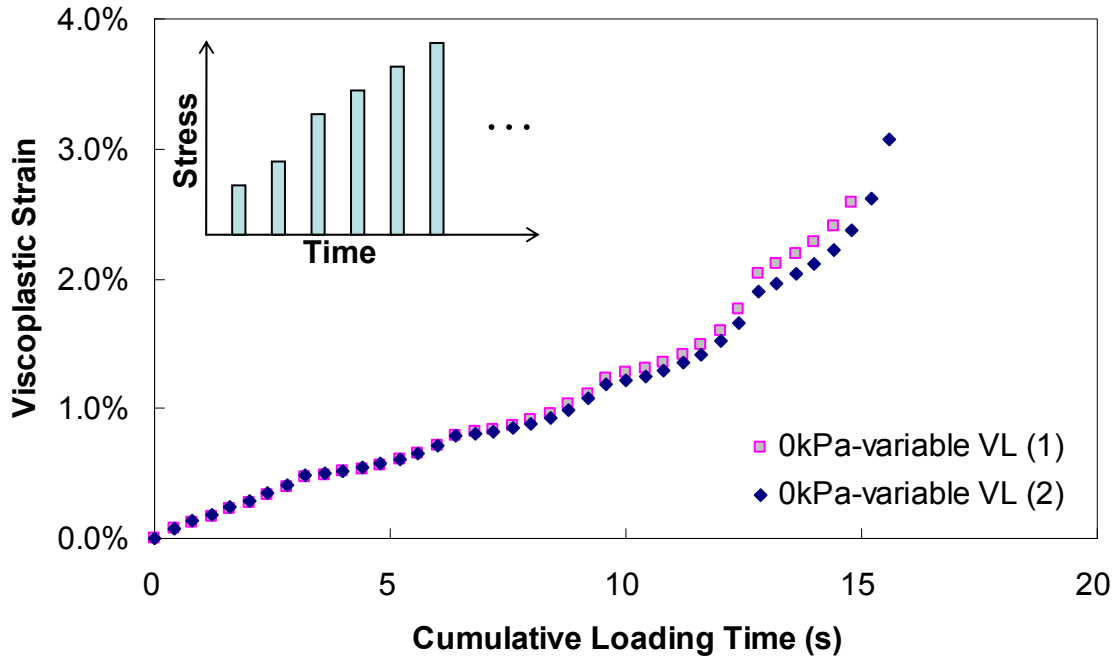


Figure 91. Graph. Viscoplastic strain versus cumulative loading time (unconfined VL).

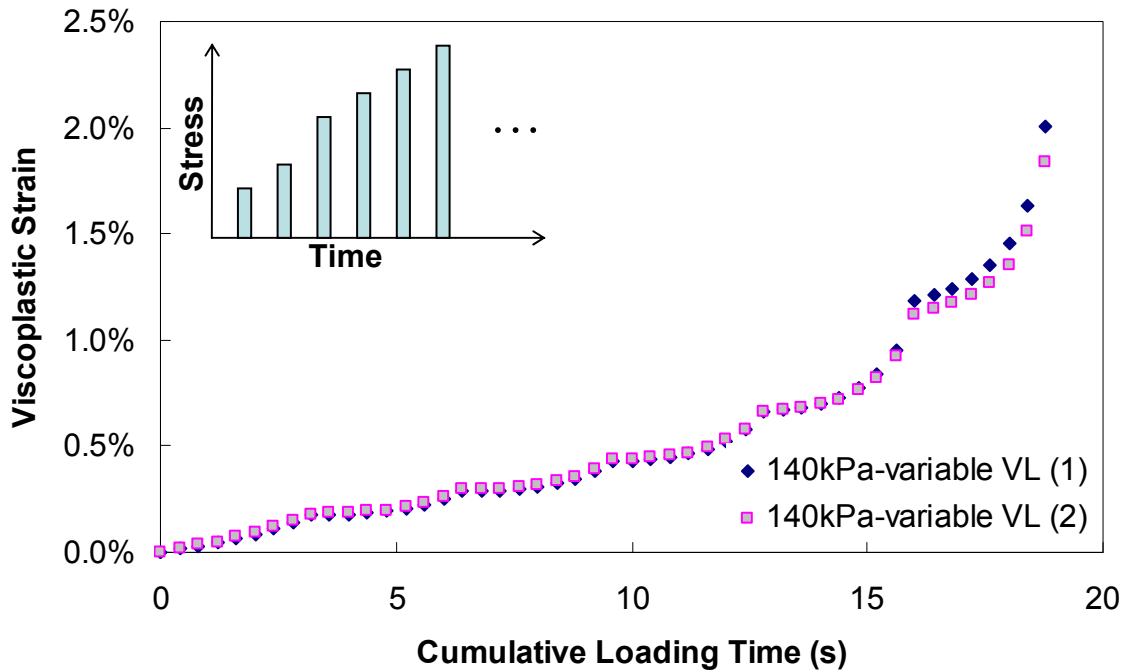


Figure 92. Graph. Viscoplastic strain versus cumulative loading time (140 kPa confinement VL).

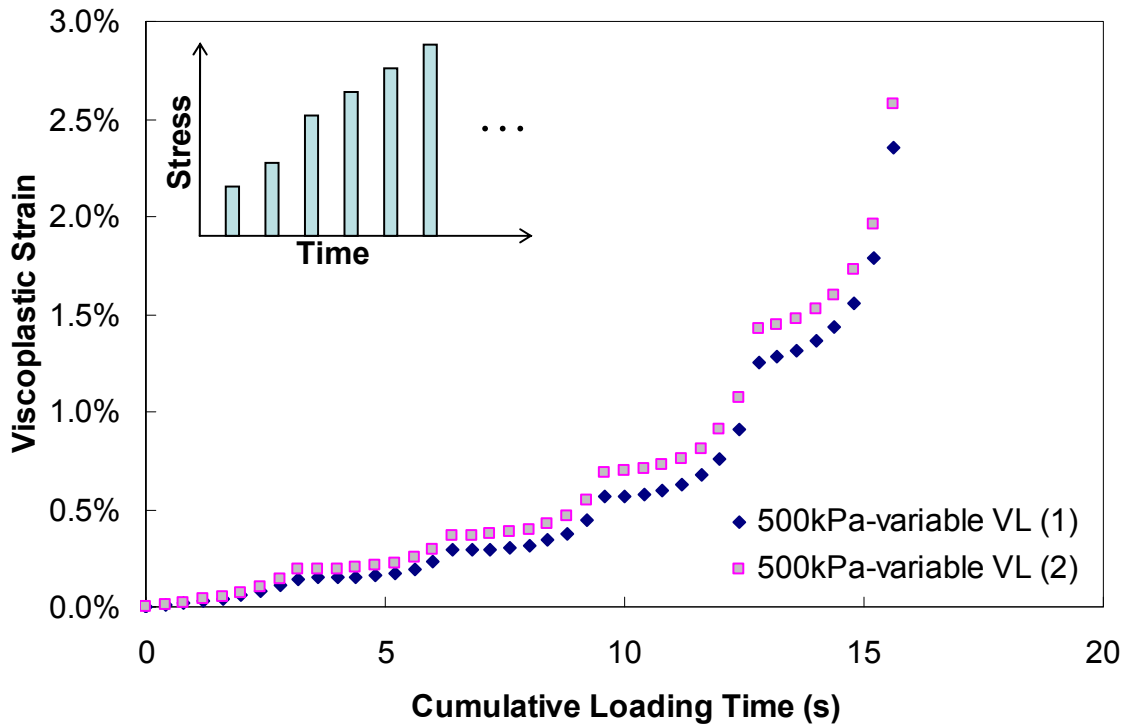


Figure 93. Graph. Viscoplastic strain versus cumulative loading time (500 kPa confinement VL).

5.1.2.2. Creep and Recovery Tests with VT and RVT

Figure 94 and figure 95 present the viscoplastic strains measured at the end of each rest period in unconfined VT and 500 kPa confinement VT, respectively. In both unconfined and confined VT testing, the overall reproducibility was sufficiently adequate to identify the effects of load level and loading sequence. In RVT testing, less viscoplastic strain was observed than in VT testing despite the fact that the test conditions were the same for both tests, with the exception of the sequence of loading, as described previously. This difference in viscoplastic strain indicated that the sequence of loading plays an important role in viscoplastic strain development. In addition, a change of slope between the two groups of viscoplastic strain, which could not be explained by the concepts inherent of the conventional viscoplastic model, was observed. It seems the characteristic behavior of HMA was affected by viscoelastic relaxation.

Although quantifying the variations in the viscoplastic strain rate under a given loading condition is necessary for rigorous modeling work, no test protocol was available that could capture only the viscoplastic strain rate because HMA showed time-dependent viscoelastic strain, too. However, trends for viscoplastic strain rates developed in repetitive creep and recovery testing could be estimated by analyzing the VT test results. Figure 96 presents incremental viscoplastic strain rates (i.e., incremental viscoplastic strain divided by pulse time). As shown in figure 96, at 1-percent viscoplastic strain, viscoplastic strain rates from 0.05-s loadings (2.0×10^{-3}) were much greater than those from 6.4-s loadings (8.0×10^{-5}). These results indicated that most of the viscoplastic strain developed at the beginning of the loading period and that the viscoplastic strain that developed during the remainder of the loading period (i.e., at 6.4 to 0.05 s) was relatively small. Because the calculated viscoplastic strain rate was the average of the viscoplastic strain rates during loading, the actual viscoplastic strain rates at the end of the loading were much smaller than 8.0×10^{-5} . This is another important behavior of HMA, along with the softening concept presented in the following section. Mathematically, this behavior can be formulated in a viscoplastic constitutive model with either increasing viscosity or increasing yield stress due to aggregate interlocking.

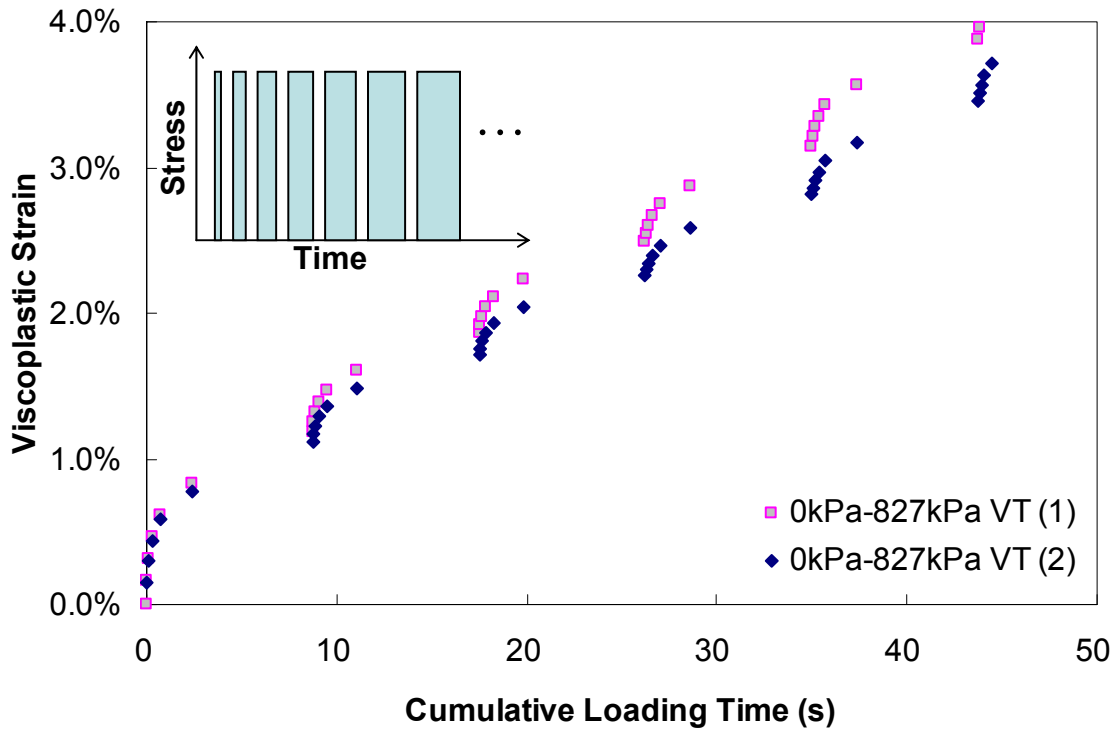


Figure 94. Graph. Viscoplastic strain versus cumulative loading time (unconfined VT testing).

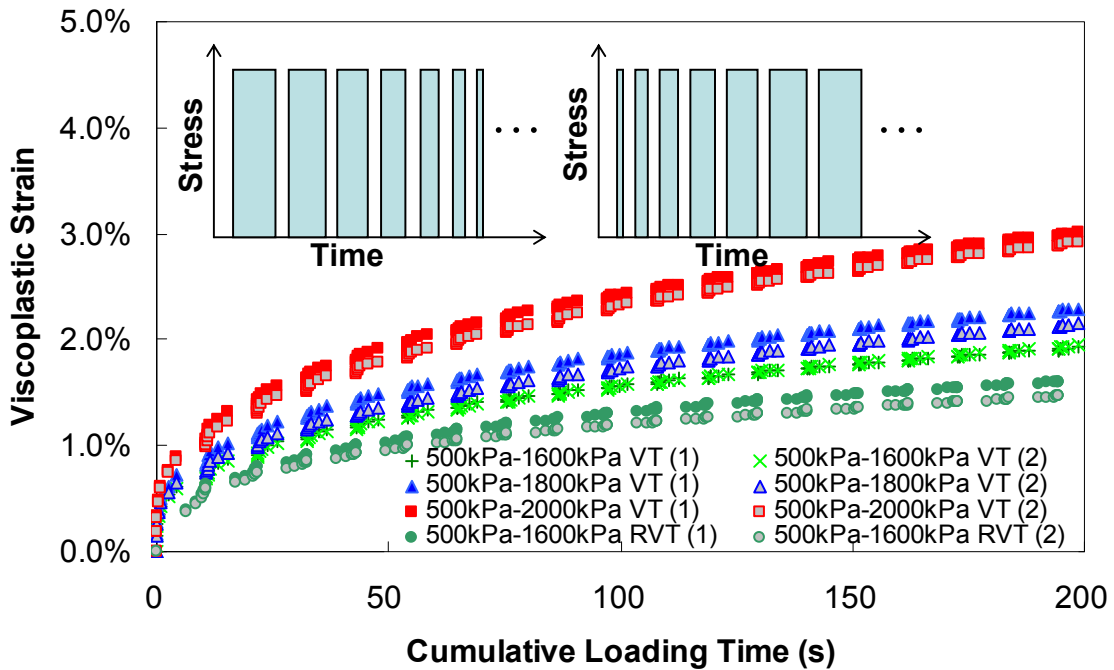


Figure 95. Graph. Viscoplastic strain versus cumulative loading time (500 kPa confinement for VT and RVT testing).

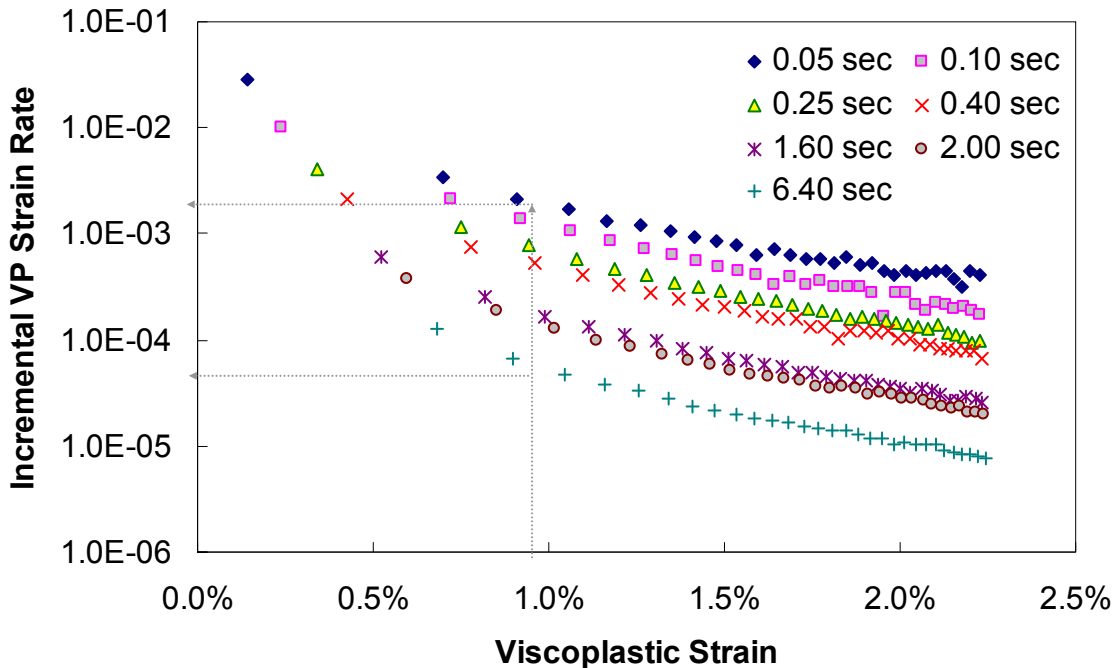


Figure 96. Graph. Incremental viscoplastic strain rate versus viscoplastic strain (500 kPa confinement, 1,600 kPa deviatoric).

5.1.2.3. Creep and Recovery Tests with Constant Load Level and CLT

Figure 97 presents the viscoplastic strain history for each loading condition with a confining pressure of 500 kPa. A smaller viscoplastic strain was observed as the pulse time increased. Even considering the ramp time of 0.005 s, which was not taken into account in the cumulative loading time, the difference in the viscoplastic strains was quite significant.

As shown in figure 97, more viscoplastic strain was observed in the CLT tests that consisted of shorter loading times at a given cumulative loading time. The differences were significant. For example, at 150 s of cumulative loading time, the viscoplastic strain in 1,800 kPa CLT testing with a 0.4-s loading time was over 3 percent, whereas it was around 1.5 percent in 1,800 kPa CLT testing with a 6.4-s loading time and was 2.2 percent with a 1.6-s loading time. One reason for this behavior could be related to the dynamic effects associated with the ramp to the target load because one difference in the tests, as they are presented in figure 97, is the number of load applications. Alternatively, because the tests are exposed to different total rest times at given cumulative loading times, the differences could be related to material softening. Furthermore, it is not beyond reason to suppose that this softening behavior could be rate dependent. For further study of this issue, two additional VT tests with 0.1- and 0.05-s rest periods were performed at a confining pressure of 140 kPa. These test results were compared with the results from VT testing with 200 s of rest. In these tests, the conditions were identical (i.e., the number of loadings and rest periods were the same for each), except for the length of the rest period. Figure 98 presents the viscoplastic strains measured at the end of the rest periods. For VT tests with 0.05 and 0.1 s of rest, 200 s of rest was allowed at the end of the testing to measure the pure viscoplastic strain because it was not possible to measure pure viscoplastic strain immediately after 0.05 or 0.1 s of rest. The deviatoric stresses were 827 and 552 kPa, and the confining pressure was 140 kPa.

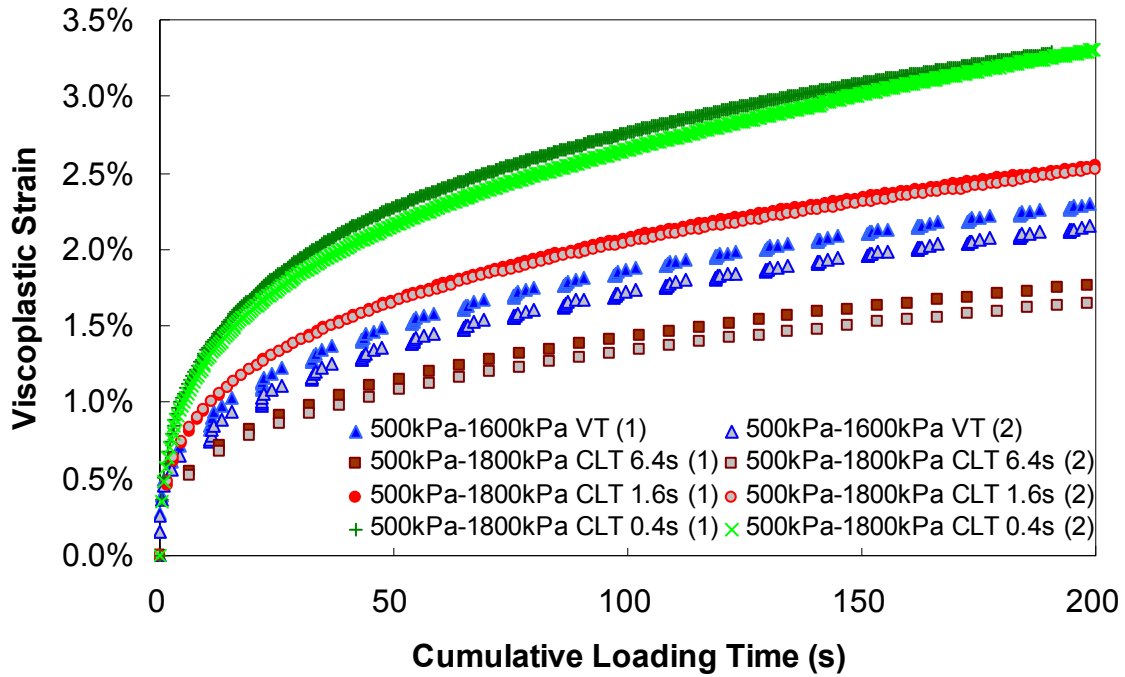


Figure 97. Graph. Viscoplastic strain versus cumulative loading time (500 kPa confinement CLT).

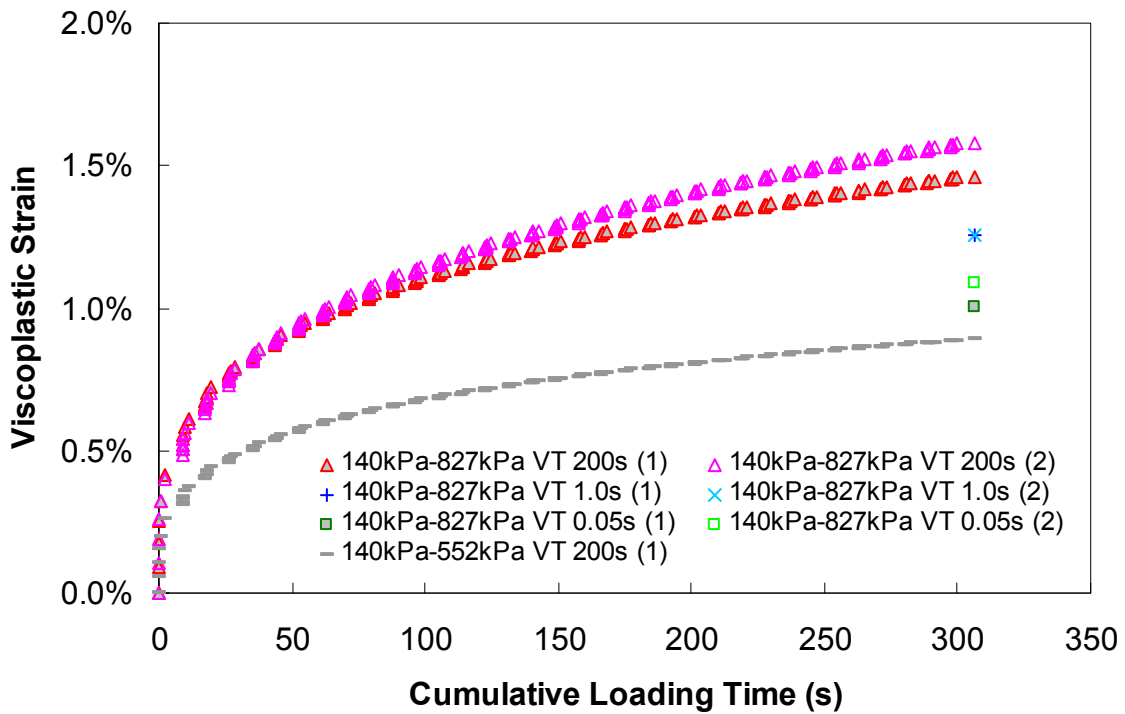


Figure 98. Graph. Viscoplastic strain versus cumulative loading time (140 kPa confinement VT).

As seen in figure 98, even though the loading histories were identical except for the length of the rest period, a smaller viscoplastic strain developed as the rest period became shorter. Furthermore, the effect of the rest period on viscoplastic development was significant considering the amount of viscoplastic strain when using 552 kPa deviatoric stress and 200 s of rest. This experimental observation did not demonstrate the effects of the dynamic loading ramp, but it did demonstrate the significant effect of rate-dependent softening during unloading. Therefore, the modeling effort focused on developing a viscoplastic model that accounted for rate-dependent hardening and/or softening.

5.1.3. t-TS with Growing Damage in Compression

The principle of t-TS is one of the fundamental and most important concepts for HMA in tension modeling because it provides a strong mechanical background and significantly reduces the experimental efforts. In order to verify the principle for the compression stress state, stress characteristic curves were constructed from constant strain-rate test results by utilizing shift factors determined from the dynamic modulus tests. Further verification was also performed using repetitive creep and recovery tests.

For the verification of the principle for monotonic loading, a wide range of eight reference-strain values were chosen according to the results of both the uniaxial and triaxial compressive constant strain-rate tests (figure 85 and figure 86). According to the procedure shown schematically in figure 55 through figure 57 and discussed in detail elsewhere, the stress and time values were determined for all of these tests at fixed strain levels.^(13,20) These plots of stress versus time are shown in figure 99 through figure 114. Then, shift factors obtained from small-strain LVE testing were applied to determine the reduced time that corresponded to each physical time. If the t-TS principle was valid with growing damage, the resulting plots of stress and reduced time would appear continuous at all strain levels. This behavior was indeed observed for the compression tests under both the confined and unconfined conditions (figure 115 and figure 116). These results verified that the t-TS concept held true for mixtures subjected to compressive loading as well as to tensile loading, even if there was severe damage and viscoplastic strain. However, to verify that the principle held for the physical mechanisms behind the behavior of repetitive creep and recovery tests, more rigorous verification was needed—this verification compared VT test results at 40 and 55 °C with the same reduced time histories.

For this verification, VT testing was first performed at 55 °C (the 200 s rest period results are used here). Next, the time history was used with the t-TS shift factors to compute the equivalent reduced time history at 40 °C. However, because the testing time was estimated to take several days (the equivalent time to 200 s at 55 °C is approximately 3,265 s at 40 °C), the following analysis was performed to finish the VT testing within a reasonable time. In this analysis, the measured strain history during the unloading portion of several load pulses was used to compute the strain rate, which was plotted against the rest period time in figure 117. To avoid issues related to the initial loading of a test, the 0.05 s data were taken from the second load block, whereas the other pulse times were taken from the first loading block of the VT test. As shown in figure 117, most of the strain rates became quite small after around 40 s, except for the rest periods following the 1.6 and 6.4 s load pulses. For this reason, 40 s was used to compute the reduced time for pulse times less than 1.6 s (653 s at 40 °C); 50 s was used for a pulse time of 1.6 s (816 s at 40 °C); and 60 s was used for a pulse time of 6.4 s (980 s at 40 °C). Note that

strain rates reached an asymptotic value of zero more quickly as the strain level increased, and thus, it was conservative to consider the times used in the first loading block as the reference times. The results of these two tests are shown figure 118. As the figure shows, viscoplastic strains measured at the end of rest periods were well matched to each other. This agreement confirmed that the t-TS principle was applicable regardless of loading sequence and the amount of damage and viscoplastic strain in asphalt concrete.

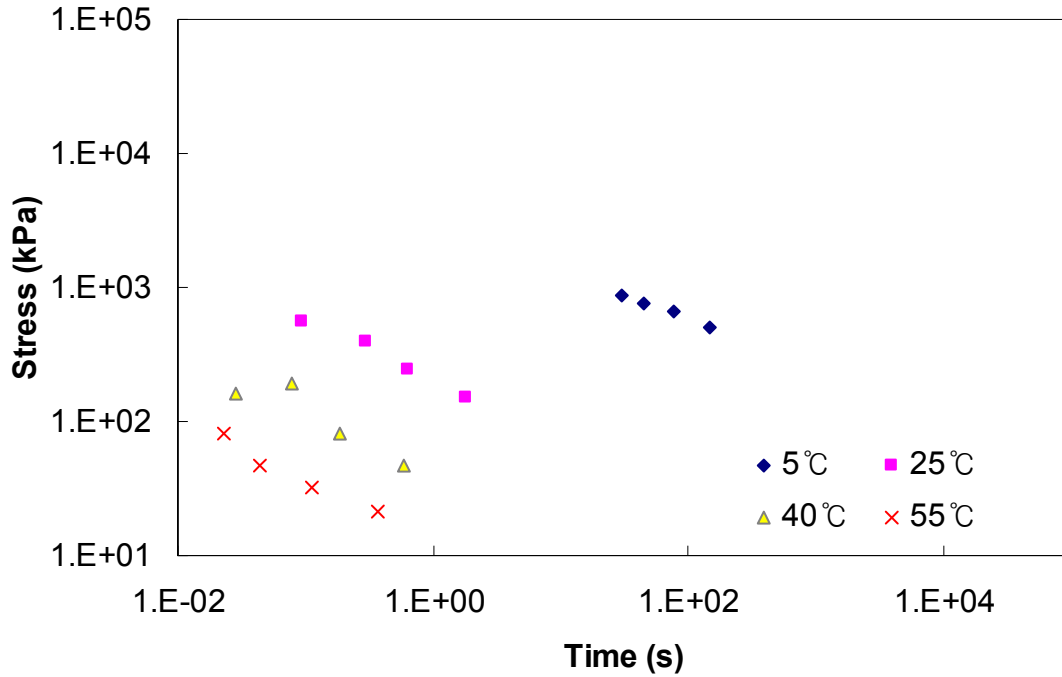


Figure 99. Graph. Stress-time curves for the Control mixture before the application of time-temperature shift factors at a 0.0001 strain level under uniaxial conditions.

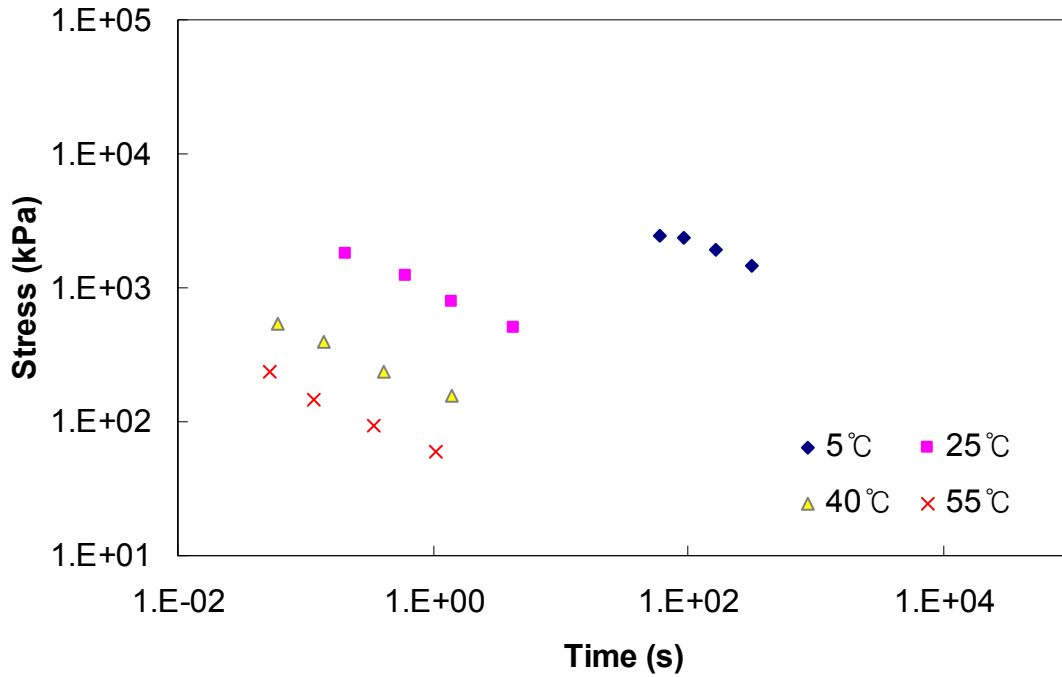


Figure 100. Graph. Stress-time curves for the Control mixture before the application of time-temperature shift factors at a 0.0005 strain level under uniaxial conditions.

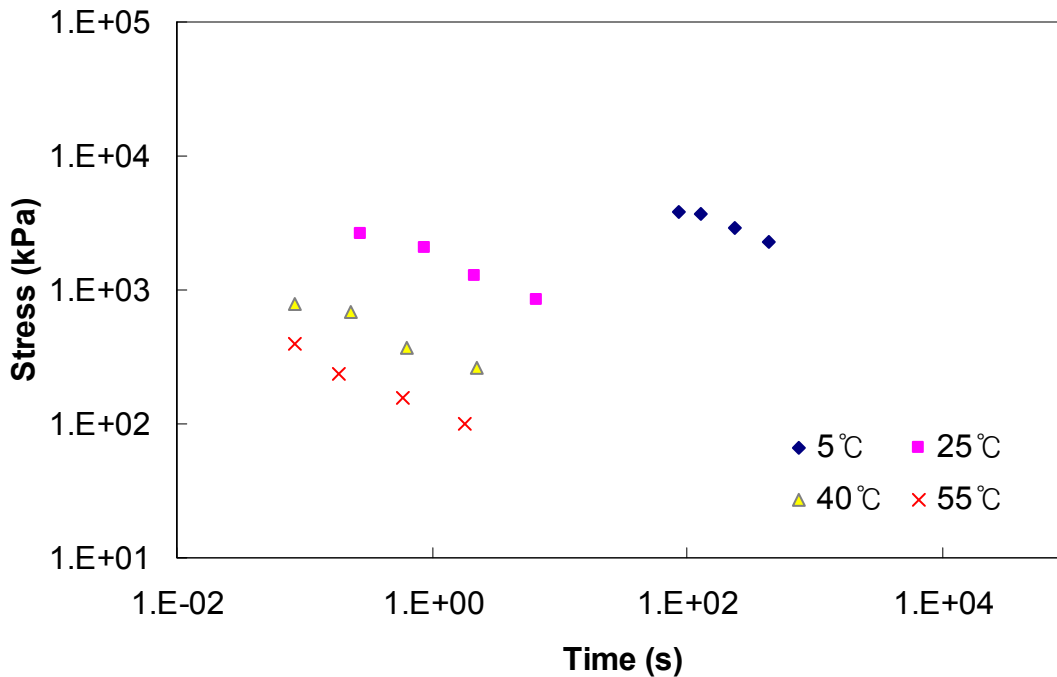


Figure 101. Graph. Stress-time curves for the Control mixture before the application of time-temperature shift factors at a 0.001 strain level under uniaxial conditions.

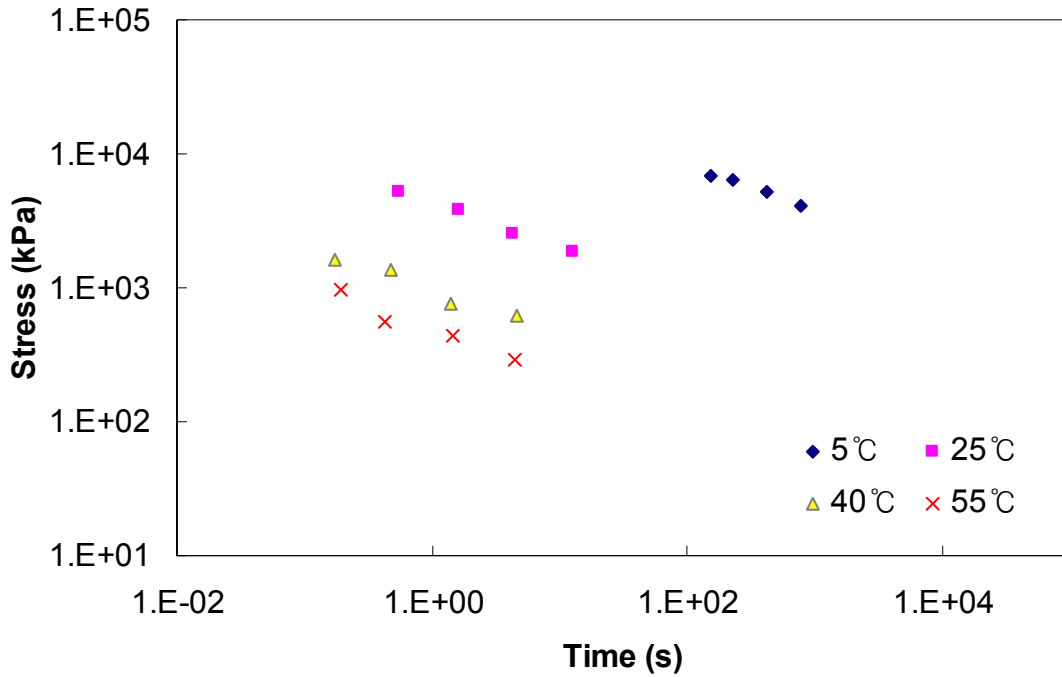


Figure 102. Graph. Stress-time curves for the Control mixture before the application of time-temperature shift factors at a 0.003 strain level under uniaxial conditions.

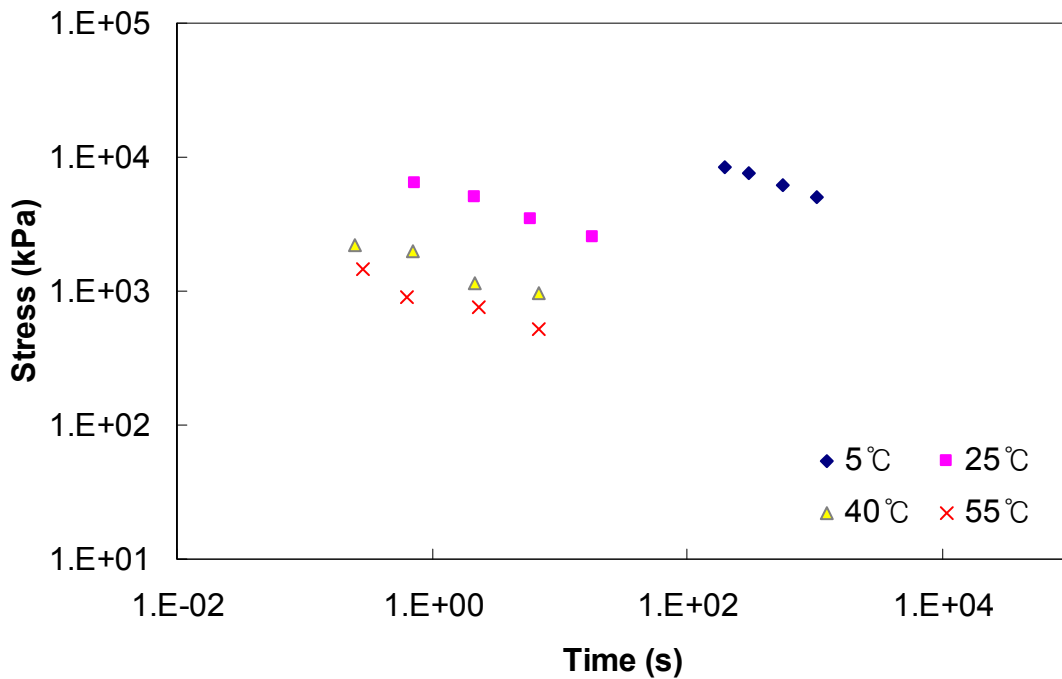


Figure 103. Graph. Stress-time curves for the Control mixture before the application of time-temperature shift factors at a 0.005 strain level under uniaxial conditions.

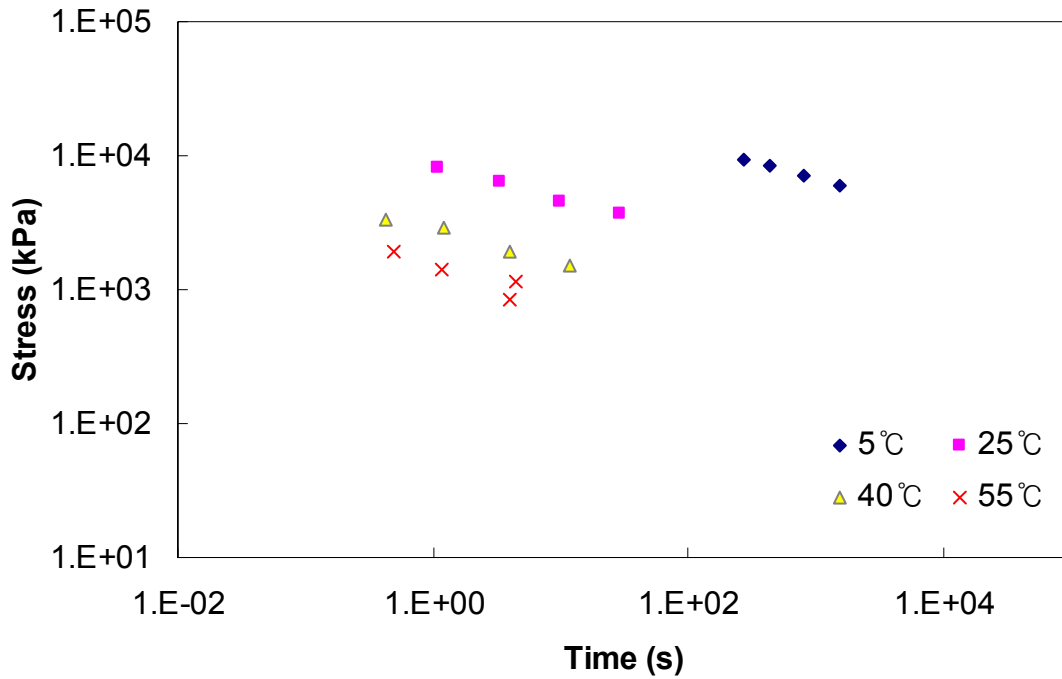


Figure 104. Graph. Stress-time curves for the Control mixture before the application of time-temperature shift factors at a 0.01 strain level under uniaxial conditions.

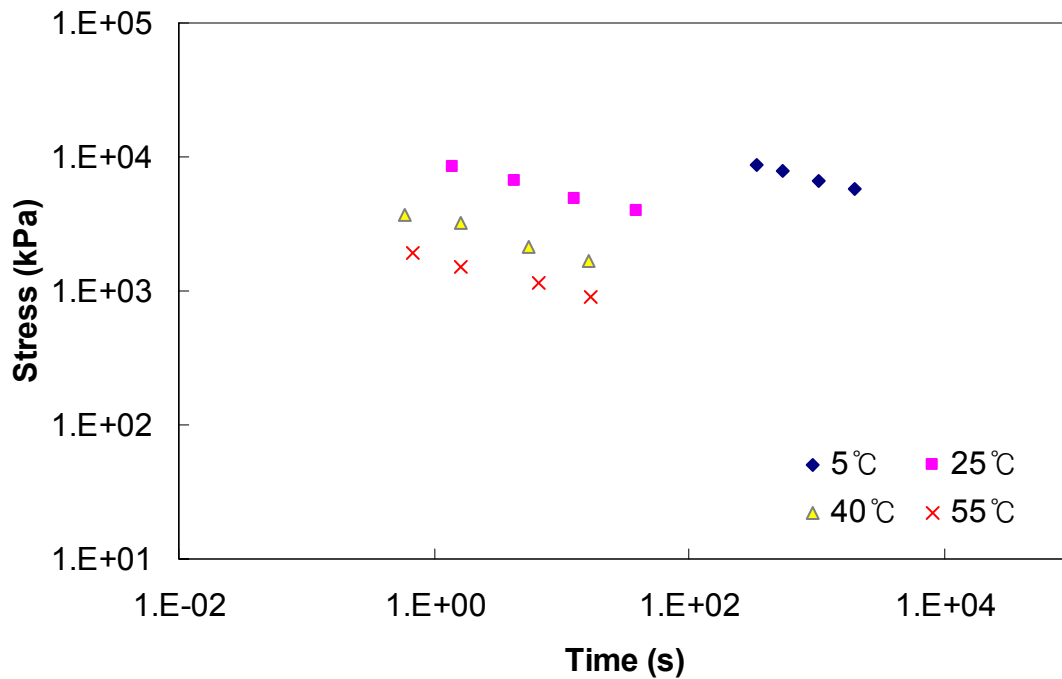


Figure 105. Graph. Stress-time curves for the Control mixture before the application of time-temperature shift factors at a 0.015 strain level under uniaxial conditions.

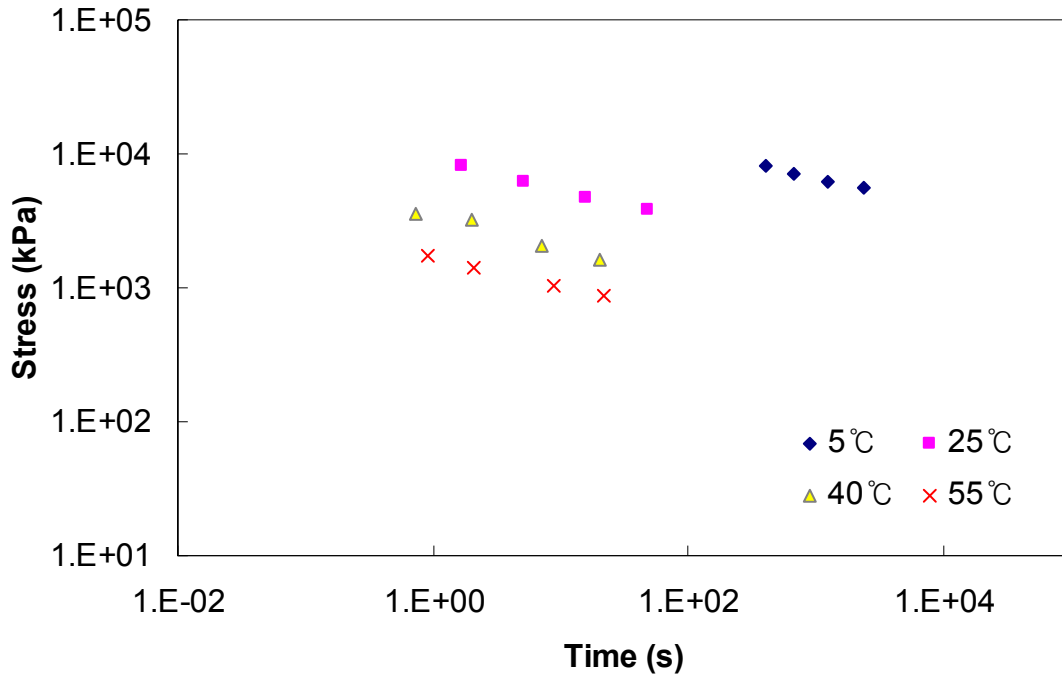


Figure 106. Graph. Stress-time curves for the Control mixture before the application of time-temperature shift factors at a 0.02 strain level under uniaxial conditions.

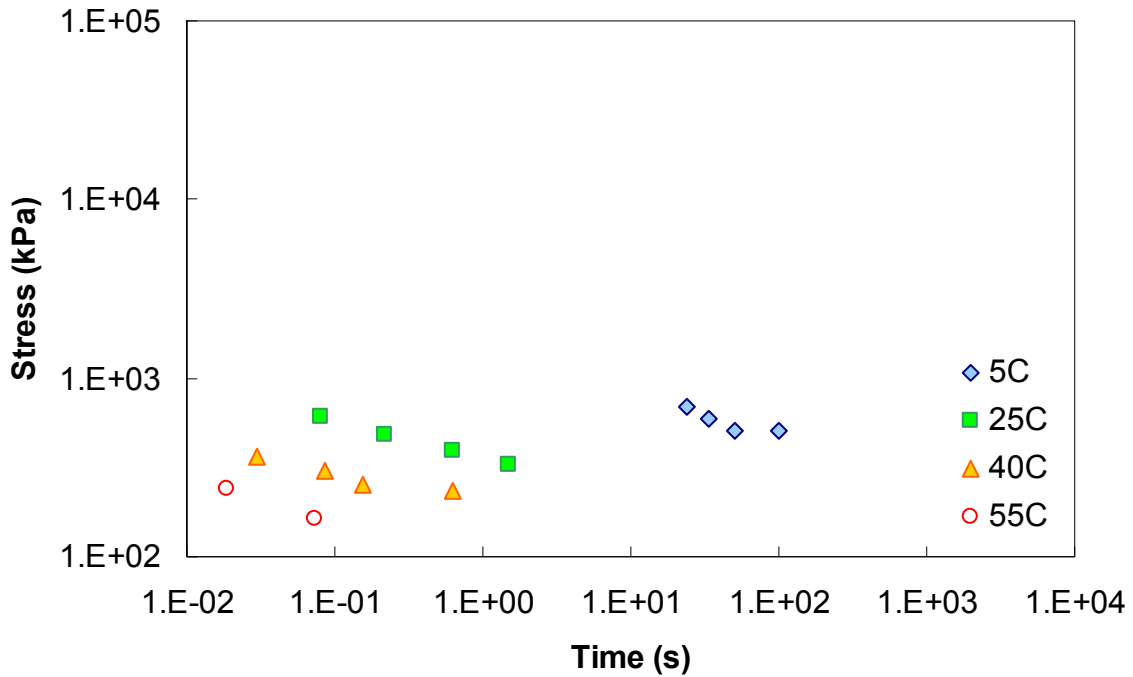


Figure 107. Graph. Stress-time curves for the Control mixture before the application of time-temperature shift factors at a 0.0001 strain level under 500 kPa conditions.

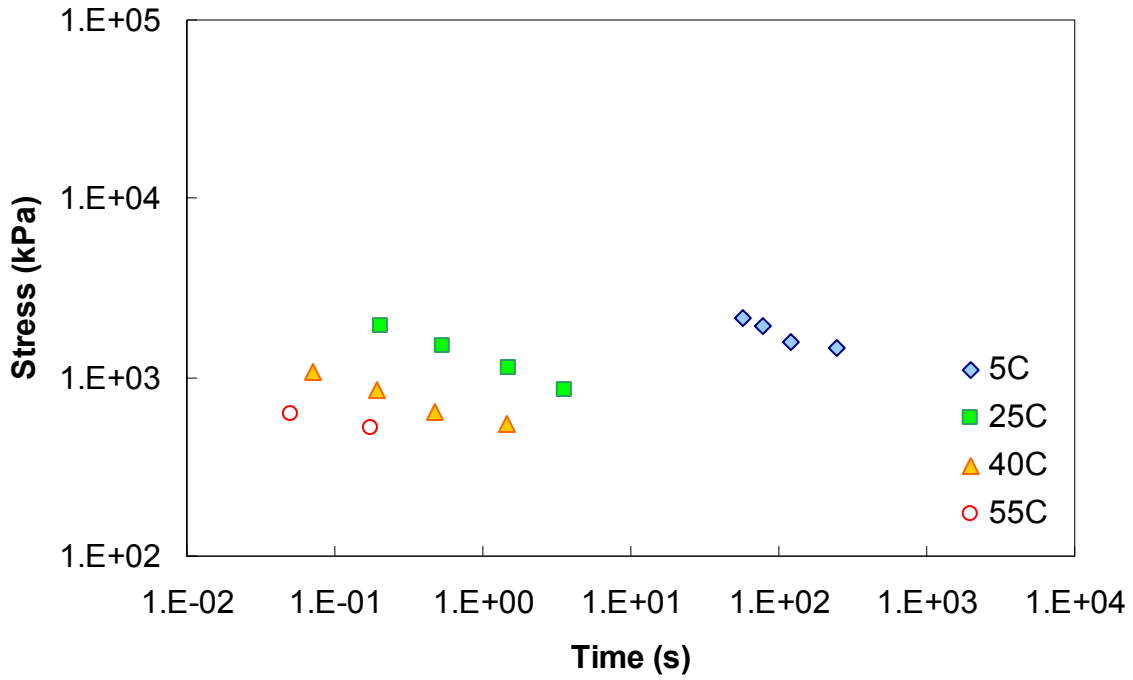


Figure 108. Graph. Stress-time curves for the Control mixture before the application of time-temperature shift factors at a 0.0005 strain level under 500 kPa conditions.

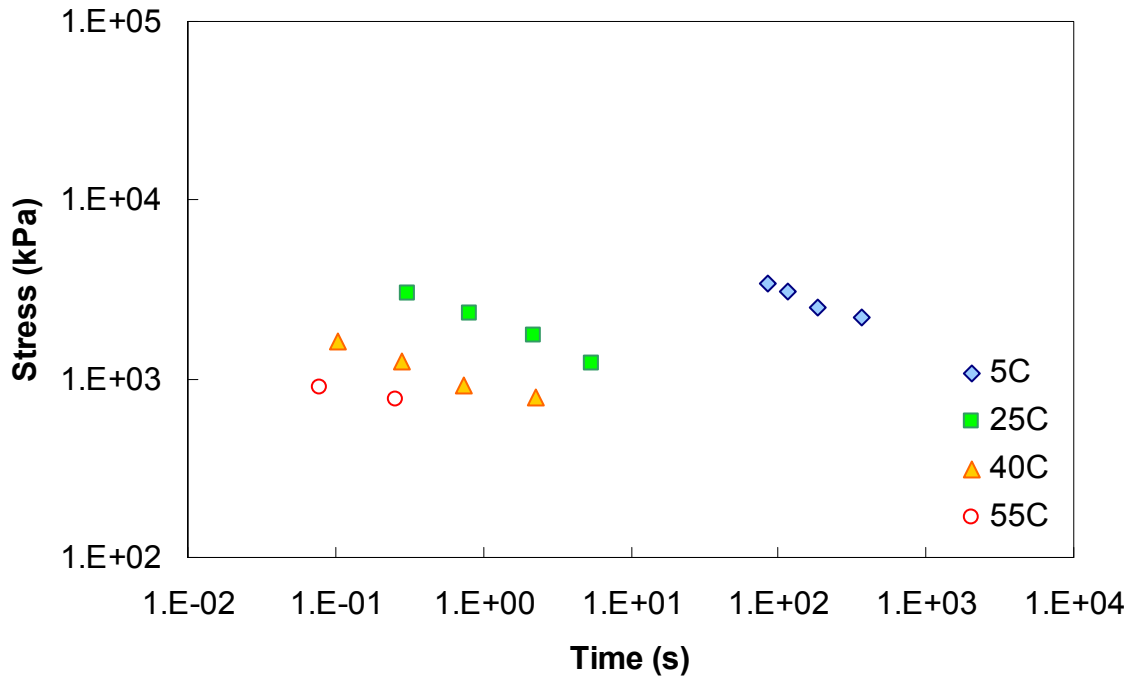


Figure 109. Graph. Stress-time curves for the Control mixture before the application of time-temperature shift factors at a 0.001 strain level under 500 kPa conditions.

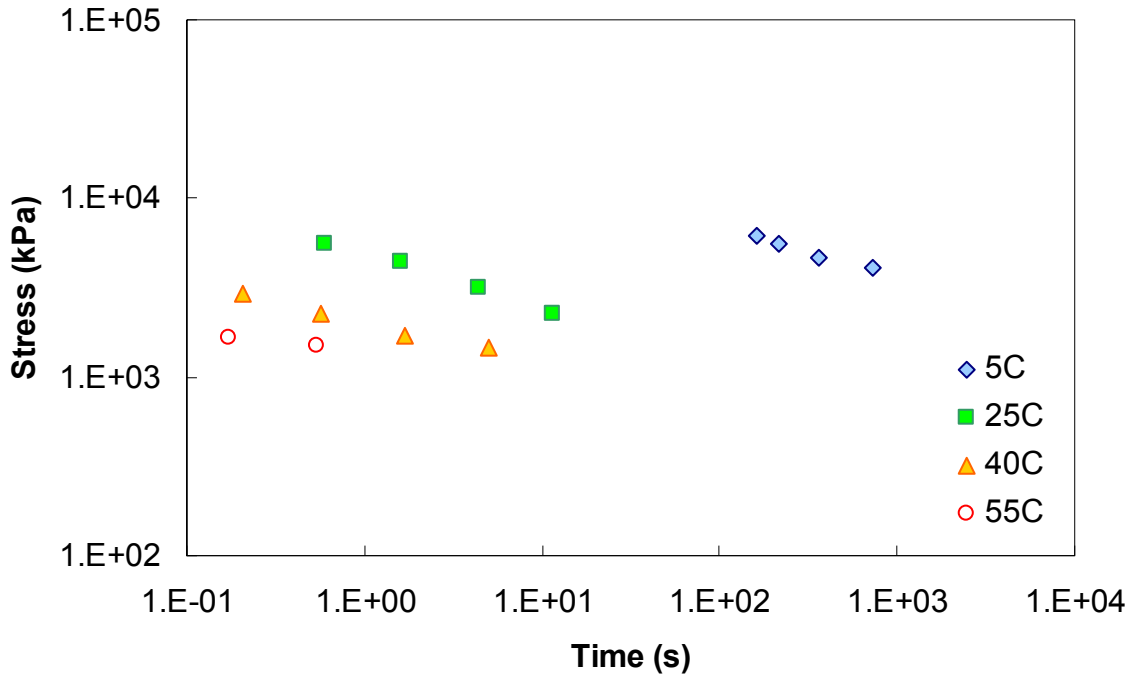


Figure 110. Graph. Stress-time curves for the Control mixture before the application of time-temperature shift factors at a 0.003 strain level under 500 kPa conditions.

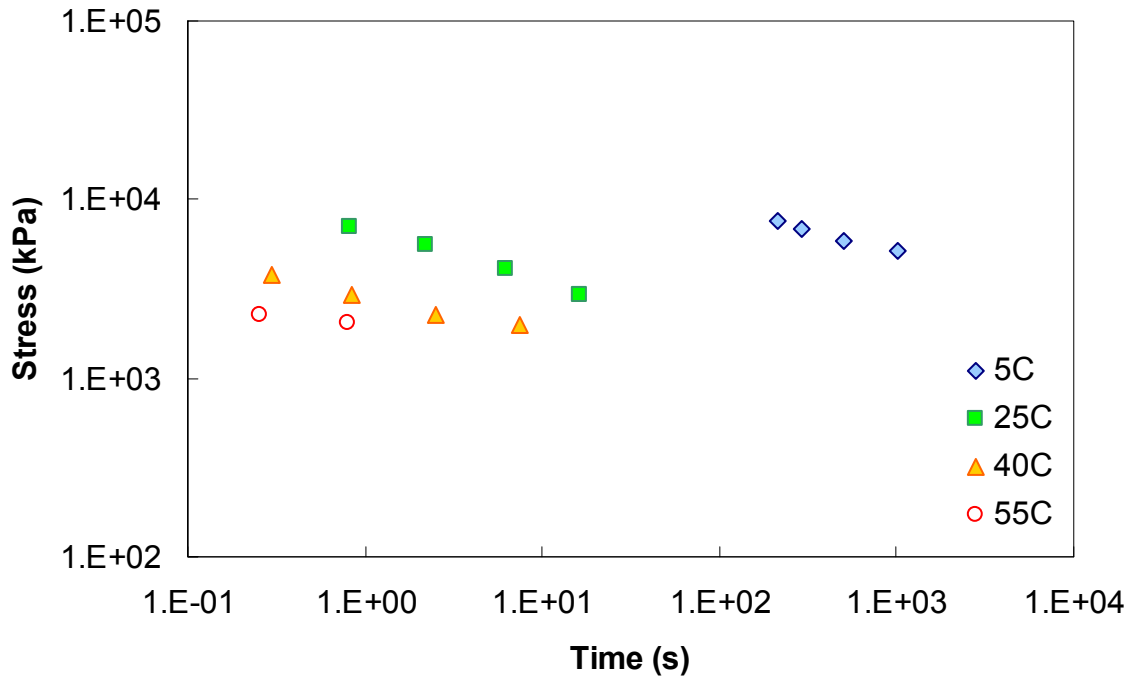


Figure 111. Graph. Stress-time curves for the Control mixture before the application of time-temperature shift factors at a 0.005 strain level under 500 kPa conditions.

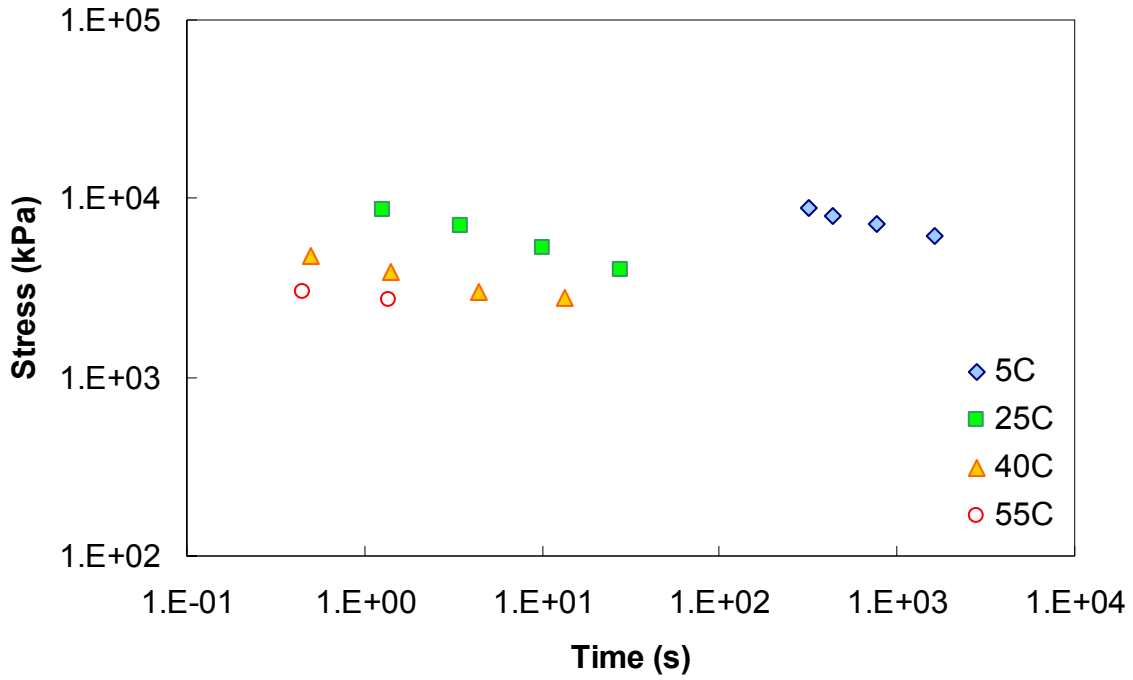


Figure 112. Graph. Stress-time curves for the Control mixture before the application of time-temperature shift factors at a 0.01 strain level under 500 kPa conditions.

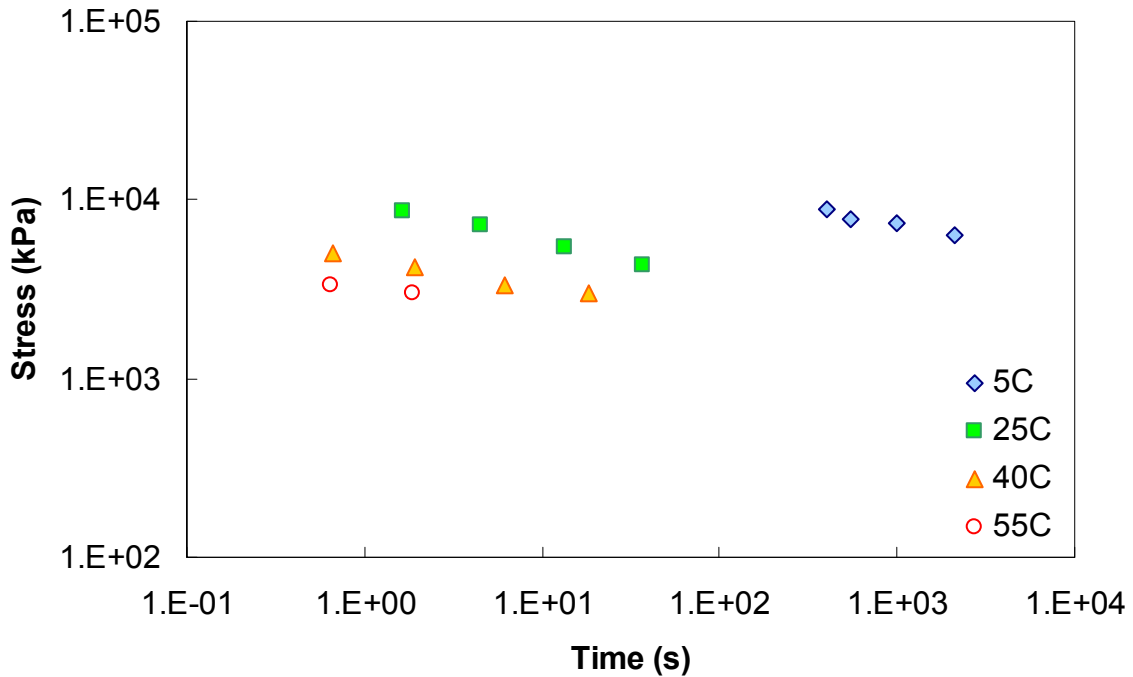


Figure 113. Graph. Stress-time curves for the Control mixture before the application of time-temperature shift factors at a 0.015 strain level under 500 kPa conditions.

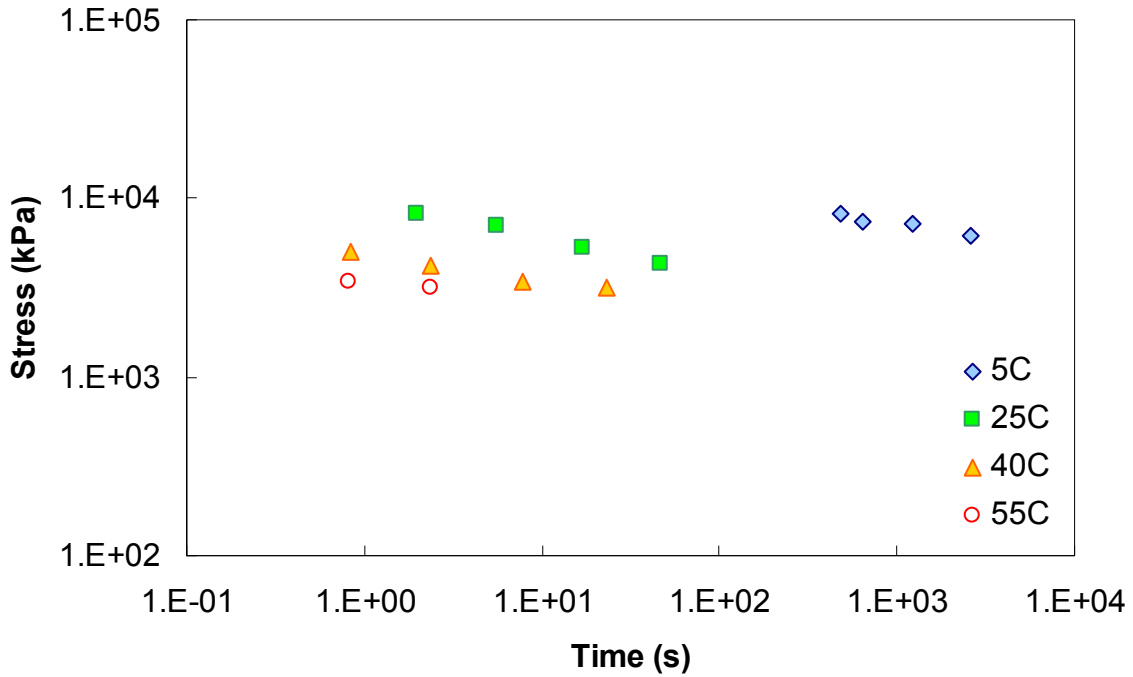


Figure 114. Graph. Stress-time curves for the Control mixture before the application of time-temperature shift factors at a 0.02 strain level under 500 kPa conditions.

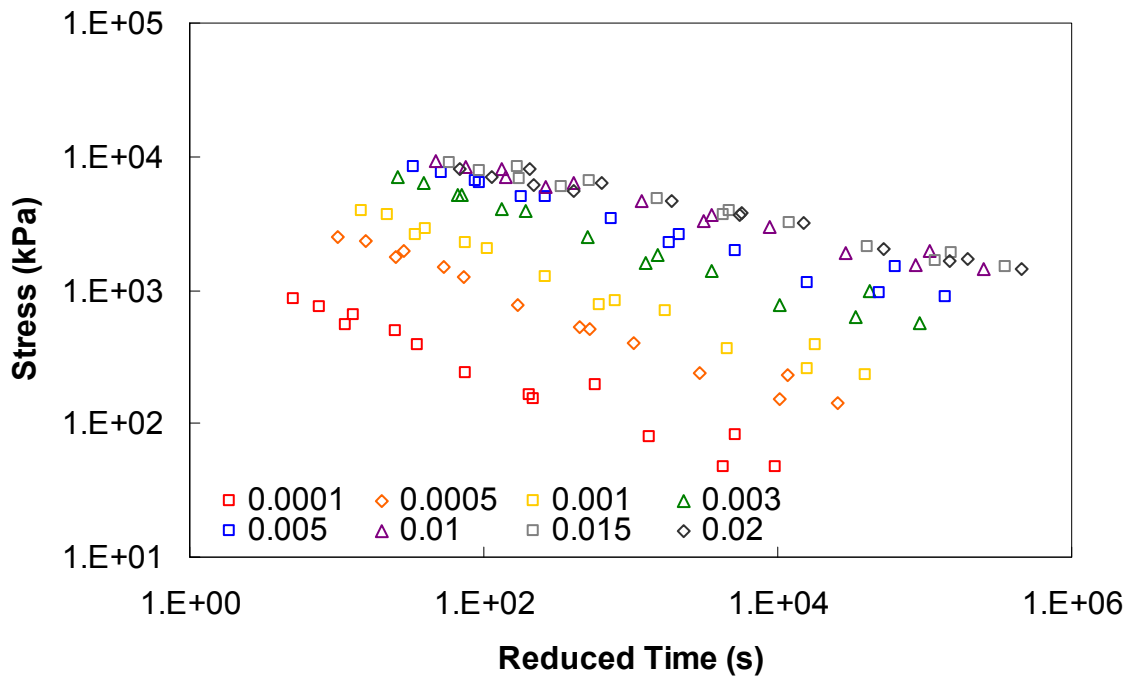


Figure 115. Graph. Stress mastercurves for the Control mixture under uniaxial conditions.

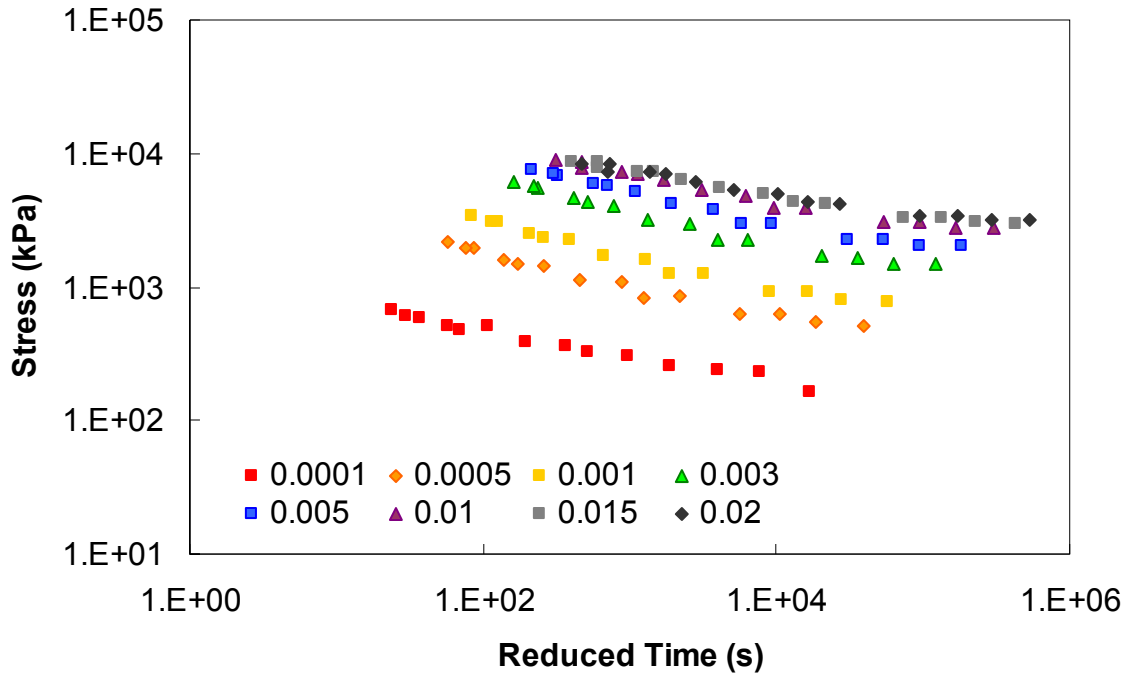


Figure 116. Graph. Stress mastercurves for the Control mixture under triaxial conditions (500 kPa).

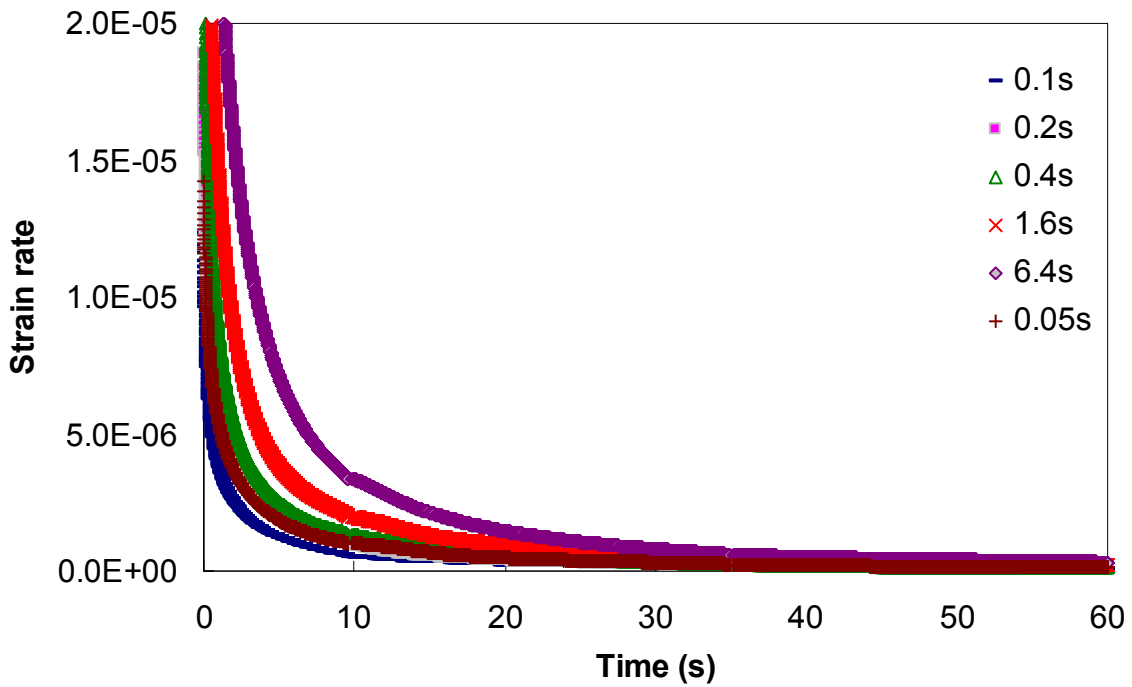


Figure 117. Graph. Variation of strain rate during unloading.

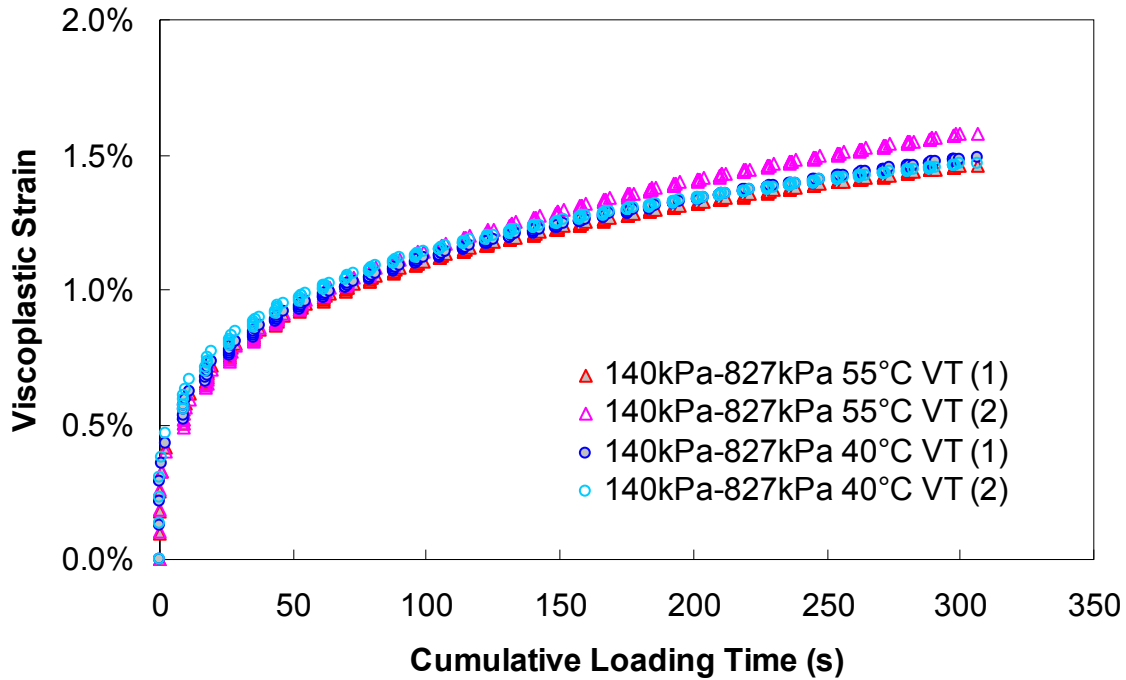


Figure 118. Graph. Viscoplastic strain versus cumulative loading time (140 kPa confinement VT at 40 and 55 °C).

5.2. MVECD CHARACTERIZATION IN COMPRESSION

5.2.1. Linear Viscoelastic Characterization

As presented in chapter 2, the first stage in MVECD characterization was the determination of the LVE properties of the material. Following the test protocols presented in chapter 3, frequency-temperature sweep tests were conducted in both unconfined and confined states. The results of this characterization under zero-maximum deviatoric stress conditions are shown for the unconfined stress state in table 16, for a confining pressure of 140 kPa in table 17 and for a confining pressure of 500 kPa in table 18. The shift factor function coefficients that resulted as part of the mastercurve construction process for each of the tests in these tables are shown in table 19.

Table 16 through table 18 show that a trend similar to that observed for the zero-mean deviatoric conditions was also observed for the zero-maximum deviatoric tests. Specifically, under confinement, the material modulus increased as a function of the confinement level. Additionally, under conditions where a given confinement state diverged from the unconfined state, the mastercurve moved toward a lower temperature and higher frequency at the higher confined stress. Additionally, a higher confining stress generally resulted in a lower phase angle (i.e., higher elasticity). Although it may be argued that increased aggregate interlocking was the cause of these behaviors, it was assumed that such an interpretation was flawed due to the strain magnitudes typically induced during the testing. The net effect of the increased dynamic modulus and phase angle was an increase in the relaxation modulus, which is shown for the different confining pressures in figure 119. These curves were obtained by the method outlined in subsection 2.2.1. Figure 119 shows that the relaxation modulus began to diverge at around

0.01 to 1 s in reduced time. These times generally corresponded to a physical time of between 1×10^{-5} and 2×10^{-7} s at 54 °C and of between 1×10^{-4} and 1×10^{-7} at 40 °C. Therefore, it was important to consider the effect of confining pressure because the time at which the relaxation modulus started to diverge was within the range of reduced time that was used in the rutting analysis.

Table 16. Linear viscoelastic characterization and variation for the Control mixture in unconfined compression state at selected frequencies and temperatures.

Temp. (°C)	Frequency (Hz)	Average E* (MPa)	Average Phase Angle (°)	E* Coefficient of Variation (%)	Phase Angle Coefficient of Variation (%)
-10	25	33,603	4.8	12.6	4.0
	10	32,251	6.1	12.1	10.0
	5	30,865	6.5	11.0	4.6
	1	28,633	7.9	11.7	2.8
	0.5	27,398	8.0	11.4	3.4
	0.1	23,909	9.7	7.9	44.1
5	25	23,707	9.7	7.0	45.6
	10	21,323	11.7	5.0	34.3
	5	20,085	12.5	9.1	4.2
	1	16,399	15.1	10.9	4.5
	0.5	14,262	17.2	11.4	3.9
	0.1	11,205	20.7	11.9	5.5
20	25	12,444	19.2	11.4	4.3
	10	10,624	21.4	14.7	4.7
	5	8,809	23.2	14.5	5.4
	1	6,229	26.2	7.0	8.4
	0.5	4,941	27.8	1.0	3.0
	0.1	2,818	32.7	5.4	2.4
40	25	2,872	32.5	3.2	0.2
	10	1,834	36.2	1.3	1.0
	5	1,386	38.0	2.5	1.7
	1	904	35.7	7.0	3.0
	0.5	640	35.9	7.0	2.6
	0.1	363	32.6	20.4	12.1
54	25	973	35.6	4.1	3.3
	10	604	35.8	5.8	2.7
	5	475	34.5	1.0	2.7
	1	321	31.3	20.8	15.4
	0.5	226	29.0	4.7	18.5
	0.1	185	24.3	11.0	38.7

Table 17. Linear viscoelastic characterization and variation for the Control mixture in 140 kPa confined compression state at selected frequencies and temperatures.

Temp. (°C)	Frequency (Hz)	Average E* (MPa)	Average Phase Angle (°)	E* Coefficient of Variation (%)	Phase Angle Coefficient of Variation (%)
-10	25	34,501	9.0	1.6	3.7
	10	33,555	7.8	0.4	4.5
	5	32,396	7.8	0.0	5.7
	1	29,413	8.5	0.0	1.1
	0.5	28,174	9.1	0.5	2.4
	0.1	25,164	10.6	0.9	2.4
5	25	24,048	11.1	1.4	0.4
	10	21,655	12.7	1.4	1.6
	5	20,663	13.4	1.2	2.0
	1	17,333	16.3	2.4	2.6
	0.5	15,097	17.9	2.8	1.9
	0.1	11,904	20.6	2.6	1.2
20	25	12,773	19.7	3.2	1.3
	10	10,458	22.4	3.2	0.5
	5	9,013	24.3	3.0	0.6
	1	6,278	29.2	4.7	0.2
	0.5	5,176	31.9	5.6	0.3
	0.1	3,376	33.2	1.7	2.2
40	25	3,489	33.1	1.2	2.0
	10	2,473	33.5	2.8	4.0
	5	1,978	33.4	3.9	5.1
	1	1,397	30.0	5.0	3.4
	0.5	1,276	27.3	4.8	0.2
	0.1	904	22.4	7.8	16.9
54	25	1,459	32.2	5.6	8.4
	10	1,328	28.0	3.9	0.2
	5	1,005	27.4	10.6	18.8
	1	896	19.9	4.5	14.0
	0.5	752	21.9	11.5	27.5
	0.1	740	14.8	5.1	30.4

Table 18. Linear viscoelastic characterization and variation for the Control mixture in 500 kPa confined compression state at selected frequencies and temperatures.

Temp. (°C)	Frequency (Hz)	Average E* (MPa)	Average Phase Angle (°)	E* Coefficient of Variation (%)	Phase Angle Coefficient of Variation (%)
-10	25	32,837	6.3	10.0	0.9
	10	31,947	7.7	11.1	0.9
	5	30,803	8.6	11.6	0.9
	1	27,616	10.3	11.0	0.5
	0.5	26,114	11.1	11.5	0.9
	0.1	22,672	13.5	11.2	0.2
5	25	23,317	13.1	8.6	2.9
	10	21,641	13.6	6.7	0.3
	5	19,651	11.9	7.0	0.4
	1	16,013	15.1	7.5	2.1
	0.5	13,834	17.2	7.3	1.6
	0.1	10,903	20.7	8.4	2.2
20	25	12,927	18.1	5.1	0.1
	10	11,312	20.1	5.3	0.2
	5	9,540	22.9	5.1	0.3
	1	7,067	27.3	4.0	0.2
	0.5	5,943	23.0	7.0	0.9
	0.1	3,996	24.0	7.5	0.5
40	25	4,621	29.2	5.8	6.2
	10	3,631	23.7	0.8	0.3
	5	3,166	23.3	2.6	0.2
	1	2,477	18.7	3.9	1.8
	0.5	2,204	16.7	3.1	1.3
	0.1	1,737	12.5	6.7	9.8
54	25	2,664	19.7	3.9	7.2
	10	2,295	17.8	4.0	2.7
	5	2,059	16.3	0.5	3.1
	1	1,674	11.7	2.5	17.6
	0.5	1,528	9.8	1.2	2.5
	0.1	1,398	7.0	3.0	7.9

Table 19. Effect of confining pressure on shift factor function coefficients for the Control mixture in compression state.

Parameters	0 kPa	140 kPa	500 kPa
α_1	0.00071	0.00090	0.00062
α_2	-0.15833	-0.17176	-0.14508
α_3	0.77385	0.83629	0.71001

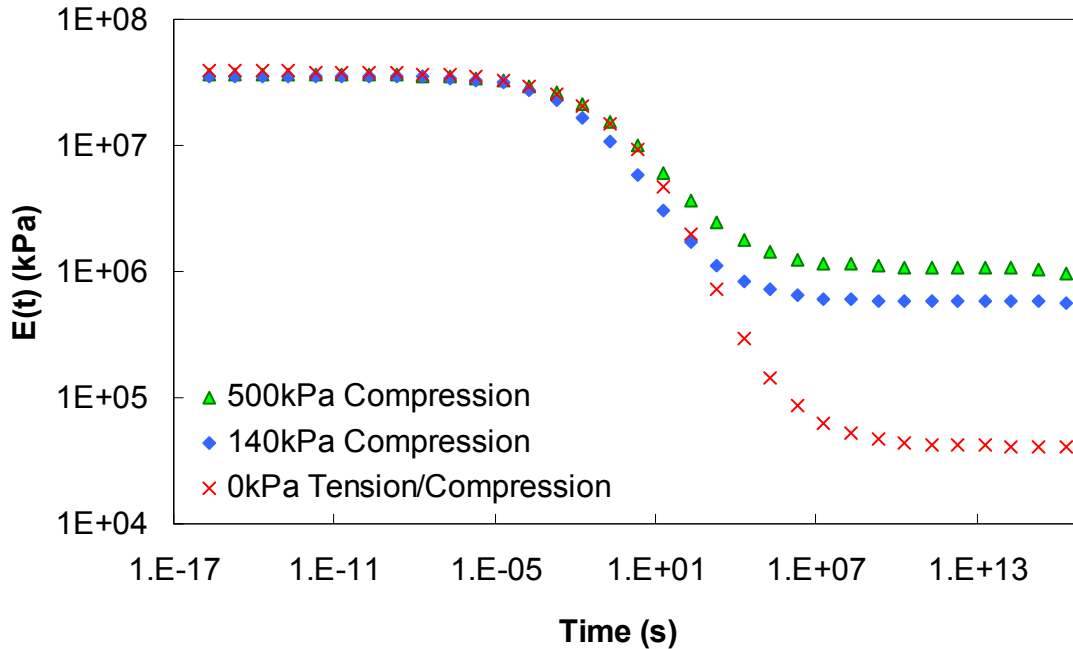


Figure 119. Graph. Confining stress effect on the relaxation modulus.

5.2.2. Comparison of Zero-Mean and Zero-Maximum Deviatoric Stress Results

Figure 120 through figure 123 present the LVE characteristics determined from the zero-mean and zero-maximum deviatoric stress states. Only the 0 and 500 kPa results are shown in the figures because they were consistent for the two test methods. Overall, the comparisons were very favorable, and little difference was seen between the zero-mean and zero-maximum deviatoric stress states. However, a noticeable difference was seen in the phase angle results, but these results were subject to higher variability. Further, the phase angle calculation was less precise due to limitations of the measurement instrumentation. These results indicated that at small strains, asphalt concrete was not bimodal, and it was only after some threshold strain had been exceeded that such behavior occurred. Such findings are consistent with the work presented elsewhere when care is taken in performing the experiments at sufficiently small strains (50 to $70 \mu\epsilon$).^(54,55) When such care is not taken, conflicting data are found in the literature.^(28,56) For modeling then, it is important that the LVE characterization is limited to the 50 to $70 \mu\epsilon$ range; in this range, either the zero-mean or zero-maximum method may be used.

As a final comparison of the two test conditions, the model developed in subsection 4.2.2 was applied to the zero-maximum deviatoric stress state tests. The results of this analysis are shown in figure 124, and good agreement was observed between the model and measured data.

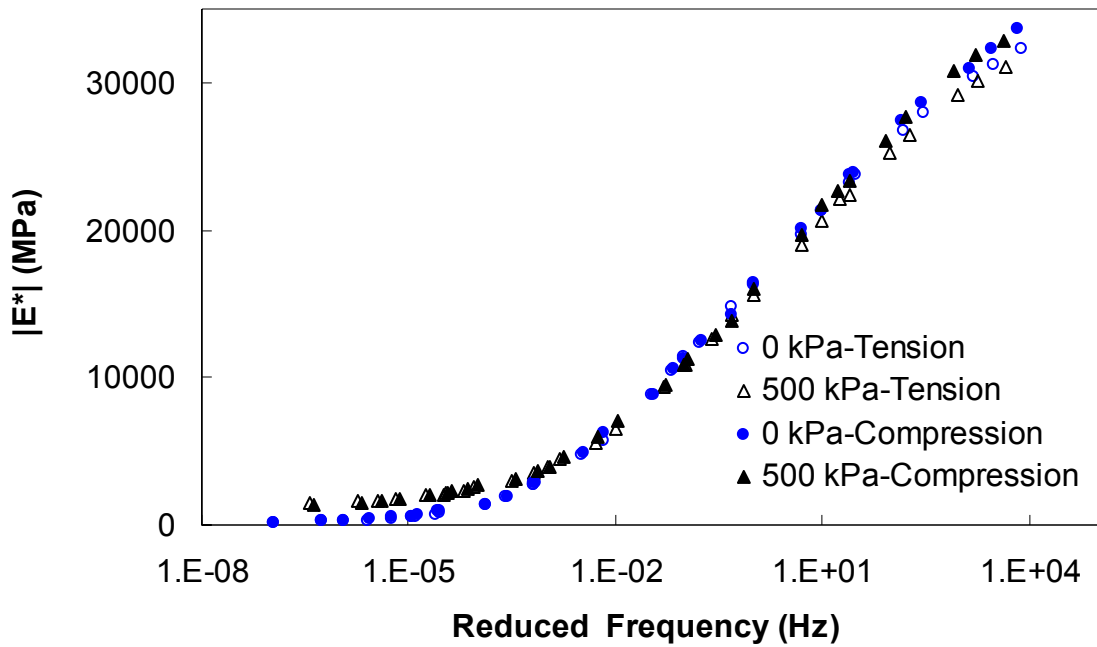


Figure 120. Graph. Comparison of zero-mean and zero-maximum deviatoric stress dynamic modulus mastercurves in semi-logarithmic scale.

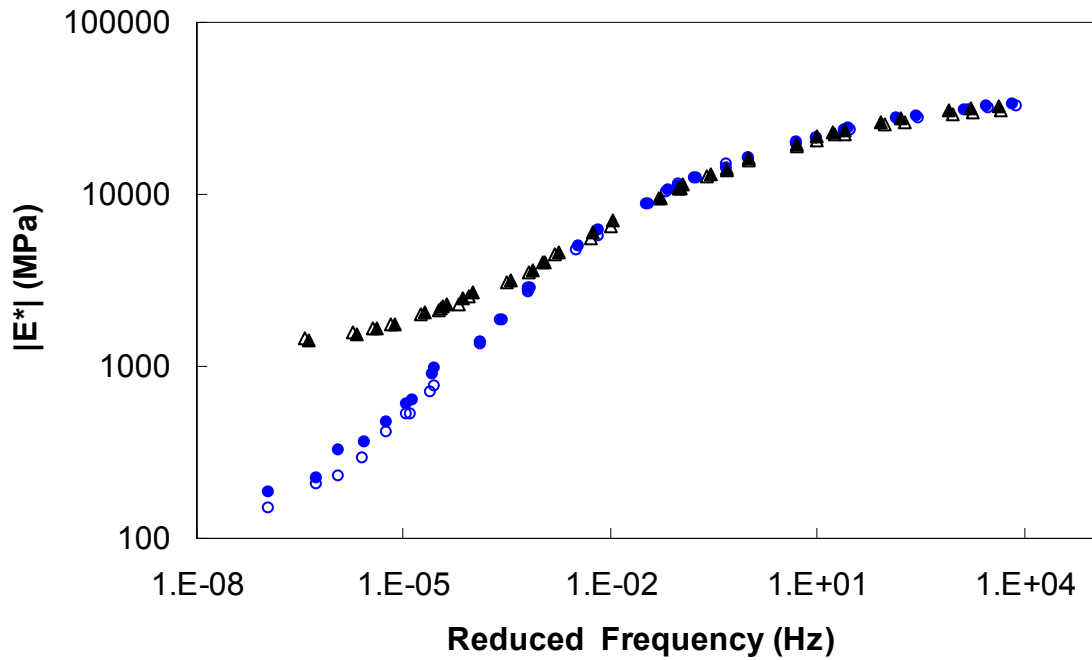


Figure 121. Graph. Comparison of zero-mean and zero-maximum deviatoric stress dynamic modulus mastercurves in logarithmic scale.

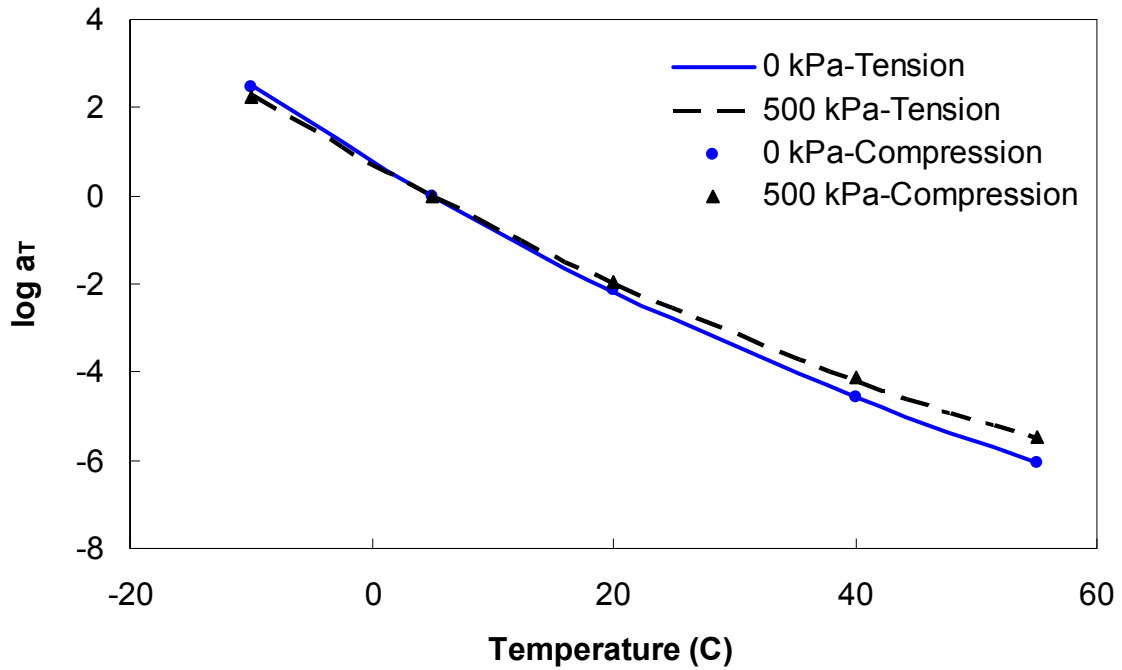


Figure 122. Graph. Effect of test method on shift factor functions.

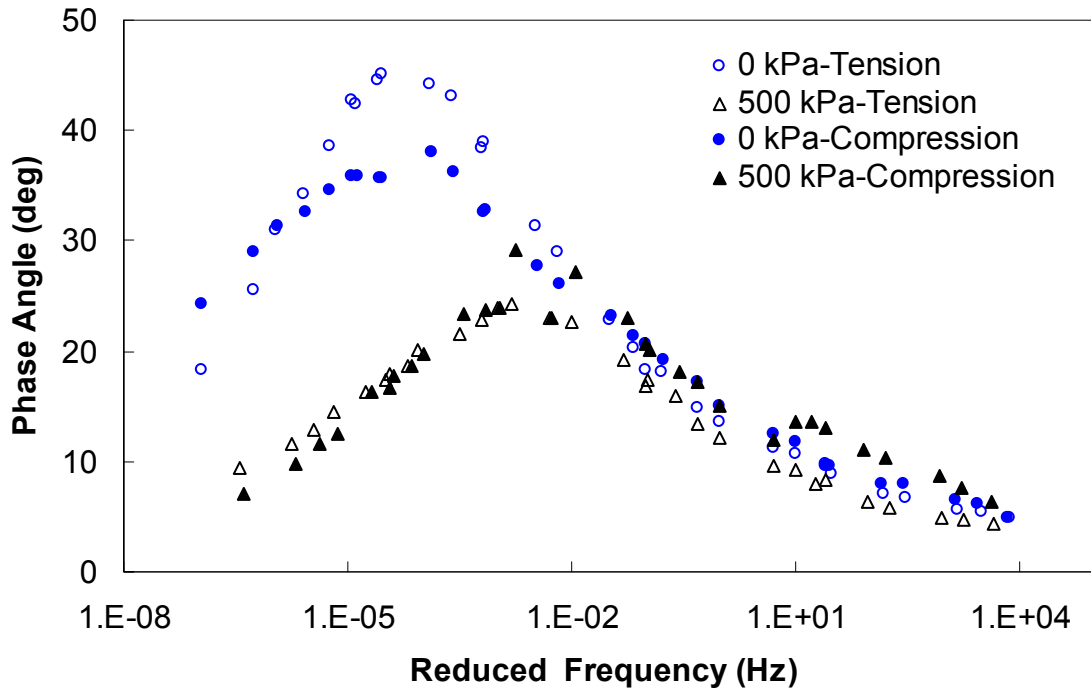


Figure 123. Graph. Comparison of zero-mean and zero-maximum deviatoric stress phase angle mastercurves.

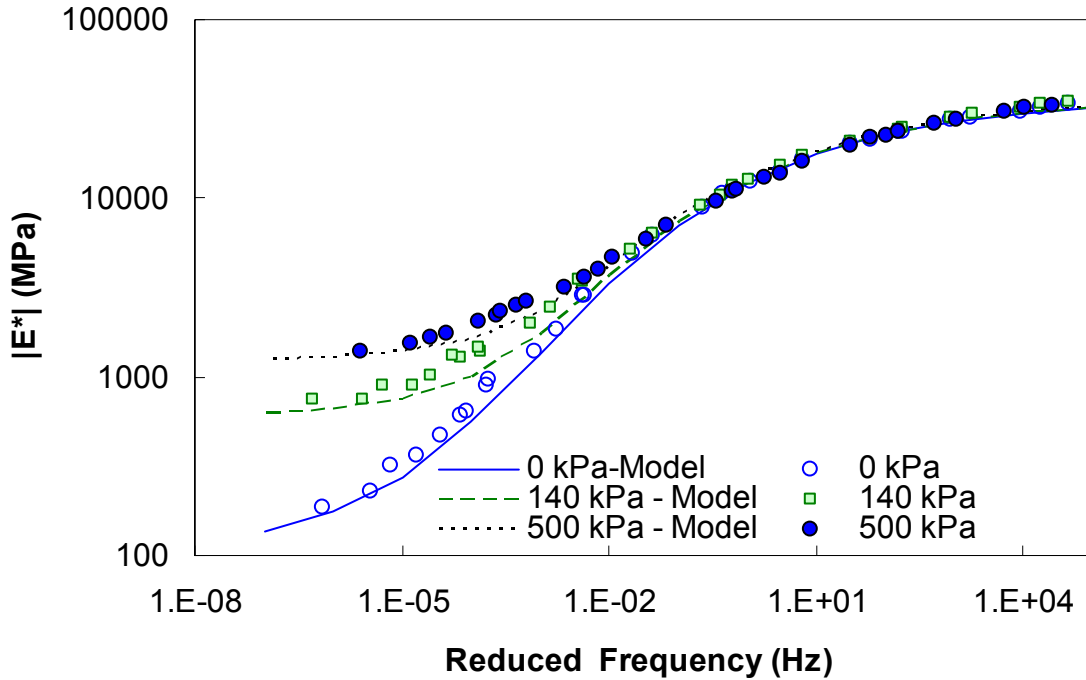


Figure 124. Graph. Application of stress state-dependent model to zero-maximum deviatoric stress tests.

5.2.3. MVECD Damage Function Characterization

Characterization of the VECD model in compression was identical in analysis and general experimental requirements to that in tension. Constant rate compression tests were performed under both unconfined and confined conditions, the results of which were then used to calculate the damage functions C_{11} , C_{12} , and C_{22} . The process was discussed previously in subsection 4.2.3 and is shown schematically in the flow diagram shown in figure 125.

5.2.3.1. Characterization of $C_{11}(S)$

Uniaxial constant rate tests were used to characterize the C_{11} damage function. Test results were used with equation 89 and equation 90 to compute the material function and damage parameter, respectively. Note that stress-hardening (equation 85) was used for this analysis. As with the tension damage function, this relationship was refined following the NCHRP 9-19 methodology.⁽²²⁾ This relationship is shown for the Control mixture in figure 126. This figure is constructed at a reference temperature of 5 °C and is only for the material under compressive loading. For this mixture, $a_1 = 7.679 \times 10^{-6}$, $a_2 = 1.6971 \times 10^{-6}$, $a_3 = 7.6793 \times 10^{-6}$, $a_4 = 4.6192 \times 10^{-7}$, $a_5 = 1.5128 \times 10^{-7}$, and $a_6 = 4.1017 \times 10^{-8}$.

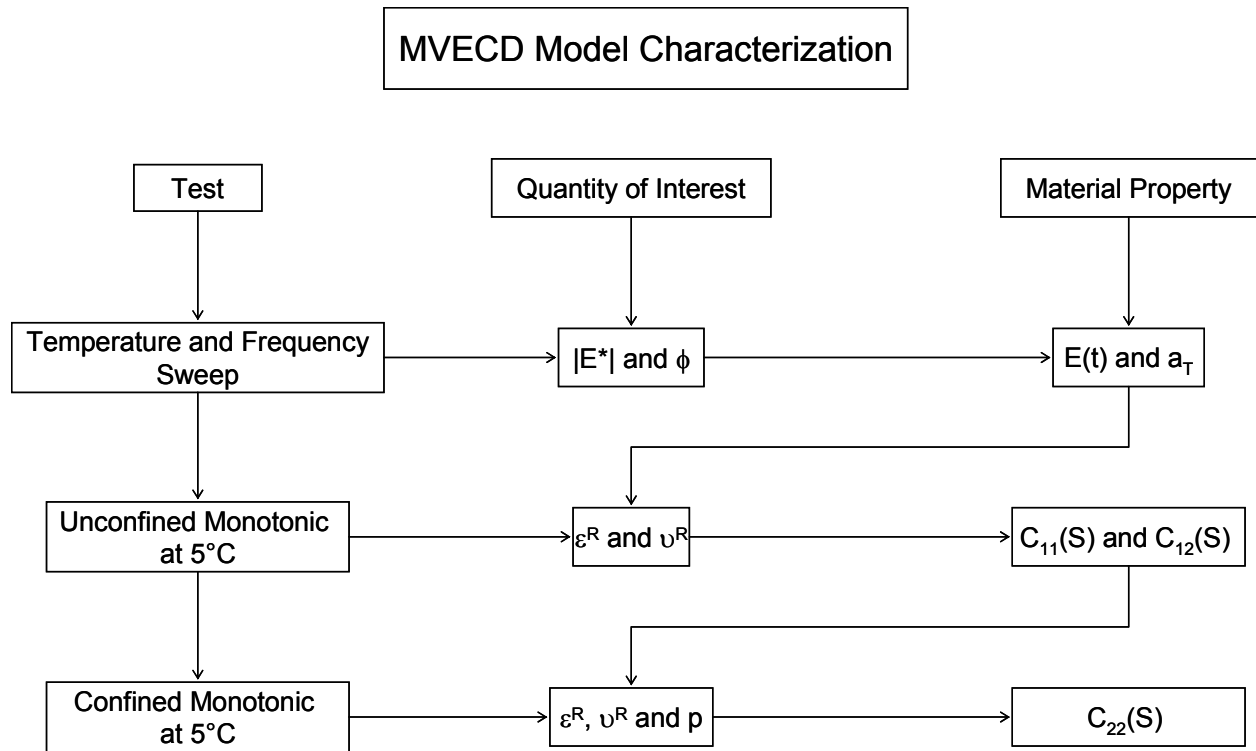


Figure 125. Diagram. MVECD model characterization.

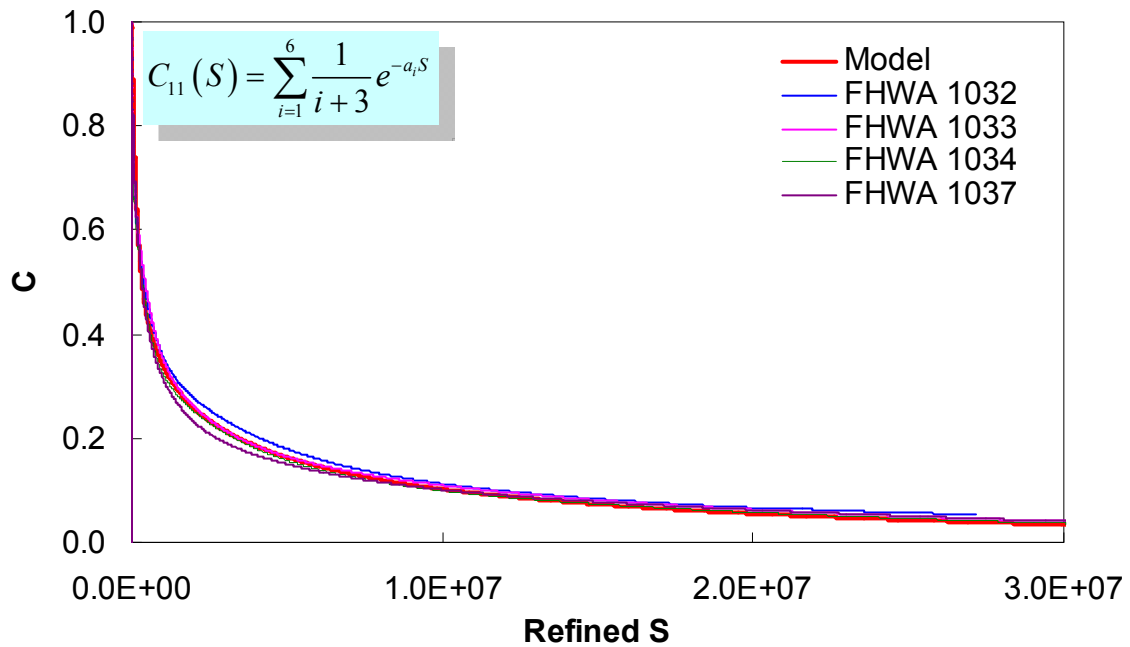


Figure 126. Graph. C_{11} versus S for compression for Control mixture (5 °C reference).

5.2.3.2. Characterization of $C_{12}(S)$

In addition to using uniaxial constant rate tests to characterize the C_{11} damage function, these test results were also used to characterize the C_{12} damage function. As with the tension tests, complications arose due to the time-dependent nature of Poisson’s ratio in asphalt concrete. Based on the analysis presented in subsection 4.2.3.2, an initial value of approximately 0.179 was assumed for C_{12} . This assumption was not unreasonable based on the results of the characterization tests. A slight difference between the initial values of the compression and tension data shown previously was observed due to the use of slightly different mixtures for the two sets of tests (Control-2006 for tension and Control for compression). Tension data for the Control mixture will be shown in subsequent sections of this report. The C_{12} material parameter was defined from equation 91, and the damage parameter was calculated and refined as before. The functional form taken for the compressive C_{12} damage function is shown along with the data in figure 127. It was observed that at early damage stages, Poisson’s ratio changed very little, but, in general, as damage increased, Poisson’s ratio reduced, as indicated by an increase in C_{12} . For this mixture, it was found that $\beta_1 = 3.5598 \times 10^{-8}$, 1.6982×10^{-8} , and 3.2756×10^{-10} .

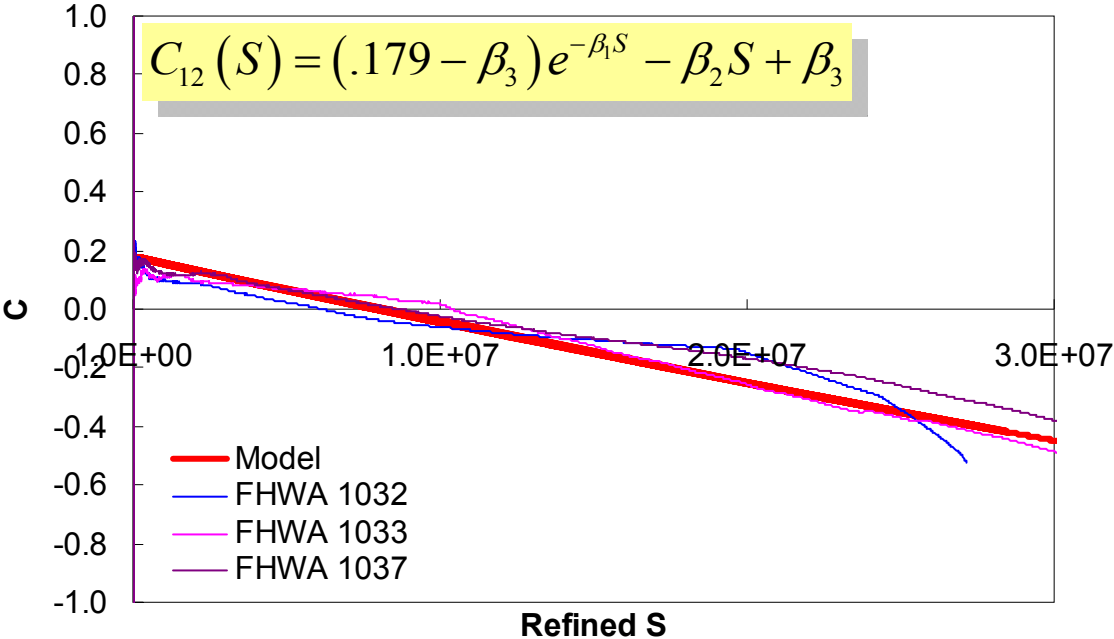


Figure 127. Graph. C_{12} versus S for compression for Control mixture (5 °C reference).

5.2.3.3. Characterization of $C_{22}(S)$

Confined constant rate tests, along with the other two damage functions, were used to characterize the final C_{22} function. Following the study conducted for the tension characterization methodology, a visual basic macro was created in Microsoft Excel® to determine the damage function by optimization. The characterized C_{22} function is shown in figure 128 along with the model function. The parameters of the model were $H_1 = -0.504959$ and $H_4 = 1.16247 \times 10^{-13}$.

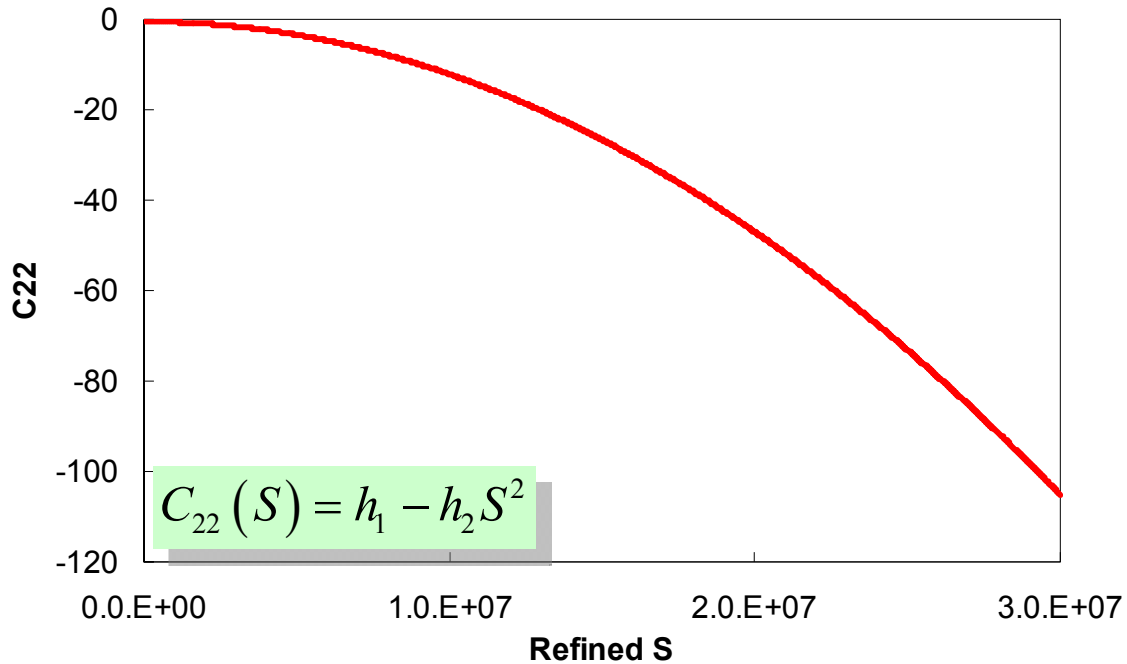


Figure 128. Graph. C_{22} versus S for compression for Control mixture (5 °C reference).

5.2.4. Comparison of MVECD Behavior in Compression and Tension

Asphalt concrete, like other composite materials, is known to exhibit bimodal behavior. In particular, the strength of the material it is in and its ductility are much higher in the compression direction than they are in the tensile direction. Comparisons of the MVECD damage functions revealed some interesting behaviors. First, when comparing the primary axial modulus damage function, C_{11} , between tension and compression, the material was substantially more resistant to damage in compression than it was tension. This behavior is shown in the same scale in figure 129. This behavior was explained by the notion that the damage parameter, S , represented some kind of crack density or volume-averaged cracked area. In tension, these cracks were oriented perpendicular to the principal loading direction, whereas, in compression, the cracks ran parallel to the principal loading direction. In constant rate loading, cracks only grew when they were under a tensile stress. Because tension was only induced (at the microscale level) in compression tests and not directly applied, the material was more resistant to a given cracking volume.

This physical interpretation for damage was also supported by the behavior of the second damage function, C_{12} . These damage functions are shown for both tension and compression in figure 130. This figure has both the C_{12} function and Poisson's ratio between the symmetric axis and perpendicular axis (ν_{3132}) for the convenience of the discussion. From the comparison shown in figure 130, it was observed that the primary Poisson's ratio showed an overall decreasing trend in tension, whereas the opposite trend occurred in compression. As with the C_{11} damage function, the tensile behavior of C_{12} was observed to be more sensitive to damage. A possible explanation of this behavior depended on understanding that Poisson's ratio indicated the degree to which the radius changed relative to a unit change in length. Applying the physical interpretation of damage in tension and compression, the physical implications of the patterns in both damage curves were identical. The tension curve was increasing, thus indicating that with

higher levels of damage, the direction parallel to the primary cracking direction (radial strain) was less sensitive to changes in strain perpendicular to the primary cracking direction (vertical strain). For compression, the primary cracking direction was parallel to the loading direction and perpendicular to the radial direction, so with the same interpretation (of damage in tension and compression), an increase in Poisson's ratio was observed. In the most general terms, the increased opening of a microcrack within a body was not necessarily accompanied by a relative increase in the parallel to the crack direction dimension of the body. In fact, the results indicated that at higher levels of cracking or damage the material became less likely to change dimension as much when loaded perpendicular to the damage orientation.

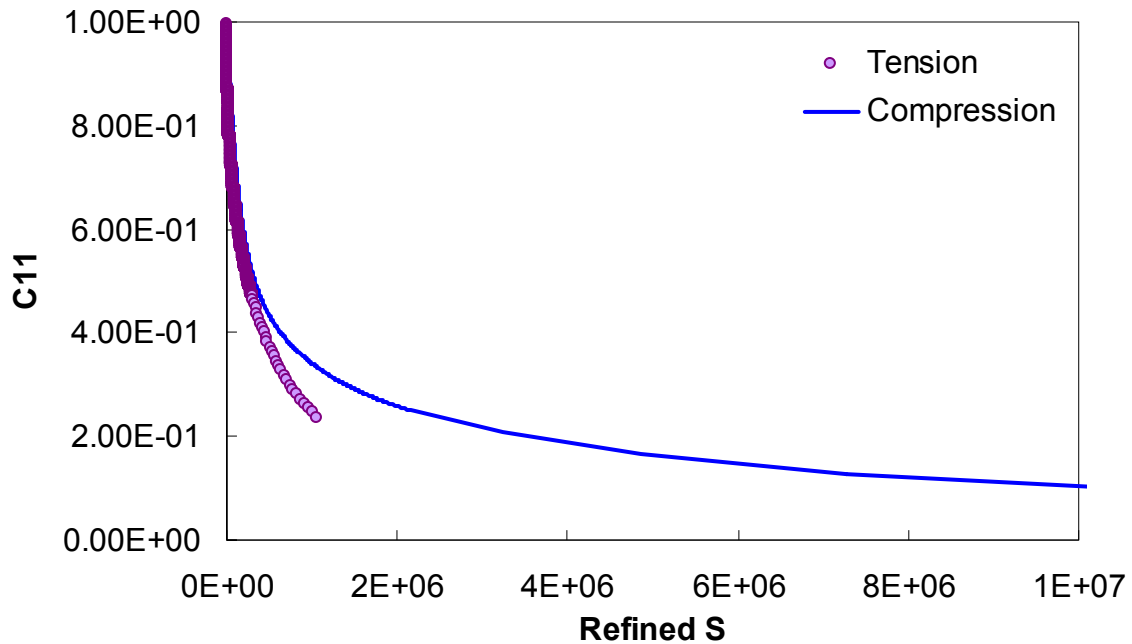


Figure 129. Graph. Comparison of tension and compression of C_{11} damage function.

The physical interpretation of the C_{22} damage function was not as straightforward as the other two damage functions. As seen in equation 45, the C_{11} and C_{12} damage functions can be directly translated to elements in the stiffness matrix. However, the C_{22} damage function entered in the denominator of multiple elements of the material stiffness matrix. Nevertheless, this damage function can be considered as a sort of volumetric compliance, which has little meaning in a transverse isotropic problem. From figure 131, though, it is seen that the material was more volumetrically compliant in compression than it was in tension.

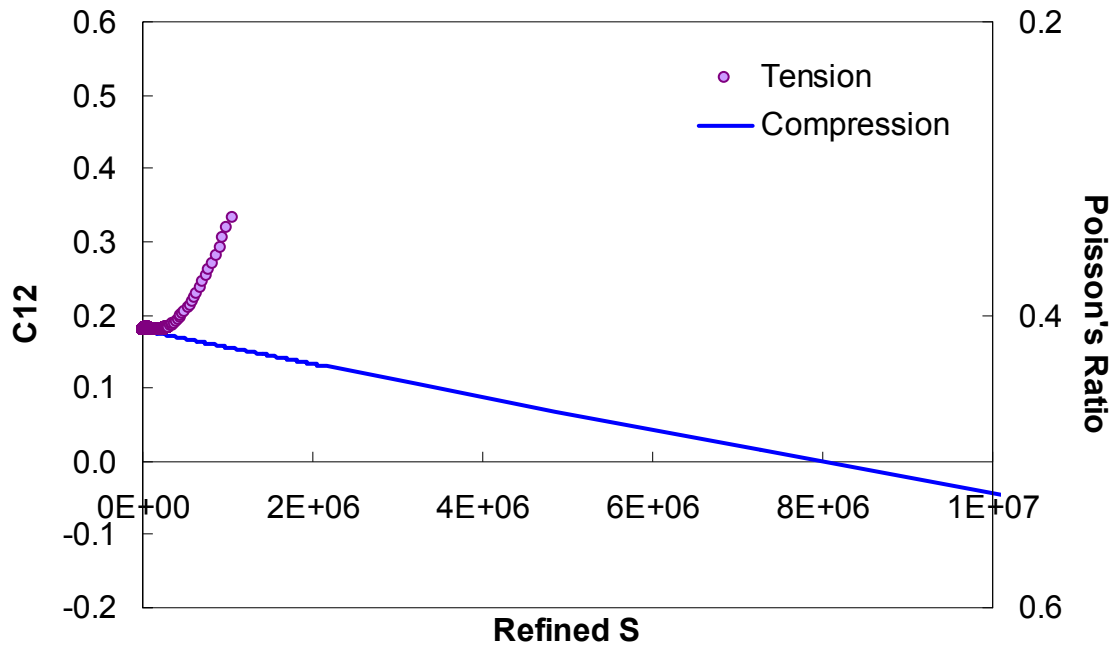


Figure 130. Graph. Comparison of tension and compression of C_{12} damage function.

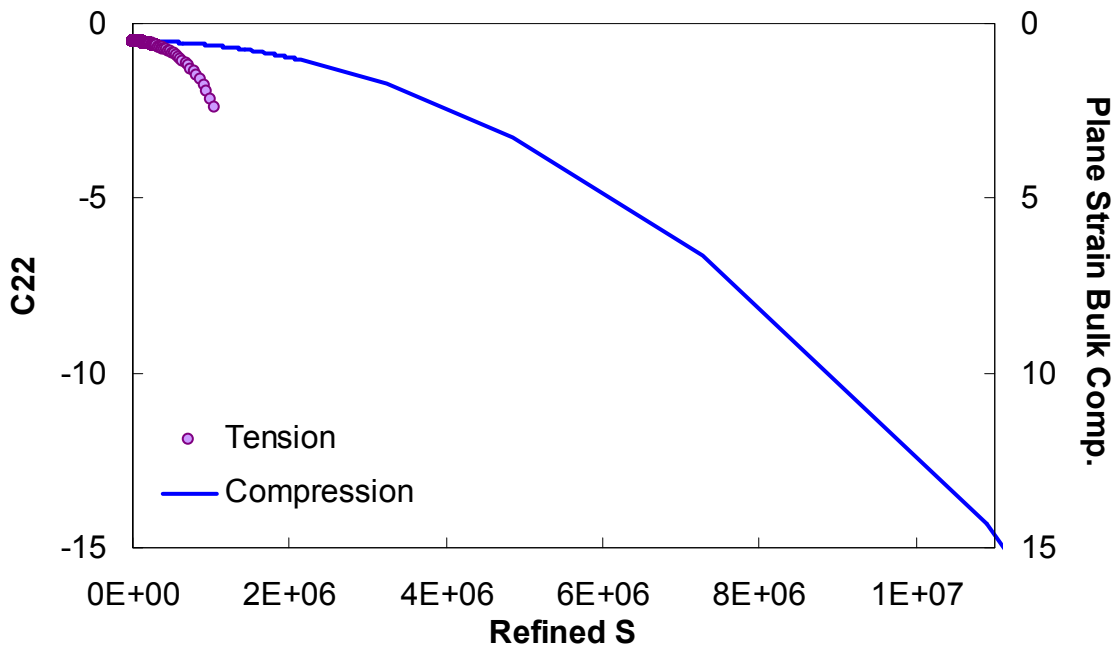


Figure 131. Graph. Comparison of tension and compression of C_{22} damage function.

5.3. VISCOPLASTIC MODELING OF ASPHALT CONCRETE IN COMPRESSION

5.3.1. A Phenomenological Model Considering Pulse Time Effects

As a first step toward developing a mechanistic material model for the behavior of HMA in compression, a series of analyses was performed on VT and VL test data, and a phenomenological model was developed. The modeling approach adopted in the phenomenological model was based on the existing strain-hardening model presented for describing the tensile behavior in section 4.3 and shown in the general form as follows:

$$\dot{\varepsilon}_{vp} = \frac{f(\sigma)}{g(\varepsilon_{vp})} \quad (158)$$

Where:

$\dot{\varepsilon}_{vp}$ = Viscoplastic strain rate.

σ = Stress.

ε_{vp} = Viscoplastic strain.

As shown in equation 158, the viscoplastic strain rate was represented by the combination of two functions, $f(\sigma)$ and $g(\varepsilon_{vp})$, which allowed the stress rate dependency and strain hardening to be taken into consideration in the model. Equation 158 can be generalized as equation 159, which accounts for the effect of the pulse time.

$$\dot{\varepsilon}_{vp} = F(\varepsilon_{vp}, \sigma, t_p) \quad (159)$$

Where:

t_p = The loading time.

The exact form of the function, F , is presented along with experimental data in the following sections.

5.3.1.1. Tests Performed in This Study

Three types of repetitive creep and recovery tests were performed for the phenomenological model development, including the creep and recovery test with VL, the creep and recovery tests with VT, and the creep and recovery test with a constant load level and CLT. All the tests were conducted at 55 °C under the confining pressure of 500 kPa. Experimental details for these tests are given in the following sections because this particular study uses different test conditions than those outlined in chapter 3.

5.3.1.1.1. Creep and Recovery Test with VL:

The creep and recovery test with a VL test was performed with 200 kPa as the starting load level. An incremental factor of 1.0245 was used for the subsequent load levels to increase the load level until the complete failure of the specimen. The loading time and rest period were 0.1 and 10 s, respectively.

5.3.1.1.2. Creep and Recovery Tests with VT:

The creep and recovery test with a VT test was performed with a loading block consisting of 30 different loading times. The loading time varied from 0.005 to 2.0 s with an incremental factor of 1.1356. The rest period for each load cycle was 30 times that of each loading time. The VT tests were performed at three different load levels, 1,800, 2,000, and 2,200 kPa.

5.3.1.1.3. Creep and Recovery Test with CLT:

In this test, a constant load level and constant loading time were used for each test. Load levels and loading times were changed between tests. Three load levels of 1,800, 2,000, and 2,200 kPa were used with the loading time of 1.6 s. For the 2,000 kPa load level, the creep and recovery tests were conducted with three additional loading times of 0.1, 0.4, and 6.4 s.

The VL and VT tests were used to understand the effects of load level and loading time on the permanent deformation behavior of HMA and to calibrate the phenomenological model. The CLT tests were used to verify the calibrated model.

5.3.1.2. Model Characterization

By observing the viscoplastic strain rate versus the viscoplastic strain VT in figure 132, a constitutive relationship between these viscoplastic media was defined, as shown in equation 160.

$$\log \dot{\varepsilon}_{vp} = a(t_p) \log \varepsilon_{vp} + D(t_p, \sigma) \quad (160)$$

Where:

$a(t_p)$ = Material function of loading time.

$D(t_p, \sigma)$ = Intercept of the curve on viscoplastic strain rate axis.

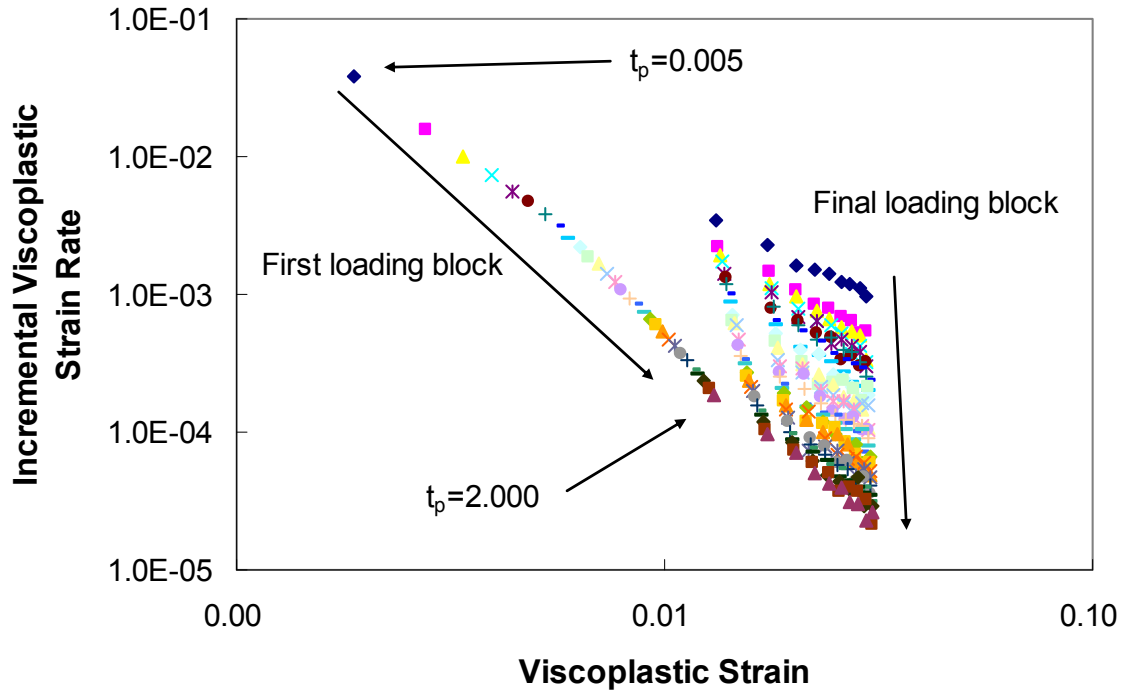


Figure 132. Graph. Incremental viscoplastic strain rate versus viscoplastic strain (500 kPa confinement, 2,000 kPa).

In equation 160, a was a function of the loading time, and D was a function of the load level and loading time. Equation 160 can be represented in equation 161, which was a generalized form of equation 158.

$$\begin{aligned}\dot{\varepsilon}_{vp} &= \left[(\varepsilon_{vp})^{a(t_p)} (t_p)^b 10^d \right] 10^{c(\sigma)} \\ &= \frac{f(\sigma)}{g(\varepsilon_{vp})k(t_p)}\end{aligned}\quad (161)$$

Where:

$k(t_p)$ = Function of loading time.

Equation 160 required the determination of $a(t_p)$ and $D(t_p, \sigma)$ to calculate the viscoplastic strain rate for a given viscoplastic strain. Values of $a(t_p)$ and $D(t_p, \sigma)$ for given loading times could be found by fitting log functions against each viscoplastic strain rate versus viscoplastic strain curve corresponding to given loading time. At this time, the values of $a(t_p)$ can be represented by the second logarithm function, as shown in equation 162.

$$a(t_p) = a_1 \log t_p + a_2 \quad (162)$$

Where:

a_1 and a_2 = Material-dependent constants.

In order to determine the form of $D(t_p, \sigma)$, it was assumed that $D(t_p, \sigma)$ could be represented by the summation of the loading time term and the load level term, as shown in equation 163.

$$D(t_p, \sigma) = b \log t_p + c(\sigma) + d \quad (163)$$

Where:

The function $c(\sigma)$ was given by $c_1 \log(\sigma)$ when the stress was less than 1,000 kPa and by $c_2 \sigma$ when the stress was greater than 1,000 kPa. The coefficient b was determined by fitting equation 163 against $D(t_p, \sigma)$ from the VT test. At this time, it was assumed that $c(\sigma)$ and d constitute one constant that accounts for the effect of load level. The function $c(\sigma)$ was then fitted by the logarithmic function and the linear function. Finally, coefficient d was determined by fitting equation 163 for the viscoplastic strain rate versus the viscoplastic strain curve of the VL and VT tests.

Figure 133 and figure 134 show the fitting results and the coefficients that were determined. Figure 135 and figure 136 presents predictions for the VT and VL tests, which were then used for the characterization process.

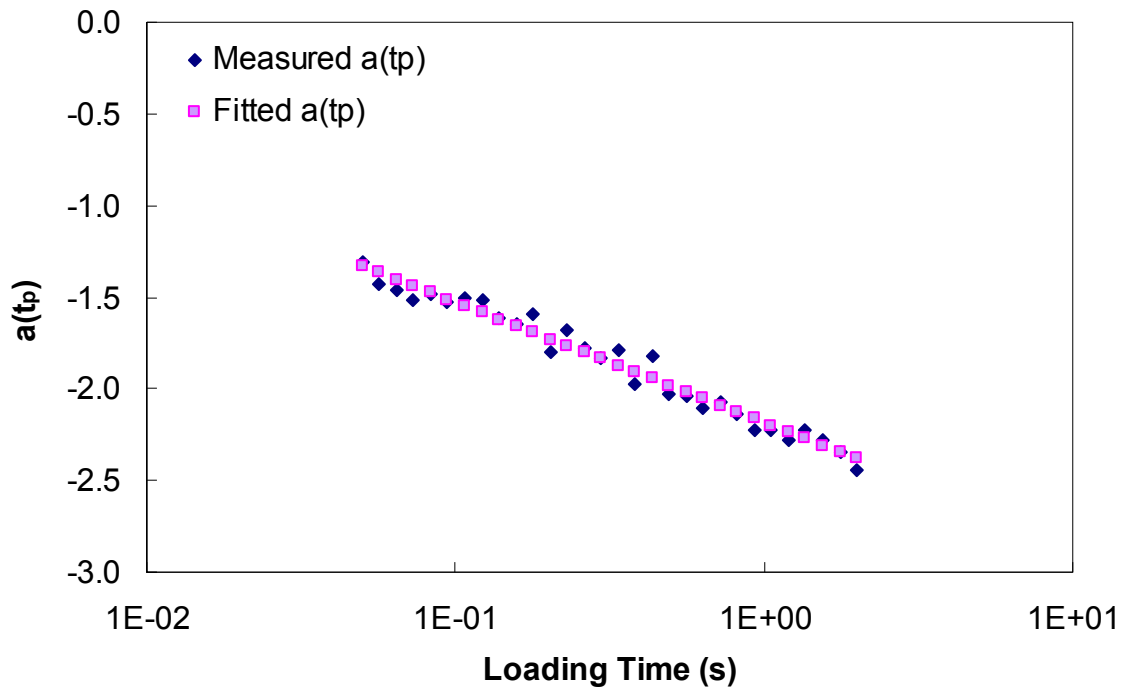


Figure 133. Graph. Determined fitting results and coefficients of function $a(t_p)$.

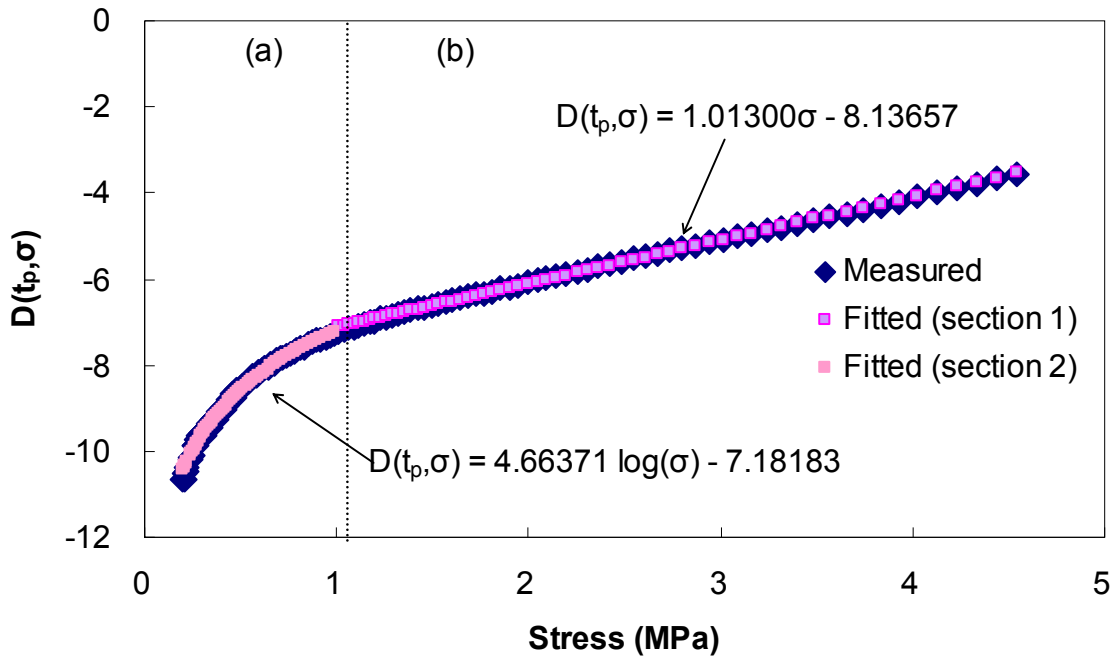


Figure 134. Graph. Determined fitting results and coefficients of function $D(t_p, \sigma)$.

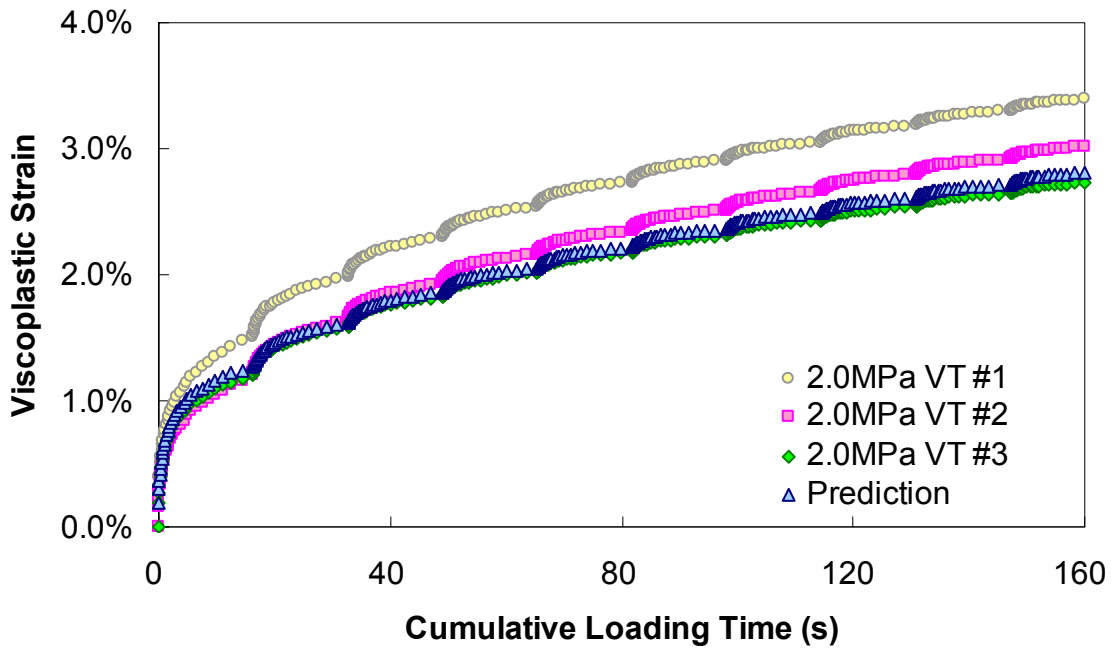


Figure 135. Graph. VT predictions.

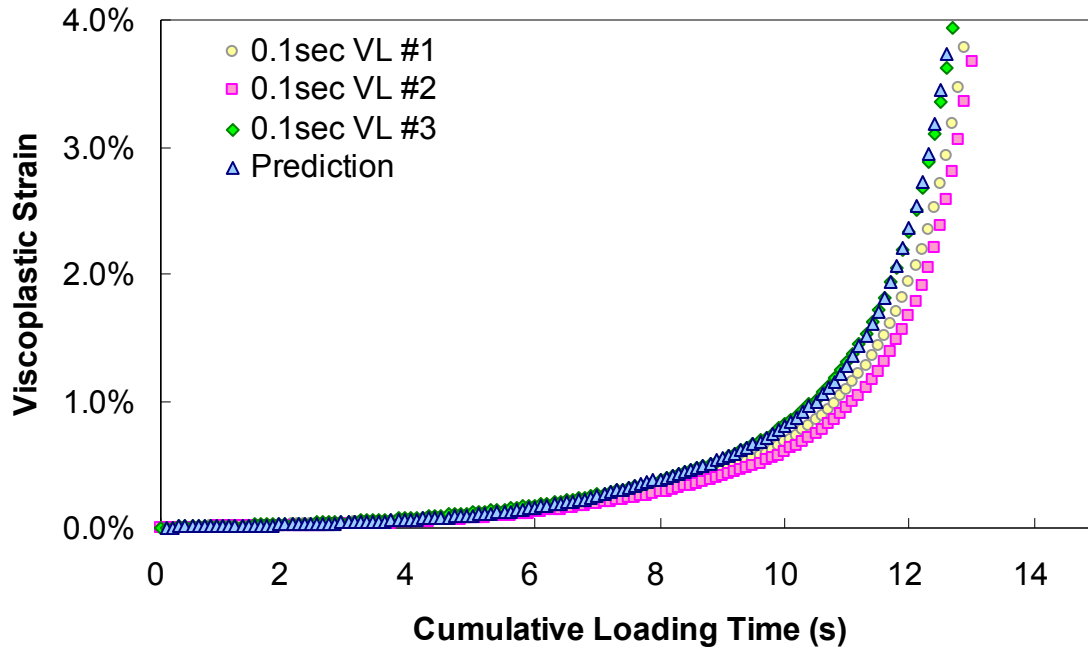


Figure 136. Graph. VL predictions.

5.3.1.3. Verification of the Model

As shown in figure 137 through figure 142, predictions were made for the CLT tests. Although the model was able to account for differences in the viscoplastic development for various loading times, overall predictions were not as accurate. Several causes for the discrepancy between viscoplastic strain predictions and measurements could be suggested. However, the inability of the model to consider strain history was a highly probable cause for this discrepancy, given that the fitting results for the VT and VL tests were acceptable.

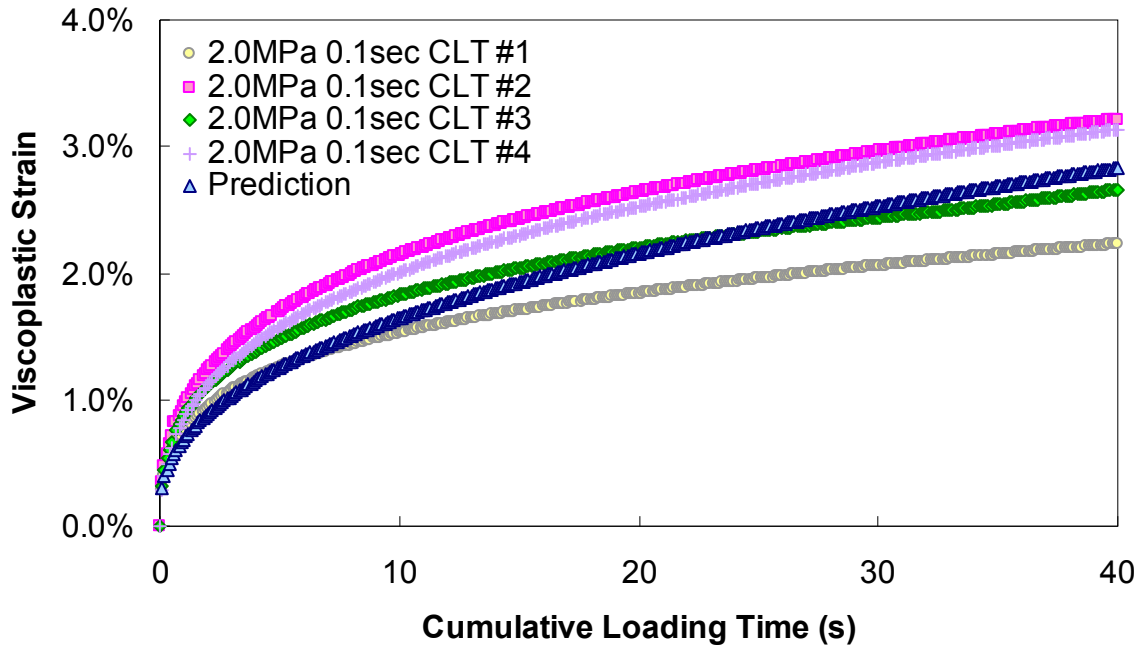


Figure 137. Graph. CLT predictions (2.0 MPa deviatoric stress—0.1-s pulse time).

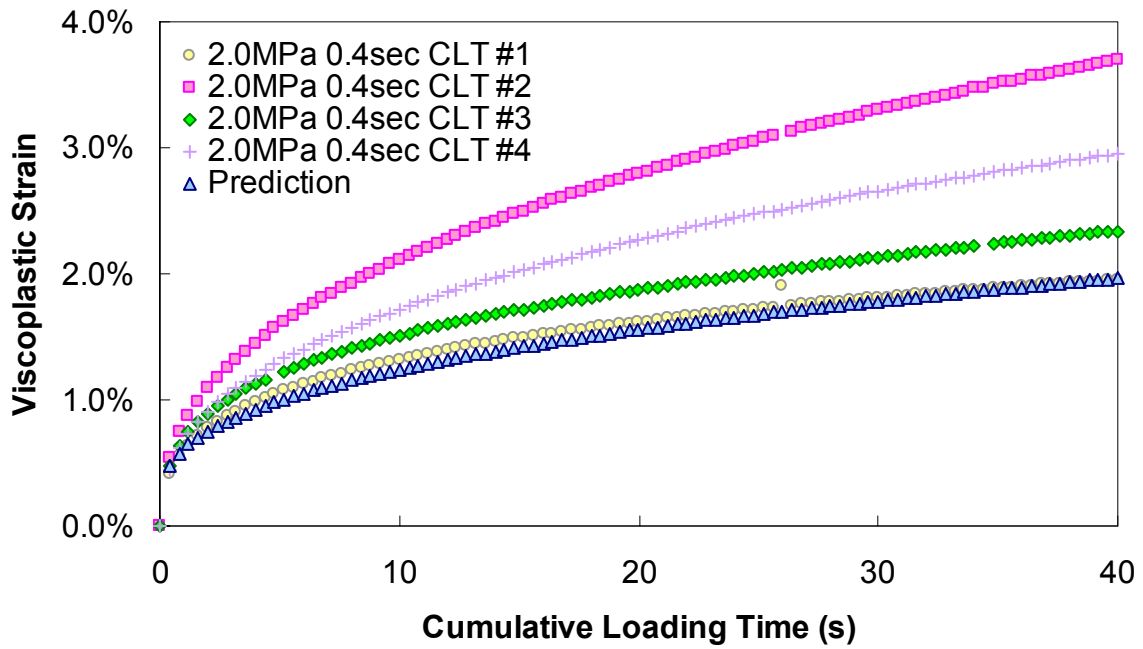


Figure 138. Graph. CLT predictions (2.0 MPa deviatoric stress—0.4-s pulse time).

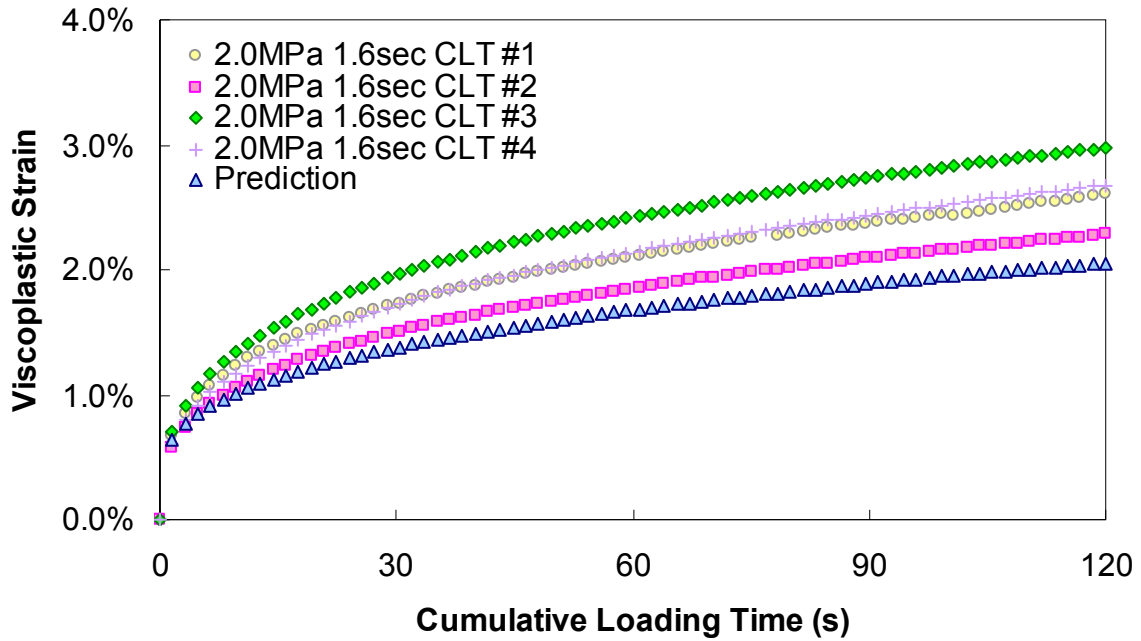


Figure 139. Graph. CLT predictions (2.0 MPa deviatoric stress—1.6-s pulse time).

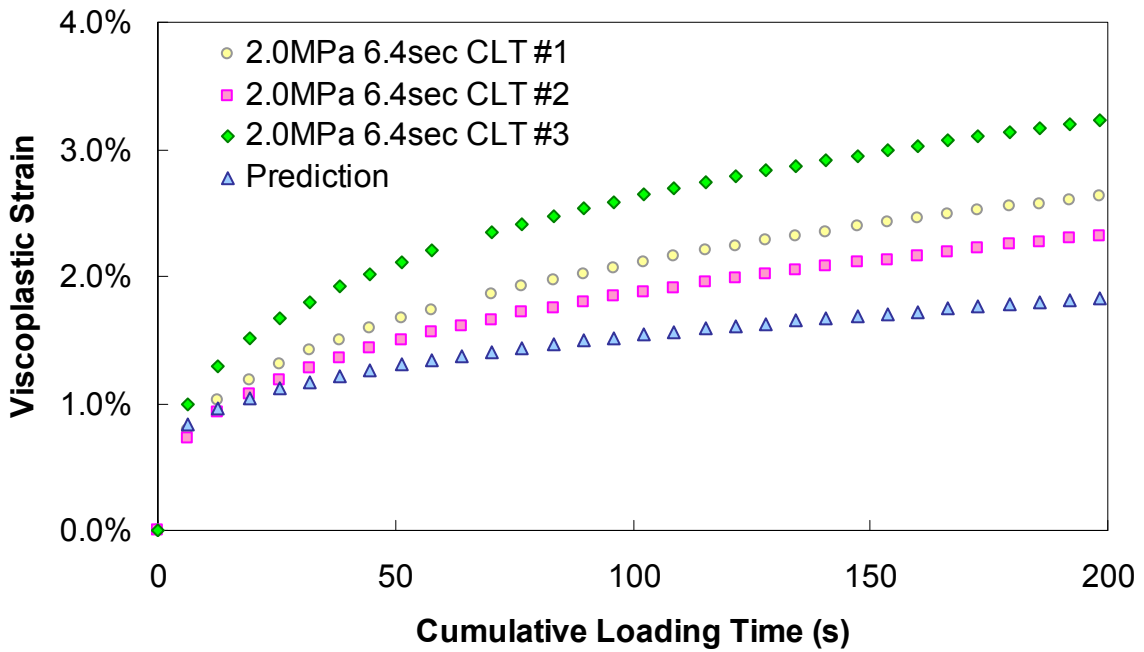


Figure 140. Graph. CLT predictions (2.0 MPa deviatoric stress—6.4-s pulse time).

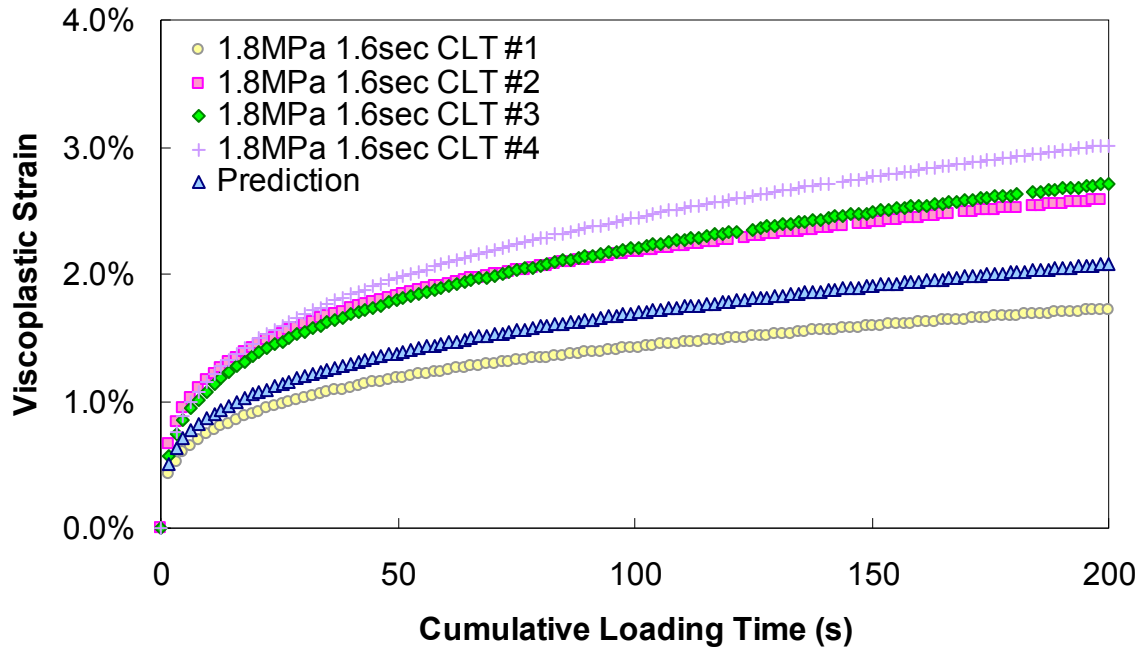


Figure 141. Graph. CLT predictions (1.8 MPa deviatoric stress—1.6-s pulse time).

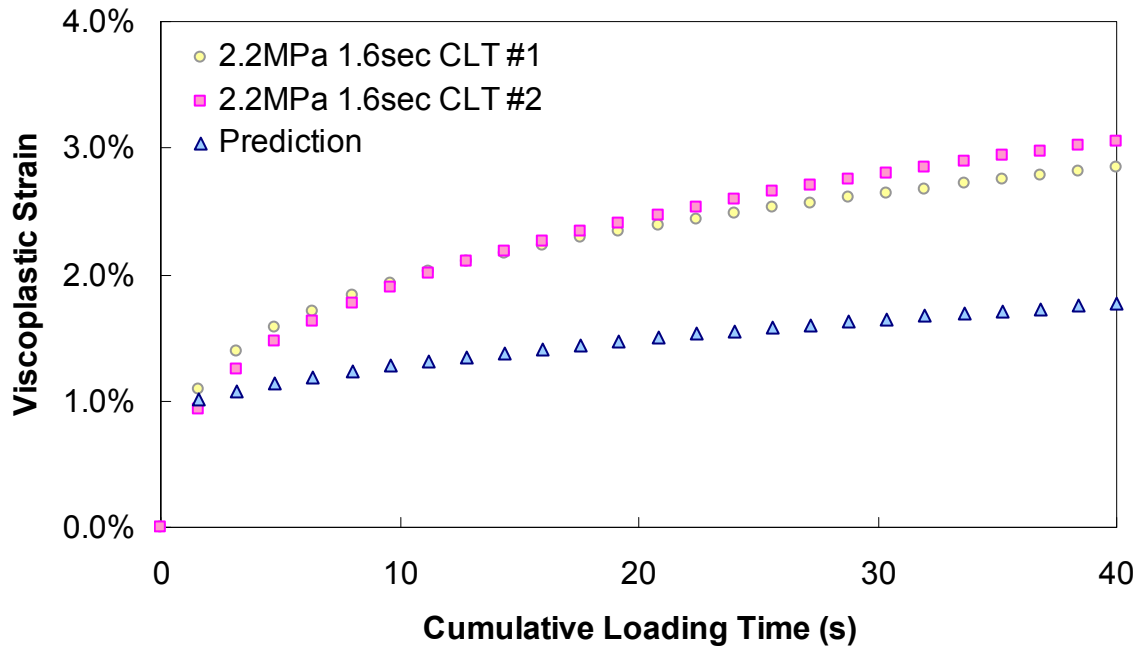


Figure 142. Graph. CLT predictions (2.2 MPa deviatoric stress—1.6-s pulse time).

5.3.2. HISS-Perzyna Model

The HISS-Perzyna model, suggested by the Delft University of Technology and the University of Maryland, was investigated with respect to the data set obtained from experimental tests.^(26,28,36) A prediction using the Delft University of Technology model was not made because of numerical problems. However, the characterization process using the t-TS principle and coefficients of the model are described in subsection 5.3.2.1.

5.3.2.1. Delft University of Technology Model

The model suggested by researchers at the Delft University of Technology required the development of several relationships between the material parameters and the strain rates obtained from constant strain-rate tests. In this research, the t-TS principle was utilized to simplify the modeling effort and to reduce the number of relationships required. With the assumption that the yield stress in deviatoric stress space was presented as circular, ($\beta = 0$), equation 72 was reduced to equation 164.

$$\sqrt{J_2} = \sqrt{\gamma(I_1 - R)^2 - \alpha(I_1 - R)^n} \quad (164)$$

Where:

γ = Softening parameter.

α = Hardening parameter.

R = Tensile strength of material when deviatoric stress is 0.

n = Parameter that determines shape of yield stress.

Figure 143 shows peak stresses for a series of compressive and tensile constant strain-rate tests; the strain rates are listed in table 4. These peak stresses were used as fundamental quantities to develop relationships between the material parameters and the reduced strain rates. R and γ_0 could be determined as functions of the reduced strain rate by plotting the compressive and tensile peak stresses obtained from the constant strain-rate tests under a certain strain rate and then taking the slope and x-intercept of the line. In the model, R and γ_0 represented the tensile strength for hydrostatic stress and the softening of the material in the post-peak region, respectively. The parameter n governs the overall shape and size of the yield function and was related to the dilation of the material. The beginning of dilation was defined as the stress at the minimum plastic volumetric strain because the plastic deviatoric strain and elastic strain (or viscoelastic strain) was assumed to not be associated with the volumetric change of a material. In addition, because HMA specimens dilated after a little compression as the compressive stress increased, the dilation stress could be determined. Once the dilation stresses were determined for several strain rates, the value of n could be determined using equation 165.

$$n = \frac{2}{1 - \frac{J_{2,dilation}}{\gamma(I_{1,dilation} - R)^2}} \quad (165)$$

Where:

$I_{1,dilation} = I_1$ at beginning of dilation.

$J_{2,dilation} = J_2$ at beginning of dilation.

Once n is determined, α_0 can be readily determined using equation 166.

$$\alpha_0 = \gamma_0 \left(\frac{R}{P_a} \right)^{2-n} \quad (166)$$

The sigmoidal function was used to represent relationships between the reduced strain rate and the material parameters. The form of the function and the coefficients determined for each parameter are listed in equation 167 and table 20. Figure 144 through figure 147 show a comparison of measured values versus predicted values at various reduced strain rates.

$$\log(\gamma_0 \text{ or } R) = a + \frac{b}{1 + e^{d - \log(\dot{\epsilon}_{reduced})}} \quad (167)$$

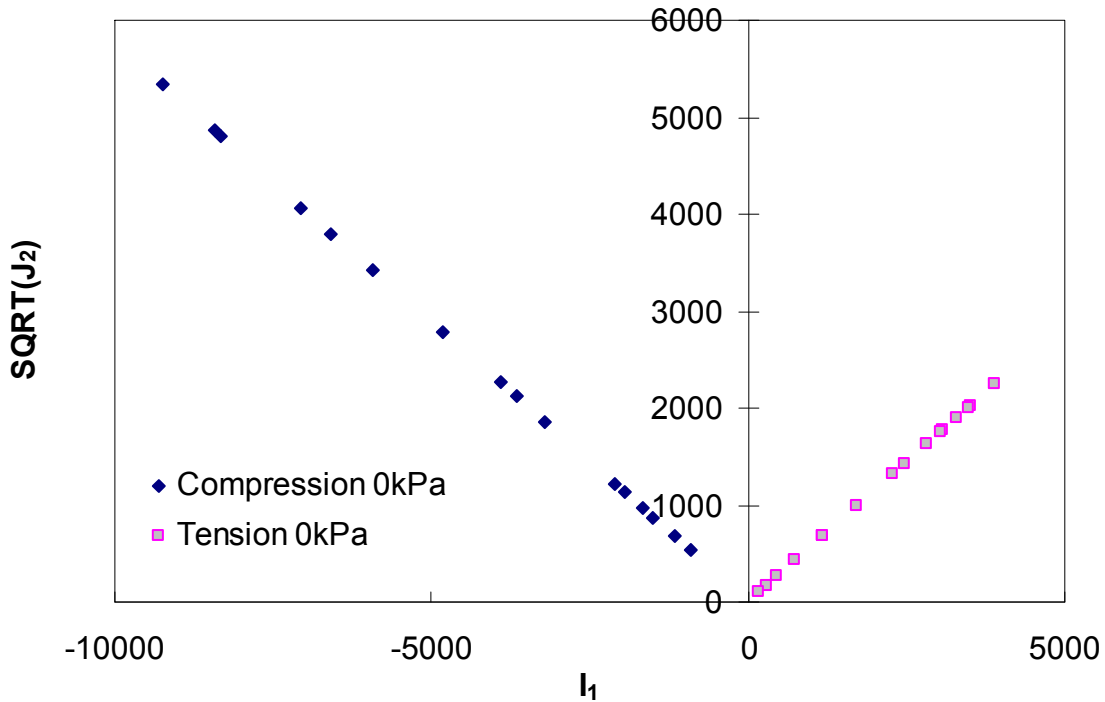


Figure 143. Graph. Compressive and tensile peak stress in $\text{SQRT}(J_2) - I_1$ space.

Table 20. Delft material model coefficients functions.

	a	b	d	e
R	316.86	17,074.55	-9.28	1.75
γ	0.20	-0.15	-13.91	2.13
n	2.00	2075.86	0.48	1.06
α	-0.63	-93.39	-5.01	1.35

Figure 148 shows the strain rate-dependent yield surface that was constructed using the characterized parameters when the viscoplastic strain was equal to zero (i.e., the initial yield surface). It was observed that the initial yield surface increased as the temperature decreased; the reduced strain rate increased. This behavior coincided with observations from constant strain-rate tests in which more viscoplastic strains were developed under a small, reduced strain rate (or higher temperature).

As shown in equation 164, the second term in the square root always had to be smaller than the first term in order to construct a valid yield surface. However, because of the numerical errors involved in the characterization process of α and n , the prediction program was often required to calculate the square root of a negative number during analysis. This situation was encountered without t-TS, as mentioned by others.⁽³⁶⁾

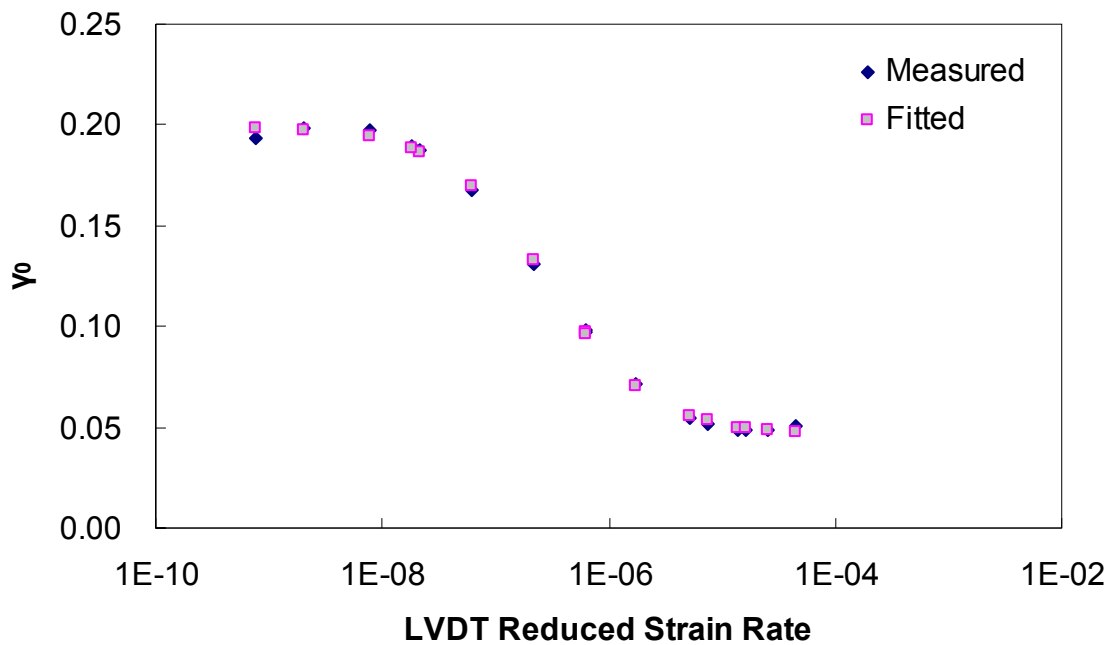


Figure 144. Graph. Determined γ_0 parameter function.

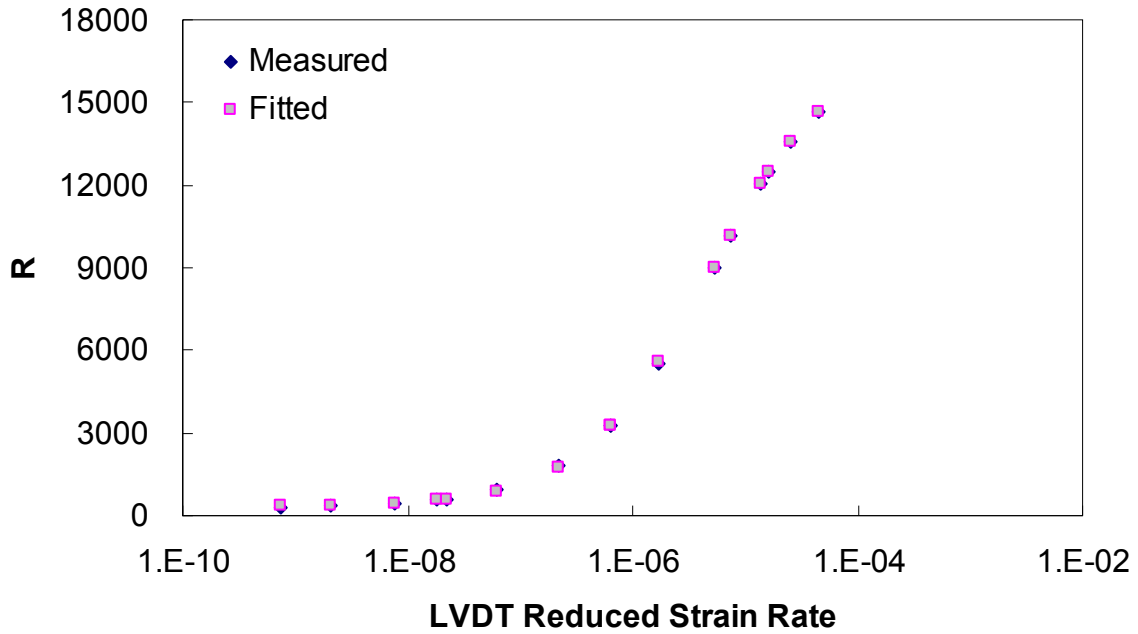


Figure 145. Graph. Determined R parameter function.

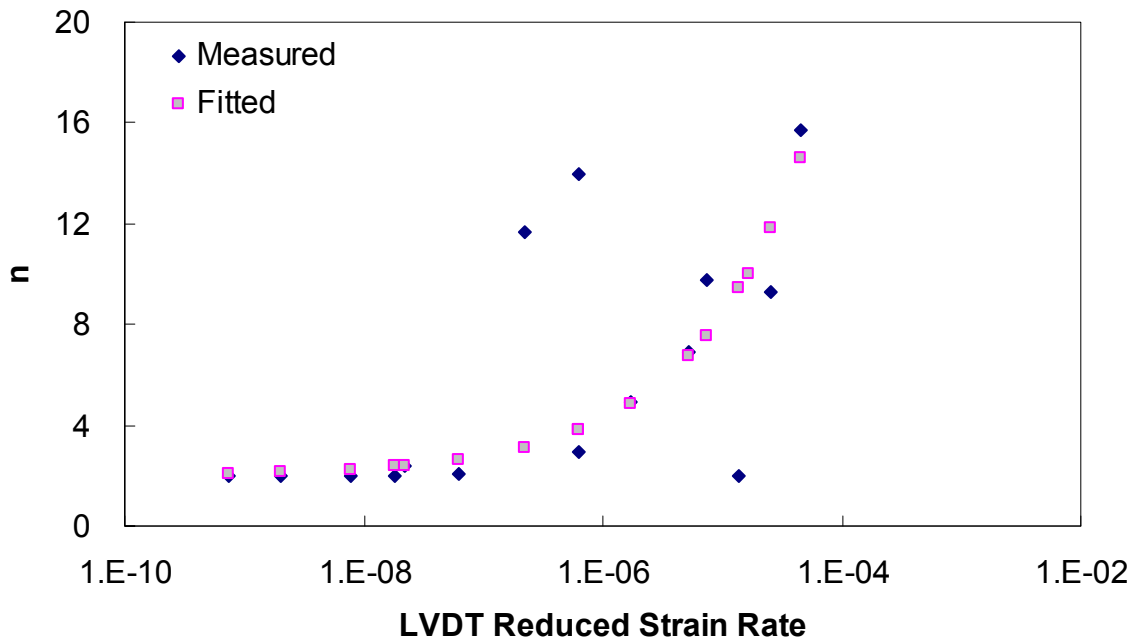


Figure 146. Graph. Determined n parameter function.

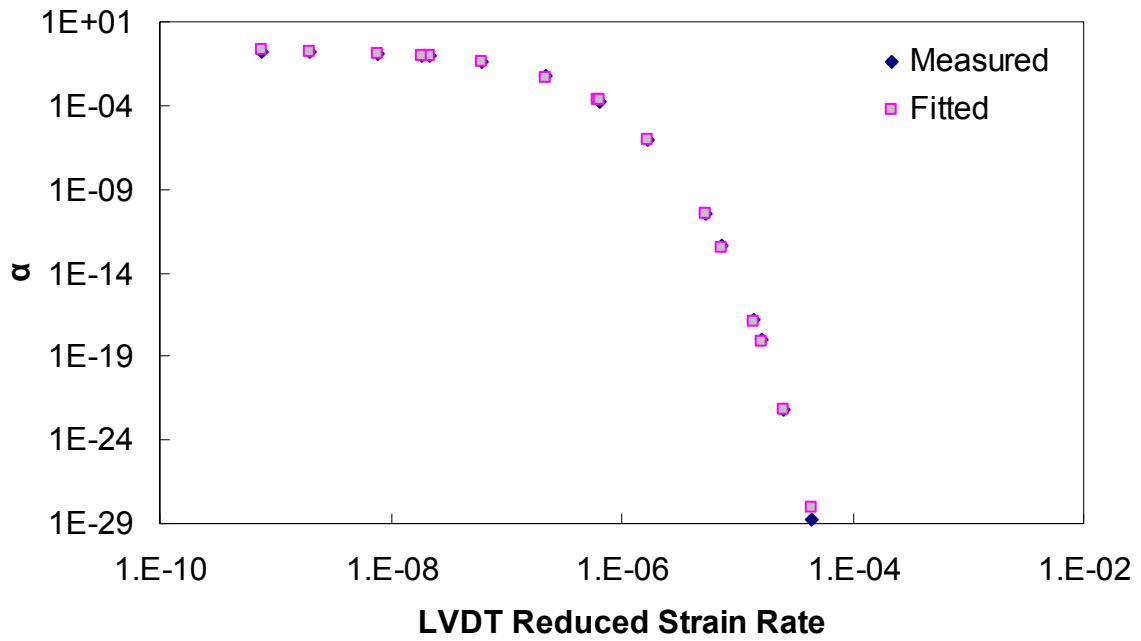


Figure 147. Graph. Determined α_0 parameter function.

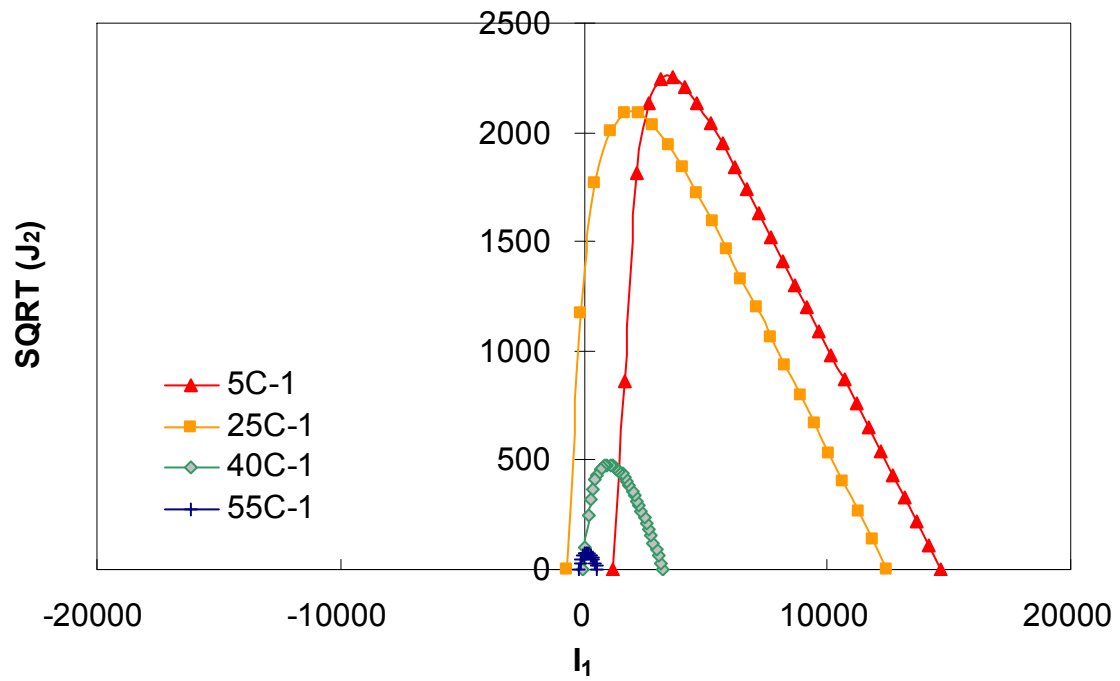


Figure 148. Graph. Rate-dependent initial yield surface.

5.3.2.2. University of Maryland Model

As shown in equation 73, a simplified HISS-Perzyna model was suggested by researchers at the University of Maryland.⁽²⁸⁾ Equation 168 represents a general form of the hardening function used for the suggested model.

$$\alpha = \alpha_0 e^{-\kappa \cdot \epsilon_{vp}} \quad (168)$$

Where:

α_0 and κ = Material constants.

However, the observation made in subsection 5.1.2.3 indicates that a single hardening function, equation 168, was not sufficient to represent the characteristic behavior of the material, such as softening during unloading. Therefore, one more variable, the viscoplastic strain increment during loading, was introduced into equation 168. Equation 169 represents the modified function α to incorporate the variation of the viscoplastic strain rate during the pulse time in the existing model. α_1 and α_2 in equation 169 describe general variations of α in terms of viscoplastic strain and a local variation of α in terms of incremental viscoplastic strain in a pulse, respectively.

$$\alpha = \kappa_1 \alpha_1 \alpha_2 \quad (169)$$

Where:

$$\alpha_1 = e^{-\kappa_2 \epsilon_{vp}} \quad (170)$$

$$\alpha_2 = \left(1 - e^{-\kappa_2 \Delta \epsilon_{vp}}\right) \quad (171)$$

Figure 149 presents the variation of α determined by using a modified alpha-viscoplastic relationship for five 6.4-s pulses with 1,800 kPa of load level. As shown, α was no longer a simple decreasing function of the viscoplastic strain, but had multiple decreasing functions of which independent variables were incremental viscoplastic strain during each load pulse and overall viscoplastic strain. The incremental viscoplastic strain was reset to zero each time the material was unloaded.

Figure 150 through figure 152 present measured and predicted viscoplastic strains by using a modified hardening function. The model was able to describe viscoplastic strain development for various loading conditions, such as VT, RVT, and CLT; this capability was not possible in the existing HISS-Perzyna model. However, even though incremental viscoplastic strain in a pulse described multiple hardening rates at certain viscoplastic strains, it was more reasonable to assume that the multiple hardening rates were caused by the viscoelastic property of the material, given the rate dependency of the softening. Therefore, a viscoplastic model with a rate-dependent hardening-softening function was developed and is presented in subsection 5.3.3.

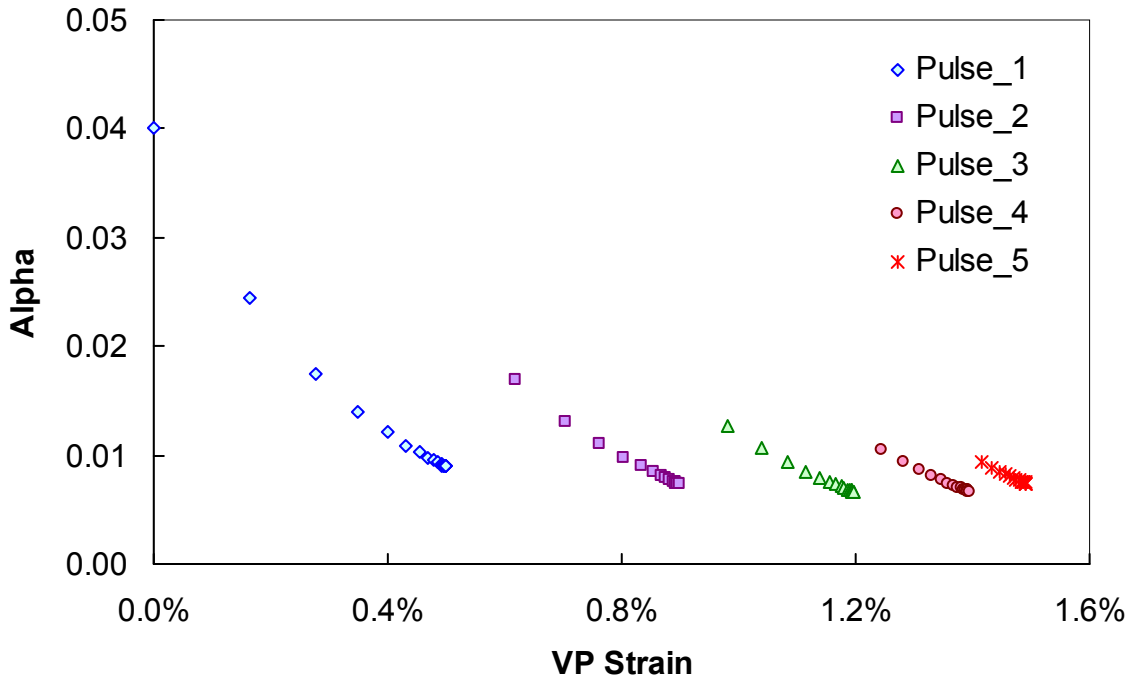


Figure 149. Graph. Variation of α for 1,800 kPa CLT loading (500 kPa confinement).

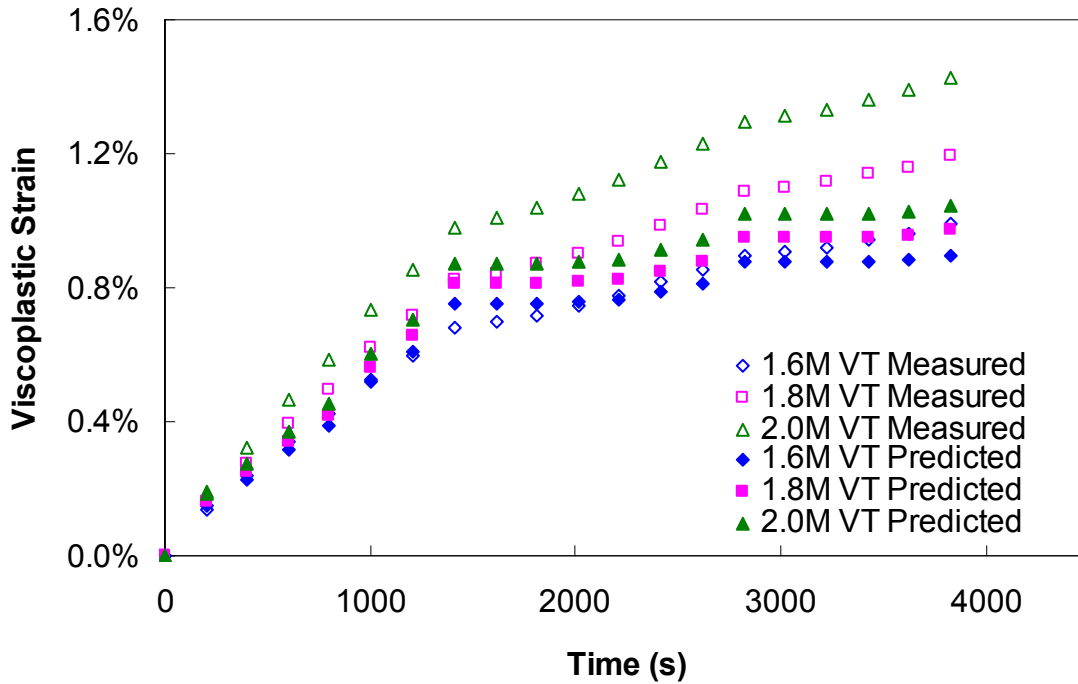


Figure 150. Graph. Viscoplastic strain predictions for VT tests (500 kPa confinement).

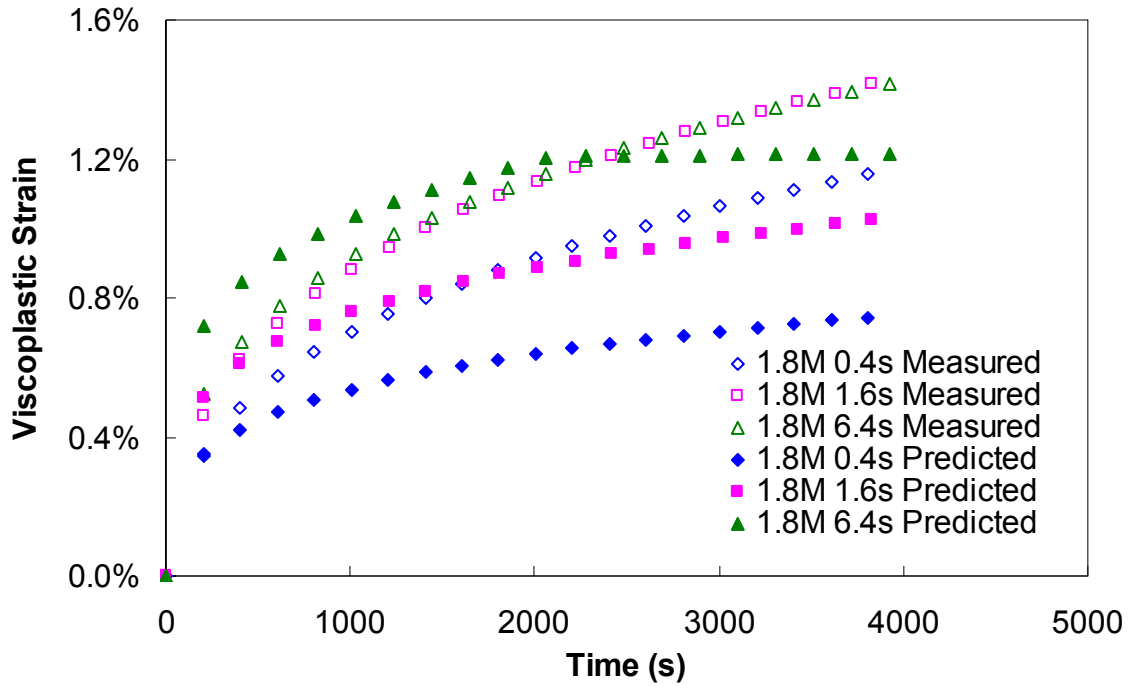


Figure 151. Graph. Viscoplastic strain predictions for CLT tests (500 kPa confinement).

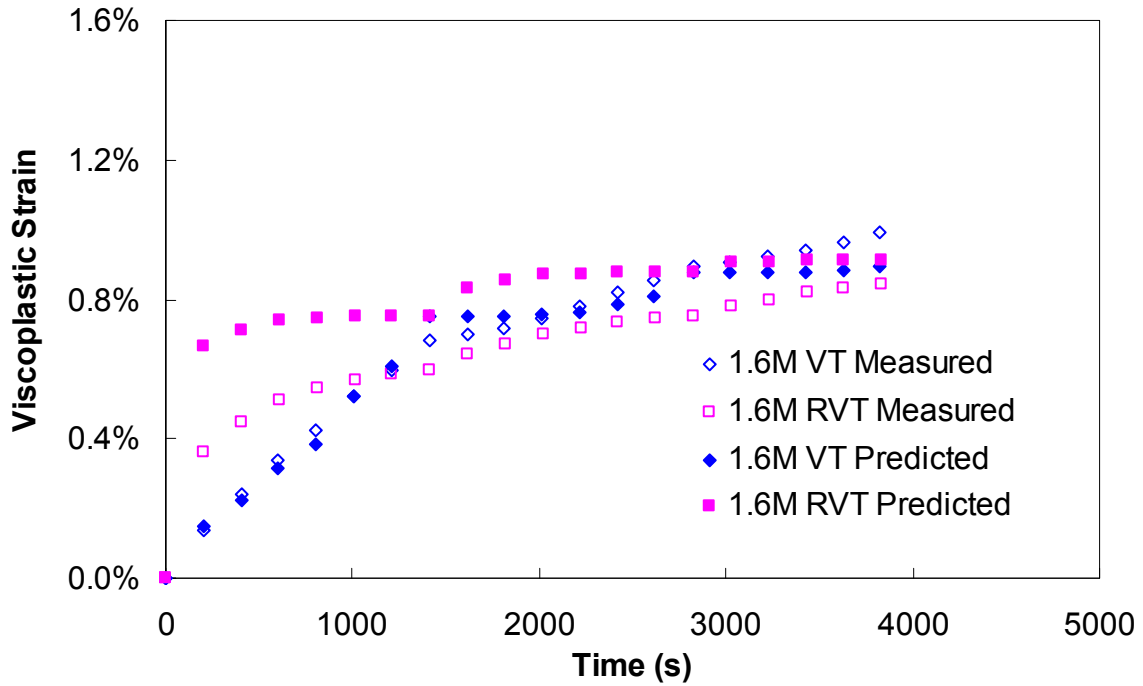


Figure 152. Graph. Viscoplastic strain predictions for RVT tests (500 kPa confinement).

5.3.3. Development of a Viscoplastic Model Using Rate-Dependent Yield Stress

The model developed in this research was capable of capturing both additional hardening that was due to aggregate interlocking and rate-dependent softening due to viscoelastic relaxation. Viscosity in Perzyna's evolution law is separated into a constant term and a viscoplastic strain-dependent term that together represent the change of viscosity in viscoplastic flow. The yield stress function that takes into account rate-dependent hardening and softening is also described in subsection 5.3.3.1.

5.3.3.1. Flow Rule and Yield Function for Developed Viscoplastic Model

As an expansion of equation 55, a general flow rule for materials exhibiting kinematic and isotropic hardening is represented in equation 172. m amplified or reduced the stress rate dependency of the model, and D determined the viscosity in the viscoplastic flow. When D was a constant, it was assumed that the effect of the change in viscosity on the response of the material was taken into account by the yield stress function. However, when variations of yield stress were affected by the viscoelastic property of the material, it seemed reasonable to consider the viscosity in the viscoplastic flow as a function that was not subjected to yield stress.

$$\dot{\epsilon}_{ij}^{vp} = \left\langle \frac{f(\sigma - \alpha) - r}{D} \right\rangle^m \frac{\partial f}{\partial \sigma_{ij}} \quad (172)$$

Where:

- α = Kinematic hardening function.
- γ = Isotropic hardening function.
- D = Viscosity parameter.
- m = Rate-dependency parameter.

Therefore, a flow rule that takes into consideration the variations of viscosity in the viscoplastic flow is suggested in equation 173 by incorporating Perzyna's flow rule and Von Mises' yield criterion. In equation 173, D was the viscosity and represented the scalar hardening and softening as described above. The anisotropic behavior of the material was also integrated by using D_{ij} . Meanwhile, G_{ij} represented the orientation-dependent isotropic hardening function that reflected the viscoplastic and viscoelastic property of the material. Because the material was subjected only to compressive stress, the kinematic hardening rule was not introduced in this model. The viscosity (D) was related to aggregate interlocking and was represented as a function of the viscoplastic strain, as shown in equation 174. Because the function could represent both increasing and decreasing viscosity according to the viscoplastic strain, it had the potential to represent the behavior of HMA mixtures in the tertiary region as well as in the primary and secondary regions.

$$\dot{\epsilon}_{ij}^{vp} = \frac{3}{2} \frac{1}{\eta_0} \left\langle \frac{J(\sigma_{ij} - G_{ij})}{D} \right\rangle^m \frac{(s_{ij} - g_{ij})}{J(\sigma_{ij} - G_{ij})} = B \left\langle \frac{J(\sigma_{ij} - G_{ij})}{D} \right\rangle^m \frac{(s_{ij} - g_{ij})}{J(\sigma_{ij} - G_{ij})} \quad (173)$$

Where:

D = Viscosity related to aggregate interlocking, equation 174.

$\eta_0, m, \alpha, \beta, \gamma$ = Material constants.

D_0 = Initial viscosity.

s_{ij} = Deviatoric stress tensor.

g_{ij} = Deviatoric back stress tensor.

σ_{ij} = Stress tensor.

G_{ij} = Yield stress tensor.

$J(\sigma_{ij} - G_{ij})$ = The second invariant of $(\sigma_{ij} - G_{ij})$.

$$D = D_0 + \alpha \sin \left[\beta \left(1 - e^{-\gamma \varepsilon_{vp}} \right) \right] \quad (174)$$

However, as discussed in subsection 5.1.2.3, rate-dependent softening, which implied the possibility of a multiple state of the material at certain viscoplastic strains, was observed when HMA was subjected to repetitive loading. In order to introduce the characteristic behavior of HMA into the viscoplastic constitutive model, equation 175, which was one of the simplest forms, was suggested as the hardening-softening function.

$$\dot{G} = g(\dot{\varepsilon}_{vp}, \varepsilon_{vp}, G) \quad (175)$$

In equation 175, the yield stress increased as the viscoplastic strain and viscoplastic strain rate increased during loading, whereas it decreased during unloading (when the viscoplastic strain rate was zero). Figure 153 presents a schematic concept of the variation of yield stress subjected to a creep and recovery loading condition. The remaining yield stress, which was yield stress at the asymptote, was governed by the viscoplastic strain at the end of the loading condition, ε_0^{vp} , and material constants E_1 and E_2 . The decreasing yield stress during unloading allowed a multiple viscoplastic strain rate at a certain viscoplastic strain.

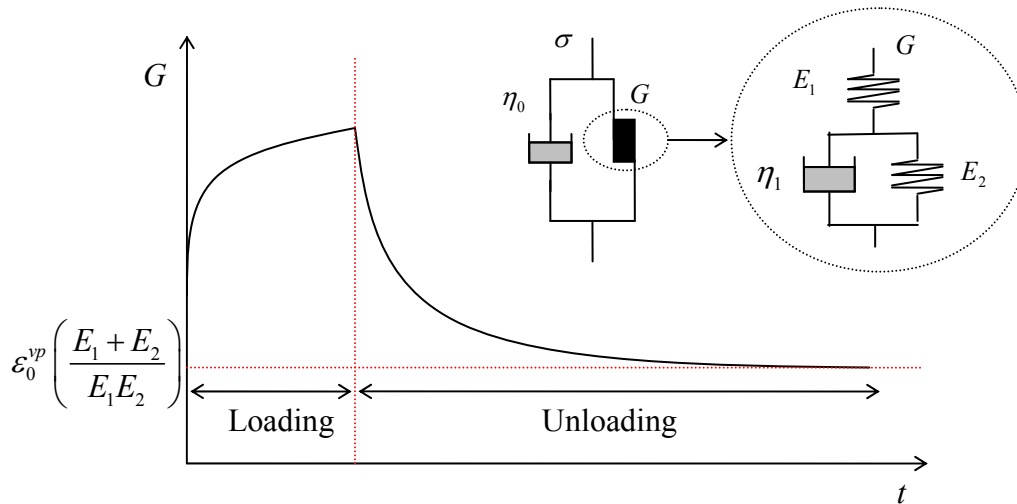


Figure 153. Illustration. Variation of yield stress (Standard Linear Solid model).

Because of their simplicity, equation 176 was suggested as a hardening-softening function to confirm the characteristics of the model for an arbitrary stress history, and equation 177 was suggested to predict the actual behavior of the HMA mixture. As shown in equation 177, the hardening-softening function was represented as the convolution integral, including the relaxation modulus. Material constants A and B were introduced into the relaxation modulus to develop a relationship between the relaxation modulus, which was the LVE property, and the viscoplastic yield stress. Additionally, by utilizing the material constants, the number of parameters needed to calibrate the model could be reduced. In calculating the yield stress, the state variable approach was used to reduce computational time, as shown in equation 178.

$$\dot{G} = \frac{E_1 E_2}{\eta_2} \varepsilon^{vp} + E_1 \dot{\varepsilon}^{vp} - \left(\frac{E_1 + E_2}{\eta_2} \right) G \quad (176)$$

Where:

E_1, E_2, η_1, η_2 = Material constants.

$$G = \int_0^t \left(A \cdot E_0 + B \cdot \sum E_i e^{-\frac{t-\tau}{\rho_i}} \right) \frac{d\varepsilon_{vp}}{d\tau} d\tau \quad (177)$$

Where:

A, B = Material constants.

E_0, E_i = Prony coefficients determined for the relaxation modulus.

ρ_i = Relaxation time.

Equation 177 was solved using the state variable approach to predict strains and calculate pseudo strains. This approach is shown mathematically in equation 178.

$$G^{n+1} = \zeta_0^{n+1} + \sum_{i=1}^m \zeta_i^{n+1} \quad (178)$$

Where:

$$\zeta_0^{n+1} = A \left[\varepsilon_{vp}^{t^{n+1}} - \varepsilon_{vp}^{t^n} \right] E_0 \quad (179)$$

$$\zeta_i^{n+1} = B \left[e^{-\frac{\Delta t}{\rho_i}} \zeta_i^n + e^{-\frac{\Delta t}{2\rho_i}} \left[\varepsilon_{vp}^{t^{n+1}} - \varepsilon_{vp}^{t^n} \right] E_i \right] \quad (180)$$

5.3.3.2. Characteristics of the Developed Model for Arbitrary Stress History

In order to confirm the characteristics of the developed viscoplastic model, the following predictions were made for the arbitrary stress histories by using equation 173 and equation 176. In this study, D was considered a constant to simplify the calibration and prediction processes.

Two sets of stress histories were generated, as shown in figure 154 and figure 157. Table 21 shows the material constants used in this analysis.

Table 21. Material coefficients used for the developed model analysis.

m	D	η_1	η_2	E_1	E_2
2	3,000	10	50,000	500	200

5.3.3.2.1. Effect of Rest Period:

Figure 154 shows two different stress histories used to check the sensitivity of the viscoplastic model to the effects of rest periods. For both stress histories, stress levels and the cumulative loading time were fixed to 2,000 units less stress and 160 s, respectively. However, for the first stress history, 8.0 s of rest between the loading pulses were allowed, whereas only 1 s of rest was allowed for the second loading history. Figure 155 presents the variation of yield stress for each stress history, and as expected, the model showed different yield stress developments depending upon the rest period.

Figure 156 presents the viscoplastic strain developed by each stress history. It shows more viscoplastic strain for a longer rest period. This result corresponded to the experimental observations made from figure 98.

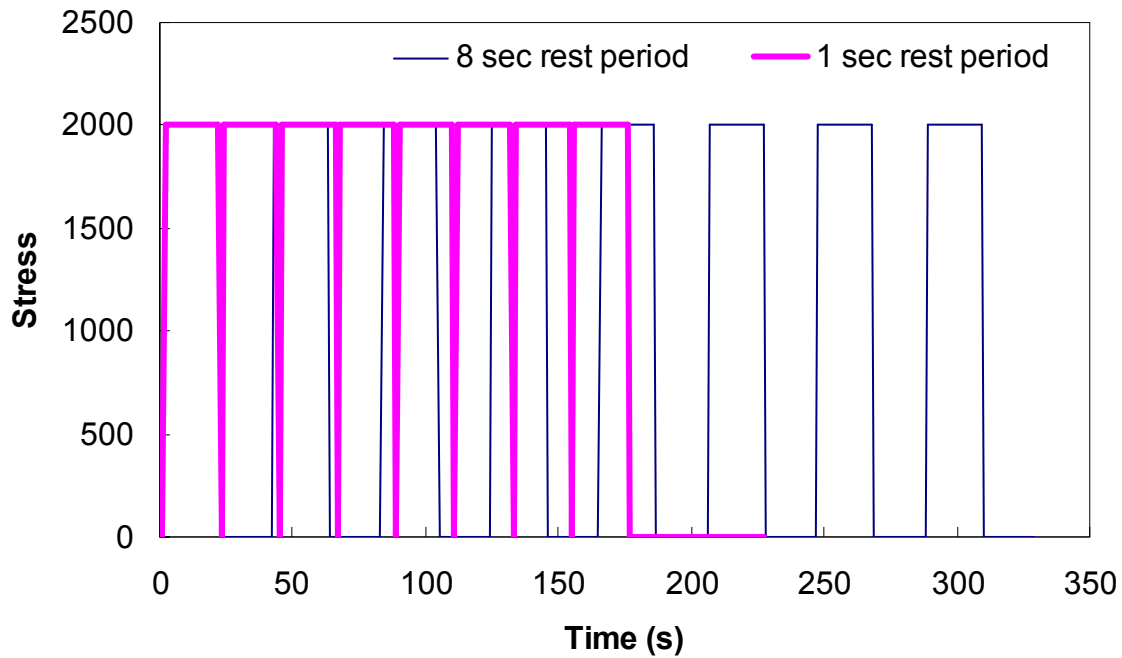


Figure 154. Graph. Stress histories for rest period analysis.

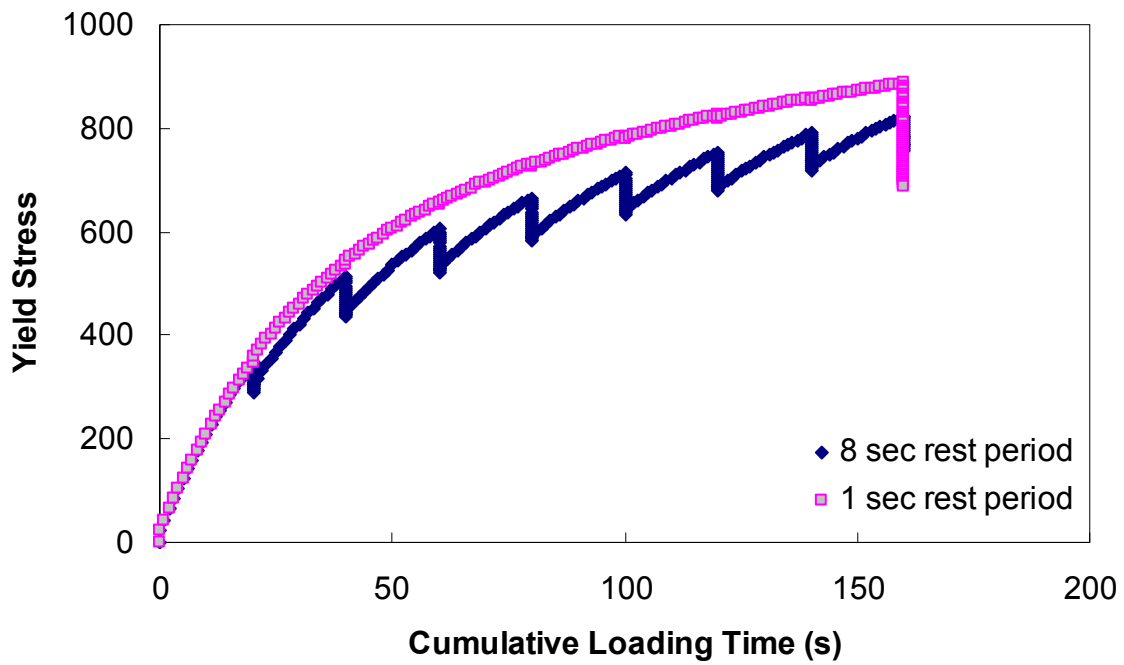


Figure 155. Graph. Yield stress versus cumulative loading time (rest period analysis).

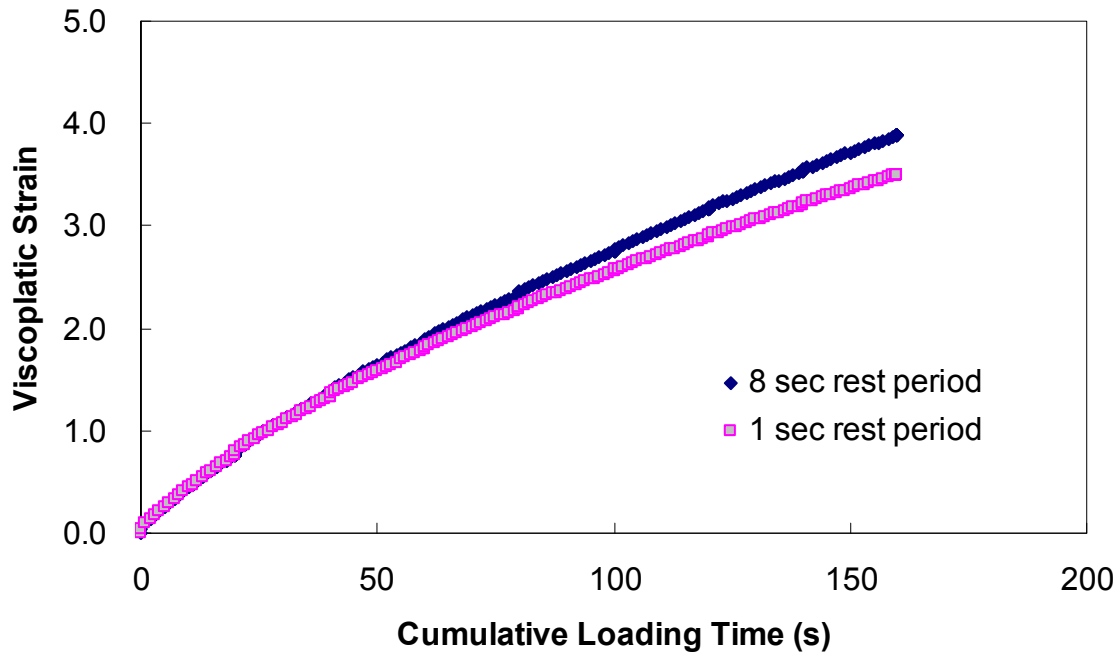


Figure 156. Graph. Viscoplastic strain versus cumulative loading time (rest period analysis).

5.3.3.2.2. Effect of Loading Time:

Figure 157 presents another set of stress histories used to check the effects of loading time. For these stress histories, the load level, rest periods, and cumulative loading time were fixed to

2,000 units, 4 and 66 s, respectively. However, the first loading history consisted of 6 pulses at 11 s long, and the second loading history consists of 22 pulses at 3 s long.

The analysis results for the given stress histories are shown in figure 158. The loading history with shorter individual loading times showed more viscoplastic strain, which was identical to the CLT test results. As shown, the viscoplastic model that incorporated the softening rule appeared to account for the pulse time effect. As shown in figure 156 and figure 158, the viscoplastic model with the rate-dependent hardening-softening capability could account for the effects of loading time.

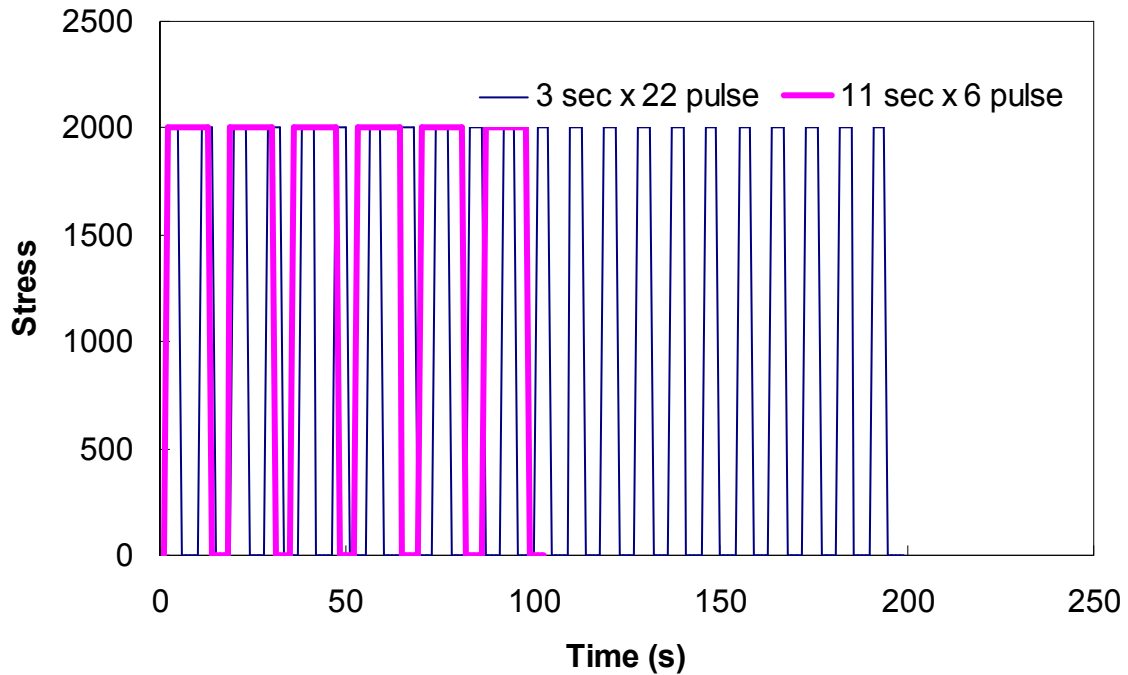


Figure 157. Graph. Stress history for loading time analysis.

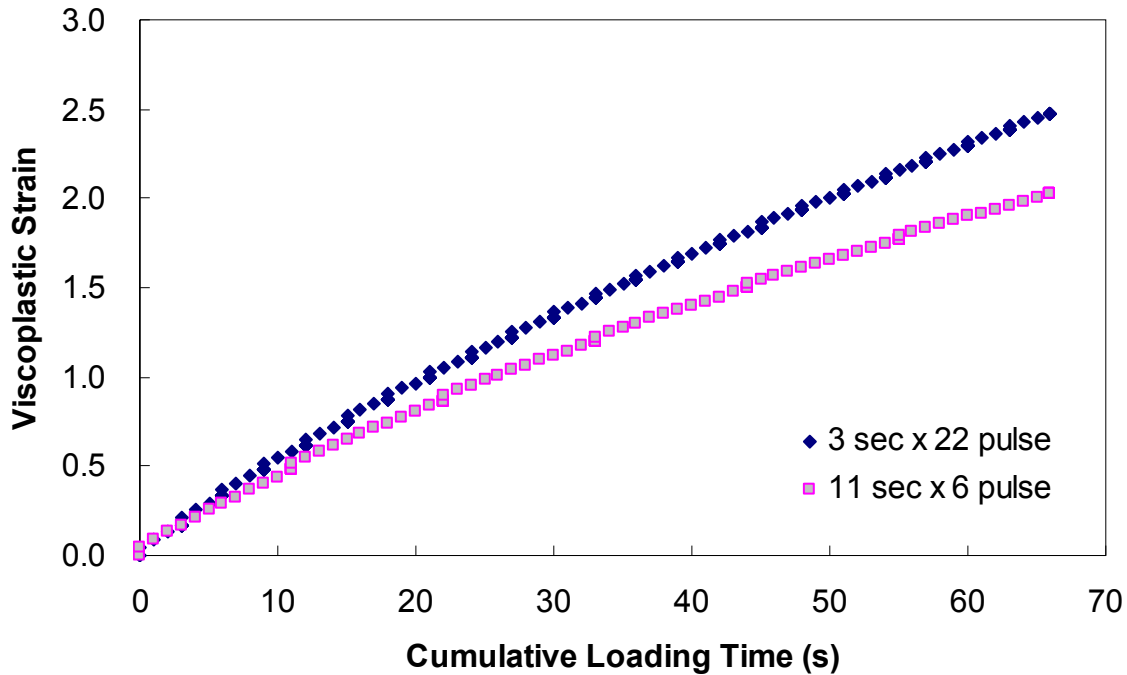


Figure 158. Graph. Viscoplastic strain versus cumulative loading time (loading time analysis).

5.4. CHARACTERIZATION AND VERIFICATION OF THE VISCOPLASTIC MODEL

5.4.1. Calibration

Prior to the calibration process, data points acquired during the unloading period were filtered to reduce the computational time. Strains measured at the end of the rest periods were defined as the objective function. The nonlinear optimization function (lsqnonlin) in Matlab™ was utilized to minimize errors between the measured and predicted viscoplastic strains. Based on the model calibrated for the VT and VL tests, the viscoplastic strains of the other loading conditions, such as CLT and VLT, could be predicted. Table 22 shows the coefficients determined from the calibration process for 140 and 500 kPa confining pressures.

Table 22. Compression viscoplastic material model coefficients.

Confining Pressure (kPa)	m	D_0	α	β	γ	A	B
140	3.83	1,951.76	2,758.93	3.07	258.34	0	6.3E-06
500	9.99	3,460.62	3,569.28	1.87	156.96	0	5.2E-03

Figure 159 and figure 160 present the calibration results for VT and VL testing at 140 kPa confining pressure, and figure 161 and figure 162 present the calibration results for VT and VL testing at 500 kPa confining pressure. In general, the predicted and measured viscoplastic strains match very well, although there was a slight discrepancy in the VT and VL 500 kPa confining pressure results.

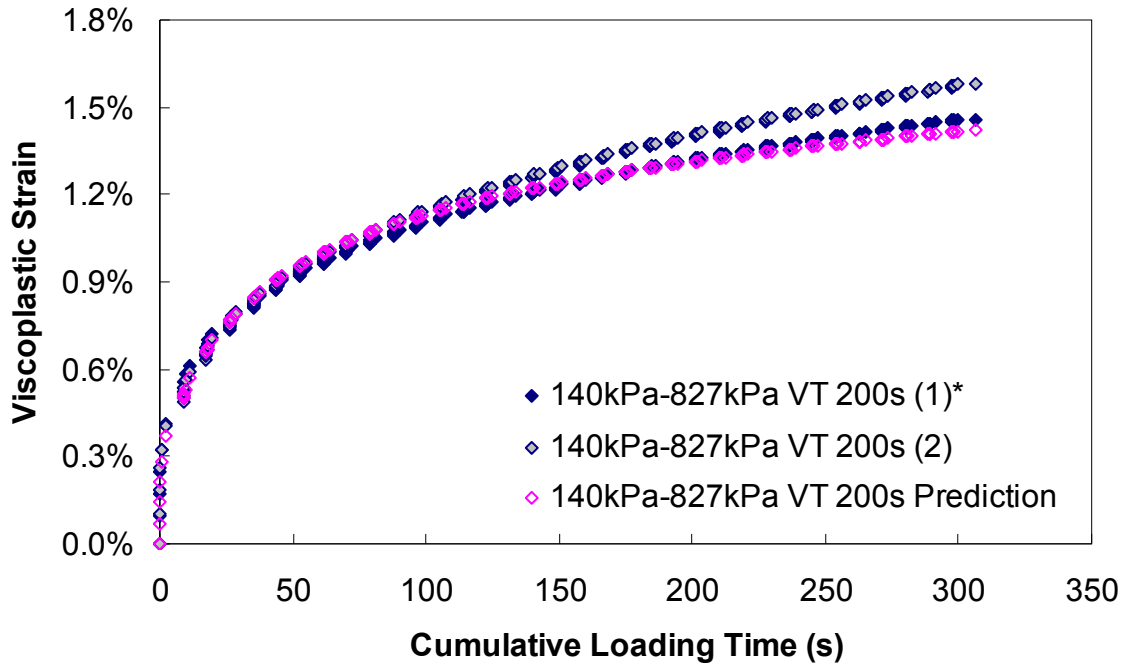


Figure 159. Graph. Viscoplastic strain versus cumulative loading time (140 kPa confinement VT).

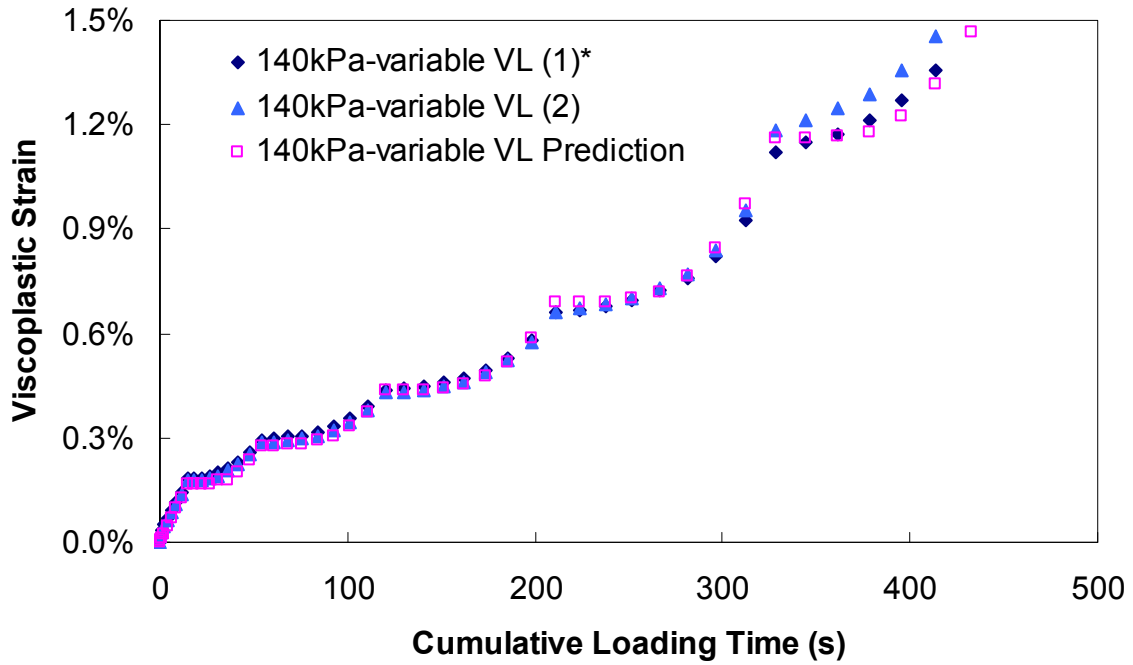


Figure 160. Graph. Viscoplastic strain versus cumulative loading time (140 kPa confinement VL).

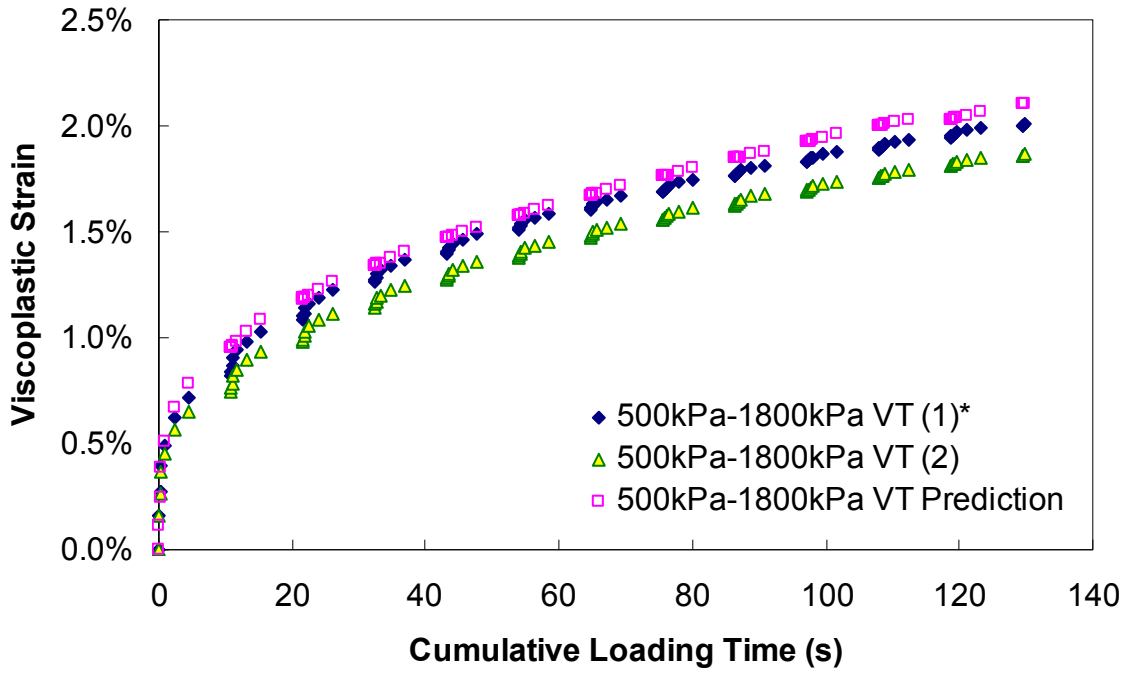


Figure 161. Graph. Viscoplastic strain versus cumulative loading time (500 kPa confinement VT).

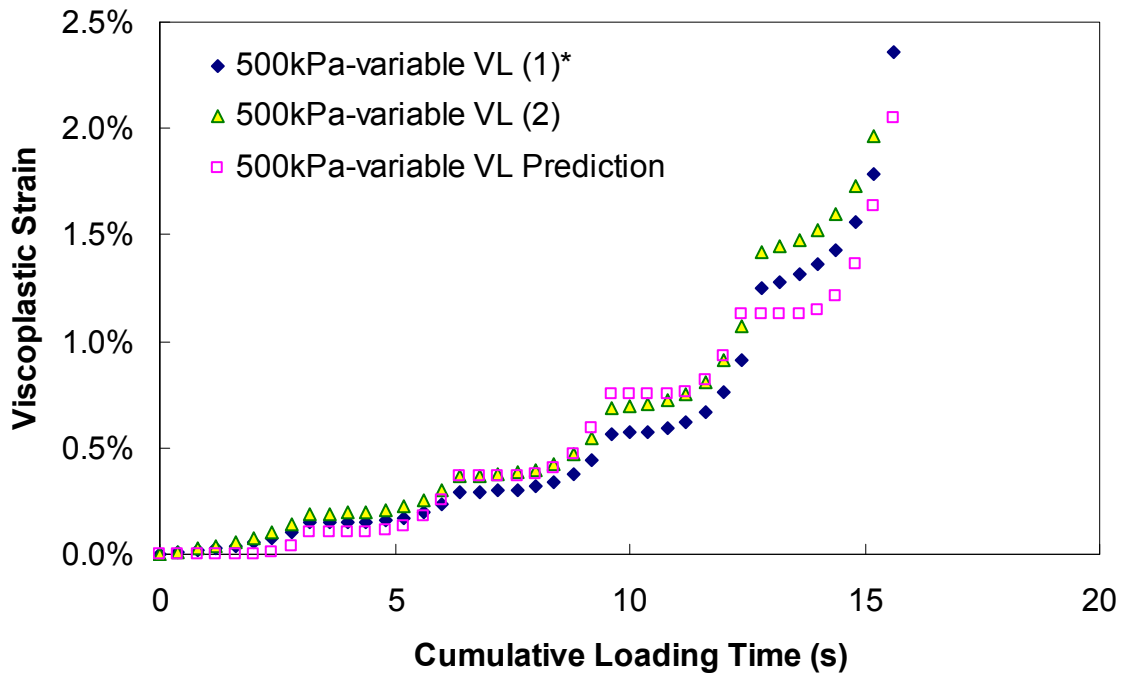


Figure 162. Graph. Viscoplastic strain versus cumulative loading time (500 kPa confinement VL).

5.4.2. Verification

Viscoplastic strain predictions for the 140-kPa confining pressure tests are presented in figure 163 through figure 166. Figure 163 shows the ability of the developed model to consider the effects of rest periods on the viscoplastic strain development even though the viscoplastic strains were slightly underpredicted. Figure 164 and figure 165 show the predictions for the VLT tests and a low load level VL test, respectively; these predictions were quite good. Figure 166 presents predictions for complex loading histories, which were a combination of VT test results and flow number test results. Up to 0.5-percent strain, the prediction of the viscoplastic strain matched well with the measured viscoplastic strain; however, the viscoplastic strain was underpredicted for the last strain level. This discrepancy could indicate a need to refine the softening function. Figure 167 to figure 172 present the viscoplastic strain predictions made for 500 kPa confining pressure tests. The overall prediction was good considering the complexity of the loading history.

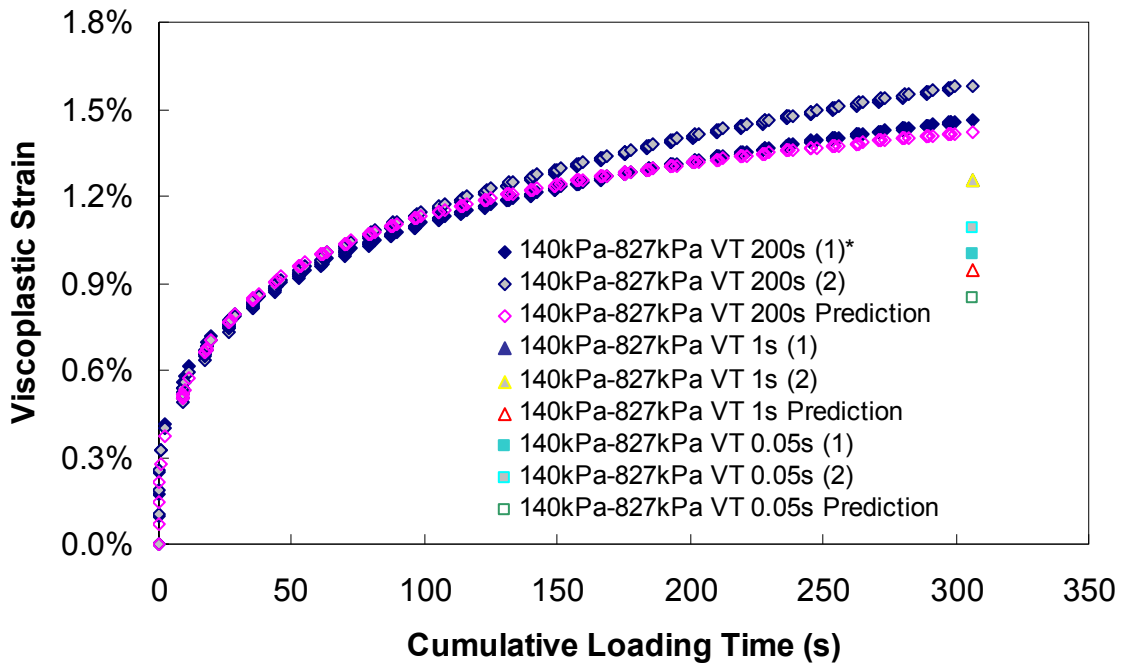


Figure 163. Graph. Viscoplastic strain versus cumulative loading time (140 kPa confinement VT).

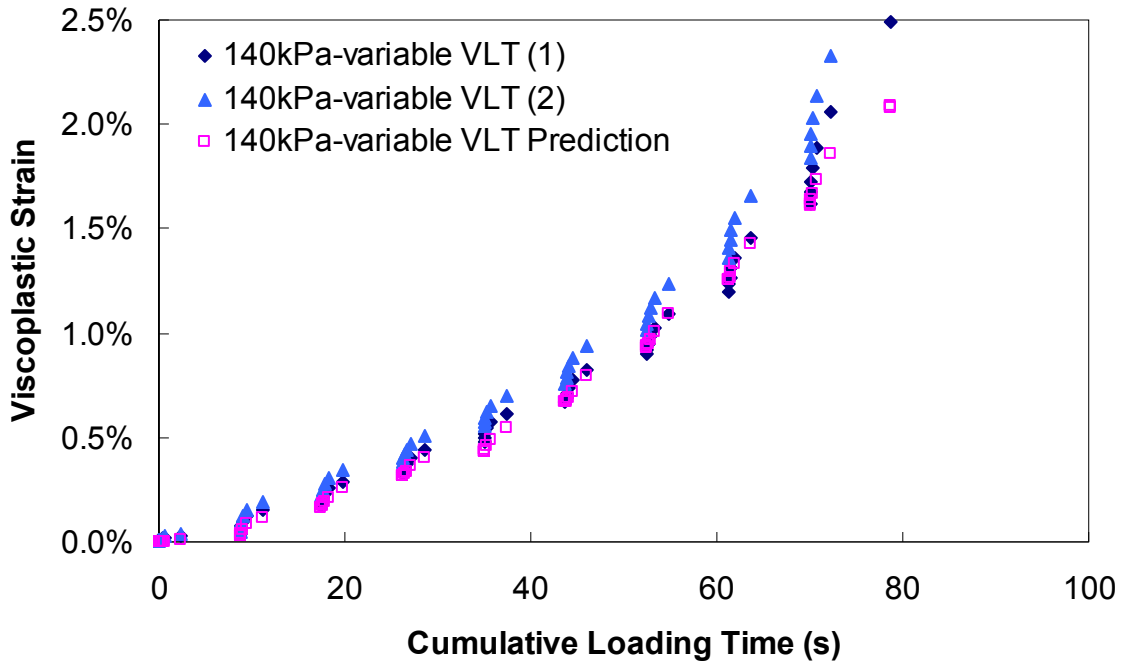


Figure 164. Graph. Viscoplastic strain versus cumulative loading time (140 kPa confinement VLT).

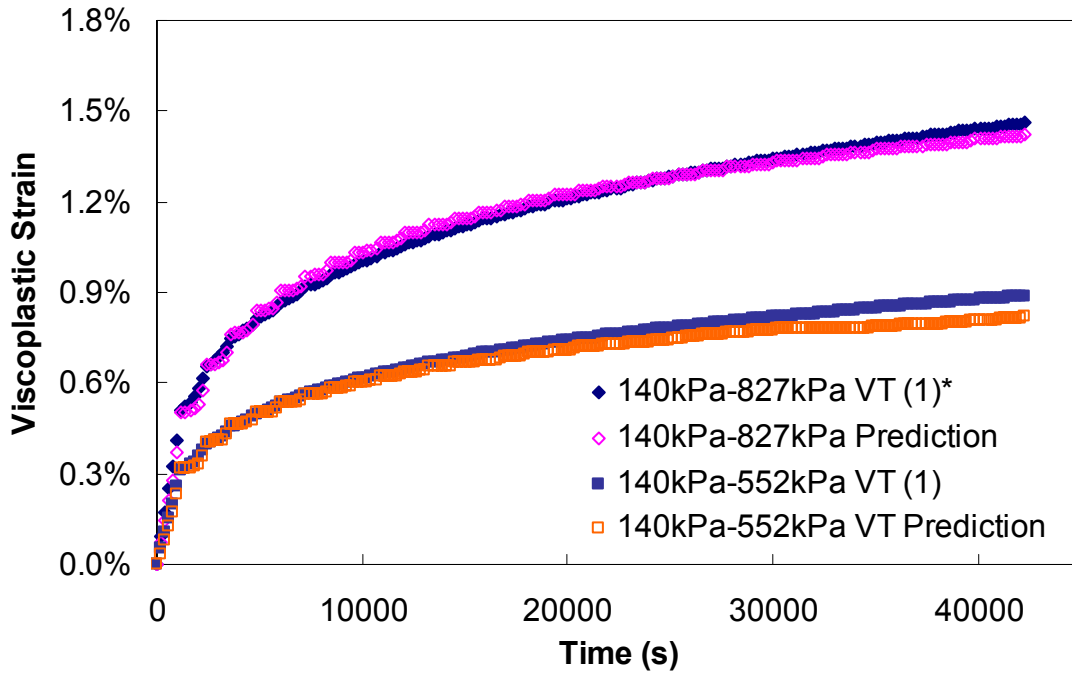


Figure 165. Graph. Viscoplastic strain versus cumulative loading time (140 kPa confinement VT).

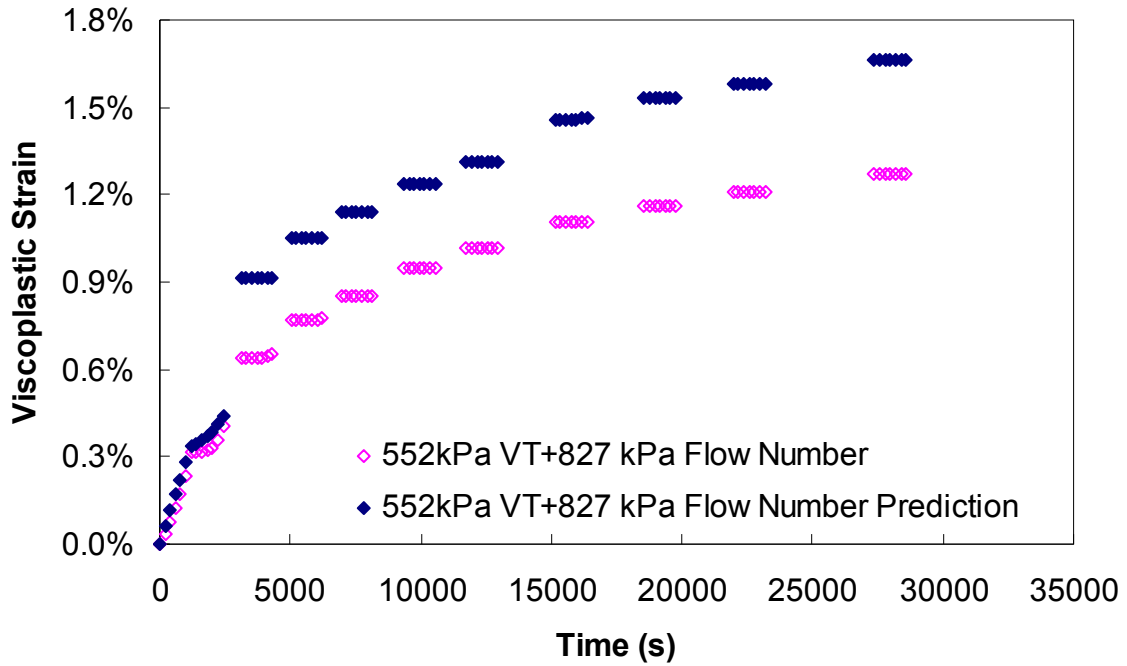


Figure 166. Graph. Viscoplastic strain versus cumulative loading time (140 kPa confinement VT + flow).

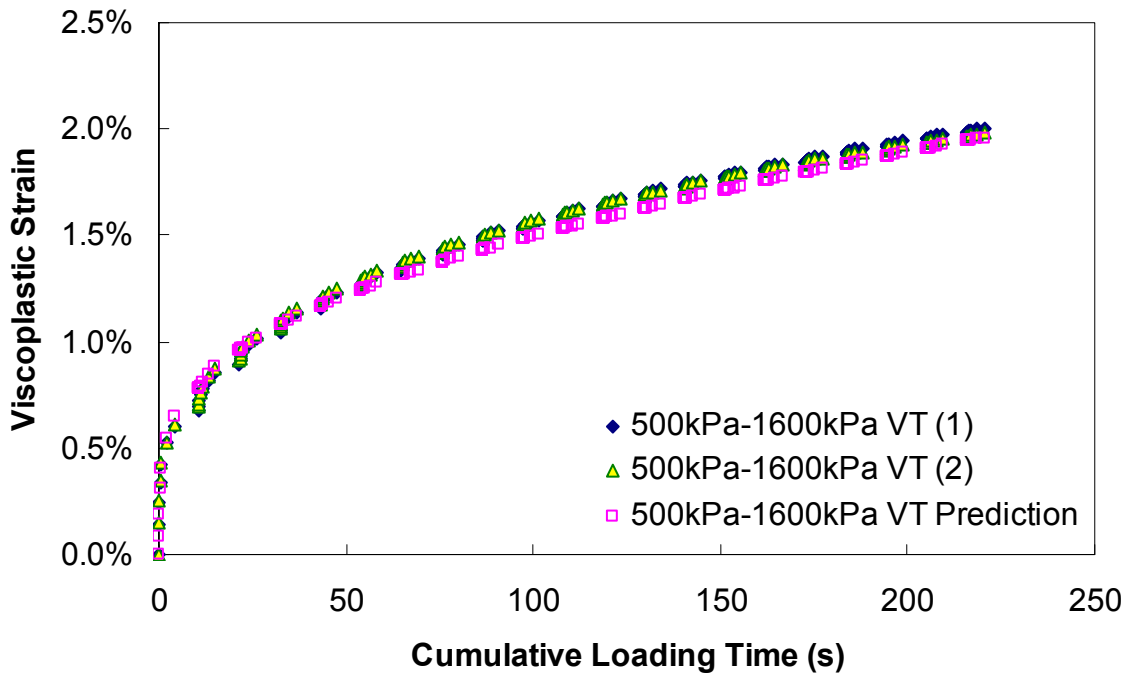


Figure 167. Graph. Viscoplastic strain versus cumulative loading time (500 kPa confinement 1,600 deviatoric VT).

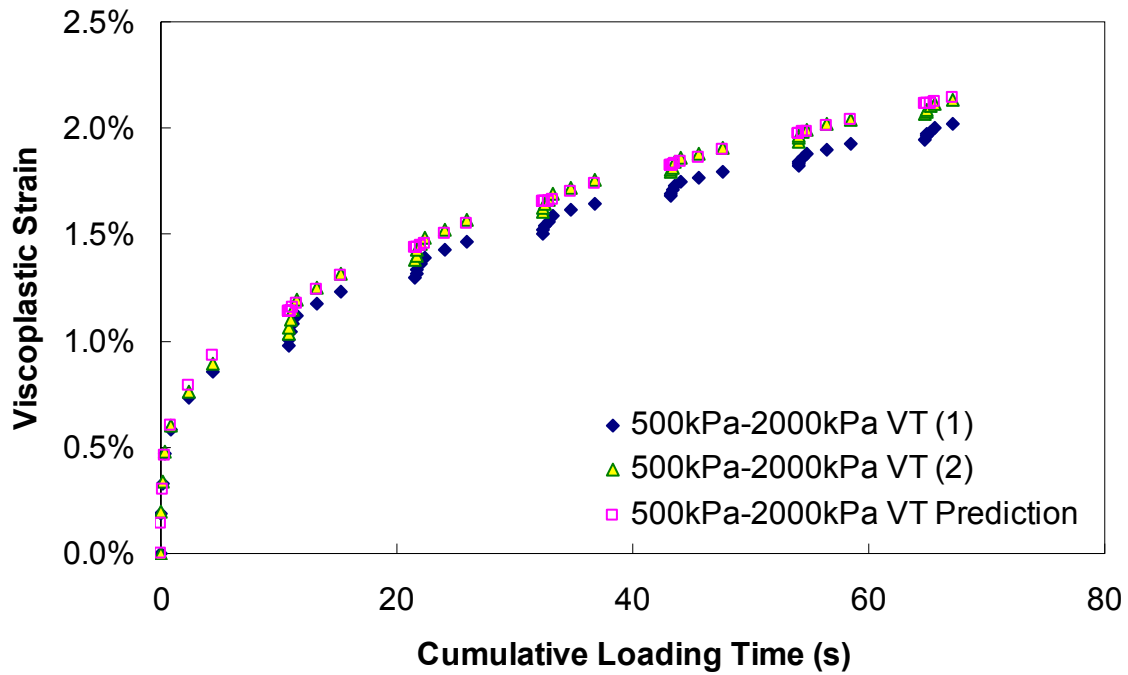


Figure 168. Graph. Viscoplastic strain versus cumulative loading time (500 kPa confinement 2,000 deviatoric VT).

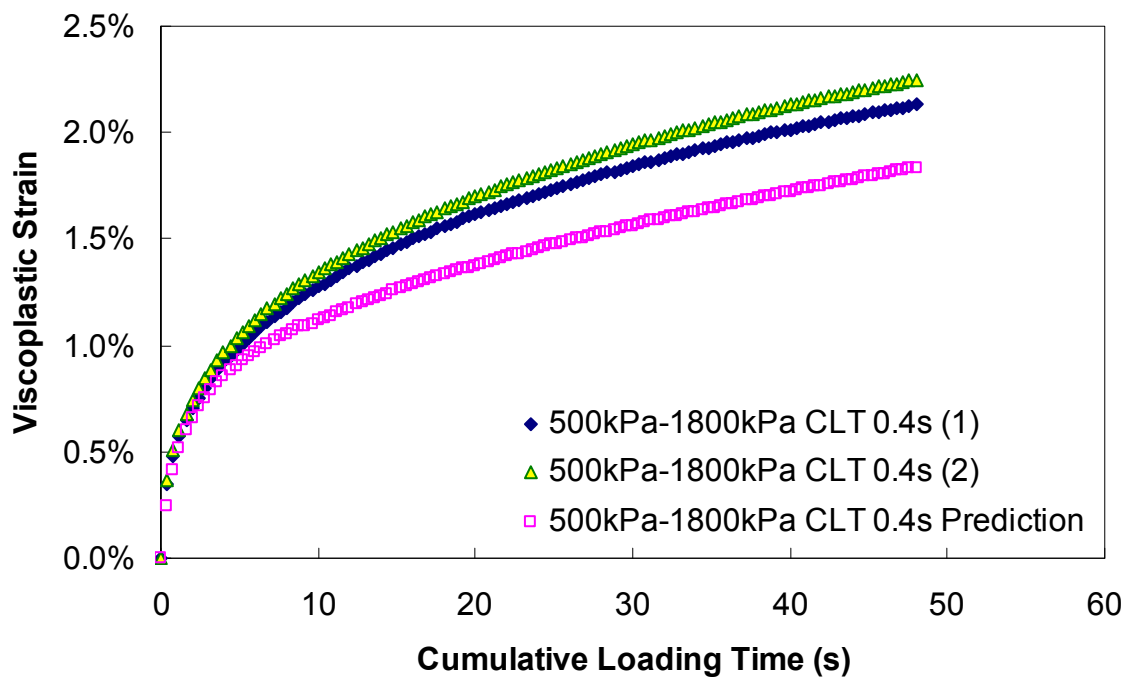


Figure 169. Graph. Viscoplastic strain versus cumulative loading time (500 kPa confinement 0.4 s CLT).

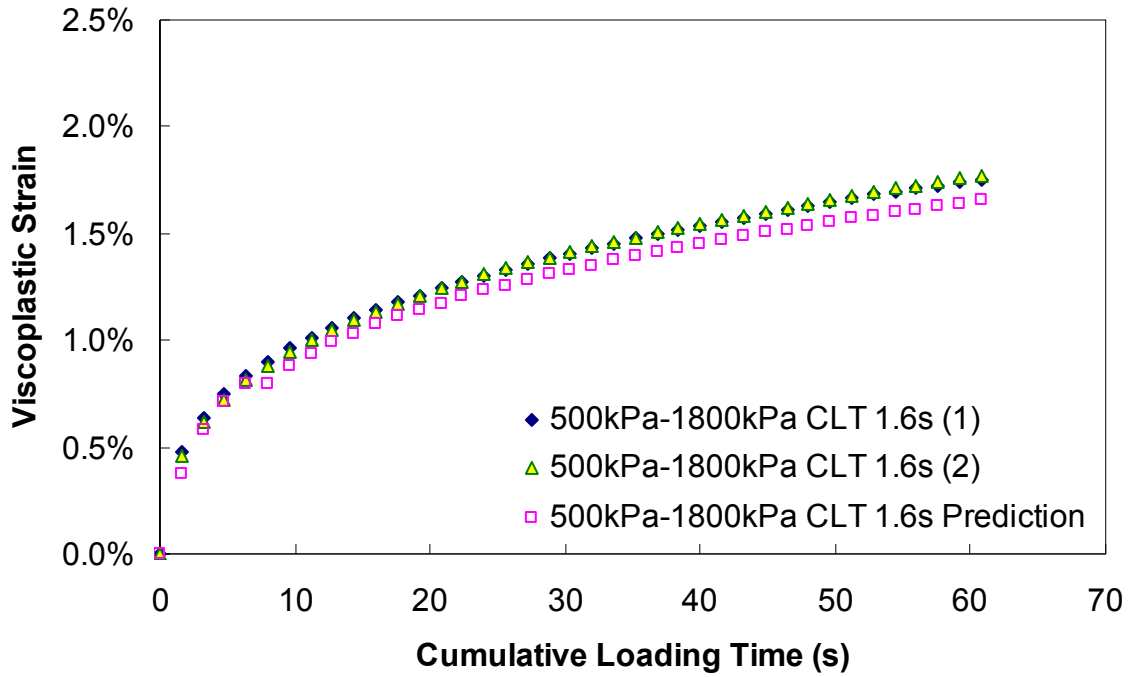


Figure 170. Graph. Viscoplastic strain versus cumulative loading time (500 kPa confinement 1.6 s CLT).

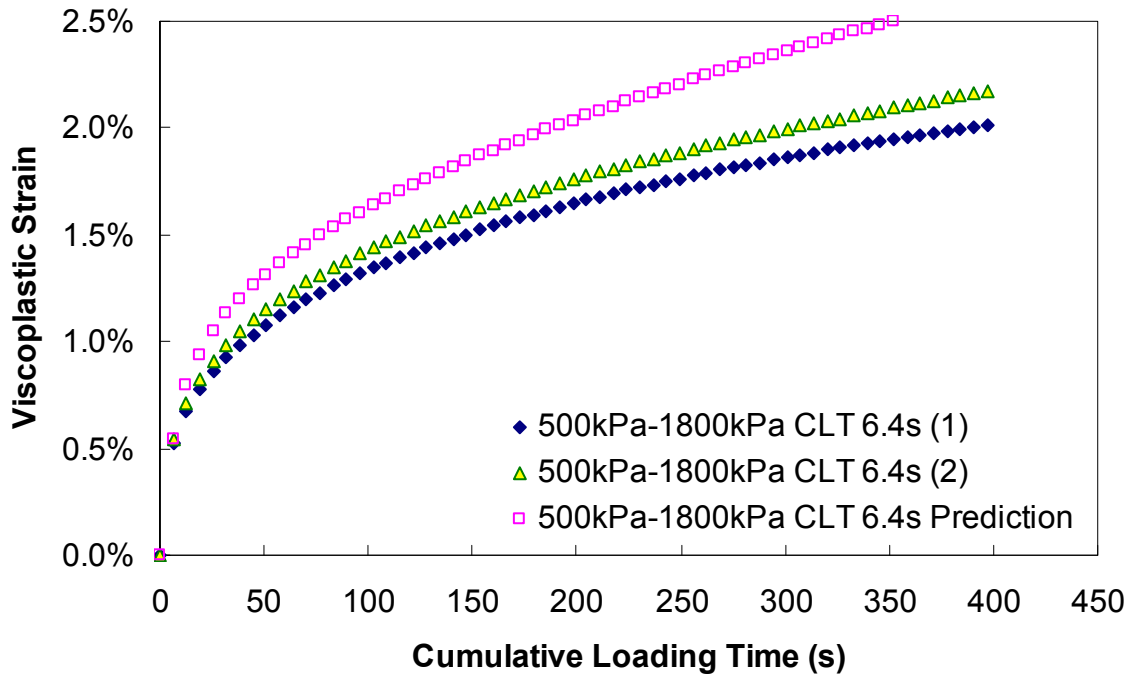


Figure 171. Graph. Viscoplastic strain versus cumulative loading time (500 kPa confinement 6.4 s CLT).

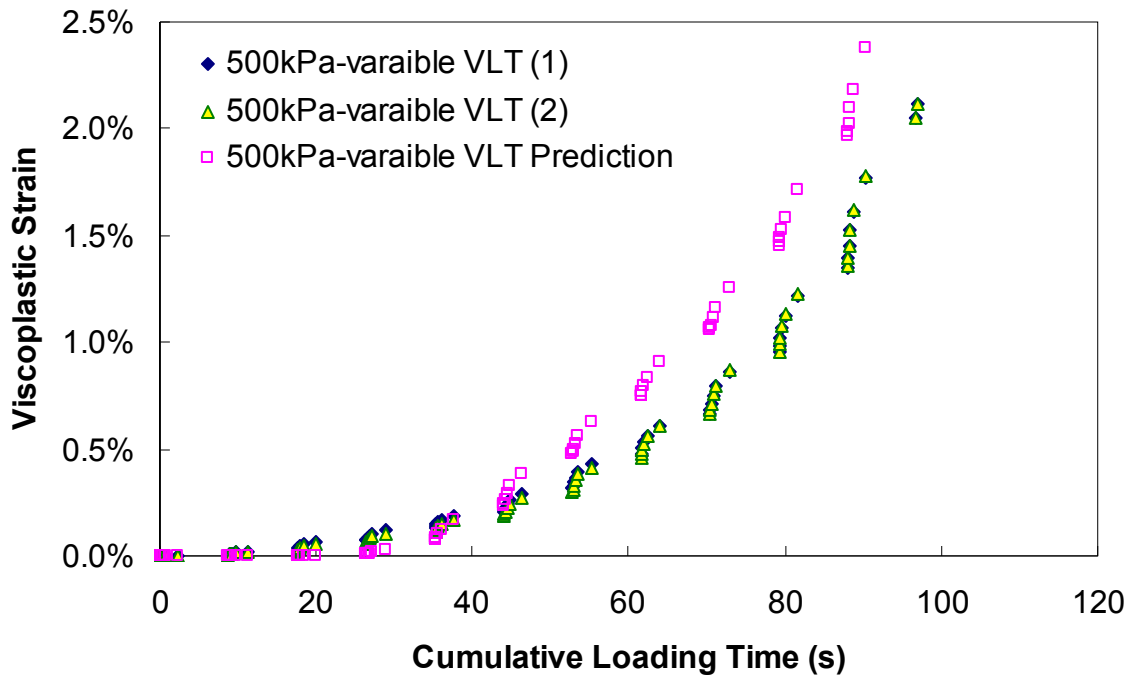


Figure 172. Graph. Viscoplastic strain versus cumulative loading time (500 kPa confinement VLT).

CHAPTER 6. ENHANCEMENT OF VEPCD-FEP++ FOR PAVEMENT MODELING

A complete redesign of FEP++ was one of the major tasks completed in this study. The redesign activity resulted in a well designed and modular code base of around 40,000 lines. All of the old features of FEP++ have been revamped and tested, and several new features have been added.

Currently, FEP++ supports the following:

1. Two-dimensional (2D) and 3D pavement models analysis.
2. Elastic, viscoelastic, and VECD material models.
3. Separate analysis for static and dynamic loads.
4. Linear, nonlinear, and quasilinear analysis.
5. Special elements for modeling pavements.
6. Elastic and viscoelastic materials thermal analysis.
7. Multipoint constraints.
8. Graphical user interface (preprocessor).

The following sections discuss the upgraded VECD model, the overall organization of the modules in FEP++, and the newly developed preprocessor.

6.1. DAMAGE IN VISCOELASTIC MATERIALS

For the sake of completeness, the original VECD model, as detailed elsewhere, is presented first in this section.⁽¹³⁾ Then, the upgraded VECD model is presented. Last, the implementation of temperature dependency for these materials is examined.

6.1.1. The Original Model

A one-parameter continuum damage model was incorporated into the viscoelastic material module. The new elements account for the evolution of isotropic damage. In this formulation, it is assumed that the stress-strain relationship obeys the following form:

$$\{\sigma\} = C(S)[E]*\{\dot{\epsilon}\} \quad (181)$$

Where:

$C(S)$ = Effect of damage on the stiffness of the material.

S = Parameter representing damage evolution.

The following evolution law governs the damage parameter:

$$\frac{\partial S}{\partial t} = \left(-\frac{\partial W}{\partial S} \right)^\alpha \quad (182)$$

Where:

W = Total energy in the material.

α = Parameter that depends on the type of loading.

Currently, based on the available experimental data, the following form for the damage function is assumed:

$$C(S) = e^{aS^b} \quad (183)$$

A plot of the above function, assuming $a = -0.001334$ and $b = 0.5725$, is shown in figure 173. The formulation presented here is not limited to the form of the damage function shown in equation 183. To show the effect of continuum damage, a 10 by 10 patch of 2D plane stress elements has been modeled and is shown in figure 174. The specimen is fixed at the bottom and loaded (in tension) on five nodes at the top. The loading history is sinusoidal as shown in equation 184.

$$f = \gamma [1 + \sin(2\pi t)] \quad (184)$$

Where:

γ = The loading amplitude.

The time history of the vertical displacement for point A () is shown in figure 175. The evolution of damage in the specimen and, consequently, a gradual increment in the displacement amplitude can be seen from the time history. This figure shows that damage has an effect on the response of the material. More quantitative tests on the effect of damage will be performed in the future.

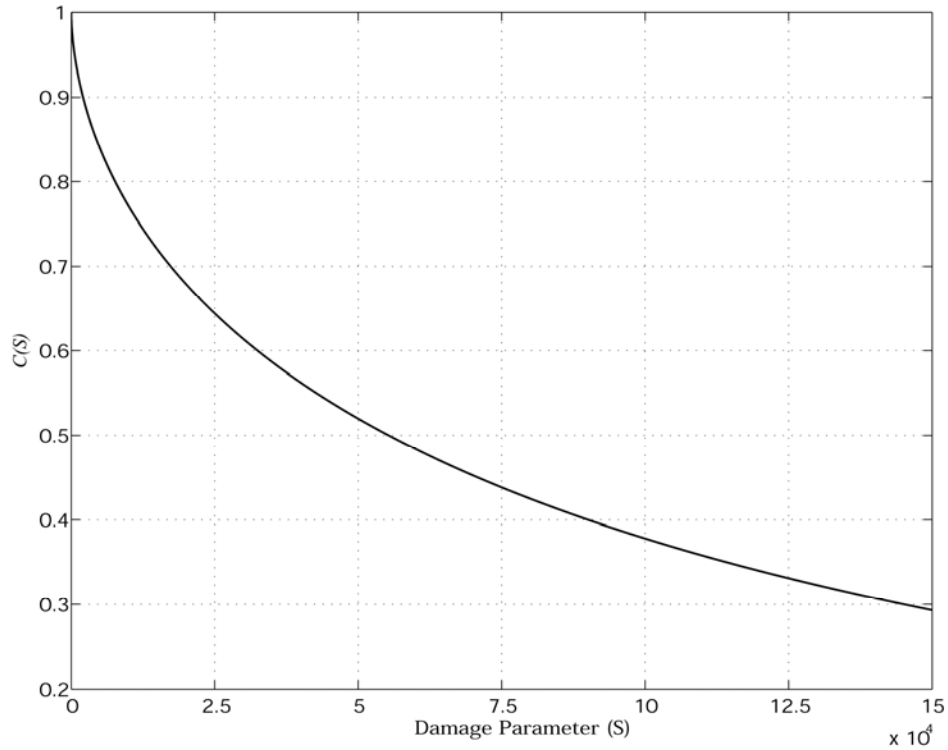


Figure 173. Graph. Damage characteristic relationship used in the finite element implementation of one-dimensional VECD model.

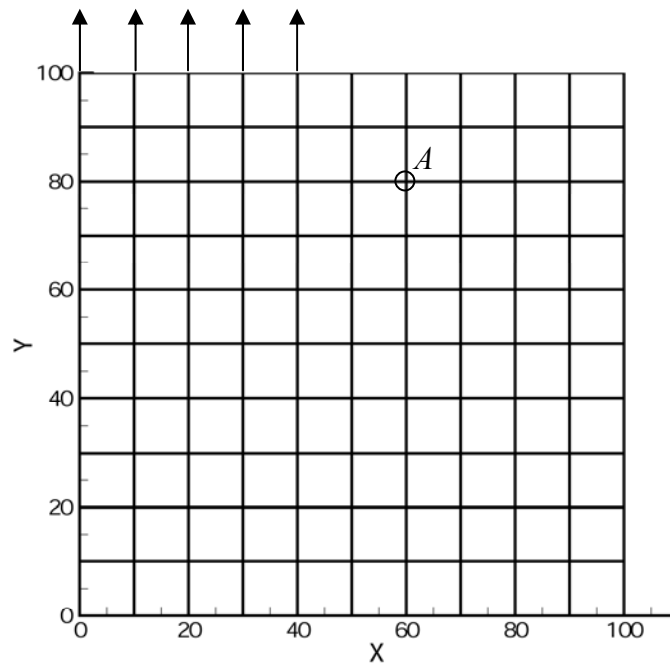


Figure 174. Graph. Layout of the numerical experiment specimen.

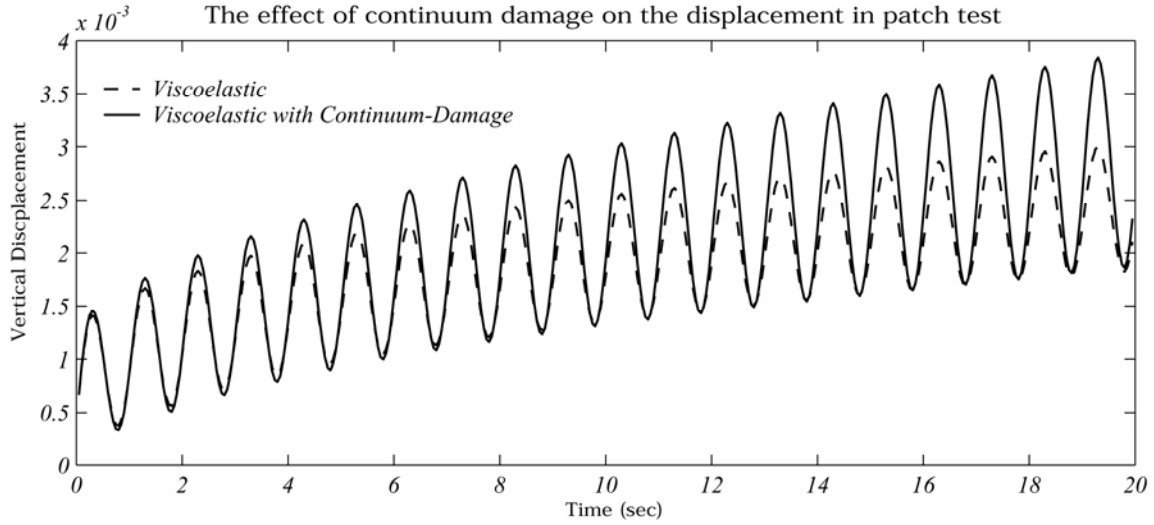


Figure 175. Graph. Effect of continuum damage evolution on the vertical displacement of the test specimen at point A in the test simulation.

6.1.2. Upgraded Constitutive Model

The continuum damage formulation was upgraded to a more rigorous model based on the work of others.⁽⁵⁷⁾ However, a one-parameter damage model was chosen instead of the two-parameter model used in the work because the experimental data needed to characterize a two-parameter damage model are not yet available.

The model assumes that a material is isotropic when undamaged and that the growth of damage under loading leads to local transverse isotropy (i.e., the material has a local axis of symmetry oriented along the maximum principal stress direction). The current framework is formulated for the axisymmetric case but can easily be extended to 3D.

Starting with the work potential theory for an elastic material and making use of viscoelastic fracture mechanics and the correspondence principle for viscoelastic materials, a pseudo strain energy density function, W^R , can be written in terms of the pseudo strains in the local axis as follows:^(8,9)

$$\begin{aligned}
 W^R &= \frac{1}{2} \left[A_{11} (e_v^R)^2 + A_{22} (e_d^R)^2 + 2A_{12} e_d^R e_v^R + A_{44} \left((\gamma_{13}^R)^2 + (\gamma_{23}^R)^2 \right) + A_{66} \left((\gamma_{12}^R)^2 + (e_s^R)^2 \right) \right] \\
 e_v^R &= \varepsilon_{11}^R + \varepsilon_{22}^R + \varepsilon_{33}^R \\
 e_d^R &= \varepsilon_{33}^R - \frac{e_v^R}{3} \\
 e_s^R &= \varepsilon_{11}^R - \varepsilon_{22}^R
 \end{aligned} \tag{185}$$

Where:

$\varepsilon_{11}^R, \varepsilon_{22}^R, \varepsilon_{33}^R, \gamma_{12}^R, \gamma_{13}^R, \gamma_{23}^R$ are the pseudo strains along the local axis.

When the local axis is also a principal axis, the shear strains are zero, and equation 185 becomes the following:

$$W^R = \frac{1}{2} \left[A_{11}(e_v^R)^2 + A_{22}(e_d^R)^2 + 2A_{12}e_d^R e_v^R + A_{66}(e_s^R)^2 \right] \quad (186)$$

In this case, ε_{11}^R , ε_{22}^R , and ε_{33}^R are the principal pseudo strains (which lie in the local axis) with the axis of isotropy oriented along direction 3. These principal pseudo strains are obtained from the pseudo strains along the global axis using standard tensor transformation and knowing the angle between the local axis and the global axis. (For the axisymmetric analysis, the hoop direction is already a principal axis because there are no shear strains along the $r\theta - \theta z$ plane.) The LVE pseudo strains along the global axis, $\varepsilon_{kl}^R(t)$, are calculated from strains along the global axis, ε_{kl} , using the convolution integral.

$$\varepsilon_{kl}^R(t) = \frac{1}{E_R} \int_0^t E(t-\tau) \frac{\partial \varepsilon_{kl}}{\partial \tau} d\tau \quad (187)$$

Where:

E_R = Reference modulus that has the same dimensions as the modulus and is usually taken as $1 E(t)$.

$1 E(t)$ = Relaxation modulus for uniaxial loading.

The calculation of the convolution integral can be very expensive in terms of computation time. In practice, therefore, the pseudo strains are calculated using a state variable approach to reduce the computational expense. When the relaxation modulus of the material $E(t)$ is represented using the Prony series of the form, shown in equation 188, an approximation can be obtained to the convolution integral in equation 187.

$$E(t) = E_\infty + \sum_{i=1}^M E_i e^{-\frac{t}{\rho_i}} \quad (188)$$

Where:

E_∞ = The relaxation modulus at $t = \infty$.

E_i = The Prony coefficients corresponding to the relaxation times, ρ_i .

The pseudo strains along the global axis can be calculated from the following:

$$\begin{aligned} \varepsilon_{kl}^R(t_{n+1}) &= \frac{1}{E_R} \left(E_\infty \varepsilon_{kl}(t_{n+1}) + \sum_{i=1}^M E_i \varepsilon_{kl}^i(t_{n+1}) \right) \\ \varepsilon_{kl}^i(t_{n+1}) &= e^{-\Delta t_{n+1}/\rho_i} \varepsilon_{kl}^i(t_n) + e^{-\Delta t_{n+1}/(2\rho_i)} \Delta \varepsilon_{kl}(t_{n+1}) \end{aligned} \quad (189)$$

Where:

$\varepsilon_{kl}^i(t_{n+1})$ ($i = 1..M$) are the internal state variables that record the history of the material up to time t_{n+1} , $\Delta \varepsilon_{kl}(t_{n+1}) = \varepsilon_{kl}(t_{n+1}) - \varepsilon_{kl}(t_n)$, and $\Delta t = t_{n+1} - t_n$. The pseudo strains at time t_{n+1} are

calculated based on the strain at times t_n and t_{n+1} which are available at the end of the finite element solution step at time t_{n+1} .

The factors A_{11} , A_{22} , A_{12} , and A_{66} are stiffness terms that can be related to a damage function, $C(S)$ as follows: ⁽⁴⁸⁾

$$\begin{aligned}
 A_{11} &= \frac{1}{9} \left[C(S) + E_R \cdot \frac{2(1+\nu)}{(1-2\nu)} \right] \\
 A_{22} &= C(S) + E_R \cdot \frac{(1-2\nu)}{2(1+\nu)} \\
 A_{12} &= \frac{1}{3} [C(S) - E_R] \\
 A_{44} = A_{66} &= \frac{E_R}{2(1+\nu)}
 \end{aligned} \tag{190}$$

Where:

ν = Poisson's ratio of the material.

$C(S)$ = A stiffness function that depends on damage in the material.

S = A damage parameter used to track the growth of damage in the specimen.

The principal stresses along the local axis can be found from equation 186 using the following:

$$\sigma_{ii} = \frac{\partial W^R}{\partial \varepsilon_{ii}^R} \quad (i = 1, 2, 3), \tag{191}$$

which gives the following:

$$\begin{aligned}
 \sigma_{11} &= (A_{11} - \frac{1}{3} A_{12}) e_V^R + (A_{12} - \frac{1}{3} A_{22}) e_d^R - A_{66} e_S^R \\
 \sigma_{22} &= (A_{11} - \frac{1}{3} A_{12}) e_V^R + (A_{12} - \frac{1}{3} A_{22}) e_d^R + A_{66} e_S^R \\
 \sigma_{33} &= (A_{11} + \frac{2}{3} A_{12}) e_V^R + (A_{12} + \frac{2}{3} A_{22}) e_d^R.
 \end{aligned} \tag{192}$$

The stresses along the global axis are then obtained by standard stress transformation and the orientation of the local axis with respect to the global axis.

6.1.3. Damage Model

The growth of the damage parameter S is modeled by extending the concepts of viscoelastic fracture to microcracking. ⁽⁸⁾

$$\frac{dS}{dt} = \left(-\frac{\partial W^R}{\partial S} \right)^\alpha \quad (193)$$

Where:

W^R = Pseudo strain energy density function shown in equation 185.

α = Material-dependent parameter.

From equation 186, the quantity $\partial W^R / \partial S$ can be calculated as a function of pseudo strains in the local axis as follows:

$$\frac{\partial W^R}{\partial S} = \frac{1}{2} \frac{\partial C}{\partial S} \left(\frac{1}{9} (e_v^R)^2 + \frac{2}{3} e_d^R e_v^R + (e_d^R)^2 \right) \quad (194)$$

Where:

$C(S)$ = Damage function that is assumed to be of the form shown in equation 195, based on experimental data.

$$C(S) = e^{aS^b} \quad (195)$$

6.1.4. Finite Element Implementation

The finite element solution of the problem requires the material tangent stiffness matrix that is used to assemble the global tangent stiffness matrix used for the solution of the nonlinear system of equations by the Newton-Raphson method. Not to be confused with the damage function, $C(S)$, the material tangent stiffness matrix, $[C]$, is given by the following:

$$[C] = \frac{\partial \{\sigma\}}{\partial \{\varepsilon\}} = \frac{\partial \{\sigma\}}{\partial \{\varepsilon^R\}} \frac{\partial \{\varepsilon^R\}}{\partial \{\varepsilon\}} \quad (196)$$

Where:

$\{\sigma\} = \{\sigma_{rr}, \sigma_{\theta\theta}, \sigma_{zz}, \sigma_{rz}\}$ and $\{\varepsilon\} = \{\varepsilon_{rr}, \varepsilon_{\theta\theta}, \varepsilon_{zz}, \varepsilon_{rz}\}$ are the stresses and strains for the axisymmetric problem.

$[C]$ = Material tangent stiffness matrix oriented along the global axis. Because the stresses along the global axis are obtained by transforming the stresses in the local axis, it is easier to construct the material tangent stiffness matrix along the local axis and then transform it to the tangent stiffness along the global axis.

The tangent stiffness matrix in the local axis, $[C_L]$, is given as follows:

$$[C_L] = \frac{\partial \{\sigma_L\}}{\partial \{\varepsilon_L^R\}} = \begin{bmatrix} \left(A_1 - \frac{2}{3}A_2 + \frac{1}{9}A_2 + A_{66}\right) & \left(A_1 - \frac{2}{3}A_2 + \frac{1}{9}A_2 - A_{66}\right) & \left(A_1 + \frac{1}{3}A_2 - \frac{2}{9}A_2\right) & 0 & 0 & 0 \\ \left(A_1 - \frac{2}{3}A_2 + \frac{1}{9}A_2 - A_{66}\right) & \left(A_1 - \frac{2}{3}A_2 + \frac{1}{9}A_2 + A_{66}\right) & \left(A_1 + \frac{1}{3}A_2 - \frac{2}{9}A_2\right) & 0 & 0 & 0 \\ \left(A_1 + \frac{1}{3}A_2 - \frac{2}{9}A_2\right) & \left(A_1 + \frac{1}{3}A_2 - \frac{2}{9}A_2\right) & \left(A_1 + \frac{4}{3}A_2 + \frac{4}{9}A_2\right) & 0 & 0 & 0 \\ 0 & 0 & 0 & A_{66} & 0 & 0 \\ 0 & 0 & 0 & 0 & A_{44} & 0 \\ 0 & 0 & 0 & 0 & 0 & A_{44} \end{bmatrix} \quad (197)$$

Where:

$\{\sigma_L\} = \{\sigma_{11}, \sigma_{22}, \sigma_{33}, \sigma_{12}, \sigma_{13}, \sigma_{23}\}$ is the stress vector along the local axis.
 $\{\varepsilon_L^R\} = \{\varepsilon_{11}^R, \varepsilon_{22}^R, \varepsilon_{33}^R, \gamma_{12}^R, \gamma_{13}^R, \gamma_{23}^R\}$ is the pseudo strain vector along the local axis.

The pseudo shear strains are zero along the local axis, but the stiffnesses corresponding to them are non-zero. The matrix, $[C]$, can be obtained by transforming $[C_L]$, as shown in the following:

$$[C] = [T_R]^{-1} [C_L] [T_R] \quad (198)$$

Where:

$[T_R]$ = The rotation and permutation matrix that changes the order of the vector components (the axis 3 along the local axis is always oriented along the maximum principal pseudo strain direction) and transforms a vector from the local axis to the global axis.

As seen in equation 193 and 194, the damage growth involves a nonlinear differential equation that can be expensive to solve in a large finite element method (FEM) problem. Hence, a semi-implicit method is used to predict the damage parameter in the next time-step, S^{n+1} , using the damage parameter in the current time-step, S^n , and the pseudo strain vector in the local axis, $\{\varepsilon_L^R\}^{n+1}$, for the next time-step, as follows:

$$S^{n+1} = S^n + \dot{S} \left(\{\varepsilon_L^R\}^{n+1}, S^n \right) \Delta t \quad (199)$$

This method should provide results similar to those of an exact nonlinear analysis when the time-steps are made small enough.

6.1.5. Verification

The continuum damage material model is verified for a monotonic uniaxial test. The test is part of the uniaxial testing on cylindrical specimens that is conducted for the damage characterization of FHWA mixtures. Verification uses the 5 °C test because there is little or no viscoplastic deformation at this temperature. For the FEM simulation, the cylindrical specimen is modeled as

a single quadrilateral (Q4) element that is 150 mm in height and 75 mm in width and is subjected to a uniform axisymmetric loading in the vertical direction. The stress history measured from the test is used as an input for the problem, with the strains calculated by analysis. Horizontal displacements are constrained along the axisymmetric axis of the element, and vertical displacements are constrained along the bottom edge of the element, which results in a uniform state of stress and strain in the element. Predicted strains are then compared against measured strains to verify the FEM implementation of the material model. The damage function is taken as $C(S) = \exp(-0.001S^{0.5737})$, based on the monotonic test results from several different specimens. The Prony series for the material is obtained from test data for the asphalt concrete mixture used in the testing.

The results of the verification are shown in figure 176 through figure 178. As seen from these figures, the prediction of strain is very good, the damage parameter consistently increases with time and the pseudo stiffness consistently decreases with time. These combined findings verify that the model has been implemented correctly.

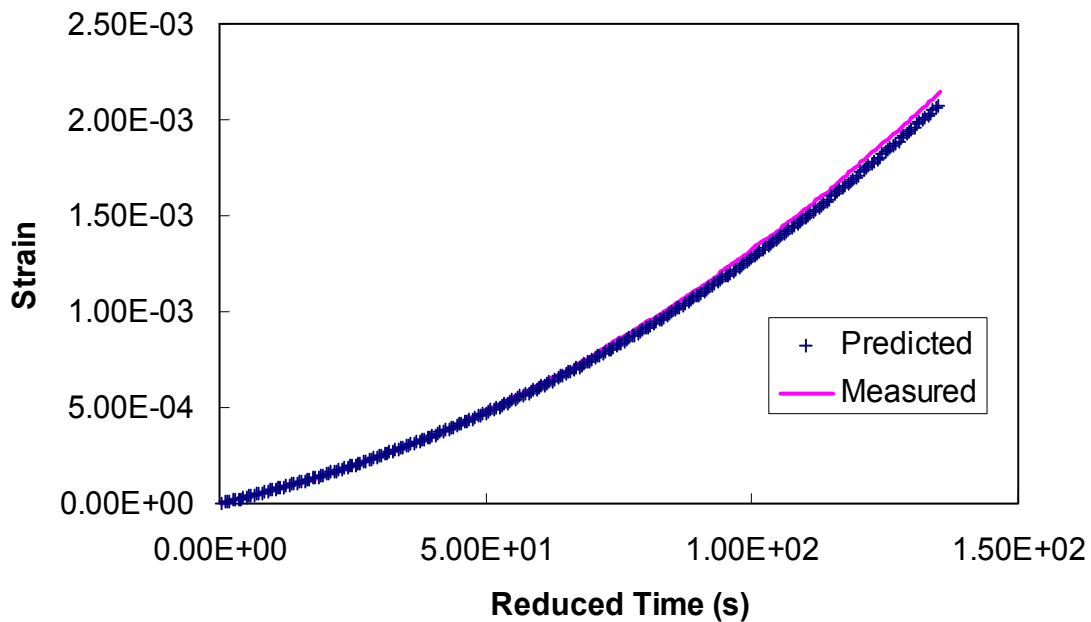


Figure 176. Graph. Verification of strain prediction for monotonic uniaxial test using the new continuum damage material model.

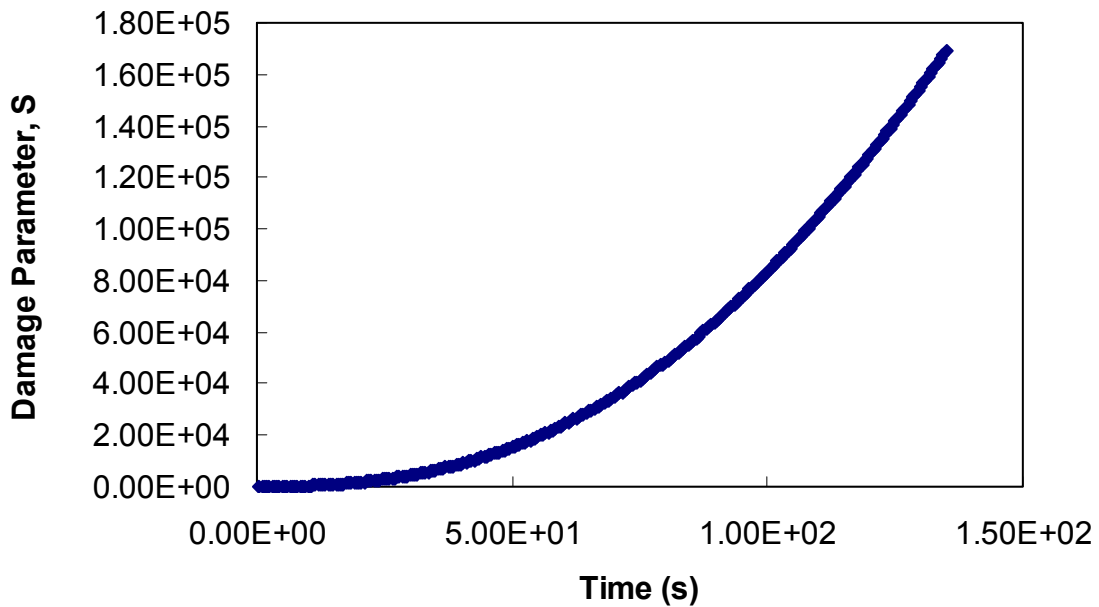


Figure 177. Graph. Evolution of damage parameter, S , for the monotonic test.

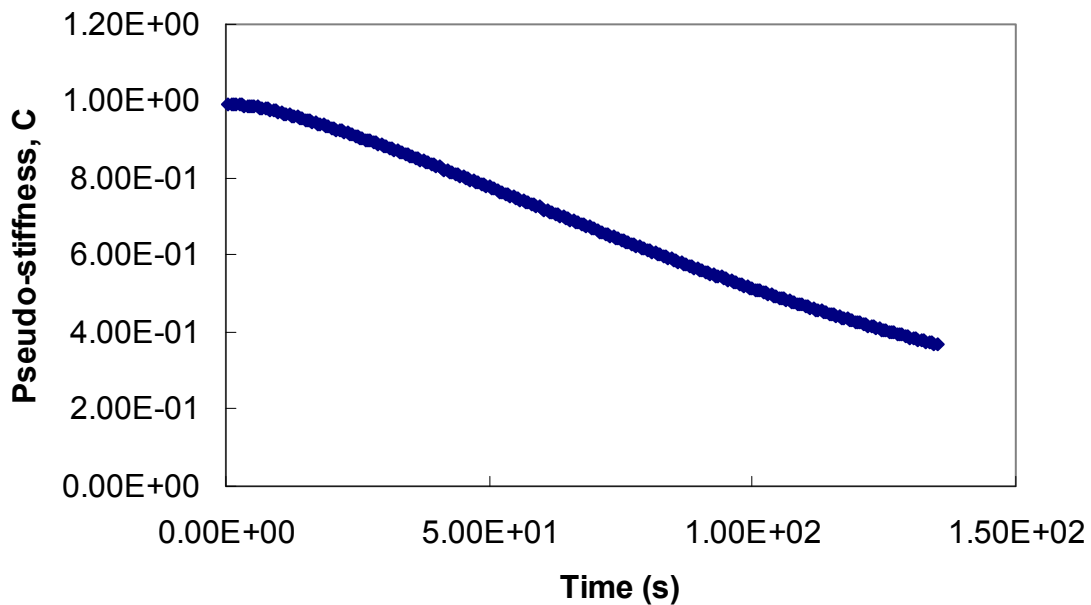


Figure 178. Graph. Plot of function $C(S)$ with time.

6.1.6. Implementation of Temperature Dependency

The variation of temperature in a pavement has two effects: (1) a change in stiffness of the asphalt concrete and (2) a change of the thermal stresses due to thermal expansion of the material. The thermal stresses are generated in the pavement depending on boundary conditions. These two effects of temperature have been implemented in FEP++.

The change in stiffness in the asphalt concrete due to temperature is taken into account using the concept of reduced time. The reduced time is calculated as follows:

$$\xi(t) = \int_0^t \frac{1}{a(T(\tau))} d\tau, \quad (200)$$

Where:

$a(T)$ = Time-temperature shift factor of the material. The time-temperature shift factor is obtained from the characterization of the relaxation modulus of the material using dynamic modulus tests at different frequencies and temperatures. The reduced time is calculated with respect to a reference time and captures the history of temperature variation on the material. The thermal stresses on the material are incorporated by defining mechanical strains, $\varepsilon_m(t)$, as follows:

$$\{\varepsilon_m(t)\} = \{\varepsilon(t)\} - \{\alpha\}(T - T_0). \quad (201)$$

Where:

$\{\varepsilon(t)\}$ = Strain in the material.

$\{\alpha\}$ = Coefficient of isotropic thermal expansion in the material (which is assumed constant for asphalt concrete) and is given by $[\alpha, \alpha, \alpha, 0, 0, 0]$ in three dimensions.

T = Current temperature.

T_0 = Reference temperature at which there are no initial stresses.

The constitutive law for a viscoelastic material undergoing damage is given as follows:

$$\{\sigma\} = [D]\{\varepsilon_m^R\}, \quad (202)$$

Where:

$\{\sigma\}$ = Stress vector.

$[D]$ = Stiffness matrix that is a function of damage.

$\{\varepsilon_m^R\}$ = Vector of mechanical pseudo strain.

The i^{th} component of the pseudo strain vector is given by the following:

$$\varepsilon_{R,i}^m = \int_0^{\xi} E(\xi - \xi') \frac{d\varepsilon_i^m}{d\xi'} d\xi', \quad (203)$$

Where:

ε_i^m = i^{th} component of the mechanical strain vector.

$E(\xi)$ = Relaxation modulus of the material characterized at reduced temperature. ξ is computed in accordance with equation 200 and is a function of the temperature history of the material.

6.2. REDESIGN OF FEP++

The older code base of FEP++ was redesigned during the course of the project, leading to a robust, modular, and standards-compliant version. These enhancements greatly improve the maintainability of the code base and significantly reduce the training necessary for a new user.

The FEP++ code base is divided into two major modules, domain and analysis. The following sections discuss the features and functionalities of these modules.

6.2.1. Domain Module

The domain module represents the core finite element component of FEP++. It encompasses the finite element classes that are involved in the modeling of the computational domain. Figure 179 presents a block diagram and the key components of the module. The following sections briefly discuss the main features of the domain module.

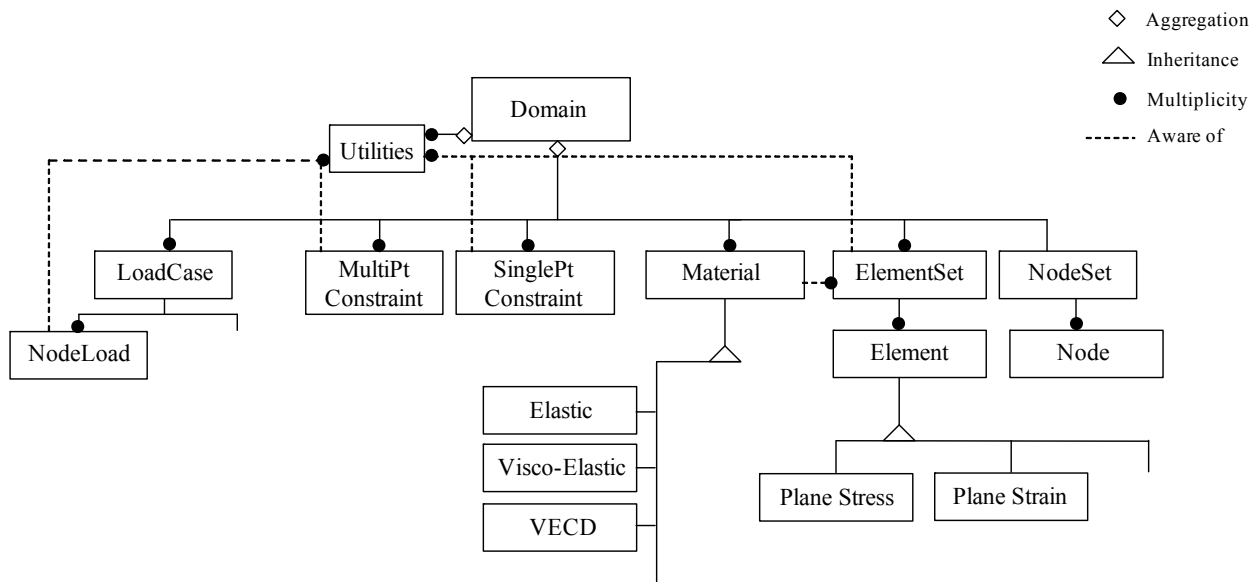


Figure 179. Diagram. Domain module.

6.2.1.1. Material Model

FEP++ provides 2D and 3D models of elastic, viscoelastic, and VECD materials for modeling a pavement layer. Detailed discussion of these models and their implementation is provided in section 6.1.

6.2.1.2. Elements

FEP++ provides two main types of elements, the quadrilateral elements for 2D analysis and the brick elements for 3D analysis of pavements. Also, special elements developed for modeling infinite domains in pavement analysis have been incorporated into FEP++. The following subsection describes the special elements and their efficiency in pavement analysis.

6.2.1.2.1. Incorporation of special elements for pavement modeling:

A finite element mesh generation methodology for incorporating special elements that reduce the computational costs of pavement analysis has been developed. An accurate mesh of special elements can be difficult to generate because it depends on the characteristics of the load applied. Development of such a methodology may also turn out to be somewhat computationally expensive if it tries to provide greater accuracy than is necessary for the problem at hand. Hence, there is a need to develop a mesh generation methodology that allows the user to easily generate a finite element mesh that models the problem at hand with specified accuracy.

To this end, work is being carried out to generate the best mesh for a specified accuracy through optimization techniques. Generating the best mesh is an involved process that could render it unfeasible for everyday analysis. Therefore, simplified rules will be developed that allow the user to easily generate a mesh that is as close as possible to the best mesh.

A simple example is given below to demonstrate the computational efficiency achieved. Figure 180 shows a layer of elastic material loaded on a rigid base. This layer is infinite in the two horizontal directions. For a strip load of width “ $2B$,” the 3D problem can be reduced to a 2D-plane strain problem. Also, symmetry allows that only one half of the problem needs to be modeled. Only the deflection and stresses under the load (the interior region) are of interest here.

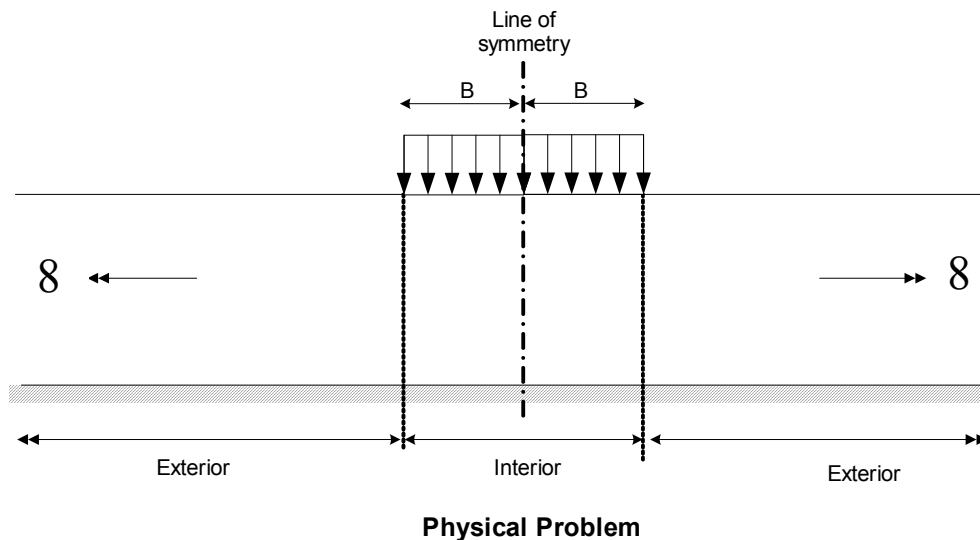


Figure 180. Illustration. Infinite elastic layer on a rigid base.

However, despite the emphasis on the interior region, the exterior region also must be modeled to a sufficient length to simulate the infinite extent of the layer. As the exterior region is extended, the solution in the interior approaches the solution of the physical problem. The objective is to model the physical problem to achieve an accuracy of at least 1 percent. A typical mesh of finite elements used to simulate this physical problem is Mesh-1, shown in figure 181. For Mesh-1, the exterior is four times the extent of the interior and hence needs four times as many finite elements as the interior to achieve an accuracy of 0.86 percent.

If, on the other hand, special elements are used, then Mesh-2 shown in figure 181 is sufficient and provides an accuracy of 0.84 percent. The total number of elements in Mesh-1 is 320, whereas the total number in Mesh-2 is 64. In order to achieve almost the same degree of accuracy as Mesh-1, far fewer special elements are required for Mesh-2. In short, because the computational time is directly proportional to the number of finite elements used to model the problem, Mesh-2 with the special elements is far more computationally efficient when compared to Mesh-1.

The development of a finite element mesh generation methodology that incorporates special elements is now complete. This methodology is being tested on various finite element models to demonstrate its efficacy. Once the results have been verified against theoretical solutions, the mesh generation methodology will be coded into FEP++ to make the discretization both automatic and efficient. (This task will be performed as part of the ongoing cooperative agreement between NCSU and the FHWA.)

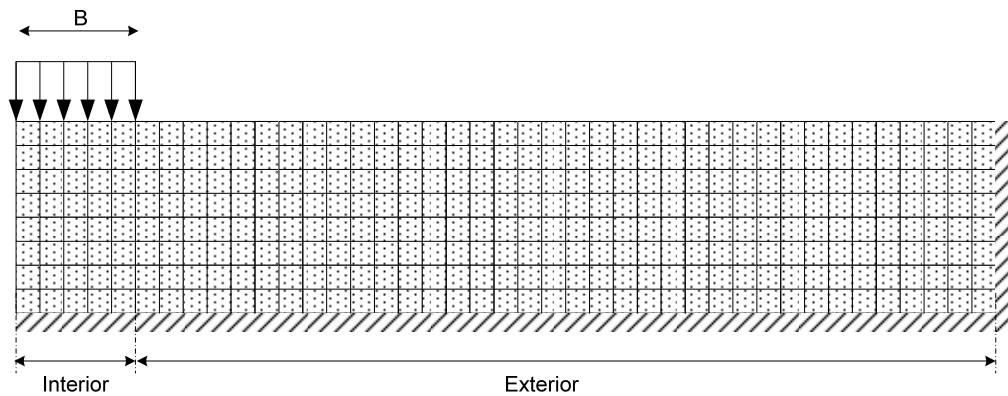


Figure 181. Illustration. Finite element mesh required to model the physical problem with 1-percent accuracy without special elements.

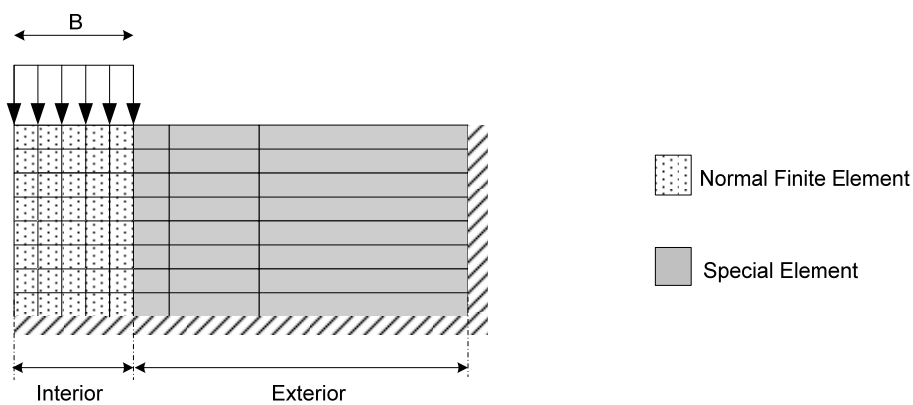


Figure 182. Illustration. Finite element mesh required to model the physical problem with 1-percent accuracy with special elements.

6.2.2. Analysis Module

The analysis module handles the generation and solution of the linear/nonlinear system of equations using the domain module. A block diagram of the classes and relationships is shown in figure 183. The following sections discuss the key components of this module.

6.2.2.1. Solution Algorithm

The solution algorithm is the component that acts as a liaison between the domain and analysis modules. This component uses the information in the domain to generate a set of equations that provides the solutions to the problem. Currently, the following static and dynamic analyses of linear, quasilinear, and nonlinear problems are available.

One significant enhancement over the earlier capabilities of FEP++ is the ability to perform quasilinear analysis. This improvement is particularly beneficial in the context of pavement analysis because the VECD material model is quasilinear. By using a quasilinear solver instead of a nonlinear solver, the analysis time is reduced by almost half.

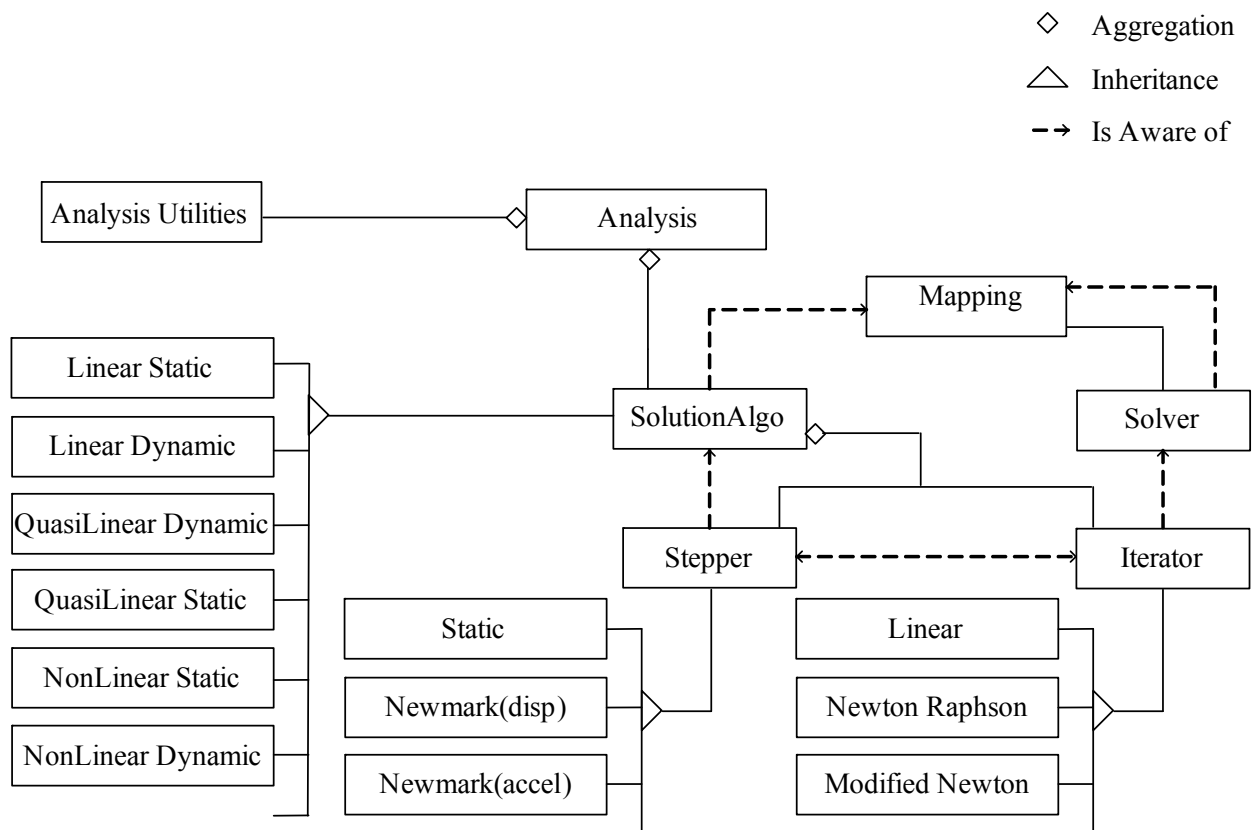


Figure 183. Diagram. Analysis module.

6.2.2.2. Solver

The solver is the workhorse of the module. It is responsible for solving the set of equations generated by the solution algorithm. The solver is also an important component in terms of the

capabilities of FEP++ in solving large computational problems because the solver determines the memory requirements and performance output. Any improvements to this module would significantly improve the overall capabilities of FEP++.

Currently, a class of direct methods called Gaussian elimination is used to solve the equations. The objective here is to enhance the component by providing an option to interface with external linear algebra packages to solve the system of equations. The benefit of such a feature would be the ability to use mature, well tested, and highly efficient libraries available in the public domain for performing the analysis. This capability would also reduce further interdependence between the domain and the analysis modules, thereby enhancing the flexibility and elegance of the code.

6.3. PREPROCESSOR

The preprocessor is a graphic user interface (GUI) front end developed for the efficient analysis of pavements using FEP++. The motivation behind the tool is to provide the user with a simplified and intuitive interface to FEP++ for pavement analysis. The tool can be used either to run an analysis directly or to generate the input files for FEP++. It also has visualization capabilities to view the mesh discretization, which makes it easy for the user to verify the input data for the analysis. Figure 184 shows a screenshot of the main window in the preprocessor.

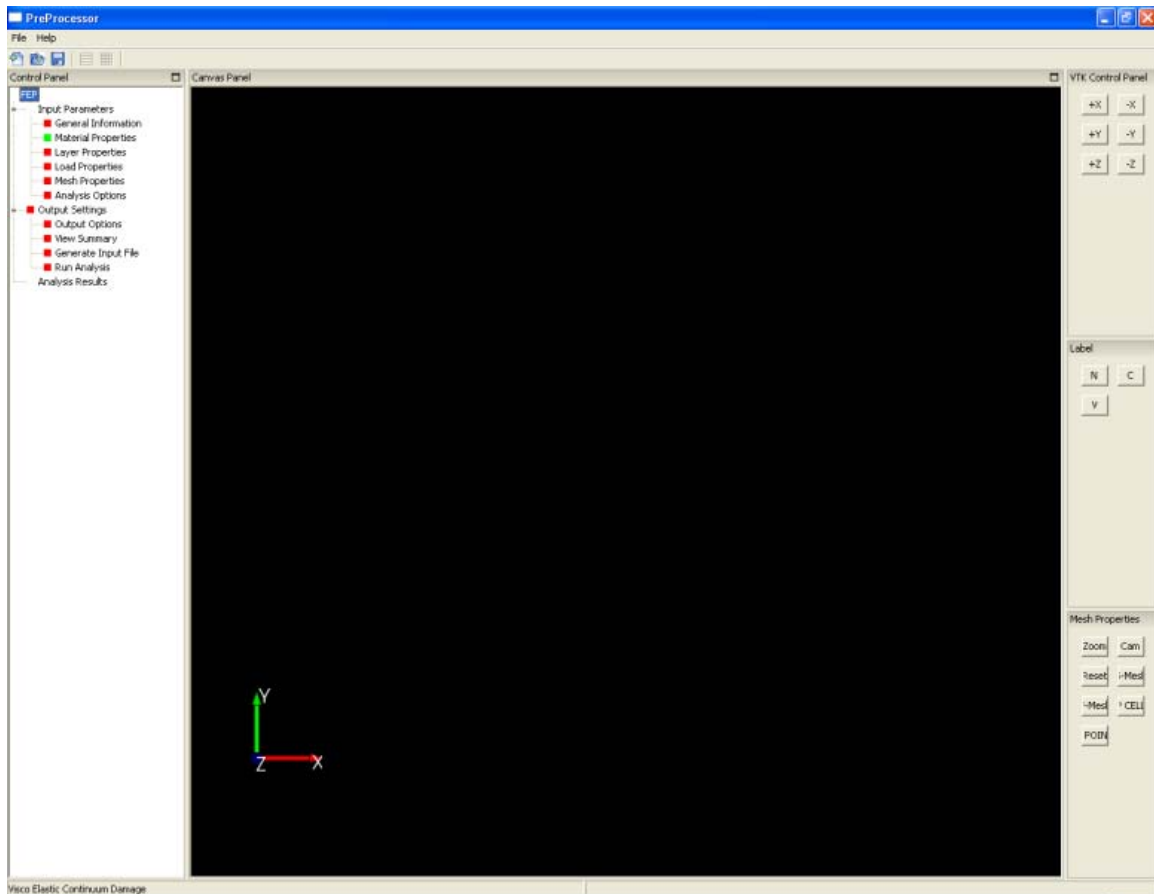


Figure 184. Screen capture. Main window of the preprocessor.

As labeled in figure 184, the main window is divided into three functional units, the control panel, the canvas panel, and the popular open-source library called Visualization Toolkit (VTK) control panel, described below.

The left-hand unit is called the Control Panel. This panel contains the controls to invoke the data-entry windows and other operations related to the analysis. Each control is either red or green, indicating the current state of the analysis. For controls corresponding to data entry operations, green indicates that no user action is required. Green, therefore, could either signal that the data entry has already been completed or that it is preset with a default set of parameters. Red indicates that some action is required from the user. The data input is considered complete only when all the controls in the input parameters block (figure 185) are green.

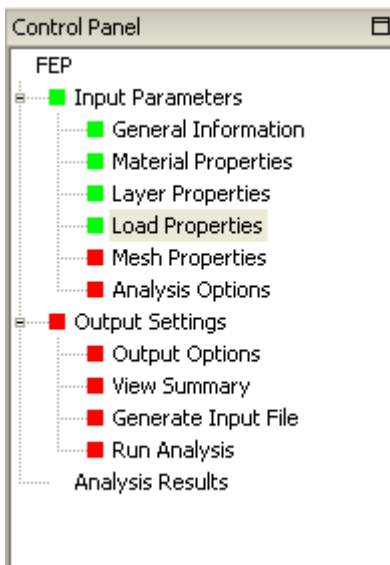


Figure 185. Screen capture. Control panel.

The middle unit is called the Canvas Panel. This panel is used for the visualization of the mesh discretization and the solid model of the pavement. The underlying graphical engine used to render the graphics is VTK. This toolkit was chosen for its stable and mature set of high-level graphical libraries. Also, it is popular and widely used in the open-source and scientific community. Figure 186 shows a sample mesh discretization in the canvas panel.

The rightmost unit provides the controls for the visualization operations supported in the preprocessor, e.g., zoom, pan, etc., and is called the VTK control panel. The following operations are currently supported:

- Projections along a plane, e.g., along the x-y plane.
- Image operations, such as zoom, pan, and rotate.
- Display nodes and cell numbers on the mesh.

The results of these operations are displayed in the view window. Figure 187 shows the zoomed version of a 2D mesh with node numbers displayed. The visual feedback from these windows is useful to verify the data inputs to the analysis. The different stages involved in performing a pavement analysis and the ways that the various analytical pieces fit together are outlined in figure 188.

The input stage corresponds to the data-entry windows that receive the input data from a user (i.e., it shows the list of data that needs to be entered by the user). The analysis stage shows the list of options available to the user once the input stage is complete. The postprocessing stage again shows the options after the analysis is completed successfully. The above mentioned stages are discussed in detail in the following sections.

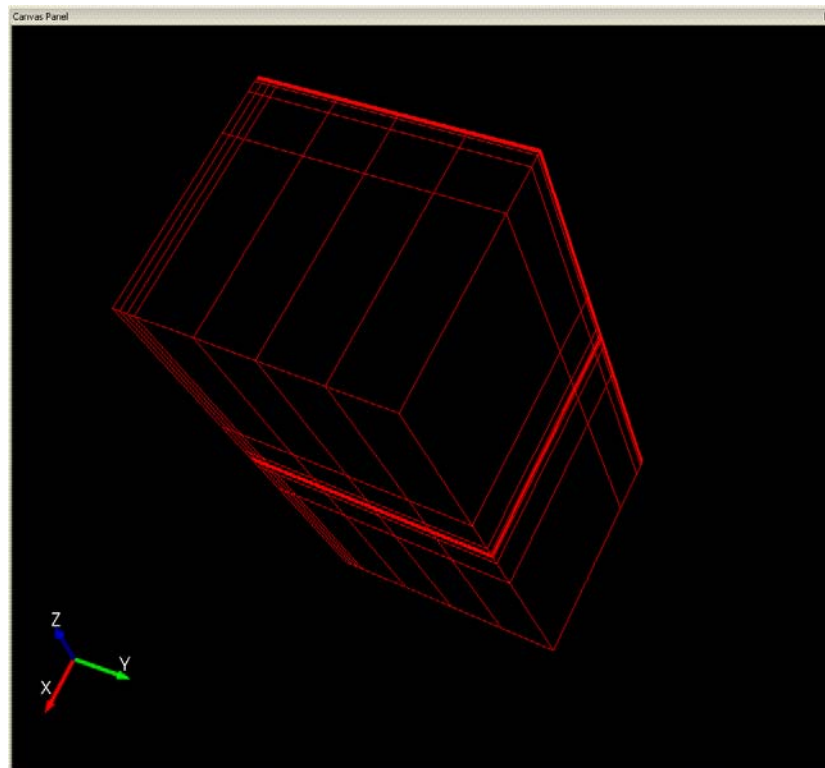


Figure 186. Screen capture. Mesh discretization.

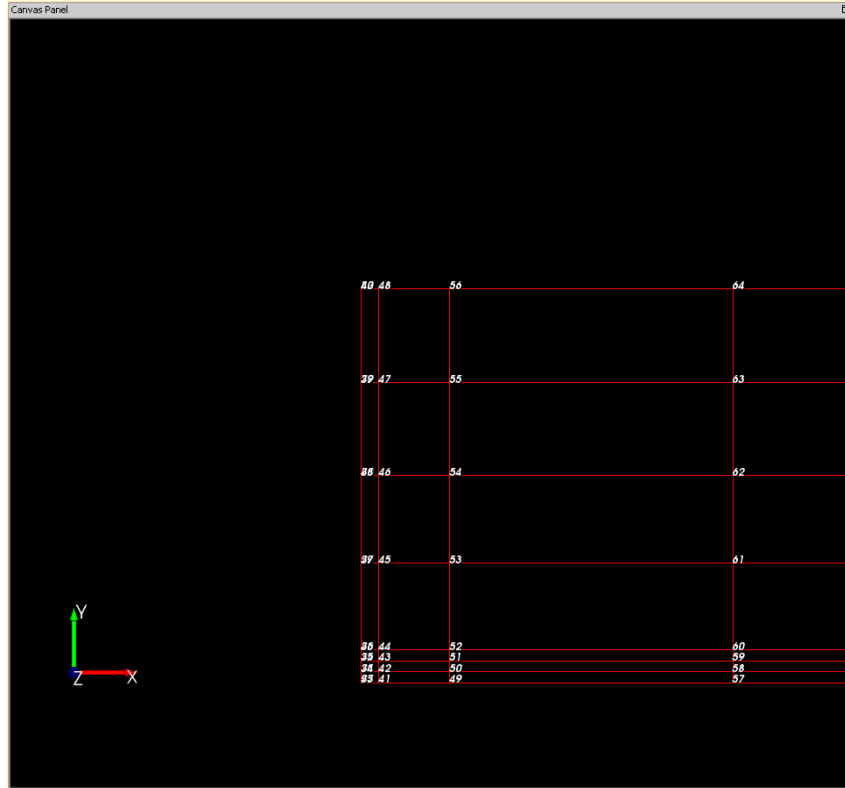


Figure 187. Screen capture. Zoom operation on a mesh.

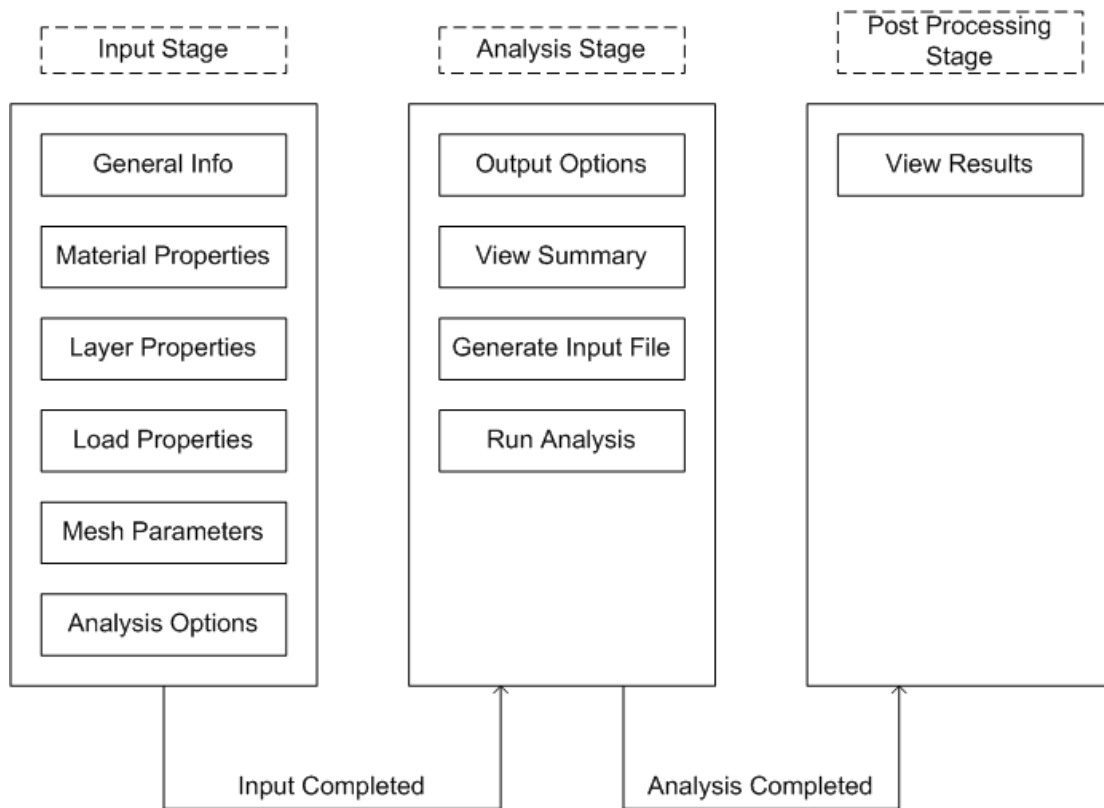


Figure 188. Diagram. Stages involved in an FEP++ analysis.

6.3.1. Input Stage

As discussed in the previous section, this stage corresponds to the data entry by the user. Each main input data entry for FEP++ corresponds to a data entry window. The user manual, with a detailed explanation of each of the data entry windows, is provided in the appendix of this report. Figure 189 shows a data entry window for entering the mesh discretization parameters for a pavement.

The data entry windows have been designed in a modular way, and effective error validation schemes have been incorporated to ensure consistent input data. Each data entry window has a data class associated with it that enforces the validation and consistency checks. There are two levels of error validations that are carried out at each data entry window, namely syntactic and semantic errors. The syntactic errors refer to invalid data entries, and they are checked by the data entry windows themselves, whereas the semantic errors refer to consistency check failures imposed by the data classes.

Once the data entry is complete for a particular block, it is validated against the checks provided in the data classes. If the validation is successful, the next data entry window can be accessed. If it fails, appropriate error messages are shown, and the user is asked to modify the incorrect data. Figure 190 shows a typical error dialog that is displayed when a consistency check fails.

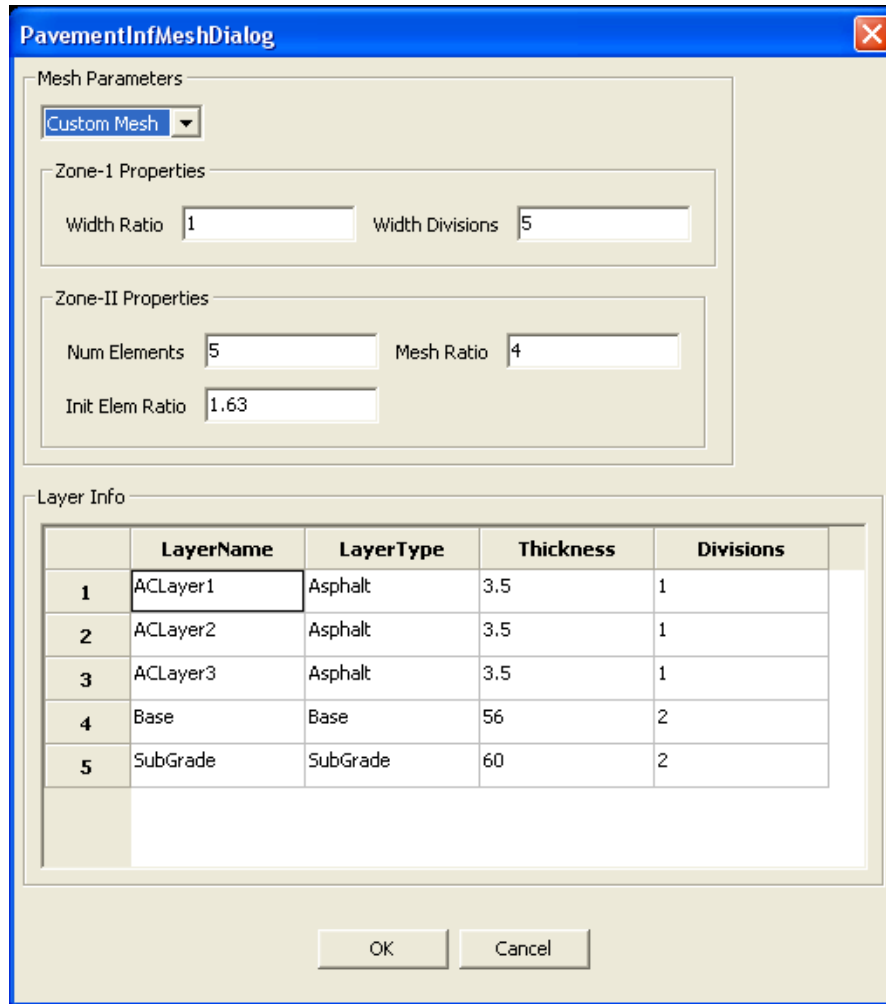


Figure 189. Screen capture. Sample data entry window.

This sequential data entry process may seem to be somewhat limiting, but it greatly simplifies the maintenance of consistency in the input data. Also, by strictly enforcing these checks in the software, there is less scope for input data corruption.

6.3.2. Analysis Stage

Once the data entry has been completed, the analysis section in the control panel turns green, signaling that the actions in the analysis stage can now be performed. The following sections discuss the actions that can be performed at this stage.

6.3.2.1. Setting the Output Options

Output options can be used to control the results that are generated by FEP++. For example, FEP++ can be configured to output data that correspond to a particular region in the domain. These options are essentially used to control the amount of data output by FEP++.

6.3.2.2. Viewing a Summary of the Input Data

The preprocessor can be used to create a user-readable report of the input data entered for an analysis. This report can be used to verify the final state of all the input data before beginning a simulation.

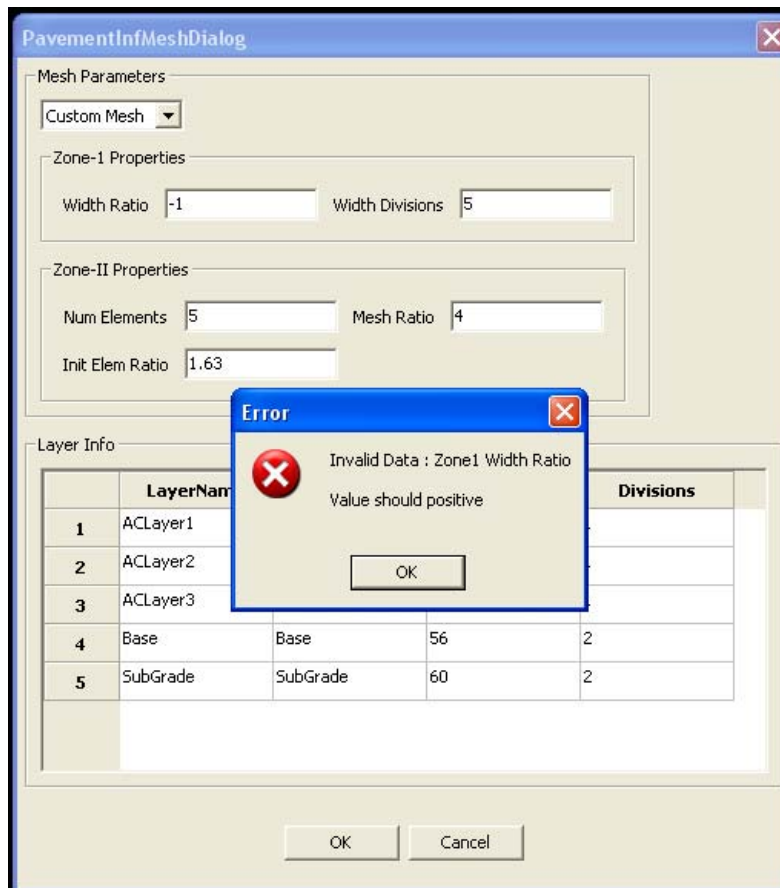


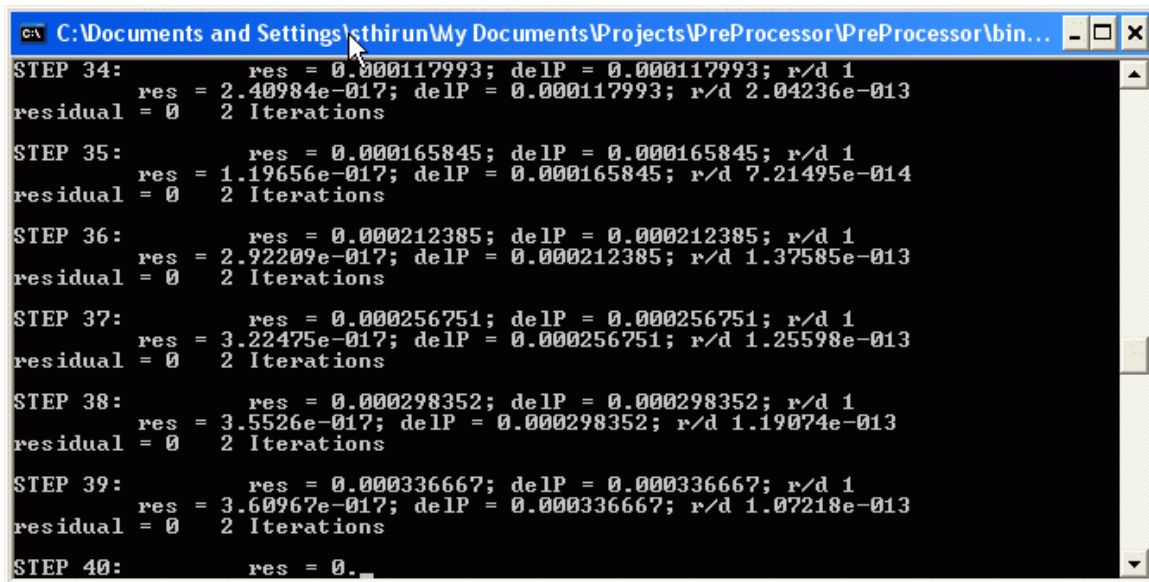
Figure 190. Screen capture. Error dialog for a semantic error.

6.3.2.3. Generating an FEP++ Input File

The preprocessor can be used to generate input files for FEP++ for different configurations that can then be saved to a remote location. This feature is helpful if the user wishes to perform multiple analyses in a script without any user intervention.

6.3.2.4. Running an Analysis

Running an analysis is the final step in pavement analysis. The analysis can be started only after the run analysis option in the control panel turns green. The preprocessor uses the user input to create an input file to FEP++ and invokes it with the generated input file. The preprocessor creates a separate instance and displays the progress of the analysis in a window, as shown in figure 191.



```
C:\Documents and Settings\sthirun\My Documents\Projects\PreProcessor\PreProcessor\bin...
STEP 34:      res = 0.000117993; delP = 0.000117993; r/d 1
            res = 2.40984e-017; delP = 0.000117993; r/d 2.04236e-013
            residual = 0 2 Iterations

STEP 35:      res = 0.000165845; delP = 0.000165845; r/d 1
            res = 1.19656e-017; delP = 0.000165845; r/d 7.21495e-014
            residual = 0 2 Iterations

STEP 36:      res = 0.000212385; delP = 0.000212385; r/d 1
            res = 2.92209e-017; delP = 0.000212385; r/d 1.37585e-013
            residual = 0 2 Iterations

STEP 37:      res = 0.000256751; delP = 0.000256751; r/d 1
            res = 3.22475e-017; delP = 0.000256751; r/d 1.25598e-013
            residual = 0 2 Iterations

STEP 38:      res = 0.000298352; delP = 0.000298352; r/d 1
            res = 3.5526e-017; delP = 0.000298352; r/d 1.19074e-013
            residual = 0 2 Iterations

STEP 39:      res = 0.000336667; delP = 0.000336667; r/d 1
            res = 3.60967e-017; delP = 0.000336667; r/d 1.07218e-013
            residual = 0 2 Iterations

STEP 40:      res = 0.
```

Figure 191. Screen capture. Analysis run-time window.

6.3.3. Postprocessing Stage

After an analysis is completed, the run-time window shown in figure 191 exits, and the results option on the control panel turns green, indicating that result files have been generated that can be viewed with a postprocessor. On choosing view results, the default postprocessor is invoked to view the results.

6.4. POSTPROCESSOR

The postprocessor is an external tool for visualizing the results of the pavement analysis. Currently, Tecplot[®] serves as the default postprocessor, but efforts to provide support for other open-source data visualization tools are underway. It has been decided that the VTK format will be used for the output file format and that MayaVi, a stable open-source python-based viewer that is popular in the finite element community, will be used as a suitable viewer. The support for external tools will be completed in the next project.

CHAPTER 7. A SAMPLE 3D PAVEMENT SIMULATION USING FEP++

As mentioned in the previous chapter, FEP++ has full support for 3D finite element analysis of elastic and viscoelastic materials. This chapter discusses the details of a 3D analysis performed using FEP++ to study the effects of temperature, material, and wheel speed on ALF pavements. The following sections discuss the analysis details and the results.

7.1. THE INPUT DATA

The pavement was modeled as a 3D cuboid, and the details are shown in table 23. A single moving wheel load with the parameters shown in table 24 is used in the analysis. The behavior of the pavement was studied for the effects of temperature, material, and wheel speed. The following subsections discuss the simulations and the results in detail.

Table 23. Properties of pavement.

Depth of AC Layer	46 cm
Pavement Length	296.5 cm
AC Material	ALF Control/ ALF SBS
Subgrade Type and Stiffness	Infinite Subgrade, 86 MPa
Ambient Surface Temperature	Winter (-5 °C)/ Summer (38 °C)

Table 24. Properties of moving wheel load.

Contact Pressure	758 kPa
Load Area	19.65 cm by 17.79 cm
Wheel Velocity	13.41 m/s/26.82 m/s

7.2. EFFECT OF TEMPERATURE

To simulate the effect of temperature, the analysis was performed at representative temperatures for winter and summer. The temperature distribution across the depth was found from simulations with the Enhanced Integrated Climatic Model (EICM). For these simulations, a typical pavement cross section was used with the Raleigh, NC, climatological database. The exact temperature variation is shown in figure 192.

The strains were expected to be larger during the summer as compared to the winter because the material stiffness was smaller at higher temperatures leading to larger deformations. Also, the material was expected to display a higher degree of viscoelasticity at higher temperatures while displaying higher elasticity at lower temperatures.

Figure 193 through figure 198 show the strain distributions for the above analysis when the wheel load reached the center of the pavement. The temperature distribution across the depth is also shown in each of the figures. Figure 193 and figure 194 show the vertical strain distribution, and, as expected, the strains were smaller for the winter loading than for the summer loading.

Also, the strain distribution was more or less symmetrical around the wheel location for winter loading as compared to the summer loading which showed some residual strain from the passing of the wheel. Thus, the viscoelastic behavior was more prominent at higher temperatures.

Figure 195 and figure 197 show the strain distributions for longitudinal and transverse strains. The strains were consistently higher in the case of summer loading than in winter loading, and the elastic nature of the material (symmetry about the wheel) was more prominent during the winter loading. Thus, the results of the FEM analysis of the effects of temperature on the material properties agreed well with the expected outcome.

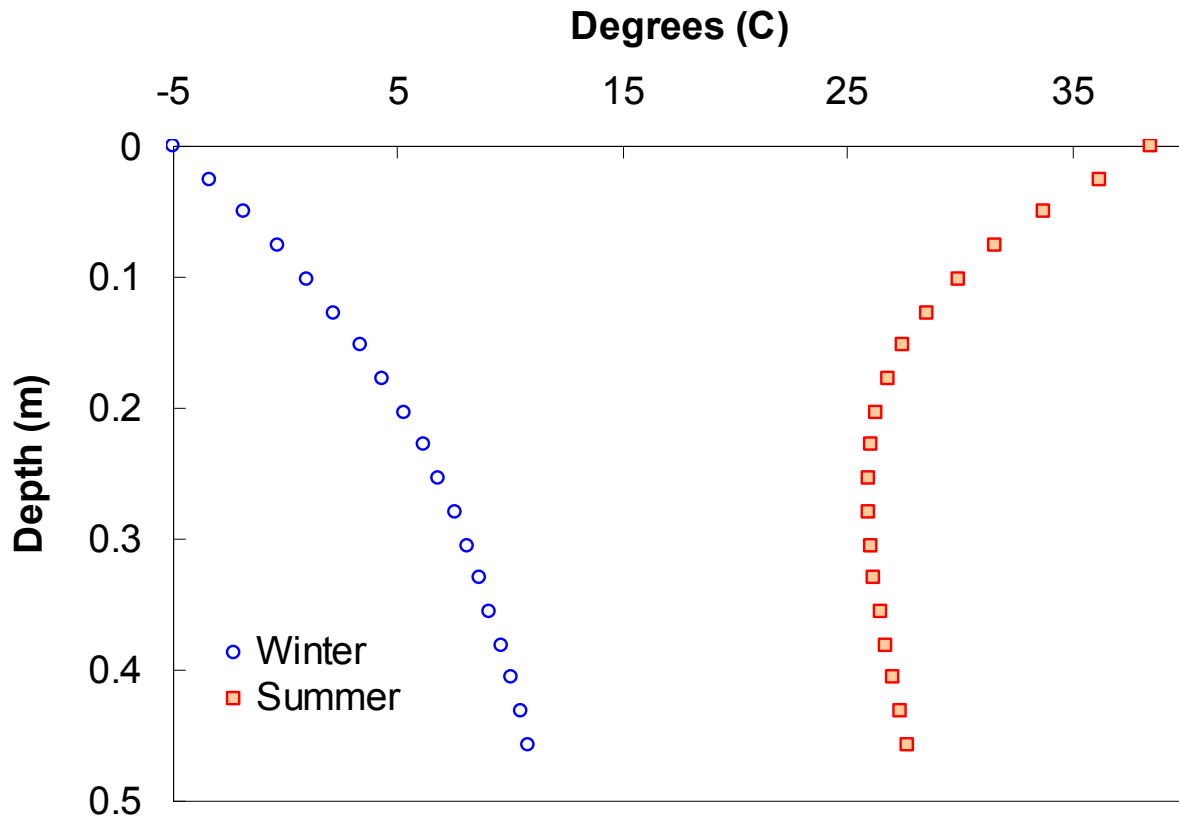


Figure 192. Graph. Temperature variations used for simulations.

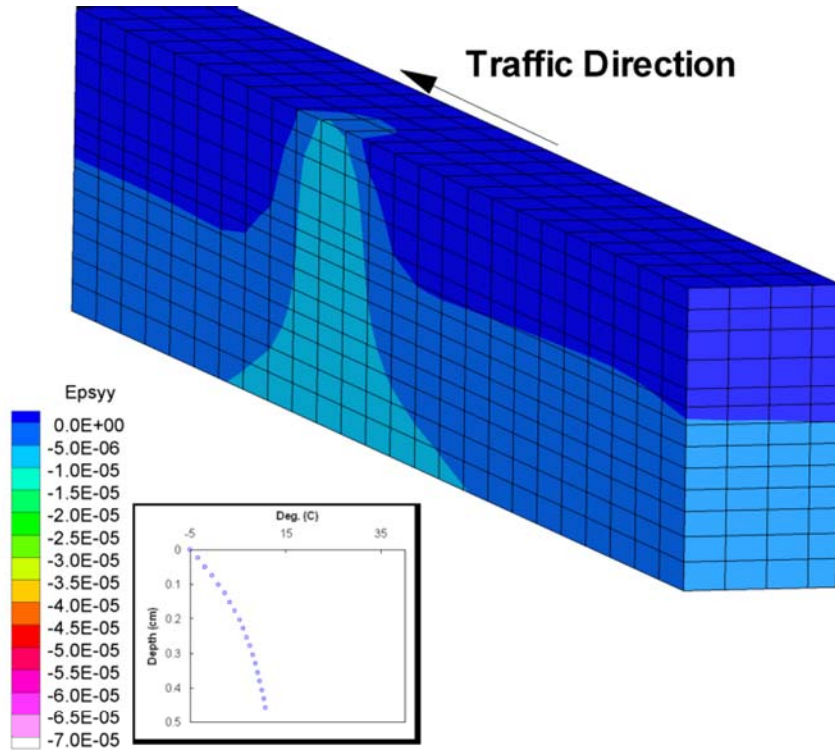


Figure 193. Illustration. Vertical strains in winter.

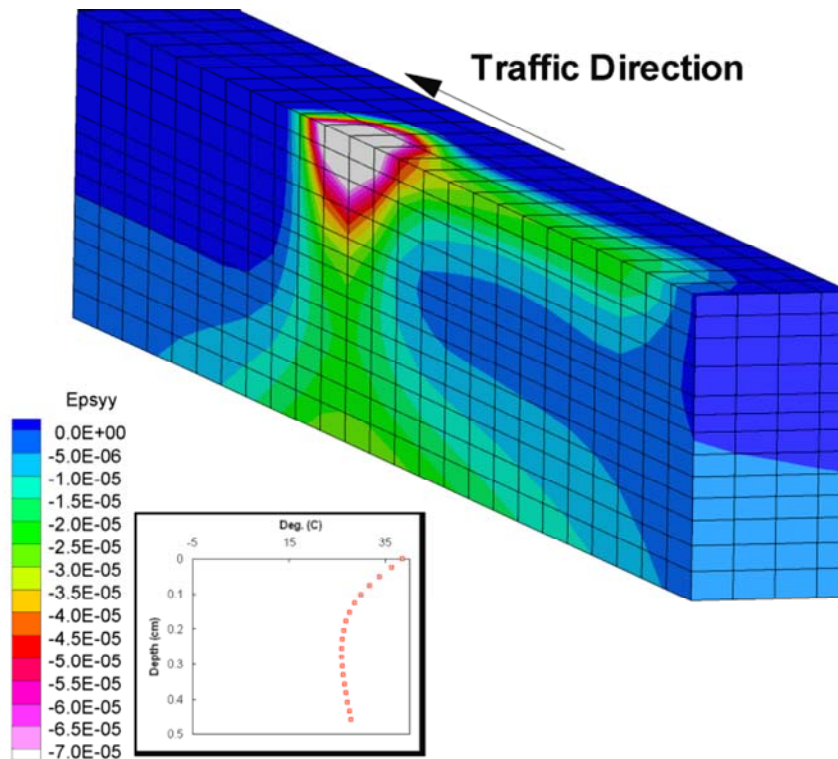


Figure 194. Illustration. Vertical strains in summer.

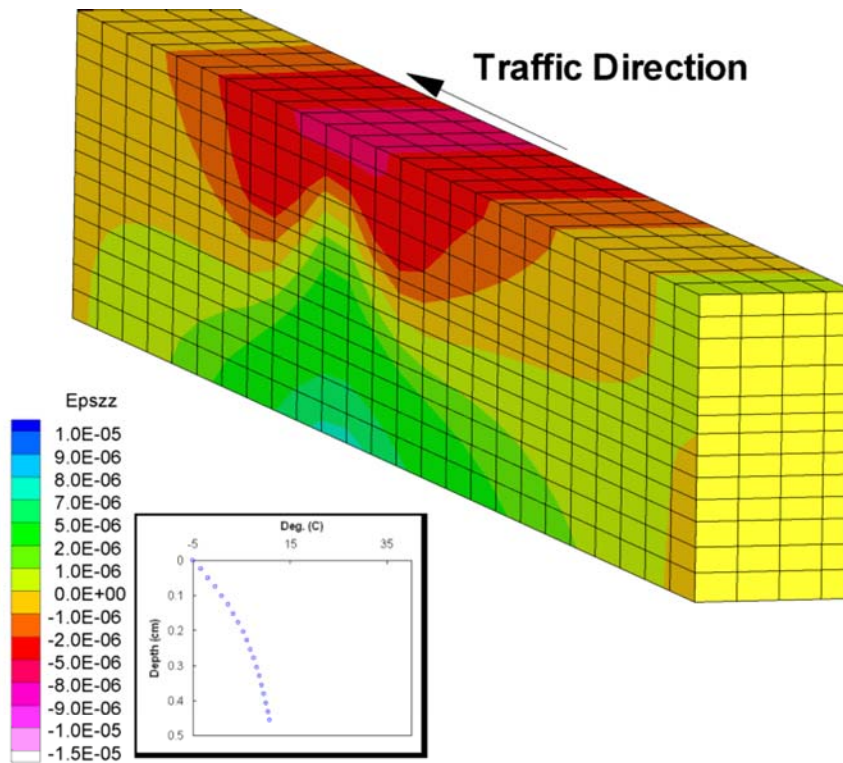


Figure 195. Illustration. Longitudinal strains in winter.

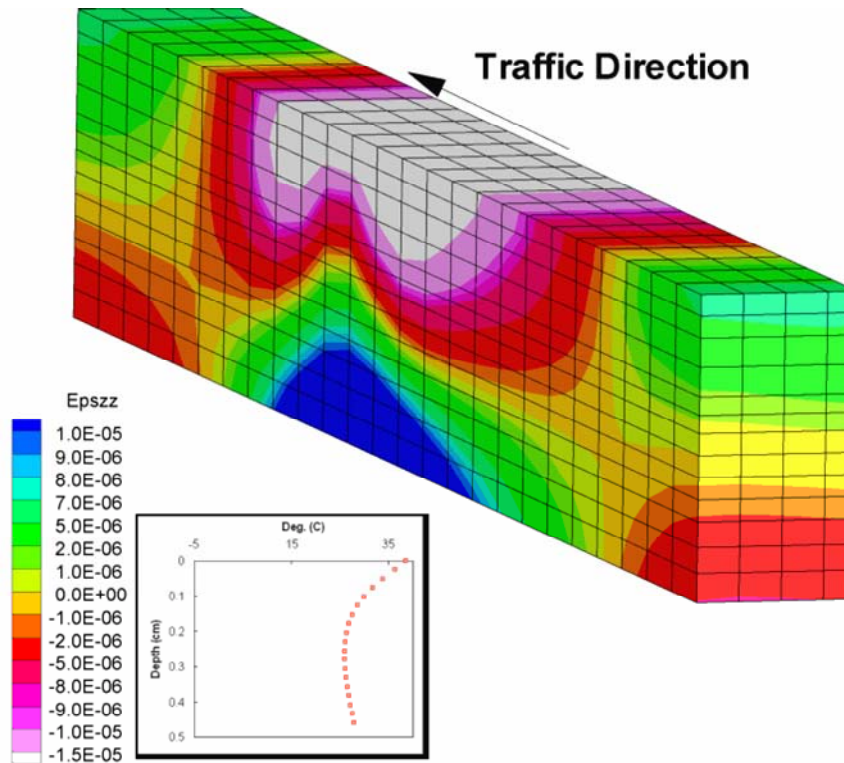


Figure 196. Illustration. Longitudinal strains in summer.

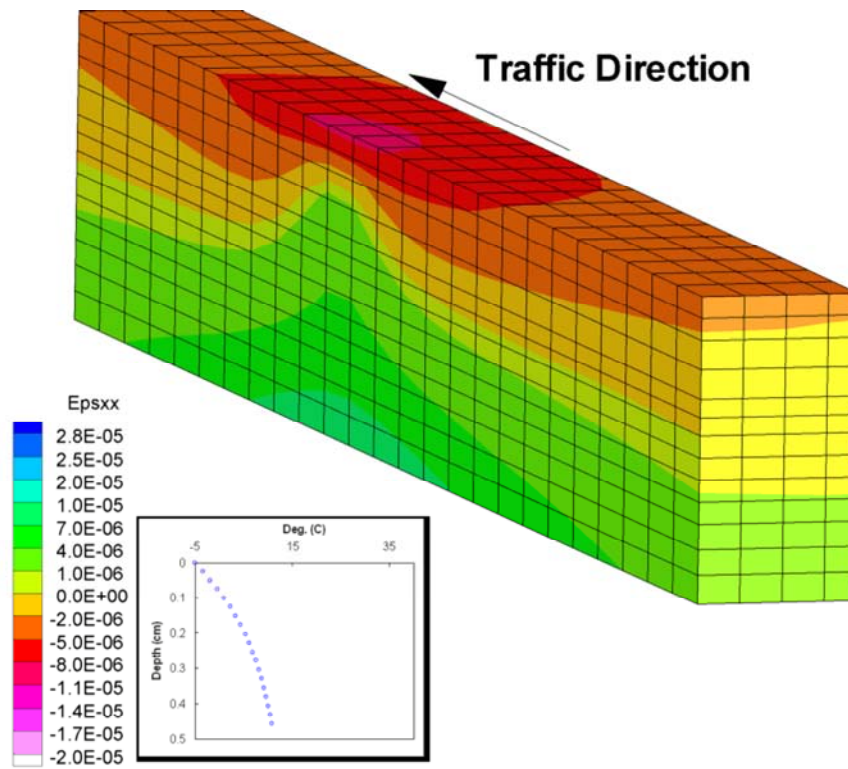


Figure 197. Illustration. Transverse strains in winter.

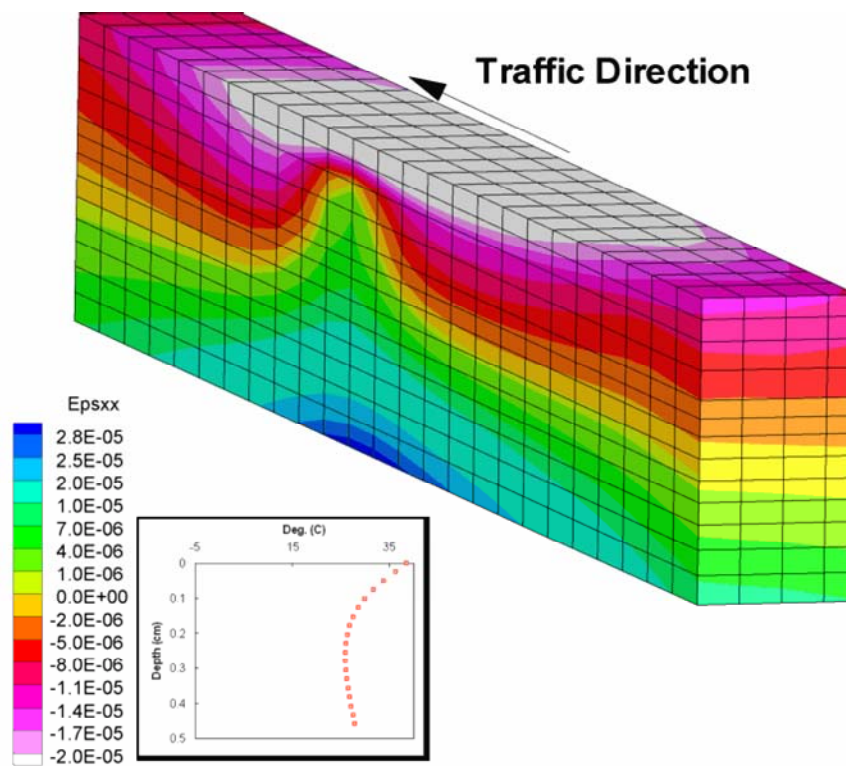


Figure 198. Illustration. Transverse strains in summer.

7.3. EFFECT OF MATERIAL

The effect of material properties on pavement behavior was analyzed next. Pavements under summer conditions, with the ALF Control mixture and the ALF SBS mixture for the asphalt concrete layer, were used for the simulations, and a wheel speed of 26.82 m/s was applied. Because the SBS pavement was less stiff compared to the ALF Control pavement, the strains were expected to be higher for the SBS pavement.

Figure 199 through figure 204 show the strain distributions for the above analysis when the wheel load reached the center of the pavement. Figure 199 and figure 200 show the vertical strain distribution; the SBS pavement had higher strains compared to the Control pavement. Also, the strains in the SBS pavement located away from the wheel location were higher, indicating that the strains in the SBS pavement took longer to recover from the passing of a wheel than those of the Control pavement.

Figure 201 and figure 202 show the longitudinal strains for the two mixtures. Again, the strains were larger for the SBS mixture than for the Control mixture, leading to larger regions of tension and compression.

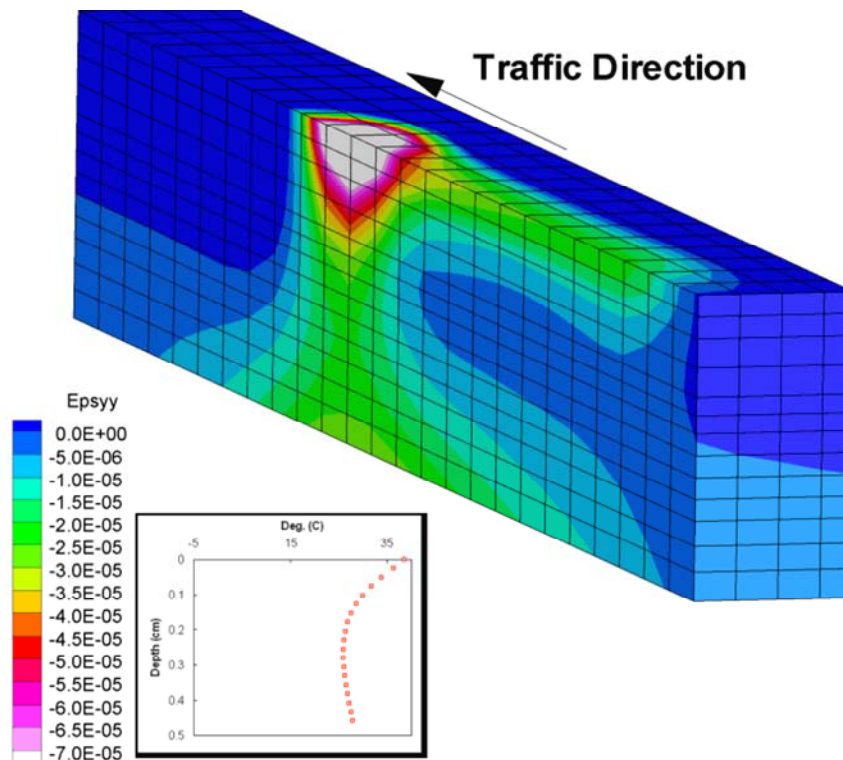


Figure 199. Illustration. Vertical strains for Control mixture.

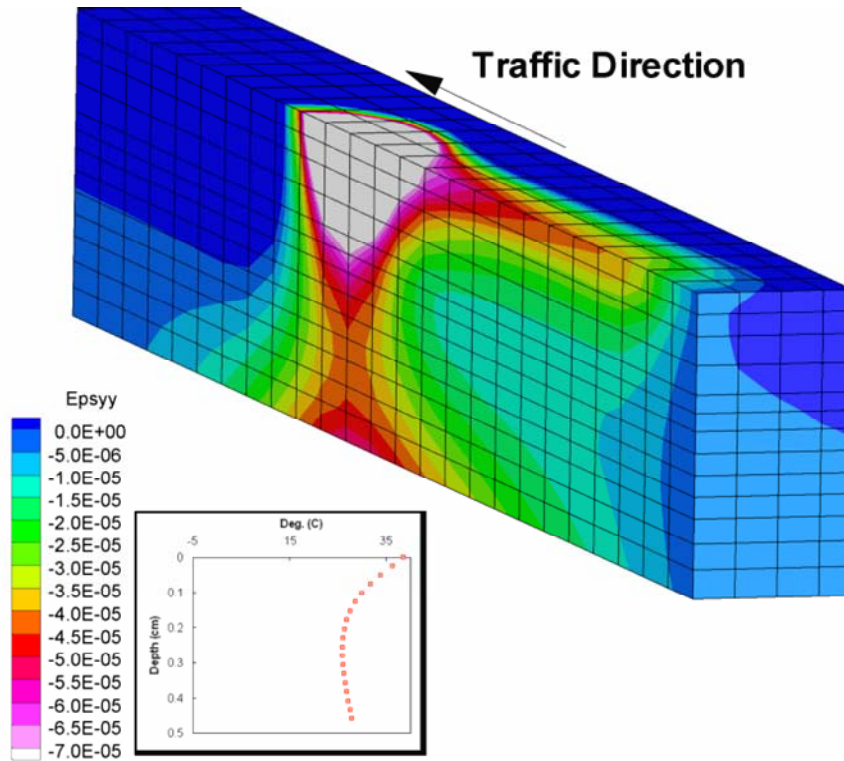


Figure 200. Illustration. Vertical strains for SBS mixture.

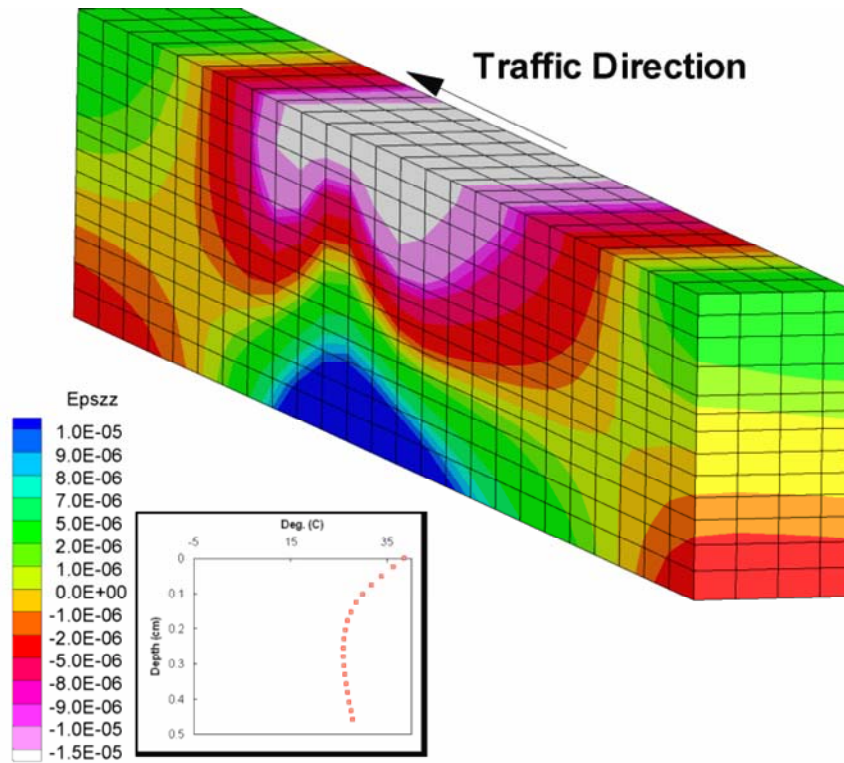


Figure 201. Illustration. Longitudinal strains for Control mixture.

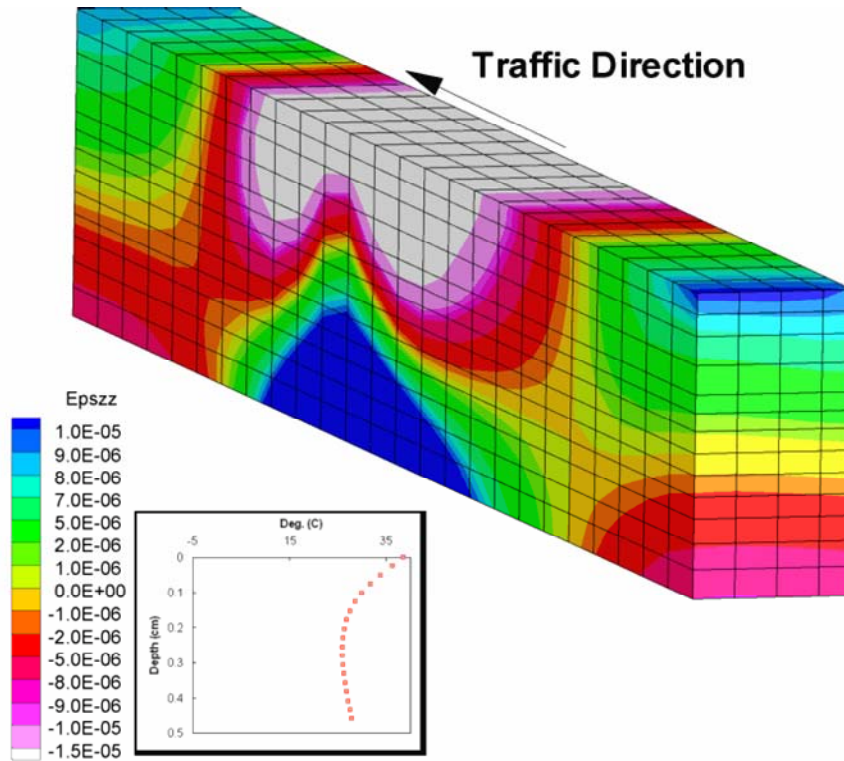


Figure 202. Illustration. Longitudinal strains for SBS mixture.

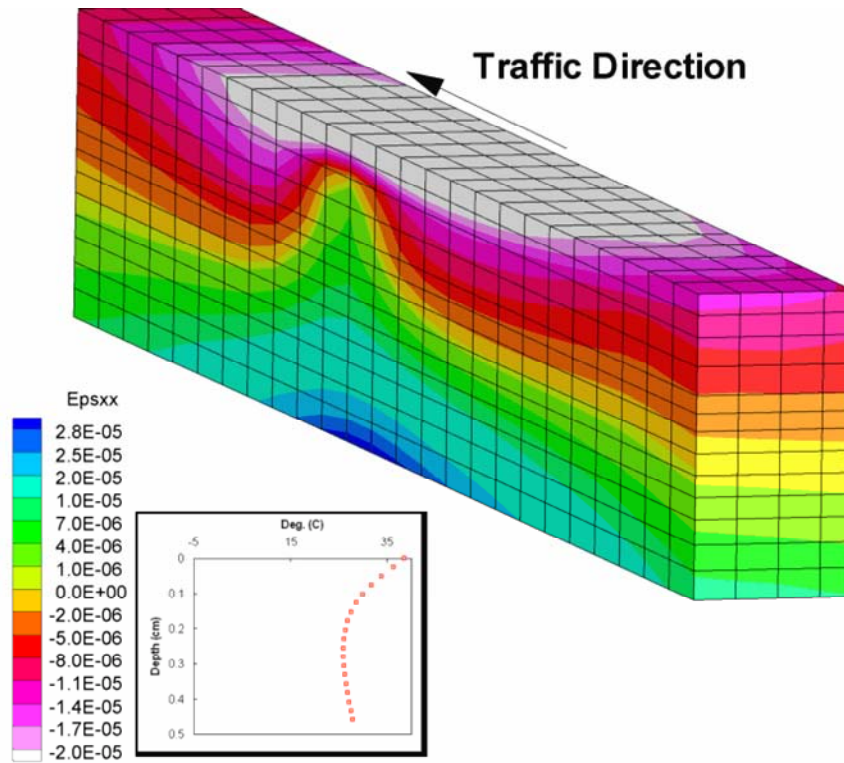


Figure 203. Illustration. Transverse strains for Control mixture.

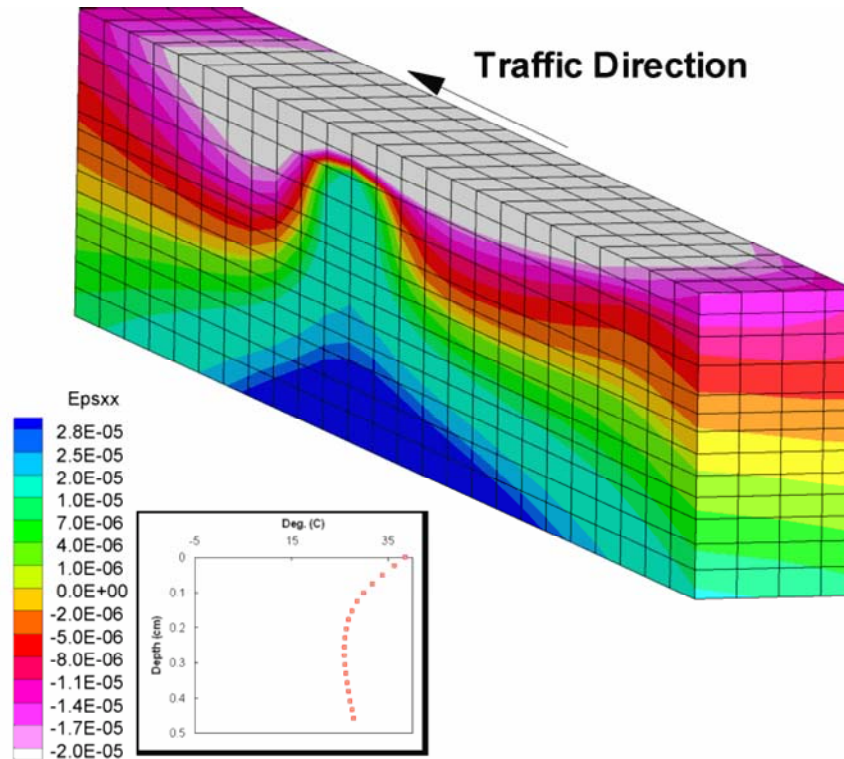


Figure 204. Illustration. Transverse strains for SBS mixture.

Figure 203 and figure 204 show the transverse strains. Again, the strains were larger for the SBS mixture than for the Control mixture. Also, the region of maximum tension at the bottom of the pavement was much larger for the SBS pavement than for the Control pavement. The area of influence on the surface of the pavement was higher for the SBS mixture than the Control mixture.

Again, the results were as expected. The SBS pavement deformed more than the Control pavement, and the area of influence was larger due to its lower stiffness.

7.4. EFFECT OF WHEEL SPEED

Finally, the effect of the wheel speed on pavement behavior was analyzed. The analysis was performed on a pavement using the ALF Control mixture for the asphalt concrete layer under summer conditions for two cases with wheel speeds of 13.41 and 26.82 m/s, respectively. Because the viscoelastic model was quasistatic, dynamic effects (acceleration/velocity) were not considered, and the effect of the wheel speed essentially affected only the load duration at each point on the pavement. Thus, the effect of a slower wheel speed could be a longer duration of the load pulse and, consequently, larger vertical strains compared to a faster wheel speed. Also, the slower wheel load could create a larger area of influence because the material recovery time may be comparable to the wheel passing time.

Figure 205 through figure 210 show the strain distribution for the analysis when the wheel load reached the center of the pavement. Figure 205 and figure 206 show the vertical strains, which were slightly larger for the slower wheel speed. The memory effect was slightly more

pronounced for the slower wheel speed, as shown by the larger strains in the pavement region passed by the wheel.

Figure 207 through figure 210 show the longitudinal and transverse strains; these strains displayed similar characteristics to the vertical strains, although the effects were much less pronounced. The vertical strains seemed to be most sensitive to the wheel speed.

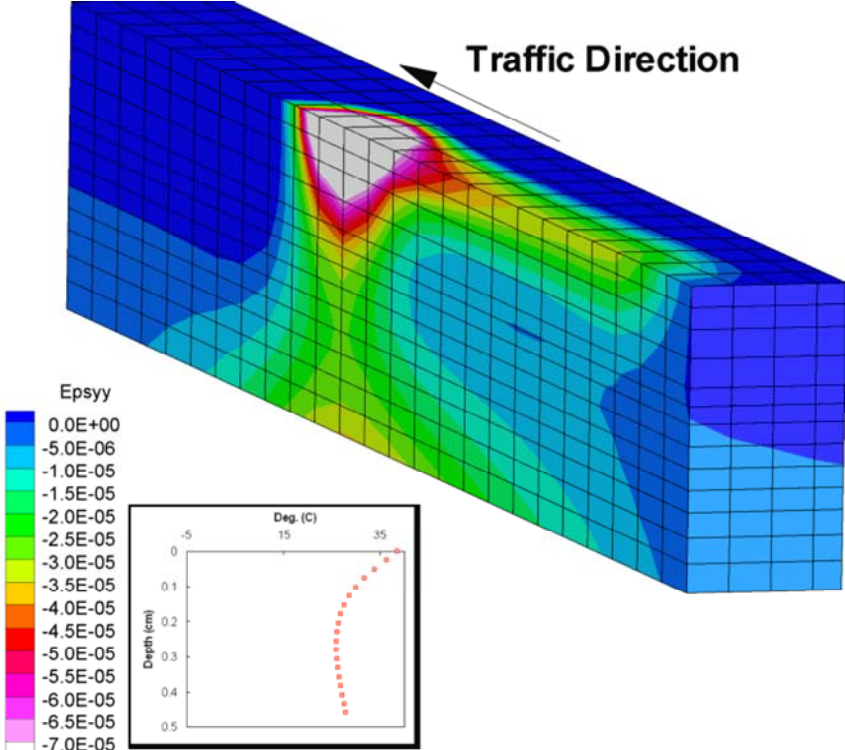


Figure 205. Illustration. Vertical strains for a wheel speed of 13.41 m/s.

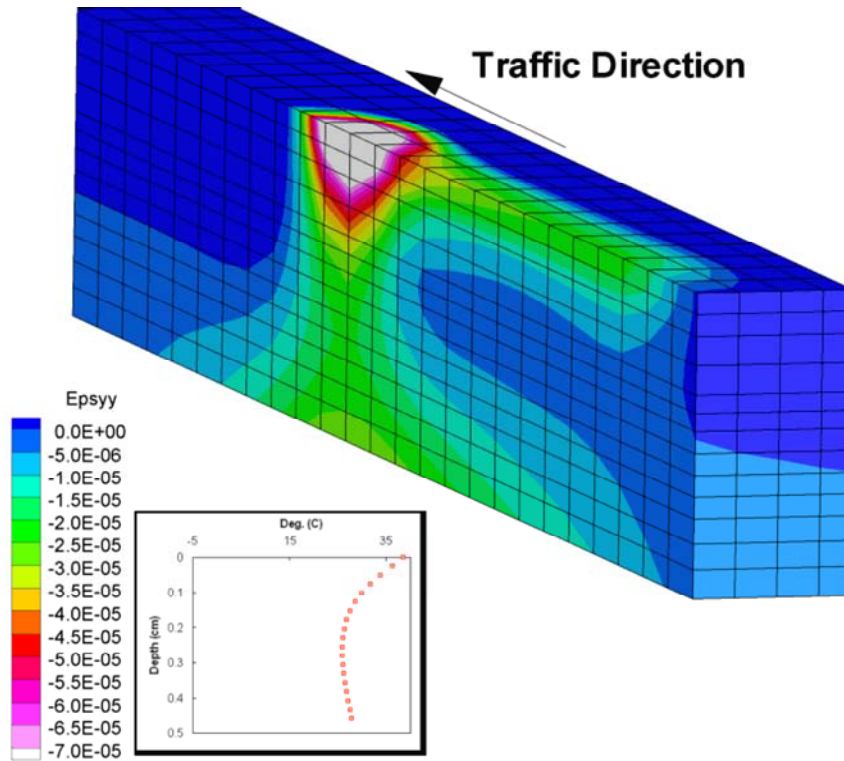


Figure 206. Illustration. Vertical strains for a wheel speed of 26.82 m/s.

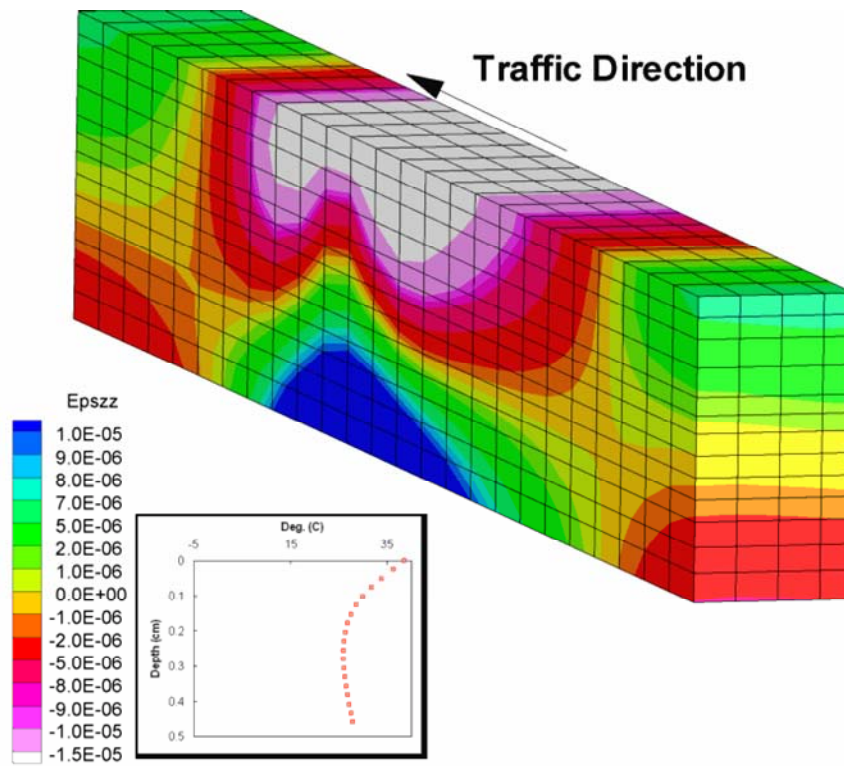


Figure 207. Illustration. Longitudinal strains for a wheel speed of 13.41 m/s.

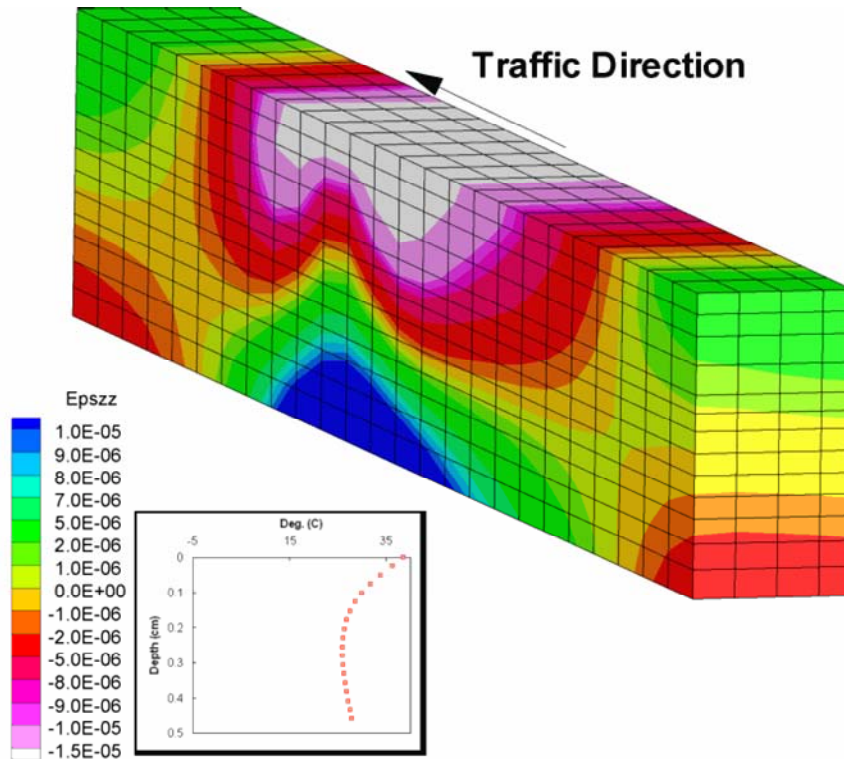


Figure 208. Illustration. Longitudinal strains for a wheel speed of 26.82 m/s.

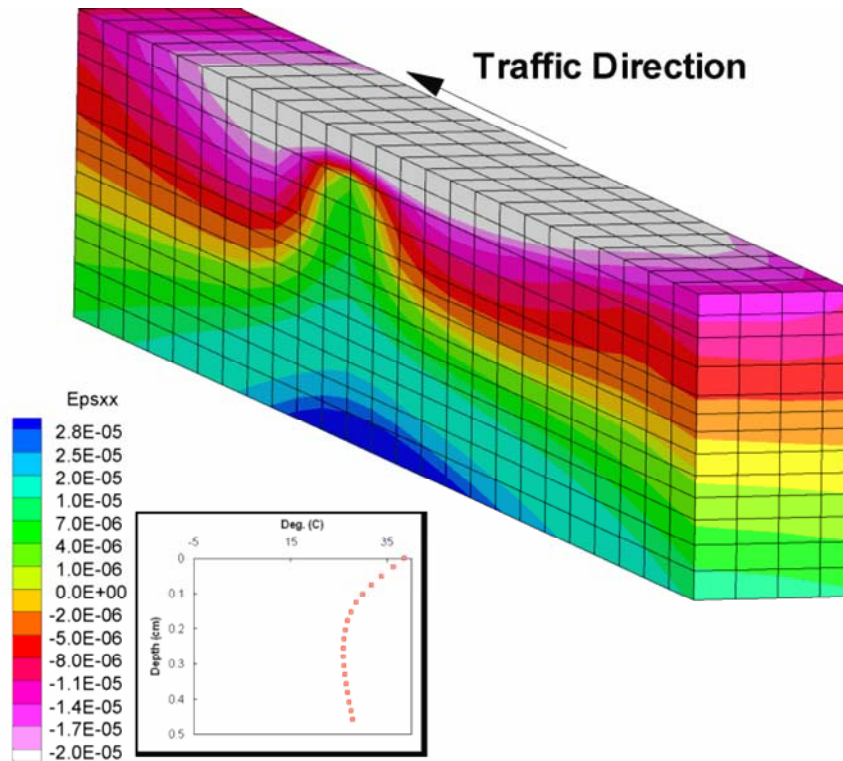


Figure 209. Illustration. Transverse strains for a wheel speed of 13.41 m/s.

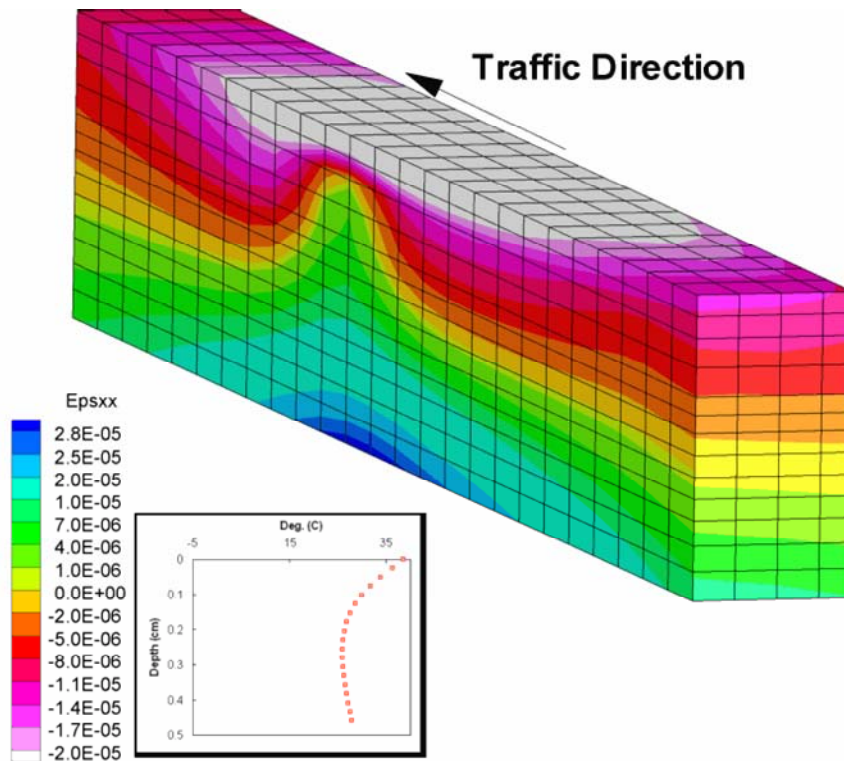


Figure 210. Illustration. Transverse strains for a wheel speed of 26.82 m/s.

CHAPTER 8. CONCLUSIONS AND FUTURE WORK

8.1. CONCLUSIONS

The approach adopted in this research to characterize asphalt concrete over a wide range of temperatures and loading rates encountered in the field divided the problem into two components: (1) characterizing the viscoelastic response and (2) characterizing the viscoplastic response. The VECD model described the time-dependent behavior of asphalt concrete with growing microcrack damage. The irrecoverable (whether time-dependent or independent) strain was described by the VP model. These two models were integrated based on the strain decomposition principle to form the VEPCD model. This model was found to be applicable to the tension mode and, in principle, to the compression mode of loading.

Through the model characterization procedures, it was also found that the dynamic modulus, if it was determined according to strict guidelines so that the linear limits of the material were not exceeded, was not dependent upon loading direction (tension compression or compression only). Further, it was found that this loading direction independence held under different confined stress states. From these confined dynamic modulus tests, a state-dependent model similar to the one used for unbound paving materials was developed and characterized.

The viscoelastic damage characteristics were found to differ in the compression and tension loading modes, with the compression mode showing the more favorable results (i.e., less reduction in the pseudo stiffness, C , for the same amount of increase in the damage parameter, S). These results were also consistent with the hypotheses that the damage parameter, S , was related to cracking density or crack volume and that the primary direction of this cracking was perpendicular to the tensile loading direction or parallel to the compressive loading direction. A simple, empirically-based viscoplastic model was found to be sufficient for explaining the tensile behavior of asphalt concrete, but it did not explain the compressive behavior.

For the compressive behavior, a rate-dependent softening mechanism, which operated during unloading, was found to be a significant factor that affected the viscoplastic characteristics of asphalt concrete. Several existing viscoplastic models that included flow rules and a yield criterion had been evaluated, but they were found to be insufficient for describing this softening behavior. To account for this characteristic behavior, the rate-dependent, hardening-softening function was suggested using Perzyna's flow rule. The relaxation modulus determined from the linear viscoelastic characterization was utilized in this process. It was shown that the developed model could account for the effects of rest periods and loading sequence on viscoplastic strain development.

In light of practical concerns related to the use of constant rate tests in the AMPT and due to the complexities of performing true time-dependent analysis of cyclic fatigue tests, a simplified VECD model was presented. This model utilized results from fatigue tests performed at nominal levels that were possible with the AMPT equipment, as well as the VECD model that specialized in such loading so as to arrive at a simple formulation to characterize the model. This formulation was found to generally agree with the results from the constant rate tests, particularly under conditions of minimal viscoplastic strain.

Another major finding in this research was the verification of the time-temperature superposition principle with growing damage, both in compression and tension, in a confined stress state. This principle was proven valid using constant rate tests under various temperatures and strain rates with an applied confining stress. Therefore, the response of a mixture with growing damage at one temperature could be predicted by shifting its response at another temperature using the time-temperature shift factor determined from the LVE complex modulus tests.

The major contribution of the time-temperature superposition principle and the damage characteristic curve was the significant reduction in testing requirements. The model allowed the prediction of the material's behavior at any temperature from a test result obtained from a single temperature and the time-temperature shift factors obtained from temperature sweep complex modulus tests. The experimental results from the previous FHWA project (DTFH61-03-H-00116) and this project verified that the time-temperature superposition principle with growing damage was valid in both tension and compression, regardless of the confined state (i.e., unconfined or confined).

To realize the full potential of the VEPCD material model for predicting pavement performance, a robust FEP++ was developed to account for the effects of loading and boundary conditions. FEP++ was designed using a top-down, object-oriented approach with great care so that further enhancements could be made by the research team in an efficient manner. Furthermore, special elements and implementation techniques were employed to increase the computational efficiency. The 2D version of the resulting software has the ability to predict stresses, strains, and damage of the pavement under repeated traffic loading. FEP++ was also extended to 3D stress analysis with the ultimate goal of 3D damage modeling of moving traffic loads. All these capabilities were made accessible to the user through carefully designed and powerful graphical pre and postprocessors. As part of the ongoing HMA-PRS project sponsored by the FHWA (DTFH61-08-H-00005), FEP++ is now being molded into an integrated software tool that can be used for robust pavement performance predictions.

To illustrate the capabilities of FEP++ and its preprocessor, a full 3D finite-element analysis was carried out. The effects of temperature, material, and wheel speed were studied and found to be in accordance with the expected results. Namely, the pavement showed an increased viscous response with increased temperature and decreased speed. The simulations also showed lower strains with higher temperatures, increased wheel speed, and a stiffer asphalt concrete material.

8.2. FUTURE WORK

The following items are recommended for future research:

- *Modeling multiaxial VEPCD*: Sensitivity analyses considering true in-field conditions should be carried out for both tensile and compressive loading to determine the influence of simplifications to and the need for the complete multiaxial formulation. If complete multiaxial modeling does not substantially change the predicted performance of the asphalt concrete, then less testing is needed for accurate pavement performance modeling.
- *Further Simplifying VECD model development*: Although constant rate tests are simple to perform, the capacity of the recently developed AMPT equipment limits the use of such

tests. A simplified model further specialized for more moderate load amplitude cyclic tests and derived rigorously will expand the application of the VECD model for further routine testing and analysis.

- *Hardening in the MVECD compression model:* A possible drawback to the current MVECD model for compression is the lack of a function to account for hardening due to aggregate interlock. It is known that such a function becomes important, especially at low confinement levels and high temperatures, but the implication of aggregate interlocking under more moderate conditions is unknown.
- *Yielding criteria in the VP compression model:* In this research, the model parameters were determined for each specific confining pressure condition. Although these parameters are not sufficient to explain the general behavior of HMA pavements, which experience an almost uniform confining pressure for certain time periods, they are, nonetheless, reasonable for introducing a yield criterion that can account for the entire confining pressure.
- *Hardening-softening of the function in the VP compression model:* Even though the current hardening-softening function reasonably accounts for the rate-dependent softening of HMA, some over and underpredictions were observed for certain stress histories. These observations may be explained by an inaccuracy in the hardening-softening function, and therefore, more research into the hardening-softening function is required.
- *Refining analysis program:* Current VEPCD modeling is aided by a software package developed at NCSU. The program is currently in the development stage and is considered to be research-grade software. Usability, therefore, is somewhat limited. Refinement of this program into a complete black box package will greatly aid the implementation of VEPCD modeling at the industrial level.
- *Advancing material models with FEP++:* Currently the 3D FEP++ code includes modules for linear elastic and linear viscoelastic materials. The MVECD model should be implemented along with other material models and functions. To model unbound paving materials accurately, a module should be added to include a nonlinear elastic material model. In addition, models that account for the effects of temperature and moisture gradients in pavement systems and the effects of aging of the HMA layer on pavement performance need to be incorporated into the FEP++. Additionally, anisotropy of the HMA and slip elements at the pavement-base interface should be included. The modular design of the 3D FEP++ allows for incorporation of new modules that pertain to advanced materials, more efficient solution techniques, and fast solvers with little or no change to the existing code.

APPENDIX. USER MANUAL FOR FEP++

A.1. INSTALLATION OVERVIEW

FEP++ can be installed using the supplied windows installer. The installer file is named “Setup.exe.” Executing the binary launches the installation wizard, which then guides through the rest of the installation procedure. Once the installation is completed successfully, an entry for FEP++ should be created in the Start Menu of Windows®. FEP++ can be launched by choosing the program from the Start Menu.

The following section describes the data entry windows in FEP++ and provides information on their functionality and the type of input they accept.

A.2. LIST OF INPUT DIALOGS

A.2.1. General Information Dialog

Figure 211 shows a screenshot of the General Information dialog. This is used to input information regarding the model and the type of analysis. This information is used by the preprocessor to customize the interface presented.

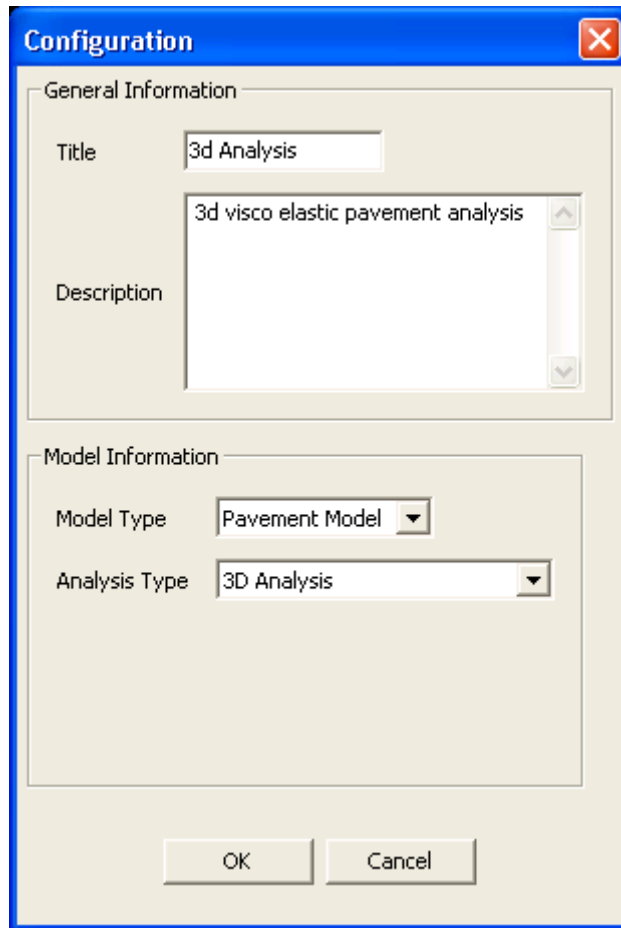


Figure 211. Screen capture. General Information dialog.

A short explanation of the entry fields is given below.

A.2.1.1. Data Entry Fields

Title, Description: This information is used in creating report/summary files and does not affect the analysis in anyway.

Model Type and Analysis Type: These data describe the type of model being solved. Depending on the model type, the user interface and analysis parameters are customized. Currently, 3D analysis, plane strain, and axisymmetric are supported.

A.2.2. Material Properties Dialog

Figure 212 shows a screenshot of the Material Properties dialog, which is used to configure the properties of materials used in the analysis. Currently, only elastic and viscoelastic materials are supported.

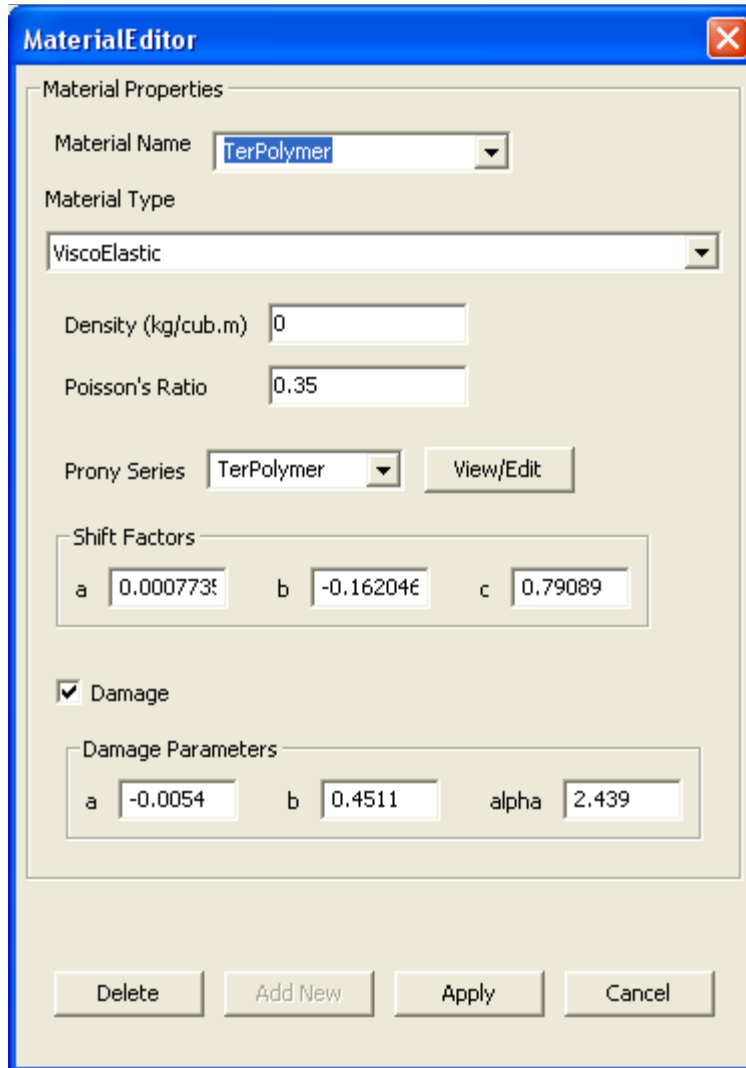


Figure 212. Screen capture. Material Properties dialog.

A short explanation of the entry fields is given below.

A.2.2.1. Data Entry Fields

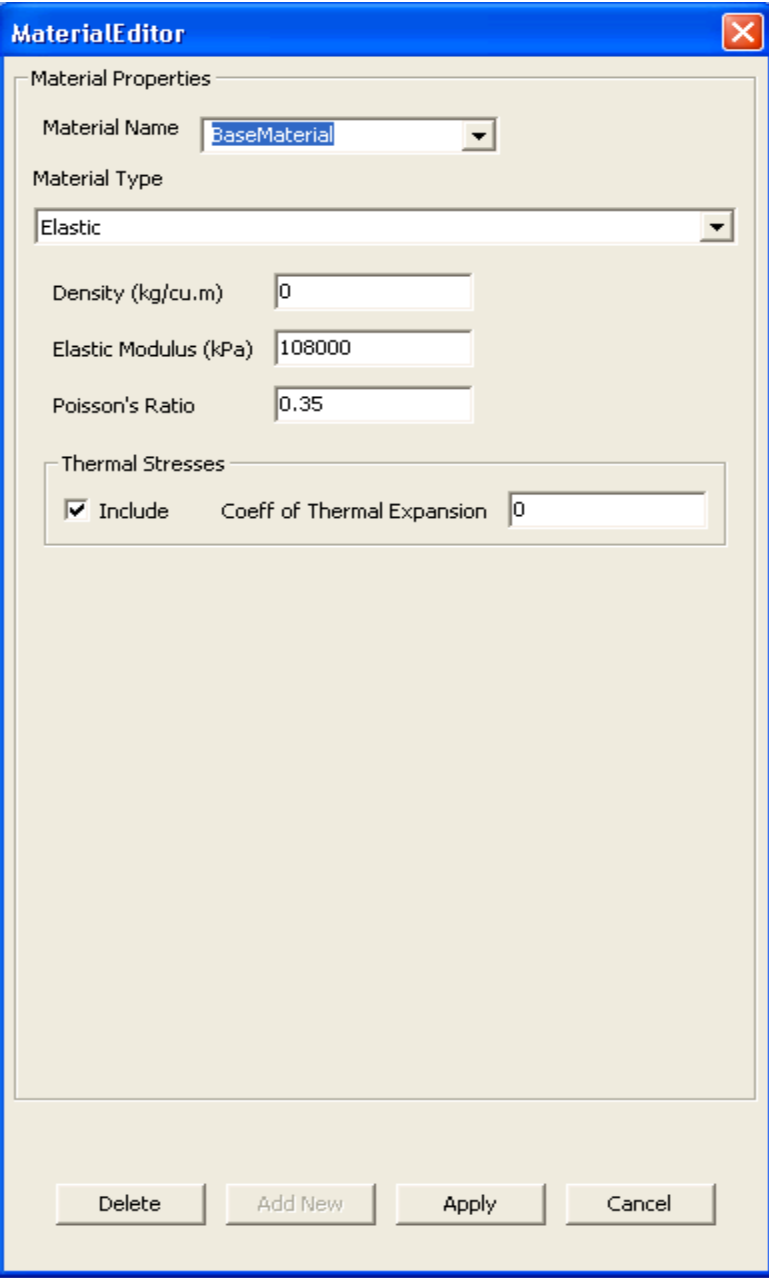
Material Name: This is a string identification used to uniquely identify a material. This is both an entry and a control. On choosing an existing identification, the dialog is populated with the properties of the material corresponding to the identification; however, entering a new value creates a new material.

Material Type: This field indicates the type of material. If an existing material is chosen, then this field is automatically populated with the material type. On creating a new material, the user should choose the material type to continue configuring the specific type of material. Currently supported types are elastic and viscoelastic.

The other fields correspond to parameters depending on the type of material and are discussed in subsequent sections.

A.2.3. Elastic Material Properties Dialog

Figure 213 shows a screenshot of the elastic material properties dialog.



The screenshot shows a dialog box titled "Material Editor" with a close button in the top right corner. The dialog is divided into two main sections: "Material Properties" and "Thermal Stresses".

Material Properties:

- Material Name:** A dropdown menu with "BaseMaterial" selected.
- Material Type:** A dropdown menu with "Elastic" selected.
- Density (kg/cu.m):** A text input field containing "0".
- Elastic Modulus (kPa):** A text input field containing "108000".
- Poisson's Ratio:** A text input field containing "0.35".

Thermal Stresses:

- Include:** A checked checkbox.
- Coeff of Thermal Expansion:** A text input field containing "0".

At the bottom of the dialog, there are four buttons: "Delete", "Add New", "Apply", and "Cancel".

Figure 213. Screen capture. Elastic material properties dialog.

A short explanation of the entry fields is given below.

A.2.3.1. Data Entry Fields

Material Properties Block: These fields are used to input the material properties like density, Poisson's ratio, and elastic modulus.

Thermal Stresses Block: These fields describe the coefficient of thermal expansion of the material. If thermal stresses are to be ignored, then the Include box should be cleared.

A.2.4. Viscoelastic Material Properties Dialog

Figure 214 shows a screenshot of the viscoelastic material properties dialog.

The screenshot shows the 'Material Editor' dialog box with the following fields and values:

- Material Name:** CRTB
- Material Type:** ViscoElastic
- Density (kg/cub.m):** 0
- Poisson's Ratio:** 0.35
- Prony Series:** CRTB_PRONY (with a 'View/Edit' button)
- Shift Factors:**
 - a: 0.000747
 - b: -0.16801E
 - c: 0.821386
- Thermal Stresses:**
 - Include
 - Coeff of Thermal Expansion: 0
- Damage:**
 - Damage
 - Damage Parameters:**
 - a: -0.0016
 - b: 0.5289
 - alpha: 2.963
 - Init States:**
 - Init C: 0.8
 - Init Crack Dir.: 0, 1, 0
 - Damage Update Exception: 1

Buttons at the bottom: Delete, Add New, Apply, Cancel.

Figure 214. Screen capture. Viscoelastic material properties dialog.

A short explanation of the entry fields is given below.

A.2.4.1. Data Entry Fields

Material Properties Block: These fields are used to input the material properties like density and Poisson's ratio.

Prony Series: This field is used to input the Prony series to be used for characterizing the relaxation modulus of the material. Existing Prony series can be chosen by selecting from the dropdown list. New Prony series can be added by clicking the View/Edit button to invoke the Prony Series dialog. Section A.2.5 describes the configuration of fields on the Prony Series dialog.

Shift Factors Block: These parameters are used along with the Prony coefficients to adjust the material properties for the temperature effects. These parameters are used to find the time-temperature shift factor.

Thermal Stresses Block: These fields describe the coefficient of thermal expansion of the material. If thermal stresses are to be ignored, then the Include box should be cleared.

Damage Parameters Block: These are the parameters for characterizing the damage law as discussed in subsection 2.2.4. If damage effects are to be ignored, then the Damage checkbox should be cleared.

A.2.4.2. Control Actions

View/Edit: This control invokes a Prony series dialog that can be used to add new series or edit an existing series. On successful completion, the identification of the selected/configured series is displayed in the Prony series dropdown list.

Delete: This control is active only when an existing material has been chosen. It can be used to delete the material from the database.

Apply: This control performs validations on the modified/input data, and if no errors are found, it saves the data to the database; however, if the validation fails, an appropriate error message is raised, and the data are not saved to the database. This does not close the dialog on successful completion and can be used to make multiple changes without having to open/close the dialog multiple times.

OK: This is similar to the Apply control in functionality; however, on successful completion, this control saves the data and closes the dialog.

Cancel: This control discards any changes made to the data and closes the dialog.

A.2.5. Prony Coefficients Dialog

Figure 215 shows a screenshot of the Prony Coefficients dialog. This dialog can be used to Add/Edit the Prony series.

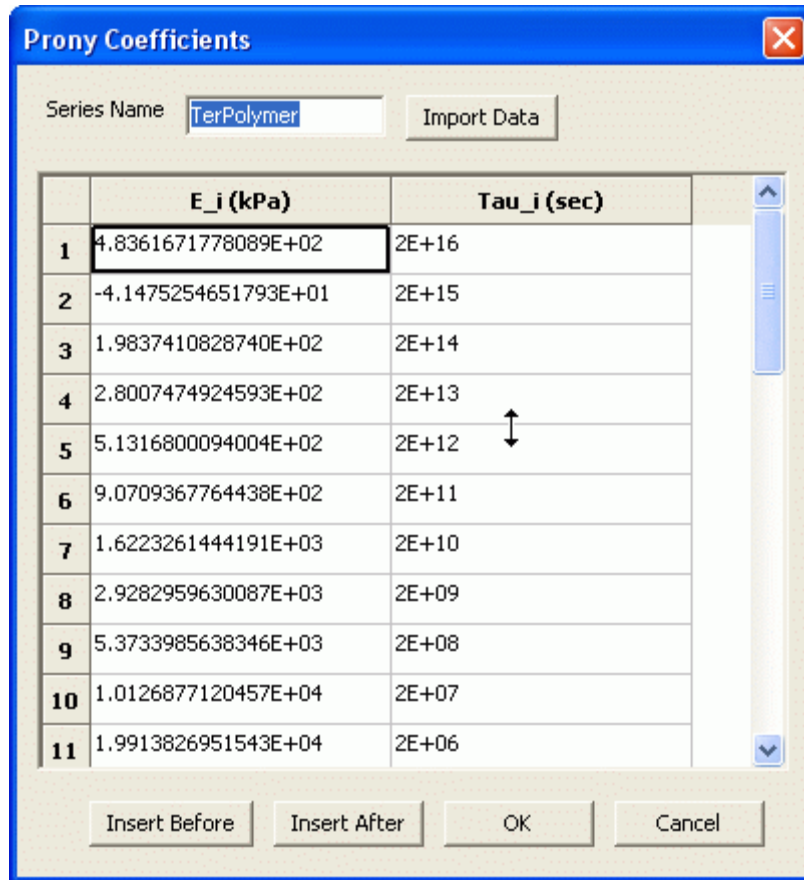


Figure 215. Screen capture. Prony Coefficients dialog.

A short explanation of the entry fields is given below.

A.2.5.1. Data Entry Fields

Series Name: This field is a string identification used to uniquely identify the Prony series.

A.2.5.2. Control Actions

Import Data: This control is used to import the Prony coefficients from a text file. Each record in the file is expected to be in the format, “E_i Tai_i”, that is, space separated values of Prony coefficients and relaxation times.

Insert Before: This control is used to edit the Prony coefficients table. It adds a new blank row above the current selected row.

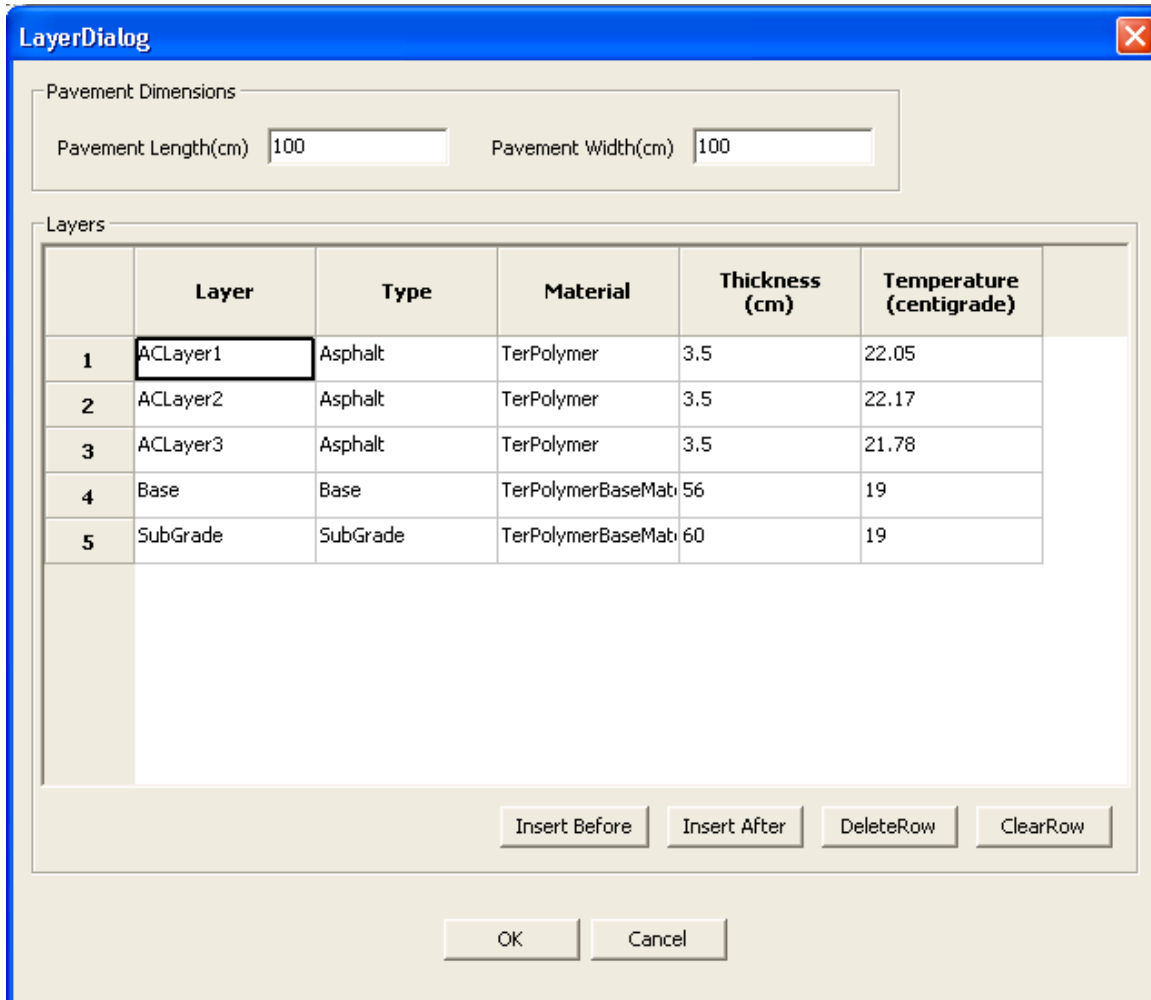
Insert After: This control is used to edit the Prony coefficients table. It adds a new blank row below the current selected row.

OK: This control performs validations on the modified data, and if no errors are found, it saves the data and closes the dialog. If validation fails, an appropriate error message is raised.

Cancel: This control discards any changes made to the data and closes the dialog.

A.2.6. Layer Properties Dialog

Figure 216 shows a screenshot of the Layer properties dialog. This dialog is customized depending on the analysis type (2D or 3D). This dialog also supports the configuration of the subgrade as a half-space.



The screenshot shows a dialog box titled "LayerDialog" with a close button in the top right corner. It contains two main sections: "Pavement Dimensions" and "Layers".

Pavement Dimensions: Two input fields are present: "Pavement Length(cm)" with a value of 100, and "Pavement Width(cm)" with a value of 100.

Layers: A table with 6 columns: "Layer", "Type", "Material", "Thickness (cm)", and "Temperature (centigrade)". The table contains 5 rows of data:

	Layer	Type	Material	Thickness (cm)	Temperature (centigrade)
1	ACLAYER1	Asphalt	TerPolymer	3.5	22.05
2	ACLAYER2	Asphalt	TerPolymer	3.5	22.17
3	ACLAYER3	Asphalt	TerPolymer	3.5	21.78
4	Base	Base	TerPolymerBaseMat	56	19
5	SubGrade	SubGrade	TerPolymerBaseMat	60	19

Below the table are four buttons: "Insert Before", "Insert After", "DeleteRow", and "ClearRow". At the bottom of the dialog are "OK" and "Cancel" buttons.

Figure 216. Screen capture. Layer properties dialog.

A short explanation of the entry fields is given below.

A.2.6.1. Data Entry Fields

The fields for this dialog are represented in the form of a table. Each row of the table represents a layer of the pavement. The column headings specify the property being configured. The columns of the table are described as follows:

Pavement Width (cm): This shows the width of the pavement layer. This can be configured only for a 3D analysis.

Pavement Length (cm): This shows length of the pavement section to be simulated. This can be configured only for a 3D analysis.

Layer: This shows a unique string identifying the pavement layer.

Type: This specifies the type of pavement layer. The valid options are AC, Base, SubBase, SubGrade, and InfiniteSubgrade. AC refers to asphalt concrete layer, and InfiniteSubgrade refers to a subgrade that is treated as a half-space. This field is not editable.

Material: This shows the type of material to be associated with the layer. The material can be chosen from the material database that was configured using the Material dialog (section A.2.2).

Thickness: This shows the thickness of the pavement layer. This must be configured for all the layers except if the type of the layer is InfiniteSubgrade. In this case, special elements are used to treat the subgrade as a half-space.

Temperature: This shows the mean temperature in the pavement layer. This is used in adjusting the viscoelastic material properties for the temperature effects.

A.2.6.2. Control Actions

Insert Before: This control adds a pavement layer above the selected pavement layer.

Insert After: This control adds a pavement layer below the selected pavement layer.

DeleteRow: This control deletes the selected pavement layer.

ClearRow: This control clears the selected pavement layer.

OK: This control performs validations on the modified data. If no errors are found, it saves the data and closes the dialog. If validation fails, an appropriate error message is raised.

Cancel: This control discards any changes made to the data and closes the dialog.

A.2.7. Mesh Parameters Dialog

Figure 217 shows a screenshot of the Mesh Parameters dialog. This dialog is used to configure the mesh discretization parameters for the finite element analysis. It is customized depending on ModelType and AnalysisType that were input in the General Information dialog.

The model is divided into the following two zones:

Zone-I: The region corresponding to the actual pavement is called Zone-I. The length and width discretization is common for all the layers, but the thickness discretization can be configured independently for each layer. A uniform discretization is used for each layer.

Zone-II: Zone-II corresponds to the boundary of the pavements and is modeled using infinite elements to simulate the effect of a half-space (semi-infinite medium). A geometric series based discretization is used for each region.

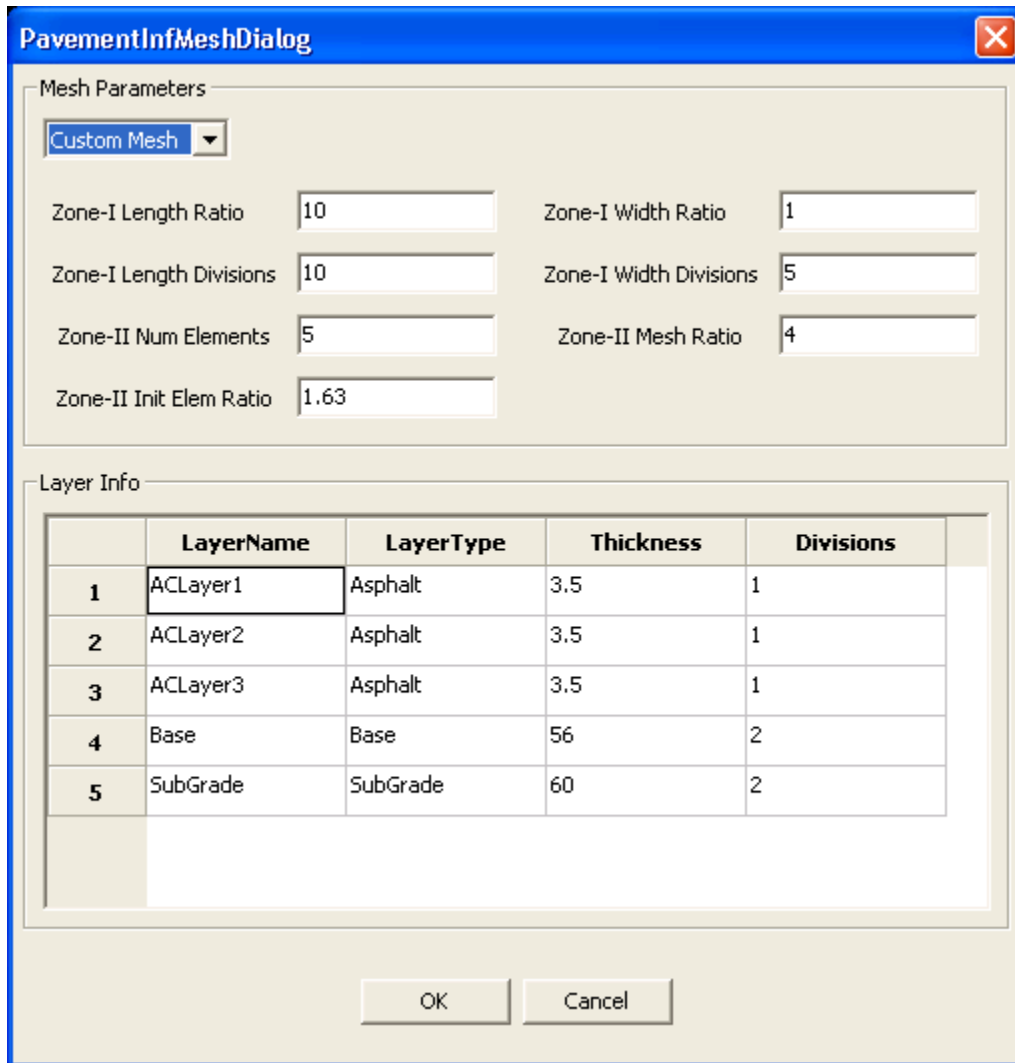


Figure 217. Screen capture. Mesh properties dialog.

A short explanation of the entry fields is given below.

A.2.7.1. Data Entry Fields (Mesh Parameters Block)

Zone-I Length Ratio: This parameter corresponds to the length of the actual pavement. The length is calculated as (Zone-I Length Ratio) multiplied by (Load Length).

Zone-I Length Divisions: This specifies the number of divisions in Zone-I along the length of the pavement.

Zone-I Width Ratio (3D analysis): This parameter corresponds to the width of the actual pavement. The width is calculated as (Zone-I Width Ratio) multiplied by (Load Width).

Zone-I Width Divisions (3D analysis): This corresponds to the number of divisions in Zone-I along the width of the pavement.

Zone-II Mesh Ratio: This specifies the geometric ratio used for creating the geometric series discretization in Zone-II.

Zone-II Init Element Ratio: This parameter corresponds to the initial element size in the geometric series discretization of Zone-II. The initial element size along direction P is calculated as (Zone-II Element Ratio) multiplied by $\min(\text{element size along perpendicular direction to } P)$.

Zone-II Num Elements: This parameter specifies the number of elements in Zone-II along any direction.

A.2.7.2. Data Entry Fields (Layer Info Block)

The fields Layer, Type, and Thickness are not editable and are taken from the data used to configure the Layer properties.

Divisions: This specifies the number of divisions for the discretization of the pavement layer along the thickness. If the layer is Infinite Subgrade, then this field is also not editable, and the data input from the Zone-II configuration is used.

A.2.7.3. Control Actions

OK: This control performs any validations on the modified data, and if no errors are found, it saves the data and closes the dialog. If validation fails, an appropriate error message is raised.

Cancel: This control discards any changes made to the data and closes the dialog.

A.2.8. Load Properties Dialog

Figure 218 shows a screenshot of the Load properties dialog. This dialog is used to configure the loading conditions for the model. This interface is customized depending on ModelType and AnalysisType fields that were configured using the General Information dialog. In these configurations, the loading area is assumed to be rectangular, and the pressure distributions are assumed to be uniform in the loading area.

The screenshot shows a dialog box titled "Pavement Load Editor". It contains the following fields and values:

- Id:** NewLoad
- Coordinates (in cms):**
 - x: 10
 - y: 0
 - z: 10
- Magnitude and Dimensions:**
 - Total Load (kN):** Selected in a dropdown menu.
 - Load Length (cm):** 10
 - Load Width (cm):** 10
- Moving Load Data:**
 - Velocity (m/s):** 10

Buttons for "OK" and "Cancel" are located at the bottom of the dialog.

Figure 218. Screen capture. Load properties dialog.

A short explanation of the entry fields is given below.

A.2.8.1. Data Entry Fields (Coordinates (in cm) Block)

X: This shows the x coordinate of the load.

Y: This shows the y coordinate of the load.

Z: This shows the z coordinate of the load.

A.2.8.2. Data Entry Fields (Magnitude and Dimensions Block)

Load Magnitude: This parameter corresponds to the load magnitude. The user can choose to specify either the Total Load or Tire Pressure by choosing the appropriate type in the dropdown box. In the screen capture shown in figure 218 the Total Load option is selected.

Load Length: This parameter specifies the length of the loading area. For the pavement problem, this is the length of the tire.

Load Width: This parameter specifies the width of the loading area. For the pavement problem, this is the width of the tire.

A.2.8.3. Data Entry Fields (Moving Load Data Block)

Velocity: This parameter specifies the velocity at which the loading area moves. For the pavement model, this corresponds to the vehicle speed.

A.2.8.4. Control Actions

OK: This control performs validations on the modified data, and if no errors are found, it saves the data and closes the dialog. If validation fails, an appropriate error message is raised.

Cancel: This control discards any changes made to the data and closes the dialog.

A.2.9. Analysis Parameters Dialog

Figure 219 shows a screenshot of the Analysis Parameters dialog, which is used to configure the parameters for the solution algorithm used in the finite element analysis.

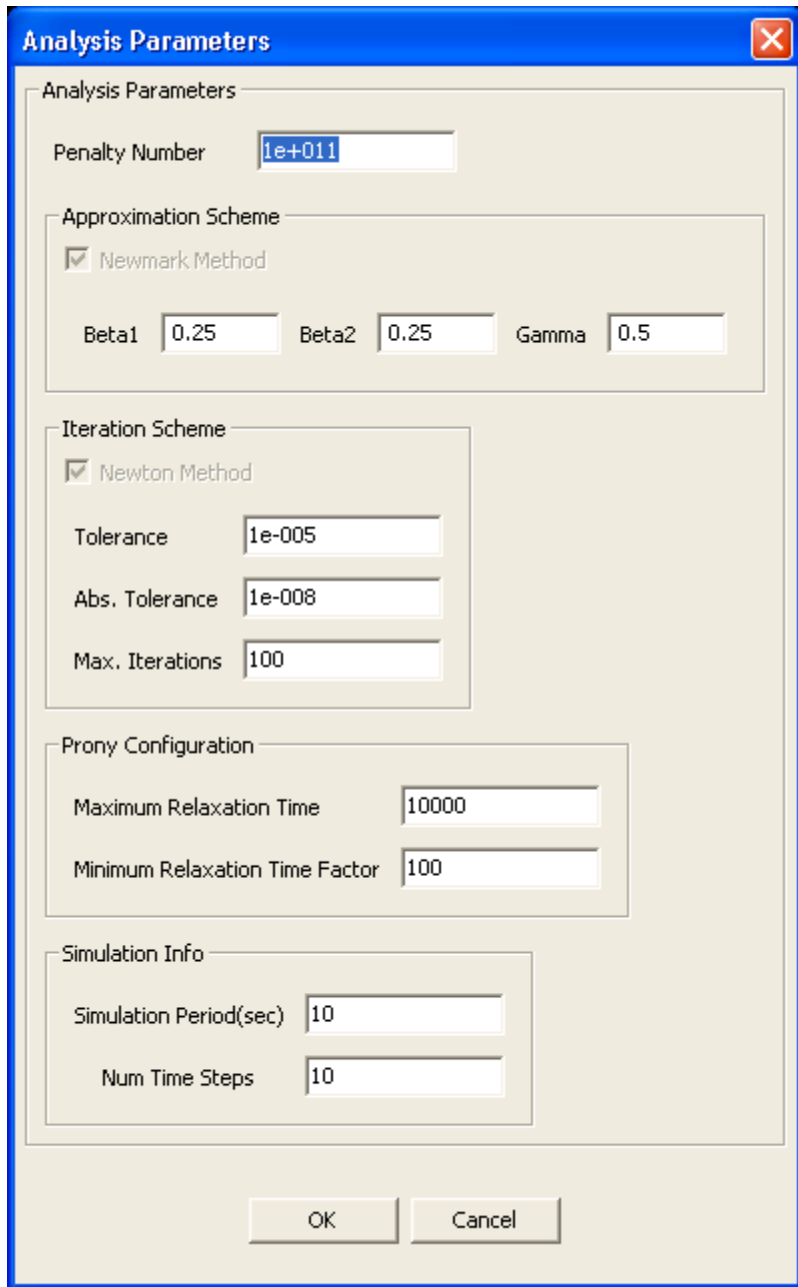


Figure 219. Screen capture. Analysis Parameters dialog.

A short explanation of the entry fields is given below.

A.2.9.1. Data Entry Fields

Penalty Number: This parameter corresponds to the Penalty Number used to model stiffness of the rigid members in finite element analysis.

Approximation Scheme Block: The parameters in this block correspond to the parameters used in the Newmark Method approximation scheme.

Iteration Scheme Block: The parameters in this block correspond to the standard parameters for an iterative solution scheme. The analysis engine currently supports only the Newton Iterations.

Prony Configuration Block: Maximum Relaxation Time: This specifies an upper bound on the Prony coefficients configured for the AC Layers.

Prony Configuration Block: Minimum Relaxation Time Factor: This specifies a lower bound on the Prony coefficients configured for the AC Layers. The lower bound is calculated as $\text{Min Relaxation Time} = (\text{time step size})/(\text{Minimum Relaxation Time Factor})$.

Simulation Info Block: Simulation Period: This specifies the total simulation time for the analysis.

Simulation Info Block: Num Time Steps: This specifies the number of timesteps that will be used in the simulation and hence fixes the timestep size.

A.2.9.2. Control Actions

OK: This control performs validations on the modified data, and if no errors are found, it saves the data and closes the dialog. If validation fails, an appropriate error message is raised.

Cancel: This control discards any changes made to the data and closes the dialog.

A.2.10. Summary Dialog

Figure 220 shows a screenshot of the Summary dialog, which is used to view a user readable report of the input data.

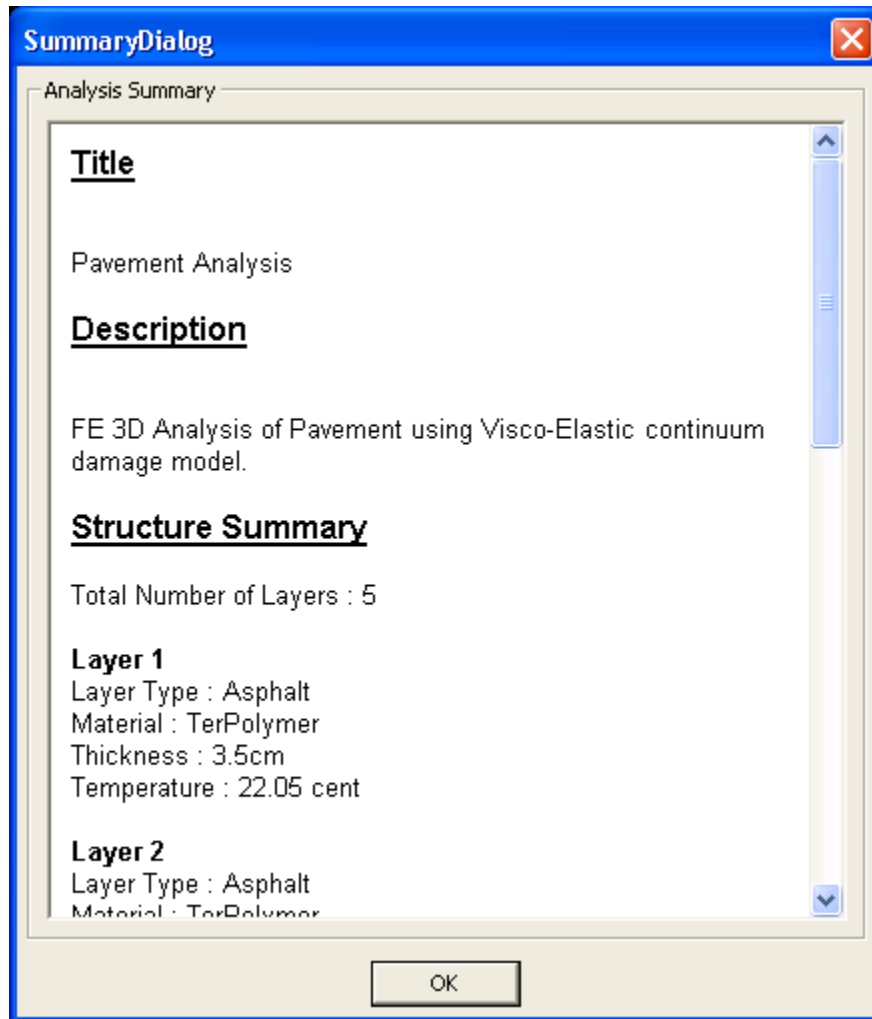


Figure 220. Screen capture. Summary dialog.

A short explanation of the entry fields is given below.

A.2.10.1. Control Actions

OK: This control closes the dialog.

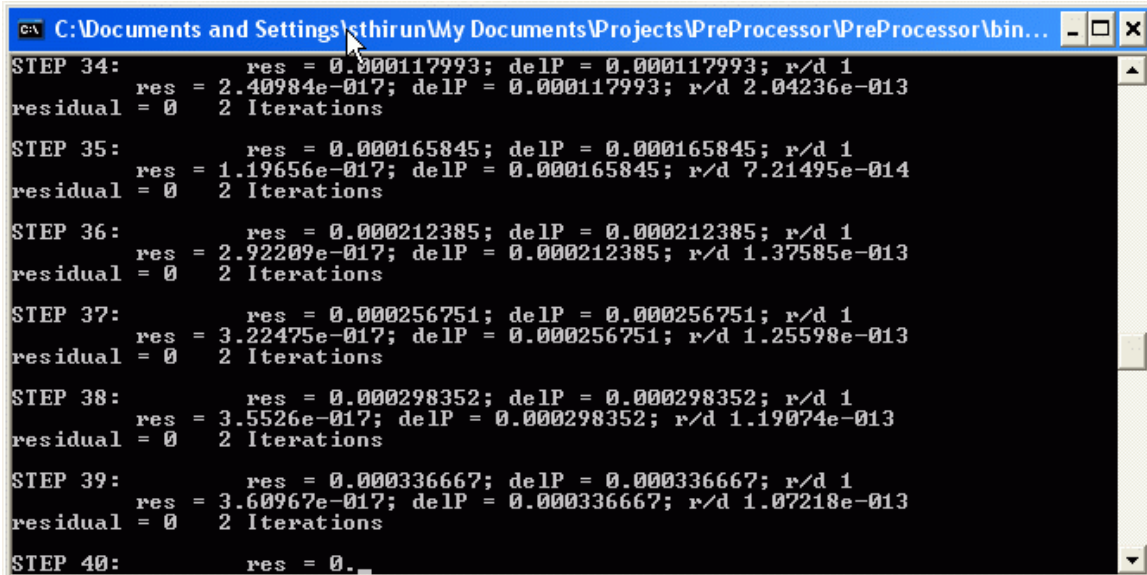
A.2.11. Generating an Input File

The user can generate an input file for FEP++ by choosing the Generate Input File item in the Control Panel. The user is prompted to specify a location for saving the generated file, and the file is created at that location. This can be used to configure multiple analyses and to store the generated input files that can then be run in a batch process.

A.2.12. Running Analysis

Figure 221 shows a screenshot of the view when an analysis is being run. The finite element analysis can be started by clicking the Run Analysis item in the Control Panel. When a user starts a new analysis, it is launched in a separate command window that displays the output from

FEP++. Once the analysis is completed, the window is closed, and the results are gathered and stored at the location of the current “db” file.



```
C:\Documents and Settings\sthirun\My Documents\Projects\PreProcessor\PreProcessor\bin...
STEP 34:      res = 0.000117993; delP = 0.000117993; r/d 1
            res = 2.40984e-017; delP = 0.000117993; r/d 2.04236e-013
            residual = 0 2 Iterations
STEP 35:      res = 0.000165845; delP = 0.000165845; r/d 1
            res = 1.19656e-017; delP = 0.000165845; r/d 7.21495e-014
            residual = 0 2 Iterations
STEP 36:      res = 0.000212385; delP = 0.000212385; r/d 1
            res = 2.92209e-017; delP = 0.000212385; r/d 1.37585e-013
            residual = 0 2 Iterations
STEP 37:      res = 0.000256751; delP = 0.000256751; r/d 1
            res = 3.22475e-017; delP = 0.000256751; r/d 1.25598e-013
            residual = 0 2 Iterations
STEP 38:      res = 0.000298352; delP = 0.000298352; r/d 1
            res = 3.5526e-017; delP = 0.000298352; r/d 1.19074e-013
            residual = 0 2 Iterations
STEP 39:      res = 0.000336667; delP = 0.000336667; r/d 1
            res = 3.60967e-017; delP = 0.000336667; r/d 1.07218e-013
            residual = 0 2 Iterations
STEP 40:      res = 0.
```

Figure 221. Screen capture. FEP++ analysis in progress.

REFERENCES

1. Kim, Y.R. and Little, D.N. (1990). "One-Dimensional Constitutive Modeling of Asphalt Concrete." *ASCE Journal of Engineering Mechanics*, Vol. 116, No. 4, pp. 751–772.
2. Lee, H.J. (1996). *Uniaxial Constitutive Modeling of Asphalt Concrete Using Viscoelasticity and Continuum Damage Theory*, Ph.D. Dissertation, North Carolina State University, Raleigh, NC.
3. Lee, H.J. and Kim, Y.R. (1998a). "A Uniaxial Viscoelastic Constitutive Model for Asphalt Concrete under Cyclic Loading." *ASCE Journal of Engineering Mechanics*, Vol. 124, No. 1, pp. 32–40.
4. Lee, H.J. and Kim, Y.R. (1998b). "A Viscoelastic Continuum Damage Model of Asphalt Concrete with Healing." *ASCE Journal of Engineering Mechanics*, Vol. 124, No. 11, pp. 1,224–1,232.
5. Daniel J.S. and Kim, Y.R. (2002). "Development of a Simplified Fatigue Test and Analysis Procedure Using a Viscoelastic Continuum Damage Model." *Journal of the Association of Asphalt Paving Technologists*, Vol. 71, pp. 619–650.
6. Chehab, G.R., Kim, Y.R., Schapery, R.A., Witzack, M., and Bonaquist, R. (2002). "Time-Temperature Superposition Principle for Asphalt Concrete Mixtures with Growing Damage in Tension State." *Asphalt Paving Technology, AAPT*, Vol. 71, pp. 559–593.
7. Chehab, G.R., Kim, Y.R., Schapery, R.A., Witzack, M., and Bonaquist, R. (2003). "Characterization of Asphalt Concrete in Uniaxial Tension Using a Viscoelastoplastic Model." *Asphalt Paving Technology, AAPT*, Vol. 72, pp. 315–355.
8. Schapery, R.A. (1984). "Correspondence Principles and a Generalized J-integral for Large Deformation and Fracture Analysis of Viscoelastic Media." *International Journal of Fracture*, Vol. 25, pp. 195–223.
9. Schapery, R.A. (1990). "A Theory of Mechanical Behavior of Elastic Media with Growing Damage and Other Changes in Structure." *Journal of the Mechanics and Physics of Solids*, Vol. 38, pp. 215–253.
10. Schapery, R.A. (1999). "Nonlinear Viscoelastic and Viscoplastic Constitutive Equations with Growing Damage." *International Journal of Fracture*, Vol. 97, pp. 33–66.
11. Schapery, R.A. (1987). "Deformation and Fracture Characterization of Inelastic Composite Materials using Potentials." *Polymer Engineering and Science*, Vol. 27, Issue 1, pp. 63–76.
12. Underwood, B.S., Kim, Y.R., and Guddati, M.N. (2006). "Characterization and Performance Prediction of ALF Mixtures Using a Viscoelastoplastic Continuum Damage Model." *Asphalt Paving Technology, AAPT*, Vol. 75, pp. 577–636.
13. Kim, Y.R., Guddati, M.N., Underwood, B.S., Yun, T.Y., Subramanian, V., and Heidari, A.H. (2005). *Characterization of ALF Mixtures Using the Viscoelastoplastic Continuum Damage Model: Final Report*, Project No. DTFH61-03-H-00116, Federal Highway Administration, Washington, DC.
14. Uzan, J. (1996). "Asphalt Concrete Characterization for Pavement Performance Prediction." *Asphalt Paving Technology, AAPT*, Vol. 65, pp. 573–607.
15. Perzyna, P. (1971). "Thermodynamic Theory of Viscoplasticity." *Advances in Applied Mechanics*, Vol. 11, pp. 313–354.
16. Park, S.W. and Schapery, R.A. (1999). "Methods of Interconversion Between Linear Viscoelastic Material Functions: Part I—A Numerical Method based on Prony Series." *International Journal of Solids and Structures*, Vol. 36, pp. 1,653–1,657.

17. Schapery, R.A. (1961). *A Simple Collocation Method for Fitting Viscoelastic Models to Experimental Data*, Report No. GALCIT SM 61-23A, California Institute of Technology, Pasadena, CA.
18. American Association of State Highway and Transportation Officials. (2003). *TP-62 Standard Method of Test for Determining Dynamic Modulus of Hot-Mix Asphalt Concrete Mixtures*, Washington DC.
19. Daniel J.S. (2001). *Development of a Simplified Fatigue Test and Analysis Procedure Using a Viscoelastic, Continuum Damage Model and Its Implementation to WesTrack Mixtures*. Ph.D. Dissertation, North Carolina State University, Raleigh, NC.
20. Chehab, G. (2002). *Characterization of Asphalt Concrete in Tension Using a Viscoelastoplastic Model*. Ph.D. Dissertation, North Carolina State University, Raleigh, NC.
21. Park, S.W., Kim, Y.R., and Schapery, R.A. (1996). "A Viscoelastic Continuum Damage Model and Its Application to Uniaxial Behavior of Asphalt Concrete." *Mechanics of Materials*, Vol. 24, No. 4, pp. 241–255.
22. Kim, Y.R. and Chehab, G. (2004). *Development of Viscoelastoplastic Continuum Damage Model for Asphalt-Aggregate Mixtures*, Part of NCHRP Report 547, CRP CD-46, National Research Council, Transportation Research Board, Washington, DC.
23. Chou, P.C. and Pagano, N.J. (1967). *Elasticity: Tensor, Dyadic and Engineering Approaches*, D. Van Nostrand Company, Inc. Princeton.
24. Park, S.W. (1996). *Development of a Nonlinear Thermo-Viscoelastic Constitutive Equation for Particulate Composites with Growing Damage*, Ph.D. Dissertation, University of Texas Austin, TX.
25. Uzan, J., Perl, M., and Sides, A. (1985). "Viscoelastoplastic Model for Predicting Performance of Asphalt Mixtures." *Transportation Research Record 1043*, pp. 78–79, Washington, DC.
26. Scarpas, A., Al-Khoury, R., Van Gurp, C., and Erkens, S. (1997). "Finite Element Simulation of Damage Development in Asphalt Concrete Pavements." In *Proceedings of the 8th International Conference on Asphalt Pavements*, pp. 673–692, University of Washington, Seattle, WA.
27. Desai C.S. and Zhang, D. (1987). "Viscoplastic Model for Geologic Materials with Generalized Flow Rule." *International Journal for Numerical and Analytical Methods in Geomechanics*, Vol. 11, pp. 603–620.
28. Gibson, N.H. (2006). *A Viscoelastoplastic Continuum Damage Model for the Compressive Behavior of Asphalt Concrete*, Ph.D. Dissertation, University of Maryland, College Park, MD.
29. Saadeh, SAR. (2005). *Characterization of Asphalt Concrete Using Anisotropic Damage Viscoelastic-Viscoplastic Model*, Ph.D. Dissertation. Texas A&M University, College Station, TX.
30. Von Mises R. (1928). "Mechanik der plastischen Formänderung von Kristallen." *ZAMM*, Vol. 8, pp. 161–185.
31. Perzyna, P. (1963). "The Constitutive Equations for Rate Sensitive Plastic Materials." *Quarterly of Applied Mathematics*, Vol. 20, pp. 321–332.
32. Prager, W. (1956). "A New Method of Analyzing Stresses and Strains in Work Hardening Plastic Solids." *Journal of Applied Mechanics*, Vol. 23, pp. 493–496.
33. Armstrong, P.J. and Frederick, C.O. (1966). *A Mathematical Representation of the Multiaxial Bauscinger Effect*, CEGB Report No. RD/B/N 731.

34. Chaboche J.L. (1986). "Time-Independent Constitutive Theories for Cyclic Plasticity." *International Journal of Plasticity*, Vol. 2, pp. 149–188.
35. Desai, C.S., Somasundaram, S., and Frantziskonis, G. (1986). "A Hierarchical Approach for Constitutive Modeling of Geologic Materials." *International Journal of Numerical Analytical Methods in Geomechanics*, Vol. 10, pp. 225–257.
36. Erkens, S.M., Liu, X., Scarpas, T., Molenaar, A.A.A., and Blaauwendraad, J. (2003). *Modeling of Asphalt Concrete—Numerical and Experimental Aspects, Recent Advances in Materials Characterization and Modeling of Pavement Systems* (E. Tutumluer, Y. M. Najjar, and E. Masad, eds.), Geotechnical Special Publication No. 123, pp. 160–177, ASCE, Reston, VA.
37. Krieg R.D. and Krieg, D.B. (1977). "Accuracies of Numerical Solution Methods for the Elastic-Perfectly Plastic Model." *ASME Journal of Pressure Vessel Technology*, Vol. 99, pp. 510–515.
38. Krempl, E. (1987). "Models of Viscoplasticity-Some Comments on Equilibrium (Back) Stress and Drag Stress." *Acta Mech*, Vol. 69, pp. 25–42.
39. Krempl, E. and Khan, F. (2003). "Rate (Time)-Dependent Deformation Behavior: An Overview of Some Properties of Metals and Solid Polymers." *International Journal of Plasticity*, Vol. 19, No. 7, pp. 1,069–1,095.
40. Cernocky, E.P. and Krempl, E. (1979). "A Nonlinear Uniaxial Integral Constitutive Equation Incorporating Rate Effects, Creep and Relaxation." *International Journal of Nonlinear Mechanics*, Vol. 14, No. 2, pp. 183–203.
41. Kwnagsoo, H.O. (2006). "Unified Constitutive Equations of Viscoplastic Deformation: Development and Capabilities." *Japanese Society of Mechanical Engineers*, Vol. 49, No. 1, pp. 138–146.
42. Witczak, W.M., Kaloush, K., Pellinen, T., El-Basyouny, M., and Von Quintus, H. (2000). *Simple Performance Test for Superpave Mix Design*, NCHRP Report 465, National Research Council, Transportation Research Board, Washington, DC.
43. Myers, L.A., Roque, R., and Ruth, B.E. (1998). "Mechanisms of Surface-Initiated Longitudinal Wheel Path Cracks in High Type Bituminous Pavements." *Asphalt Paving Technology, AAPT*, Vol. 67, pp. 401–432.
44. Myers, L.A. and Roque, R. (2001). "Evaluation of Top-Down Cracking in Thick Asphalt Pavements and the Implications for Pavement Design." *Transportation Research Circular: Perpetual Bituminous Materials*, pp. 113–122, Washington, DC.
45. Pellinen, T. (2002). *Evaluation of Surface (Top-Down) Longitudinal Wheel Path Cracking in Indiana*, Joint Transportation Research Program, Purdue University, West Lafayette, IN.
46. Rao Tangella, S.C., Craus, J., Deacon, J.A., and Monismith, C.L. (1990), *Summary Report on Fatigue Response of Asphalt Mixtures*, Report TM-UCB-A-003A-89-3. Strategic Highway Research Program, National Research Council, Washington, DC.
47. Deacon, J.A., Tayebali, A.A., Rowe, G.M., and Monismith, C.L. (1995). "Validation of SHRP A-003A Flexural Beam Fatigue Test." *Engineering Properties of Asphalt Mixtures and the Relationship to Their Performance*, ASTM STP 1265, pp. 21–36.
48. Ha, K. and Schapery, R.A. (1998). "A Three-Dimensional Viscoelastic Constitutive Model for Particulate Composites with Growing Damage and Its Experimental Validation." *International Journal of Solids and Structures*, Vol. 35, No. 26, pp. 3,497–3,517.
49. Pellinen, T. (2001). *Investigation of the Use of Dynamic Modulus as an Indicator of Hot-Mix Asphalt Performance*, Ph.D. Dissertation, Arizona State University, Tempe, AZ.

50. Ferry, J.D. (1961). *Viscoelastic Properties of Polymers*, John Wiley and Sons, Inc., New York.
51. Petersen, J.C., Robertson, R.E., Branthaver, J.F., Harnsberger, P.M., Duvall, J.J., Kim, S.S., Anderson, D.A., Christensen, D.W., and Bahia, H.U. (1994). *Binder Characterization and Evaluation: Volume I*, Strategic Highway Research Program, National Research Council, Washington, DC.
52. Desai, C.S. (2001). *Mechanics of Materials and Interfaces: The Disturbed State Concept*. CRC Press, Boca Raton, FL.
53. Gibson, N.H., Schwartz, C.W., Schapery, R.A., and Witczak, M.W. (2003). "Viscoelastic, Viscoplastic, and Damage Modeling of Asphalt Concrete in Unconfined Compression." *Transportation Research Record*, No. 1860, pp. 3–15.
54. Kim, Y.R., Seo, Y., King, M., and Momen, M. (2004). "Dynamic Modulus Testing of Asphalt Concrete in Indirect Tension Mode." Presented at the Transportation Research Board 83rd Annual Meeting (CD ROM), National Research Council, Washington, DC.
55. Underwood, S., Heidari, A.H., Guddati, M., and Kim, Y.R. (2005). "Experimental Investigation of Anisotropy in Asphalt Concrete." *Transportation Research Record*, No. 1929, pp. 238–247, Washington, DC.
56. Advanced Asphalt Technologies. (2004). Asphalt Concrete Mixture Performance Testing and Analysis: Western Research Institute Test Sections, Interstate 15, Clark County, NV.
57. Hinterhoelzl R.M. and Schapery, R.A. (2004). "FEM Implementation of a Three-Dimensional Viscoelastic Constitutive Model for Particulate Composites." *Mechanics of Time-Dependent Materials*, Vol. 8, pp. 65–94.
58. Reese, R. (1997). "Properties of Aged Asphalt Binder Related to Asphalt Concrete Fatigue Life." *Journal of the Association of Asphalt Paving Technologists*, Vol. 66, pp. 604–632.
59. ARA Inc. (2004). "Guide for Mechanistic-Empirical Design of New and Rehabilitated Pavement Structures." NCHRP Final Report 1-37A, National Research Council, Transportation Research Board, Washington, DC.

